Vlasov Simulations of Kinetic Enhancement of Raman Backscatter in Laser Fusion Plasmas

by

David J. Strozzi

A.B., Physics
Princeton University (1999)

Submitted to the Department of Physics
in partial fulfillment of the requirements for the degree of

Doctor of Philosophy

at the

MASSACHUSETTS INSTITUTE OF TECHNOLOGY

October 2005

Signature of Author .....
Department of Physics
7 October 2005

Certified by .....
Abraham Bers
Professor of Electrical Engineering and Computer Science
Thesis Supervisor

Accepted by .....
Thomas J. Greytak
Professor of Physics, Associate Department Head for Education

Vlasov Simulations of Kinetic Enhancement of Raman Backscatter in Laser Fusion Plasmas

by

David J. Strozzi

Submitted to the Department of Physics
on 7 October 2005, in partial fulfillment of the
requirements for the degree of
Doctor of Philosophy

Abstract

Stimulated Raman scattering (SRS) is studied in plasmas relevant to inertial confinement fusion (ICF). The Eulerian Vlasov-Maxwell code ELVIS was developed and run for this purpose. Plasma waves are heavily Landau damped in the regimes of interest, and coupled-mode theory predicts back-scattered SRS is a convective instability. Simulations in a finite length, homogeneous plasma show electron trapping drastically elevates the reflected light over convective gain values ("kinetic enhancement"). Average reflectivities are $\sim 10\%$, while the instantaneous reflectivity is chaotic and does not reach a steady state. Trapping reduces the plasma-wave Landau damping and downshifts the observed frequencies from their linear values. Two longitudinal acoustic ($\omega \propto k$) features and light from possible stimulated electron acoustic scattering (SEAS) are present. The phase-matched SEAS plasmon lies on the observed acoustic mode with phase velocity $1.3(T_e/m_e)^{1/2}$.

As the pump laser intensity is increased or the electron temperature is decreased, SRS transitions sharply from the coupled-mode steady state to kinetically enhanced levels. Enhancement happens for different back SRS seed levels and monochromatic or broadband seeds. Simulations with a Krook relaxation operator to mimic speckle sideloss display enhancement when resonant electrons complete a bounce orbit before escaping, with a sharp onset as the relaxation rate varies. The sudden development of kinetic enhancement as parameters change suggests trapping makes SRS absolutely unstable. Simulations with mobile ions give kinetic enhancement until a burst of activity occurs near the laser entrance, after which back SRS is low. The burst contains several Brillouin and Raman re-scatters and subsequent Langmuir decay instability (LDI), although no LDI of back SRS is seen.

SRS runs in a density gradient show kinetic enhancement for long scale lengths and coupled-mode convective levels for shorter ones. The reflectivity is higher when the pump propagates toward higher, rather than lower, density. The amplitude of externally-driven plasma waves in a density gradient is also enhanced over linear levels and displays a similar directional asymmetry.

These results imply kinetic enhancement of SRS may be a concern in hohlraum plasmas for ICF experiments such as the National Ignition Facility.

Thesis Supervisor: Abraham Bers
Title: Professor of Electrical Engineering and Computer Science

Contents

Foreword **7**

Preamble **8**

1 Laser-Plasma Interactions and Inertial Confinement Fusion **14**

1.1 Inertial confinement fusion 14

1.1.1 ICF overview: direct and indirect drive 14

1.1.2 Indirect-drive coronal conditions: plasmas and laser beams 16

1.2 Laser-plasma interactions (LPI) 16

1.2.1 Raman scattering 18

1.2.2 Other LPI 19

1.2.3 Relevance of LPI to ICF 19

1.3 Past work on Raman scattering 20

1.4 Experimental motivation 22

1.5 Findings of the thesis 24

1.6 Thesis outline 25

2 Coupled-Mode Descriptions of SRS without Trapping **27**

2.1 Fluid-PDE SRS equations 28

2.1.1 Nonlinear PDE model with pump depletion 29

2.1.2 Action amplitude envelope representation 32

2.2 Linear fluid dispersion relation for fixed pump 34

2.3 Coupled-mode equations (CMEs) 37

2.3.1 Derivation of the CMEs 38

2.3.2 CME conservation laws, Manley-Rowe relations 39

2.4 Instability analysis of the CMEs . . . 41
2.5 Kinetic description of SRS . . . 44
2.5.1 Kinetic linear dispersion relation . . . 45
2.5.2 CMEs from kinetic description . . . 47
2.5.3 Strong damping limit (SDL): steady-state solution . . . 49
2.6 SRS in ICF hohlraums . . . 51
2.6.1 Plasma conditions and electron-ion collisions . . . 51
2.6.2 Linear predictions for SRS growth . . . 53
2.6.3 Comparison with other LPI . . . 56

3 Simulations of Raman Scattering from Homogeneous Plasmas 58

3.1 The base case run `BC1` . . . 59
3.1.1 Run parameters and setup . . . 59
3.1.2 Reflected and transmitted light . . . 62
3.1.3 Plasma waves . . . 64
3.2 Pump strength I_0 scan . . . 70
3.3 Dependence on electron temperature . . . 72
3.4 Noise levels and seeding . . . 75
3.4.1 Thermal radiation via Kirchoff's law . . . 75
3.4.2 Thermal radiation via the fluctuation-dissipation theorem . . . 77
3.4.3 Role of seed strength . . . 79
3.4.4 Role of edge Krook operator . . . 81
3.5 Seed bandwidth and possible SEAS . . . 83
3.6 Kinetic ions . . . 85
3.6.1 LDI . . . 86
3.6.2 SBS . . . 87
3.6.3 Simulation with kinetic ions . . . 88
3.7 Loss mechanisms . . . 93
3.7.1 Speckle sideloss . . . 94
3.7.2 1-D collisions . . . 94
3.7.3 pitch-angle scattering . . . 95
3.7.4 Simulations with sideloss . . . 96

4 Trapping Effects in Electron Plasma Waves **98**

4.1 Trapping overview . . . 98

4.2 Landau damping reduction by trapping . . . 100

4.3 Nonlinear frequency shift . . . 103

4.4 Natural and $\varepsilon_r = 0$ EPWs . . . 105

4.5 Driven plasma waves in a density gradient . . . 107

4.5.1 Derivation of the envelope equation . . . 108

4.5.2 Analytic ODE solution . . . 109

4.5.3 The strong damping limit (SDL) . . . 111

4.5.4 Numerical examples . . . 112

4.5.5 Vlasov simulations . . . 114

5 Simulations of SRS from Inhomogeneous Plasmas **116**

5.1 Coupled-mode equations in a density gradient . . . 116

5.1.1 Derivation of inhomogeneous CMEs . . . 116

5.1.2 The strong damping limit . . . 118

5.1.3 Comparison with undamped solution . . . 120

5.2 SRS simulations in a density gradient . . . 120

6 Conclusions and Future Work **125**

6.1 Conclusions . . . 125

6.2 Future work . . . 127

A ELVIS: an Eulerian Vlasov-Maxwell Solver **130**

A.1 Overview: continuum methods for kinetic equations . . . 130

A.2 ELVIS model, geometry, and governing equations . . . 131

A.2.1 Kinetic equation . . . 132

A.2.2 Electromagnetic and transverse fields . . . 133

A.3 Grids . . . 134

A.4 Time evolution . . . 135

A.4.1 The overall time step . . . 135

A.4.2 Evolving f: splitting the time step . . . 136

A.4.3 Evolving f: shifting by interpolation . . . 137

A.4.4 Evolving f: the Krook operator . . . 140
A.4.5 Solving for E_x . . . 140
A.4.6 Evolving the transverse fields . . . 142
A.5 Code logistics . . . 143
A.6 Diagnostics . . . 143
A.6.1 Conserved quantities . . . 144
A.6.2 Instantaneous frequency . . . 144
A.7 Benchmarks . . . 145
A.7.1 Electron dynamics: plasma waves and recurrence . . . 145
A.7.2 Ion dynamics: ion acoustic waves . . . 146

B Plasma Waves Driven by Two Light Waves **148**

Bibliography **151**

Foreword

Many people deserve praise for assisting me with my thesis. First I thank my parents for all their support and love, and dedicate this thesis to them. Prof. Abraham Bers has been a dedicated, interested, and patient mentor throughout the last several years. I am especially grateful to him for helping to arrange my summer 2004 internship at the Lawrence Livermore National Laboratory with Drs. Ed Williams and A. Bruce Langdon. My once and future Livermore advisors have provided invaluable mentorship, and in particular sparked my interest in plasma inhomogeneity. Dr. Abhay K. Ram gave much advice in the early stages of this work and in my first first-author physics paper [1]. The ELVIS code would never have worked without the generous guidance from and provision of the initial source code by Dr. Magdi M. Shoucri. It gave him much satisfaction to see me benefiting from and extending his work; similarly I look forward to others making use of the ELVIS code. I am also grateful to Dr. Jesus Ramos for advising my research on magnetic reconnection at the start of my graduate work. Several people, including Dr. Bedros Afeyan, Dr. Larry Suter, Dr. Ralph Schneider, and Prof. Miklos Porkolab were instrumental in securing funding for the later stages of this work. My thesis committee members (Prof. Bruno Coppi, Prof. Porkolab, and Dr. Rick Temkin) all gave useful guidance. I thank Laura von Bosau, Carol Arlington, Ted Baker, and the rest of the MIT administrative staff for taking care of many practical and bureaucratic matters. I may not have become interested in plasma physics were it not for a summer internship with Profs. Wendell Horton and Phil Morrison of UT Austin. Many other teachers and advisors throughout my lengthy education deserve acknowledgement as well.

No one makes it through a thesis without generous support and understanding from friends. I especially thank Lynn Johnson, Darius Torchinsky, Jeffrey Swers, Daniel Giblin, Daniel Greenbaum, Mukund Thattai, Andrew Linshaw, James Barabas (thanks for the laptop screen), and the usual Mafia players.

I warn the reader that this thesis contains color figures, some not entirely to my liking. The best way to view them may be in an electronic version of the thesis, available upon request. Only pages where color is essential were printed in color.

Biographical Note: David Jerome Strozzi was born on June 19, 1977 and spent his entire childhood in Edison, New Jersey. He entered Princeton University in 1995 and received a A. B. degree in physics with High Honors in 1999. In 1999 David began graduate school in physics at the Massachusetts Institute of Technology to research plasma physics and nuclear fusion. He completed his Ph.D. in 2005. His interest in plasma physics is partly motivated by fusion energy, and he is more generally interested in energy and environmental issues.

Of the many things I've learned in graduate school, one of the most important was best summarized by Calvin Coolidge:

> Nothing in the world can take the place of Persistence. Talent will not; nothing is more common than unsuccessful men with talent. Genius will not; unrewarded genius is almost a proverb. Education will not; the world is full of educated derelicts. Persistence and determination alone are omnipotent.

Preamble

- **Fourier conventions:** We Fourier decompose a physical field u as $u = (1/2)\tilde{u}\exp i\psi + c.c.$ For $\tilde{u}$ and ψ real, $u = \tilde{u}\cos\psi$. We sometimes omit the tilde when the context (PDE with ∂_x, ∂_t or algebraic equation with k, ω) indicates an equation's domain.
- **Complex numbers:** x_r, x_i are the real and imaginary parts of a complex x: $x = x_r + ix_i$. In polar form, $x = r\exp i\theta$. The argument of a complex number $\arg x \equiv \arctan(x_i/x_r) = \theta$.
- **Stimulated Raman Scattering:** We label the pump light wave (laser) mode 0, the daughter scattered light wave mode 1, and the daughter plasma wave mode 2.
- **Units:** We use SI units, except temperatures are in eV. We use standard SI abbreviations, like ns, μm, W, Ω for nanosecond, micron, Watt, Ohm. We also define some quantities in commonly-used units with subscripts:

  λ_μ: wavelength in microns I_{15}: intensity in 10^{15} W/cm^2 n_{26}: number density in 10^{26} m^{-3} T_{kV}: temperature in keV.
- **Density profiles:** We use $n_B(x)$ for the time-independent background electron density. For a homogeneous plasma, n_B = constant. When considering inhomogeneous plasmas we frequently use $n_0 = n_B(x_0)$, the density at a reference point x_0. For homogeneous plasmas we use n_B and n_0 interchangeably.
- **Mathematics:** We follow the notation of Abramowitz and Stegun [2] for special functions whenever possible.

Acronym	**Meaning**
a.u.	arbitrary units
BGK	Bernstein-Greene-Kruskal (not Bhatnagar-Gross-Krook)
c.c.	complex conjugate
CMEs	coupled-mode equations
$\varepsilon_r = 0$ mode	longitudinal "mode" found by solving $\varepsilon_r(k_r, \omega_r) = 0$; see Chap. 4
e^-; e	electron; positron charge
EDI	electromagnetic decay instability: EPW→EMW+IAW
EMW, e/m	electromagnetic wave (light wave, photon), electromagnetic
EPW	electron plasma wave (plasmon)
SBS	stimulated Brillouin scattering: EMW→EMW+IAW
(F,B)SRS	(forward, backward) stimulated Raman scattering: EMW→EMW+EPW
IAW	ion acoustic wave (phonon)
ICF	inertial confinement fusion
Krook	Bhatnagar-Gross-Krook relaxation operator
LDI	Langmuir decay iInstability: EPW→EPW+IAW
(L,R)HS	(left, right)-hand side of an equation
LPI	laser-plasma interactions
LSV	linearized spatial variation (see p. 109; just keep $\varepsilon_r \approx \varepsilon_{xr}x$)

Acronym	Meaning
NIF	National Ignition Facility
(O,P)DE	(ordinary, partial) differential equation
PIC	particle-in-cell
PPD	plasmon-phonon decay: EMW→EPW+IAW
SCS	stimulated Compton scattering
SDL	strong damping limit
SEAS	stimulated electron acoustic scattering: EMW→EMW+EAW
TPD	two plasmon decay: EMW→EPW+EPW

Definitions and Notation

Sym.	Name	Definition	Comment
e	positron charge	1.6022×10^{-19} C	positive
m_e	e^- mass	9.1094×10^{-31} kg	511 keV/c^2
$n_B(x)$	background e^- density	#/volume	$n_B = (\omega_p^2/\omega_0^2)\, n_c$
n_0, ω_{p0}	reference n_B, ω_p	$n_0 = n_B(x_0)$	x_0 = reference point
T_s	species temperature		
m_s	species mass		
Z_s	species charge state	$Z_s = q_s/e$	
ω_p	e^- plasma frequency	$\omega_p^2 = n_B e^2/(\varepsilon_0 m_e)$	$\omega_p(\text{fs}^{-1}) = 0.564 n_{B,26}^{1/2}$
λ_D	e^- Debye length	$\lambda_D^2 = \varepsilon_0 T_e/(n_0 e^2)$	$\lambda_D(\text{nm}) = 23.5\left(\frac{T_{e,kV}}{n_{B,26}}\right)^{1/2}$
v_{Ts}	species thermal speed	$v_{Ts} = \omega_{ps}\lambda_{Ds} = \left(\frac{T_s}{m_s}\right)^{1/2}$	$v_{Ts} = 0.0442 T_{s,kV}^{1/2}\left(\frac{m_e}{m_s}\right)^{1/2}$
N_λ	e^- in Debye cube	$N_\lambda = n_0\lambda_D^3$	$N_\lambda = 1300\, T_{e,kV}^{3/2}/n_{B,26}^{1/2}$
d_e	e^- skin depth	$d_e = c/\omega_p = \frac{\lambda_{0v}}{2\pi}\left(\frac{n_c}{n_B}\right)^{1/2}$	$d_e(\mu\text{m}) = 0.531 n_{B,26}^{-1/2}$
ν_{ei}	e^--ion collision freq.	$\nu_{ei}/\omega_p = 0.021 f_i Z_i^2 \log\Lambda/N_\lambda$	$f_i = n_i/n_0$

GENERAL WAVES

$\vec{k}$, k	wavevector, wavenumber	$\vec{k} = \nabla\psi$, $k = \lvert\vec{k}\rvert$	
ω	frequency	$\omega = -\partial\psi/\partial t$	
ψ	phase	$\psi = \int_{x_a}^{x} d\vec{x}' \cdot \vec{k}(x') - \omega t$	allows for $k(x)$
$\vec{v}_p$	phase velocity	$\vec{v}_p = (\omega/k^2)\vec{k}$	
$\vec{v}_g$	group velocity	$\vec{v}_g = \partial\omega/\partial\vec{k}$	
ν	time damping rate, s^{-1}	$\nu = -\operatorname{Im}\omega$	
σ	space damping rate, m^{-1}	$\sigma = \nu/\lvert v_g\rvert > 0$	$k_i = \sigma\vec{v}_g/\lvert\vec{v}_g\rvert$
$\vec{E}$	electric field amplitude	$\vec{E}(\vec{x},t) = \frac{1}{2}\vec{E}\exp i\psi + cc$	
W	energy density	$\frac{\varepsilon_o\omega}{4}\vec{E}^* \cdot \partial_\omega \overleftrightarrow{D}^h \cdot \vec{E}$	$\overleftrightarrow{D}$ = dispersion tensor
N	action density	$N = W/\omega = aa^*$	
a	action amplitude	$a = N^{1/2}\exp i\theta$	$\arg a = \arg E$
$\vec{Z}$	action flux	$\vec{Z} = \vec{v}_g N$	
Δ	dispersion factor	$\Delta = -\omega^2 + v_p^2 k^2 + \omega_p^2$	← fluid example
δ	detuning frequency	$\delta = \Delta/(2\omega)$	

PLASMA WAVES, TRAPPING

χ	susceptibility	$\chi = -\frac{1}{2(k\lambda_D)^2} Z'(\zeta)$	Z: plasma dispersion func.
$\hat{\varepsilon}$	permittivity	$\hat{\varepsilon} = 1 + \chi$	dielectric $\varepsilon = \varepsilon_0 \hat{\varepsilon}$
ζ	normalized v_p	$\zeta = v_p/(v_T\sqrt{2})$	$\gg 1$ in fluid limit
v_g	group vel.	$-\partial_k \hat{\varepsilon}/\partial_\omega \hat{\varepsilon}$	$\approx 3v_{Te}^2/v_p$ (fluid limit)
ν	time damping rate, > 0	$\nu = \hat{\varepsilon}_i/\partial_\omega \hat{\varepsilon}_r$	
σ	space damping rate, > 0	$\sigma = \nu/\lvert v_g\rvert$	$= -\mathrm{sgn}(v_g)\,\hat{\varepsilon}_i/\partial_k \hat{\varepsilon}_r$
n_1, $\hat{n}$	wave amplitude	$\delta n = n_1 \cos\psi$	$\hat{n} \equiv n_1/n_0$
v_{tr}	trapping island half-width	$v_{tr} = 2\frac{\omega_B}{k} = 2\sqrt{\frac{eE}{m_e k}}$	$= 2v_{Te}\sqrt{\frac{e\phi}{T_e}} = 2\frac{\omega_p}{k}\hat{n}^{1/2}$
ω_B	bounce frequency	$\omega_B = \sqrt{\frac{eEk}{m_e}}$	$= kv_{Te}\sqrt{\frac{e\phi}{T_e}} = \omega_p \hat{n}^{1/2}$
k_B	bounce wavenumber	$k_B = \omega_B/v_p$	$= k\frac{\omega_p}{\omega}\hat{n}^{1/2}$
τ_B	bounce period	$\tau_B = 2\pi/\omega_B$	
L_B	bounce length	$L_B = v_p \tau_B$	$= 2\pi\frac{\omega}{\omega_p}\frac{1}{k}\hat{n}^{-1/2}$
$\hat{f}$	normalized 1-D dist.	$(v_T\sqrt{2\pi})^{-1} e^{-v^2/2v_T^2}$	$\int dv\ \hat{f} = 1$

E/M WAVES

Subscripts v, p indicate a quantity (e.g., wavelength λ) in vacuum, plasma respectively.

c	speed of light in vacuum	$c = 299.79\ \mu$m/ps	
Z_0	free-space impedance	$Z_0 = \sqrt{\mu_0/\varepsilon_0}$	$= 1/(\varepsilon_0 c) = 376.73\ \Omega$
P_{em}	useful e/m power factor	$P_{em} = m_e^2 c^5 \varepsilon_0/e^2$	0.693 GW
η	index of refraction	$\eta = c/v_p = \sqrt{1 - \frac{n_0}{n_c}}$	$v_g/c = \eta$
n_c	critical density	$\omega^2 = n_c e^2/(\varepsilon_0 m_e)$	$n_{c,26} = 11.1/\lambda_\mu^2$
I	intensity (W/m^2)	$I = \frac{1}{2} Z_0^{-1} E^2$	$E(x,t) = E\cos\psi$
E_p	E field in plasma	$E_p = (2Z_0 I/\eta)^{1/2}$	$E_p = 86.8\left(\frac{I_{0,15}}{\eta}\right)^{1/2}\ \frac{\mathrm{MV}}{\mathrm{mm}}$ E swells by $1/\eta$ vs. vac.
B_p	B field in plasma	$B_p = (2\mu_0 I_0/v_p)^{1/2}$	$B_p = 290(I_{0,15}\eta)^{1/2}$ Tesla B shrinks by η
v_{os}	e^- oscillation (quiver) vel.	$v_{os} = eE/(m_e\omega)$	
v_{os}^2/c^2		$I\lambda_v^2/(2\pi^2 P_{em})/\eta$	$7.3\times10^{-4} I_{15}\lambda_{v,\mu}^2/\eta$
v_{os}^2/v_{Te}^2			$0.374\ I_{15}\lambda_{v,\mu}^2\ /\ (T_{e,kV}\eta)$
B_c	critical B: $\omega_{ce}(B_c) = \omega$	$B_c = 2\pi c m_e/(e\lambda)$	$1.07\times10^4/\lambda_{v,\mu}$ Tesla

THREE-WAVE INTERACTIONS

These are for coupled-mode description. Some are just for SRS. More are defined below in tables for the standard parameters.

K	coupling constant	$\frac{k_2}{\sqrt{\omega_0\omega_1\omega_2}}\frac{\omega_p^2}{\sqrt{8n_Bm_e}}$ (SRS)	units: 1/(time*action)
γ	temporal growthrate	$-\frac{\nu_1+\nu_2}{2}+\sqrt{\gamma_0^2+\left(\frac{\nu_1-\nu_2}{2}\right)^2}$	coupled-mode result
γ_0	undamped growthrate	$K\left\|a_0\right\| = k_2 v_{os0}\frac{\omega_p}{4\sqrt{\omega_1\omega_2}}$	
γ_c	threshold γ	$\sqrt{\nu_1\nu_2}$	$\gamma_0 > \gamma_c$: instability
γ_a	absolute threshold γ	$\frac{1}{2}\sqrt{\left\|v_{g1}v_{g2}\right\|}\left(\sigma_1+\sigma_2\right)$	$\gamma_0 > \gamma_a$: absolute inst.
α	spatial gain rate	$\frac{\sigma_2-\sigma_1}{2}-\sqrt{-\alpha_0^2+\left(\frac{\sigma_1+\sigma_2}{2}\right)^2}$	valid for backscatter
α_0	undamped gain rate	$\alpha_0 = \gamma_0/\sqrt{\left\|v_{g1}v_{g2}\right\|}$	
α_{SDL}	strong damping limit α	$\alpha_{SDL} = \gamma_0^2/\left(\left\|v_{g1}\right\|\nu_2\right)$	for $\left\|\partial_x a_2\right\| \ll \left\|\sigma_2 a_2\right\|$
α_k	kinetic α	$\alpha_k = \frac{2\gamma_0^2\omega_2}{\left\|v_{g1}\right\|\omega_p^2}\,\mathrm{Im}\left[\chi/\hat{\varepsilon}\right]$	SRS

Longitudinal permittivity and the Z function

The longitudinal ($\vec{k}||\vec{E}$) permittivity for a Vlasov (kinetic, collisionless) plasma is $\hat{\varepsilon} = 1+\chi$ where

$$\chi = -\frac{\omega_p^2}{k^2 n_0}\frac{d}{dv_p}\int_{-\infty}^{\infty} dv\,\frac{f_0(v)}{v-v_p}, \qquad v_p = \omega/k. \tag{1}$$

For a Maxwellian f_0, this becomes

$$\chi = -\frac{1}{2\left(k\lambda_D\right)^2}Z'(\zeta), \qquad \zeta = \frac{\omega}{kv_{Te}\sqrt{2}}. \tag{2}$$

χ is the kinetic susceptibility. The natural modes are given by $\hat{\varepsilon} = 0$. Z is the so-called plasma dispersion function [3] and Z' is $dZ(\zeta)/d\zeta$. In terms of the complimentary error function erfc ([2], p. 297), $Z(\zeta) = i\sqrt{\pi}e^{-\zeta^2}\mathrm{erfc}(-i\zeta)$. $\mathrm{erfc}(z) = 1-\mathrm{erf}(z)$ where $\mathrm{erf}(z) \equiv \int_0^z dt\,e^{-t^2}$ is the error function. There are several widely-available numerical routines that calculate the Faddeeva function $w(\zeta) = -i\pi^{-1/2}Z(\zeta)$ [4]. When numerically computing the Z function, we use a Matlab routine by J. A. C. Weideman for $w(\zeta)$ ([5], code available at `http://dip.sun.ac.za/~weideman/research/cef.html`).

We define, for arbitrary complex ζ, $Z(\zeta) = Z_r(\zeta) + iZ_i(\zeta)$ where $Z_r(\zeta) = -2e^{-\zeta^2}\int_0^\zeta dt\ e^{t^2}$ and $Z_i(\zeta) = i\sqrt{\pi}\exp(-\zeta^2)$. The motivation for these definitions is Z_r, Z_i are real, imaginary for real ζ. $Z_r(\zeta_r) = -2w_D(\zeta_r)$ where $w_D(x) = e^{-x^2}\int_0^x dt\ e^{t^2}$ (x is real) is called Dawson's integral ([2] p. 319). In the "fluid limit," for $|x| \gg 1$ and x real, we have [6, App. A]

$$Z_r(|x| \gg 1) \approx -x^{-1} - \frac{1}{2}x^{-3} - \frac{3}{4}x^{-5} + O(x^{-7}); \tag{3}$$

$$Z_r'(|x| \gg 1) \approx x^{-2} + \frac{3}{2}x^{-4} + \frac{15}{4}x^{-6} + O(x^{-8}). \tag{4}$$

$Z_r'(x) = 0$ only at $x = \pm x_0$ where $x_0 = 0.924$. Expanding about x_0 ([7], Eq. (26b)),

$$Z_r'(x) \approx \frac{2}{x_0}(x-x_0) + (x-x_0)^2, \qquad |x-x_0| \ll 1. \tag{5}$$

Standard Parameters

We frequently use a set of reference plasma conditions, called the standard parameters:

$\lambda_0 = 351$ nm; $\quad I_0 = 2\times10^{15}$ W/cm^2; $\quad n_0/n_c = 0.1$; $\quad T_e = 3$ keV.

We sometimes include ions (e.g., for collisional damping). In chapter 2 the ions consist of a 50-50 quasi-neutral hydrogen-helium mixture:

$Z_H, Z_{HE} = (1,2)$; $\quad n_H = n_{He} = n_0/3$; $\quad T_H = T_{He} = T_e/3$; $\quad m_H, m_{He} = (1,4)m_p$.

Elsewhere they are pure helium:

$Z_{HE} = 2$; $\quad n_{He} = n_0/2$; $\quad T_i = T_e/4$; $\quad m_{He} = 4m_p$.

When we use standard parameters but vary, say, T_e, all the other parameters take on these values. "Collisional" vs. "collisionless" standard parameters denotes whether collisional damping of the daughter waves is included (Landau damping of mode 2 always is). We now give numerical values for some quantities in the standard parameters.

Table columns: | symbol | normed: (time, length, vel) in (ω_p^{-1}, d_e, c) | SI-eV | comment |

PLASMA

n_0	1	9.049×10^{26} m^{-3}	
T_e		3 keV	
v_{Te}	0.07662	22.97 μm/ps	
ω_p	1	1.697 rad/fs	
d_e	1	0.17666 μm	c/ω_p, skin depth
λ_D	0.07664	13.54 nm	
$n_0^{-1/3}$		1.03 nm	inter-e^- spacing
N_λ	2244		e^- in Debye cube
$\log\Lambda$	7.88		Coulomb logarithm
ν_{ei}	1.2×10^{-4}	0.210 ps^{-1}	collision freq., total over ions

MODE 0 (PUMP)

I_0		2×10^{15} W/cm^2	intensity
λ_{0v}	1.9869	351 nm	vacuum wavelength
k_{0p}	3	1.6.98 μm^{-1}	k in plasma; $k_{0p}\lambda_D = 0.230$
ω_0	$3.162=\sqrt{10}$	5.367 rad/fs	frequency
n_c	10	9.049×10^{27} m^{-3}	critical density
ν_0		1.051×10^{10} s^{-1}	collisional amplitude damping rate
σ_0^{-1}		2.71 cm	collisional damping length = v_{g0}/ν_0
v_{os0}	0.01342	4.023 μm/ps	e^- osc. vel.; $v_{os0}/v_{Te} = 0.175$
$v_{p0,p}$	1.054	316 μm/ps	phase vel. in plasma
$v_{g0,p}$	0.9488	284 μm/ps	group vel. in plasma
E_{0p}		0.126 MV/μm	wave E field in plasma

MODE 1 (BACKSCATTER)

λ_{1v}	3.25	574 nm	wavelength in vacuum
ω_1	1.933	3.28 rad/fs	frequency
k_{1p}	1.6542	9.364 μm^{-1}	wavenumber in plasma; $k_{1p}\lambda_D = 0.127$
ν_1	1.66×10^{-5}	28.13 ns^{-1}	collisional amplitude damping rate
σ_1	1.94×10^{-5}	109.63 m^{-1}	spatial damping rate

MODE 2 (EPW)

k_2	4.6542	26.35 μm^{-1}	$k_2\lambda_D = 0.357$
ω_2	1.229	2.086 rad/fs	
v_{p2}	0.2641	79.16 μm/ps	phase vel.
ν_{2LD}	0.03799	64.47 ps^{-1}	Landau damping rate
$\nu_{2\,\mathrm{col}}$	2.71×10^{-5}	46.02 ns^{-1}	collisional damping rate
v_{g2}	0.0667	29.16 μm/ps	group vel.

SRS W/ COLLISIONAL AND LANDAU DAMPING

γ_{SRS}	2.52×10^{-3}	4.27 ps^{-1}	
γ_0	0.01013	17.7 ps^{-1}	undamped growthrate
γ_c	2.64×10^{-3}	1.347 ps^{-1}	instability threshold
α	3.33×10^{-3}	0.01882 μm^{-1}	spatial gain rate

SRS W/ ONLY LANDAU DAMPING

α	3.35×10^{-3}	0.01895 μm^{-1}	spatial gain rate
γ_a	0.0563	95.6 ps^{-1}	absolute inst. threshold $\gamma_0 > \gamma_a$
I_a		5.87×10^{16} W/cm^2	absolute inst. threshold $I_0 > I_a$

Chapter 1

Laser-Plasma Interactions and Inertial Confinement Fusion

The passage of intense light through plasma is a very rich physical process of much practical importance. Light waves of high intensity can modify the medium they propagate in, while the medium also affects the light waves. Some of the resulting distortions of the light wave have found useful applications, while others impede efforts to use the light for its intended end.

One area where researchers are attempting to utilize interactions of light with matter is inertial confinement fusion (ICF). In this scheme, lasers are used to compress a pellet of hydrogen to the density and temperature required for thermonuclear fusion. In either the direct or indirect drive approaches to ICF, complicated light-matter interactions are used to uniformly irradiate the pellet and drive its ablative compression to densities thousands of times that of ordinary liquids. Efforts to achieve ICF have also been hampered by instabilities that occur when the laser interacts with plasma surrounding the pellet. This thesis studies one of these laser-plasma instabilities, stimulated Raman scattering (SRS), in regimes relevant to ICF. The current chapter first reviews the ICF process and the plasma conditions where Raman scattering occurs. It then describes the various underdense laser-plasma interactions (LPI) and relevant past work on SRS. Recent experiments on SRS in conditions of strong Landau damping, as well as evidence for stimulated electron acoustic scattering, are discussed. We then present the findings and outline of this thesis.

1.1 Inertial confinement fusion

1.1.1 ICF overview: direct and indirect drive

Thermonuclear fusion for significant energy gain occurs when a collection of nuclei capable of exothermic fusion reactions are kept at a high enough density and an optimal temperature for a long enough time. For controlled fusion on Earth, the first two conditions have proven much easier to achieve than an adequate confinement time. Efforts to achieve fusion energy have centered on either magnetic or inertial confinement of quasi-neutral (electron-ion) deuterium-tritium (DT) plasmas. Since charged particles are constrained to gyrate around a strong magnetic field, various magnetic geometries such as the tokamak, stellarator, spherical torus, and field-reversed configuration have been studied as possible avenues to magnetic confinement. Inertial confinement, however, relies

on the fact that all particles have a finite mass (inertia); an unconfined plasma still takes a finite amount of time to disperse into the surrounding space (roughly the system length divided by the sound speed). If the conditions are favorable, which usually implies densities hundreds of times ordinary solids, fusion can occur before the particles fly away.

ICF conditions are produced by imploding a pellet of fuel, usually cryogenic, solid DT, to high temperatures and extremely high densities via some external driver. The hydrogen bomb demonstrates that fusion can be so achieved. ICF research is dedicated to using the same principle in a controlled and less violent way. The idea is to implode the fuel so that fusion occurs in a central, hot region. The fusion products then must deposit enough energy in the cooler outer region of the pellet to cause fusion to start there too, and so on. The achievement of such a thermonuclear burn wave is the ignition criterion for ICF.

Current ICF schemes use intense light to drive the ablative compression of the pellet. As light is absorbed in the pellet's outer layers, it heats electrons which then ablate (evaporate) off the surface. This imparts momentum to inner layers of the pellet, as in a rocket, and causes compression. The direct drive approach to laser fusion involves shining many lasers directly on the pellet. This requires a very symmetric implosion, including uniform arrangement of beam imprints on the pellet and a smooth pellet surface, to avoid Rayleigh-Taylor and other fluid instabilities. The indirect drive approach mitigates these symmetry requirements by shining the lasers on a high-Z metal cage (such as gold), called a hohlraum. The lasers heat the metal to ∼200-300 eV, which then emits x-rays via blackbody radiation. This produces a uniform bath of x-rays which implode the pellet. The drawbacks of indirect drive include the inefficiencies of converting the lasers to x-rays and the geometrical effect that most of the x-rays do not hit the pellet. In addition, indirect drive hohlraums contain large, uniform regions of underdense plasma (the next subsection explains its origin), which allow LPI to occur.

Many current or planned ICF systems, such as NIF, OMEGA, and LMJ (Laser Mega-Joule), use Nd:glass lasers with a fundamental wavelength of 1057 nm. Some early attempts at ICF, for example the Antares laser at Los Alamos (see [8] and references therein) used much more efficient and higher repetition-rate CO_2 lasers which produce 10.6 μm light. Unfortunately, most LPI growth rates scale like $I\lambda^2$ (I is laser intensity and λ its wavelength), and these experiments were plagued with hot electron generation, probably due to Raman scattering. Less efficient but shorter wavelength (1.06 μm) Nd:glass lasers, such the Shiva laser system [9, Sec. II], also showed much laser energy converted to hot electrons by SRS once the corona density reached $n_c/4$ (the critical density n_c is defined by $\omega_0^2 = n_c e^2/\varepsilon_0 m_e$ where ω_0 is the laser frequency). To avoid this, the light is frequency tripled to 351 nm. Nd:glass laser fusion systems have very low efficiencies (light energy out per electrical energy in) and very low repetition rates (a few shots per hour). For inertial fusion energy reactors (∼1 GW power output), where ∼10 pellets each with a net energy gain of ∼100 MJ must be ignited per second, other ICF drivers are being explored. Advanced laser systems, such as diode-pumped solid-state and KrF lasers, operate at shorter fundamental frequencies, higher efficiencies, and higher repetition rates than Nd:glass lasers. A Z-pinch can be used to generate the x-ray bath instead of heating a hohlraum with lasers. Heavy ion beams may also provide a much more efficient way to heat a hohlraum than lasers.

1.1.2 Indirect-drive coronal conditions: plasmas and laser beams

In this thesis, we focus on parameters relevant to the underdense plasma away from the pellet in indirect-drive ICF (loosely called "blowoff" or "coronal" plasma, even for indirect-drive). It is these regions in the hohlraum where a large, uniform plasma forms, and is most susceptible to LPI. Cylindrical hohlraums planned for NIF have diameters of ∼5 mm and lengths of ∼1 cm. The lasers must travel through the laser entrance holes at either end of the hohlraum and several mm of plasma to reach the gold wall. Hohlraum designs typically include a fill of low-Z material to tamp the gold ions from filling the hohlraum, such as a 50-50 hydrogen-helium mixture or a low-Z foam. A gold fill would absorb the laser via inverse-bremsstrahlung in the wrong locations and produce an x-ray bath without the needed symmetry.

The coronal plasma is formed when the laser ionizes the tamp material, and also includes some ablated plasma from the pellet. For instance, a low-Z gas fill quickly ionizes as the laser strips electrons off atoms and then accelerates the former; they ionize other atoms via collisions. Figure 1-1 shows the plasma conditions and beam intensity along an inner beam in a typical NIF simulation, from [10]. The red box on the upper-left plot indicates the region where SRS has the highest linear gain. We shall be interested in plasmas conditions roughly similar to these: the ions are low-Z (such as H, He), the density is around 10% critical, T_e is several keV, the density and temperature scale lengths are several mm, and the average beam intensity is several 10^{15} W/cm^2.

The laser beams in ICF experiments undergo much processing before reaching the target. As mentioned above, the 1.06 μm light from the Nd:glass laser is frequency tripled to mitigate LPI. The resulting beam, however, does not have a smooth spatial profile, or spot. Rather, there are regions of very low and high intensities. The latter, called hot spots, are most susceptible to LPI. Several smoothing techniques, such as random or kinoform phase plates (RPPs or KPPs), polarization smoothing (PS), and smoothing by spectral dispersion (SSD) are used to reduce hot-spot intensities, produce a more uniform spot, or vary the speckle pattern in space and time [10, p. 375]. The smoothed beam has a known intensity distribution, typically of the form $P(I) \sim \exp(-I/I_0)$ or $\sim I\exp(-2I/I_0)$, where $P(I)$ is the fraction of beam power located in a region of intensity $> I$. For planned NIF shots, most of the spot will have an intensity around 10^{15} W/cm^2 with hot spots reaching $\sim 2\times 10^{16}$ W/cm^2.

This discussion of ICF ignition experiments, and NIF in particular, describes the regime of physical parameters considered here. This thesis is not an attempt to simulate or make predictions about NIF. For our purposes, important qualitative features of ignition hohlraum plasmas are that SRS is expected to be convectively but not absolutely unstable, involve a strongly Landau-damped plasma wave, and have linear gain lengths of 10's to 100's of μm. This is demonstrated in Chap. 2. Now we discuss LPI and how it can harm ICF.

1.2 Laser-plasma interactions (LPI)

It is a simple exercise in undergraduate electromagnetism to show that light passing through a plasma becomes evanescent when the electron number density n_0 exceeds the critical density n_c, where the plasma frequency $\omega_p \equiv (n_0e^2/\varepsilon_0 m_e)^{1/2}$ equals the light frequency ω_0: $(n_ce^2/\varepsilon_0 m_e)^{1/2} = \omega_0$. However, there is a series of nonlinear laser-plasma interactions besides this linear reflection which can alter, absorb, or reflect the laser over the whole range of densities $n_0 \le n_c$. Many LPI start out as parametric processes that involve the coupling of a small number of coherent

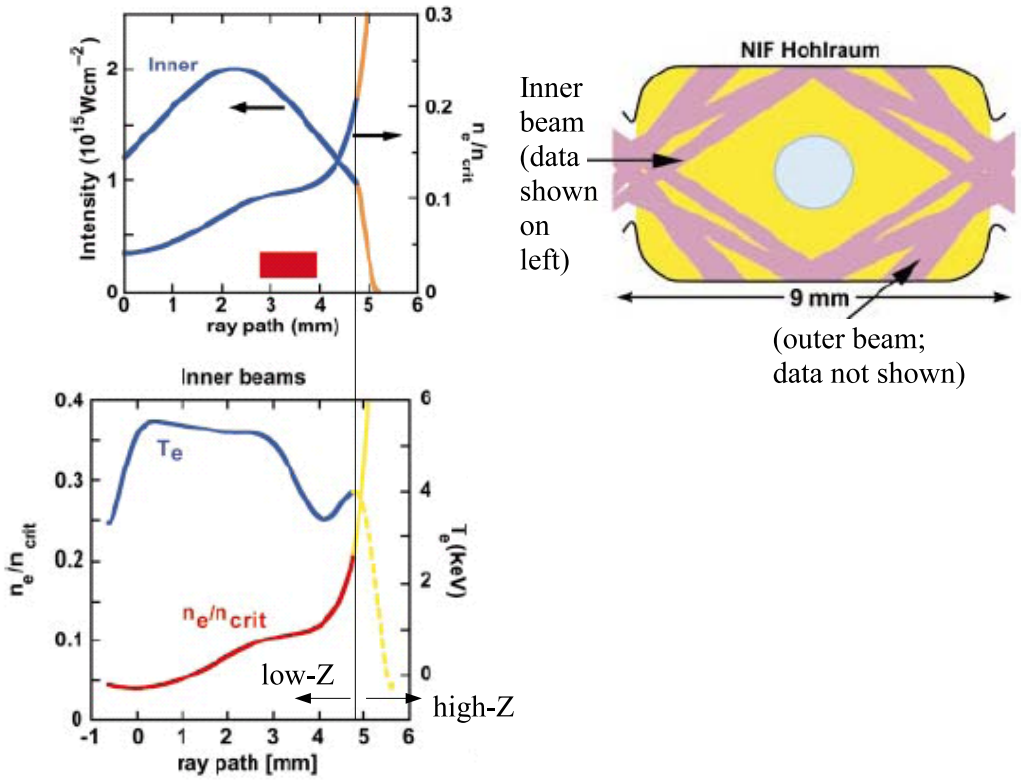

Figure 1-1: NIF hohlraum and typical electron density, temperature, and beam intensity for an inner beam [10, pp. 368-369].

natural modes of the plasma via the excited transverse electromagnetic plasma wave (from here on frequently called "the laser") as a "pump." The simplest to describe are three-wave interactions, where a pump wave (the laser, labeled 0) decays into two daughter waves (labeled 1 and 2). Each wave is nonlinearly driven by the beating of the other two waves. Three-wave processes are resonant, in that they occur when the waves nearly satisfy matching conditions:

$$\vec{k}_0 = \vec{k}_1 + \vec{k}_2, \qquad \omega_0 = \omega_1 + \omega_2. \tag{1.1}$$

These represent conservation of momentum and energy, respectively. Three-wave interactions have been studied for many years, in fluid dynamics, plasma physics, semiconductor physics, nonlinear optics, and other areas.

One can view the pump as being part of the equilibrium, and the parametric interaction as a linear instability of the modified, linearized plasma dynamics. Such an approach neglects pump depletion, or the modification of the pump by the parametric interaction. If the daughter waves are undamped, then the growth rate of the parametric instability γ_0 is proportional to the pump amplitude. When the daughters are damped, the pump amplitude must exceed a threshold for instability to occur, which can be expressed as a threshold for the undamped growthrate:

$$\gamma_0 > \gamma_c = \sqrt{\nu_1 \nu_2}. \tag{1.2}$$

ν_1, ν_2 are the amplitude damping rates of the daughter waves.

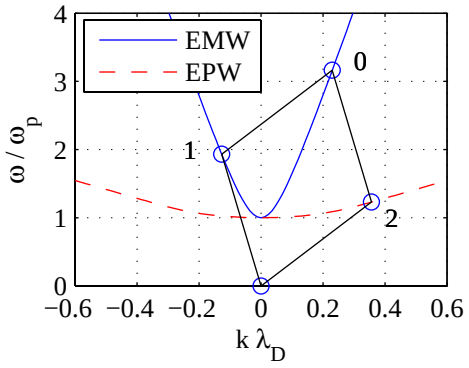

Figure 1-2: EPW and EMW dispersion relations and BSRS modes for the standard parameters.

We now review the laser-plasma interactions that occur in an underdense plasma ($n_0 < n_c$).

1.2.1 Raman scattering

Stimulated Raman scattering (SRS) is the coupling of a pump light or electromagnetic wave (EMW, mode 0 in the plasma, created by the laser) to a daughter light wave (EMW, mode 1) and an electron plasma wave (EPW, mode 2). The dispersion relations for these modes are

$$\omega^2 = \omega_p^2 + c^2k^2; \qquad \text{(EMW)} \tag{1.3}$$

$$\omega^2 = \omega_p^2 + 3v_{Te}^2k^2. \qquad \text{(EPW)} \tag{1.4}$$

$v_{Te} = (T_e/m_e)^{1/2}$ is the electron thermal speed and c is the speed of light. The simplest geometry that allows for SRS is for all three waves' $\vec{k}$ to be collinear (although the scattered light $\vec{k}_1$ may be parallel or ani-parallel to the pump $\vec{k}_0$). The plasma wave is then driven by the $\vec{v} \times \vec{B}$ force from the beating of the two light waves. Each light wave is driven by the current density ($= -en_1\vec{v}_e$) due to the product of the plasma-wave density fluctuation (n_1) and the electron oscillation velocity ($\vec{v}_e$) due to the other light wave. For the frequencies to match, it is necessary that $\omega_0 \geq \omega_p$, which translates to $n_0 \leq n_c/4$. The weak damping of light waves in a plasma is called inverse bremsstrahlung, and is due to electron-ion collisions. The plasma wave is damped due to collisions and the collisionless process of Landau damping. For the high-temperature plasmas relevant to ICF, $k\lambda_{De}$ of the plasma wave is large ($\gtrsim 0.3$). Landau damping grows dramatically with $k\lambda_{De}$ and generally dominates collisional damping in this regime.

Fig. 1-2 displays the EPW and EMW dispersion relations, as well as the three modes involved in back-scattered SRS (BSRS) for $n_0/n_c = 0.1$, $T_e = 3$ keV, and $\lambda_0 = 351$ nm (vacuum). We call these conditions the "standard parameters" and refer to them frequently; they are listed in the thesis preamble. In one dimension the matching conditions Eq. (1.1) can be viewed geometrically, as requiring the three modes in a three-wave process to lie on a parallelogram with one vertex at the origin of $\omega(k)$. When interpreting spectra from simulations is it very helpful to have this picture in mind and try to draw parallelograms that couple the various excited waves. Parametric processes involve a small number of coherent, narrow-band modes, unlike strongly turbulent situations where energy cascades through a broad, continuous range of modes.

Three-wave models of Raman scattering, discussed in Chap. 2, using the linear Landau damping rate for the plasma wave predict convective SRS gain lengths (distance for amplitude e-folding) $\sim$100 μm in ICF plasmas. This suggests SRS arising from thermal noise reaches large amplitudes (say, in 10 e-foldings) only in plasmas that are homogeneous over $\sim$ 1 mm. These conditions occur for plasmas in indirect-drive hohlraums, making SRS a potential threat. Recent experiments on Nova gasbags [11] give reflectivities much higher than convective-gain calculations using linear Landau damping. Moreover, the SRS level shows almost no variation with $k\lambda_D$ and thus the Landau damping of the EPW, which was changed by adjusting the plasma density. This implies a nonlinear mechanism is enhancing, rather than limiting, SRS. A main culprit is thought to be kinetic effects, in particular the trapping of electrons in the plasma wave and the resultant Landau damping reduction and nonlinear frequency or wavenumber shift of the EPW. It is understanding and extending these results that motivates this thesis.

1.2.2 Other LPI

The three-wave interaction analogous to Raman scattering, but with an ion acoustic wave (IAW) playing the role of the plasma wave, is stimulated Brillouin Scattering (SBS). The role of nonlinear IAW behavior in Brillouin scattering [12–14], as well as its interaction with Raman scattering [15, 16], is under active investigation. The decay of a light wave into two plasma waves is known as the two plasmon decay (TPD). Since both plasma waves have frequencies near ω_p, this generally happens near $n_0 \approx n_c/4$ to satisfy frequency matching. The growth rate is largest when the two plasma wave $\vec{k}$'s are both $\approx$45° from $\vec{k}_0$ and in the plane determined by $\vec{k}_0$ and $\vec{E}_0$. Near $n_0 = n_c/4$, TPD and SRS become intertwined. Near the critical density a laser can decay into a plasma wave and an ion wave, in the plasmon-phonon decay (PPD, so named due to the analogy between phonons in a crystal lattice and ion waves in a plasma). Filamentation or self-focusing of the laser can also occur, where density fluctuations transverse to the beam's propagation direction can focus the beam into filaments or "hot spots," and also steer the beam. The various LPI in ICF conditions and their relation to SRS are discussed in Sec. 2.6.3.

1.2.3 Relevance of LPI to ICF

LPI poses obstacles to ICF that must be mitigated. The major problems caused by LPI are loss of laser energy, hot electron generation, and loss of symmetry or control, in space or time, of energy deposition. The laser intensities needed for ignition are above the instability thresholds for many LPI. The daughter waves are usually sufficiently damped that these instabilities are convective rather than absolute. One can hope that a convectively-unstable pulse is not amplified to a dangerous level as it propagates through space. However, linear calculations of convective gains along beam paths frequently give SRS and SBS gains large enough to amplify thermal noise to reflectivities near unity, much higher than what is observed in experiments conducted on comparable plasmas. Nonlinearities are clearly important.

SRS is a concern because it can remove substantial energy from the laser (especially deleterious for back or side scatter), both in light waves and in EPWs. The plasma waves can have hot electrons associated with them, which may pre-heat the pellet before it ignites. The compression is designed to be mostly adiabatic, with the central, imploding fuel being heated when it stagnates. Pre-heating the pellet degrades the compression: it requires more pressure to compress a hot gas than a cold gas. SBS is worrisome since it removes laser energy; it can take place for $n_0 \leq n_c$ and

so is somewhat more effective than SRS, which only happens for $n_0 \leq n_c/4$. Very little energy is transferred to the ions in SBS due to the Manley-Rowe relations, and the daughter IAWs have phase velocities much less than v_{Te}. Hot electrons are thus not generated.

"Electrostatic" LPI (TPD and PPD) involve at least one plasma wave and can generate hot electrons, besides absorbing laser energy at undesired locations or times. To satisfy frequency matching, TPD and PPD only take place very near $n_c/4$ and n_c, respectively. This makes TPD a serious concern for direct drive, where the laser runs into high densities as it approaches the pellet. PPD is seldom a problem now since spatial gradients are very strong near the critical surface $n_0 = n_c$, and the laser energy is heavily absorbed there anyway. For indirect drive, the laser only encounters plasma with high enough density as it approaches the hohlraum walls. This plasma is very high Z due to gold ions and has short scale lengths, both of which heavily limit TPD and PPD.

Laser filamentation is worrisome since it can focus the laser beam and alter its propagation direction. Beam-line bending can ruin the needed pattern and timing of laser implant on the hohlraum or pellet, and thus produce a radiation drive without the desired intensity pattern. High-intensity filaments are also more likely to undergo Raman and Brillouin scattering.

The major concerns about LPI in indirect drive ICF are: SRS and SBS for back-scattering laser energy; SRS for generating hot electrons; and filamentation for beam steering and producing hot-spots. Due to the stringent symmetry requirements to avoid fluid instabilities, and the precise timing needed to compress the fuel with shock waves, small levels of backscatter ($\sim$5%) may prevent ignition on indirect-drive machines like NIF.

1.3 Past work on Raman scattering

SRS in plasmas has been studied for at least four decades [17], and has been an important concern in efforts to achieve ICF since the program's beginning. This section reviews past work on SRS, related developments in other LPI, and parametric instabilities that is relevant to this thesis. It is impossible to give a comprehensive literature review, so we emphasize nonlinear and kinetic aspects of SRS and its coupling to other parametric decays. A central mystery about SRS in ICF-relevant experiments is that the reflectivities are much lower than fluid coupled mode theory predicts. Understanding the physics behind this is needed to develop predictive capability of LPI levels. There are a host of nonlinearities that can saturate SRS, such as pump depletion, parametric decay of the plasma wave, modification by SBS, Langmuir wave collapse, and wave-breaking. Electron trapping, however, is one of the few nonlinearities that can *enhance* the reflectivity. This thesis explores how trapping affects SRS in both homogeneous and inhomogeneous plasmas, and suggests what experimental conditions may reveal the role of trapping.

The importance of kinetic effects in the SRS-generated plasma wave has long been appreciated. Electron trapping in large-amplitude plasma waves leads to a reduction and eventual elimination of Landau damping as trapped particles complete many orbits. This effect was studied analytically by O'Neil [18] and Al'tshul' and Karpman [19]. The former found the wave amplitude eventually becomes constant, while the latter found the wave amplitude to oscillate indefinitely. When a collision operator is included, there is a nonzero, amplitude-dependent "residual" damping rate, calculated for a Vedenov (diffusive) and Krook operator in Refs. [20] and [21], respectively. Kinetic SRS simulations have been conducted since the 1975 work of Forslund et al. [22] where electron

trapping and wave-breaking were seen. This and its accompanying theory paper [23] summarize the contemporary thinking and literature on SRS and SBS at that time. A unified, kinetic, linear treatment of decays of a light wave involving a daughter light wave, such as SRS, SBS, and SCS (Compton scatter), was given by Drake et al. in [24]. This includes pump modification of the linear modes, and gives the bandwidth around resonance for growth. Cohen and Kaufman studied electron trapping in driven plasma waves [25] with PIC simulations, and deduced a nonlinear damping and frequency shift which qualitatively agree with the analytic calculations of O'Neil [18] and Morales [26] for free waves. They then studied the full SRS problem [27], showing generalized Manley-Rowe relations for action transfer could be very useful in understanding numerical results. PIC simulations also showed the generation of hot electrons [28] and were used to explore the role of density gradients and collisions [29].

There is also broad interest in parametric interactions in their own right. Three-wave interactions (3WI) in homogeneous media have been well studied and admit soliton solutions for integrable cases (undamped waves) (see [30] and references therein). Three-wave SRS models allow simple analyses of whether the instability is convective or absolute and the role of pump depletion, discussed in Chap. 2. Inhomogeneous media detune 3WI due to wavenumber mismatch: the k of a mode with a well-defined ω varies with position, and thus the k resonance condition can only be satisfied at one point. Early work found inhomogeneous 3WI's to always be convective [31], although later work showed boundary effects in a finite gradient [32,33] or fluctuations [34,35] can make them absolute. A review of inhomogeneous work is in [36]. In SRS, density and temperature gradients, as well as pump strength variation from focusing and hot spots, make inhomogeneity important. Nonlinear k shifts in parametric interactions may counteract the detuning and yield auto-resonance [37]. Auto-resonance due to fluid [13] and kinetic trapping [14] nonlinearities has been applied to SBS. 3WI can also produce spatiotemporal chaos, as shown in [38] for two linearly damped and one growing wave when a diffusive term is included in the growing mode's envelope equation to limit growth at very short wavelengths. When cascading occurs there can also be spatiotemporal chaos when no modes are growing and without any diffusive terms, as shown for coupled SRS and the Langmuir decay instability (LDI) by Salcedo [39, 40].

Ion motion can play an important role in reducing or saturating Raman scatter. LDI is the parametric decay of a plasma wave to another plasma wave and an ion acoustic wave. Karttunen first proposed LDI as a saturation mechanism for both SRS and TPD [41]. Subsequently he and Heikkinen [42], as well as Bonnaud and Pesme [43], studied SRS saturation by ion dynamics numerically. The second group's later fluid SRS simulations with no enveloping show a large IAW generated by LDI, and a subsequent conversion of the original EPW into a Bloch wave [44]. Simulations of coupled, enveloped fluid Zakharov and electromagnetic wave equations [45,46] revealed LDI saturation of SRS, as well as the occurrence of LDI cascades and ensuing enhanced scattering by SBS, forward SRS, and anti-Stokes (upshifted, $\omega \approx \omega_0 + \omega_p$) SRS. Experiments by Drake and Batha [47] show the SRS reflectivity greatly *increases* with plasma-wave damping; they interpret this to mean the SRS plasma wave grows until it reaches the LDI threshold, which increases with IAW and secondary EPW dampings. Several Nova experiments show SRS reflectivity increasing with ion wave damping (which was controlled via ion composition) and suggest LDI saturated SRS [48, 49]. These papers discuss possible electromagnetic decay instability (EDI: EPW→EMW + IAW) in saturating SRS [50]. Thomson scattering data from the LULI laser at École Polytechnique provide direct observation of the LDI daughter modes [51]. More recent Trident experiments by Montgomery, Focia, et al. [52, 53] have shown evidence for LDI cascading, as well as possible stimulated electron acoustic scatter (SEAS) [54]. The coupled-mode equation simulations by Sal-

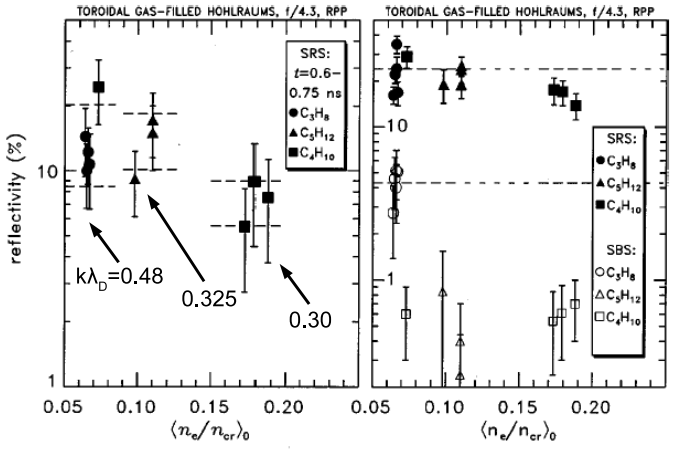

FIG. 5. Left: Instantaneous R_{SRS} at time=0.675±0.075 ns based on the measured light leaving the hohlraum are plotted versus initial n_e/n_c of the gas fill. A range equal to one standard deviation above and below the average reflectivity for each density is indicated. Right: Similar plot of the time-averaged R_{SRS} and R_{SBS}. For all these shots, the laser intensity at the hohlraum LEH is $2-3\times10^{15}$ W/cm^2.

Figure 1-3: Experimental results from Fig. 5 of [11], showing a flight increase of SRS reflectivity with $k\lambda_D$ of the EPW.

cedo also demonstrate SRS-induced LDI cascades, SRS cascades, and spatiotemporal chaos [39, 40]. The relation of SBS to SRS is discussed in Sec. 3.6.

There has been much recent work in kinetic effects in Raman scattering. As discussed further in Chap. 4, electron trapping in an EPW flattens the electron distribution function at the wave phase velocity, nonlinearly reduces the Landau damping rate, and gives an amplitude-dependent frequency downshift. Nova experiments showed very large (near 50%) SRS reflectivities in long scale-length plasmas, with very little dependence on the EPW Landau damping (which was varied by changing the plasma density) [11]. This is inconsistent with a steady-state convective gain picture, where the reflectivity decreases strongly with Landau damping. More recently, Thomson scattering measurements on Trident experiments reveal multiple co- and counter-propagating EPWs indicative of LDI cascading for $k\lambda_D \lesssim 0.29$, while above this value a single, frequency-broadened EPW is observed that is consistent with trapping nonlinearities [55]. Reduced PIC [56] simulations and accompanying coupled-mode calculations by Vu et al. show trapping and the subsequent damping reduction greatly enhance Raman backscatter, a process they term "kinetic inflation" [57, 58]. Moreover, they find the nonlinear frequency shift may saturate SRS and lead to temporally bursty behavior. Brunner and Valeo also see a trapping enhancement of the reflectivity but attribute the saturation to the trapped particle instability [59]. This work, along with the Montgomery-Focia SEAS observations, have led to renewed interest in nonlinear plasma-wave theories that account for trapping and speckle sideloss [60, 61]. Electron acoustic scatter has been observed in PIC simulations of plasmas overdense to SRS ($n_0 > n_c$) [62]. Ion trapping has also been examined in Brillouin scatter [12, 63].

1.4 Experimental motivation

This section discusses some experimental evidence for a kinetic enhancement of SRS, as well as observations of SEAS. Fernández et al. performed experiments on the Nova laser in toroidal hohlraums with a low-Z gas fill [11]. The observed reflectivities, shown in Fig. 1-3, slightly *increase* with $k\lambda_D$ of the SRS EPW. This flatly contradicts the steady-state coupled-mode gain result (presented in Chap. 2), where the reflectivity strongly decreases with Landau damping and thus with $k\lambda_D$. The

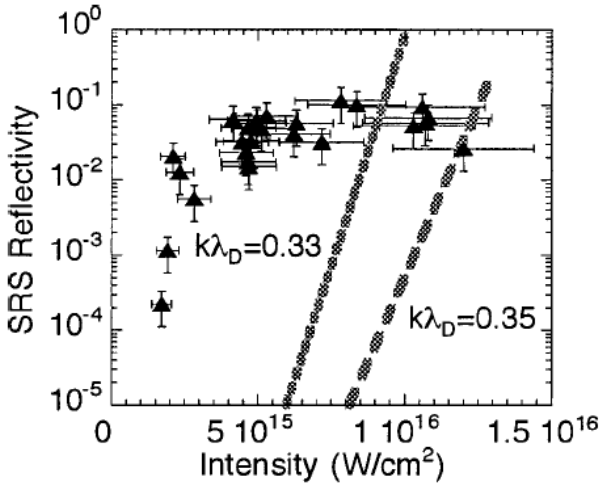

FIG. 5. Peak SRS reflectivity versus laser intensity for plasma conditions $k\lambda_D \approx 0.33-0.35$. The dashed lines show predictions from the SRS steady-state model for this range of conditions. The linear SRS model severely underestimates reflectivities in this regime, from which we infer lower than classical damping.

Figure 1-4: Reflectivity vs. pump intensity for Trident single hot spot experiments; Fig. 5 of [53].

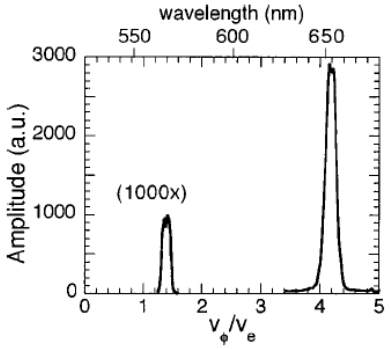

FIG. 9. Plot of SEAS and SRS backscatter spectrum vs electrostatic wave v_ϕ/v_e for single hot spot experiment. SEAS mode is shown 1000× larger. Upper axis corresponds to the scattered light wavelength.

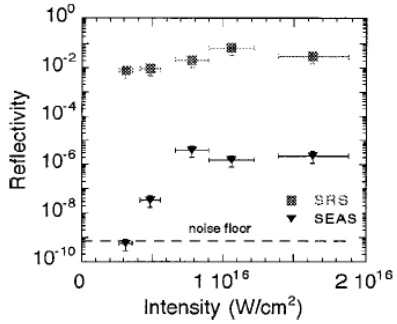

FIG. 10. Plot of measured reflectivity in SRS and SEAS vs laser intensity. SEAS reflectivity drops below detection level for $I \lesssim 3\times10^{15}$ W/cm^2, and is ~3000× below the SRS levels for higher intensity.

Figure 1-5: EPW phase velocity (left) and reflectivity (right) for SRS and SEAS from Trident single hot spot experiments; Figs. 9 and 10 of [53].

authors attribute this to an anomalously low damping. Trapping can reduce Landau damping and therefore may be operative. Experiments on the Trident laser facility studied LPI in a single hot spot [53]. Figure 1-4, which contains Fig. 5 from Ref. [53], shows a sharp increase in reflectivity as the pump laser intensity is increased. The reflectivity saturates for pump strengths above this level. Moreover, the reflectivity is well above convective gain estimates (shown as the dashed lines), which also increase much more gradually with pump strength than the experimental results. This again indicates Landau damping is being reduced. Reflected light which the authors designate SEAS was also recorded in these experiments when SRS was strong, as displayed in Fig. 1-5.

Chapter 3 of this thesis presents Vlasov simulations where a kinetic enhancement of SRS due to

electron trapping occurs. The enhancement develops suddenly as the pump intensity is increases, as in the Trident experiments. We also see evidence of both reflected light and electron acoustic activity corresponding to SEAS.

1.5 Findings of the thesis

This thesis explores stimulated Raman scattering (SRS) of laser light in regimes relevant to indirect-drive inertial confinement fusion with kinetic computer simulations and analytic modeling. Coupled-mode theories predict SRS is a convective rather than absolute instability in hohlraum conditions. The gain lengths vary with plasma parameters from tens to hundreds of microns, implying long scale lengths (of order a millimeter) are needed for significant reflectivity. Collisional damping is usually much weaker than Landau damping and can be neglected without making SRS absolute or changing the gain length. Strong Landau damping for high temperatures and low densities allows side and forward Raman scatter to grow faster than backscatter [64].

Vlasov simulations with a monochromatic seed back SRS light wave in a finite length, homogeneous plasma show that kinetic effects, in particular electron trapping, substantially elevate the reflected light over coupled mode convective gain values (we call this "kinetic enhancement"). Large ($\sim 10\% - 20\%$) reflectivity results from plasmas of length $\lesssim 100$ μm, distances over which coupled-mode theory predicts very little scattering. The simulations are performed with the 1-D Eulerian Vlasov-Maxwell solver ELVIS, developed by the author for this thesis. Trapping nonlinearly reduces the plasma-wave Landau damping ($k\lambda_D = 0.357$), and may allow SRS to become absolute. Raman backscatter becomes temporally bursty, demonstrates chaotic behavior, and contrary to coupled-mode theory does not reach a steady state. The plasma waves have frequencies downshifted from the linear EPW dispersion curve, consistent with the frequency shift associated with trapping. As the EPW frequency downshifts, the back SRS light upshifts and experiences Raman re-scatter. The electron distribution f_e shows coherent vortices which become irregular for large plasma-wave amplitude; the space-averaged f_e is significantly flattened near the phase velocity. Two acoustic ($\omega \propto k$) features in the longitudinal electric field spectrum are present, along with reflected light from possible stimulated electron acoustic scatter (SEAS).

For low pump laser intensities or high electron temperatures the reflectivity equals the coupled-mode value and SRS approaches a steady state. Increasing the pump strength reveals a sharp transition to kinetically enhanced Raman levels even for $k_2\lambda_D$ up to 0.45. The transition roughly occurs when a trapped electron starting at one end of the plasma undergoes a bounce motion before transiting the domain. Kinetic enhancement also happens in runs with different seed levels and without numerical edge plasma-wave damping. A broadband backscatter seed also produces large reflectivities, a flattened f_e, acoustic longitudinal features, and potential SEAS light. A simulation with kinetic helium ions gives high reflectivity until a strong burst of apparently chaotic activity occurs near the laser entrance, after which back SRS is low. Spectral analysis shows the activity contains several Raman and Brillouin re-scatters and subsequent Langmuir Decay Instability (LDI). The coupling of several parametric interactions may produce chaotic dynamics. Simulations with a Krook relaxation operator to mimic transverse escape (sideloss) of electrons from a laser speckle display kinetic enhancement if resonant electrons escape before completing a bounce orbit. For large relaxation rates the reflectivity is given by the coupled-mode convective gain level, but as the relaxation rate is lowered the reflectivity increases rapidly and saturates at a high level.

Electron trapping modifies f_e and thus the small-amplitude plasma waves. Besides downshifting

the EPW frequency, it also allows the two acoustic modes observed in SRS simulations to exist. The higher phase velocity feature agrees with that of the second most weakly-damped Landau mode (root of the complex, linear EPW dispersion relation), while the lower phase velocity mode matches the undamped, acoustic wave found by Schamel [7] and Rose [60]. The plasmon that satisfies the matching conditions for the possible SEAS seen in our runs lies on the low phase-velocity curve.

We also examine the relation of plasma inhomogeneity to kinetic enhancement. First we solve for the steady-state plasma waves driven by a fixed external force (similar to light-wave beating in SRS) in a density gradient using an envelope equation derived from a space-time permittivity operator. The wave amplitude maximizes near the resonance point where the drive is a natural EPW, although it is shifted due to advection. Nonlinearity, such as the trapping-induced damping reduction and wavenumber shift, alter the driven response in electrostatic ELVIS simulations. Runs of the full SRS problem in a density gradient show kinetic enhancement occurs as long as the scale length is not too short; coupled-mode steady-state results are recovered for sharp gradients. The reflectivity is consistently, although not drastically, higher when the pump propagates toward higher, rather than lower, density. The plasma waves driven by a fixed external force display a similar nonlinear left-right asymmetry.

1.6 Thesis outline

The thesis is organized as follows. Chapter 1 reviews laser-plasma interactions, inertial confinement fusion, plasma conditions in ICF hohlraums, relevant past work on SRS, and the thesis's results. We study envelope descriptions of SRS without trapping in Chap. 2. We derive a fluid-PDE system for SRS and find the slowly-varying action amplitude envelope equations, or coupled-mode equations (CMEs). A linear instability of the CMEs reveals the absolute or convective nature of SRS and gives the temporal and spatial growth rates. Chapter 2 also presents a linear, kinetic model for SRS, based on a permittivity operator containing slow space and time envelope variation. Using this kinetic description we solve the steady-state CMEs in the strong damping limit (plasma wave damping dominates its advection) including pump depletion. We explore SRS for plasma conditions typical of ICF hohlraums.

Chapter 3 contains our results for kinetic simulations of SRS from homogeneous plasmas. All simulations are performed with the Eulerian Vlasov-Maxwell code ELVIS, which the author wrote for this thesis work [65,66]. We extensively analyze a reference run labeled `BC1`, which demonstrates kinetic enhancement, to understand the effects of trapping. Runs matching `BC1` but for varying pump strength and electron temperature show a sharp threshold for the enhancement. We estimate the light- and plasma-wave thermal noise levels from which SRS grows, and find they are much smaller than the EMW seed used in our simulations. Varying the seed strength, or eliminating the seed as well as the numerical edge Krook relaxation operator, still gives large, bursty SRS. A rerun of `BC1` with seed light of several frequencies is shown, where strong reflectivity, trapping, and SEAS still ensue. We then study a run like `BC1` but with helium ions, where SRS is high until strong activity occurs near the laser entrance. Many parametric processes appear in this run, although pump SBS and LDI of the BSRS EPW are not among them. The absence of the latter is consistent with the large Landau damping of the LDI daughter waves. Chapter 3 ends with several BC1 reruns using a central Krook relaxation operator which replicates speckle sideloss.

Electron plasma waves with trapped electrons are studied in detail in Chap. 4. We review the physics of trapping, including the reduction of Landau damping and frequency downshift.

The difference between linear, natural modes and small-amplitude waves with trapping (which we call "$\varepsilon_r = 0$ modes") is discussed in Sec. 4.4. We study the acoustic modes produced by both descriptions, and find they agree with the two acoustic features seen in Vlasov simulations of Chap. 3; the "$\varepsilon_r = 0$" acoustic mode matches the branch containing possible SEAS plasmons. We then consider plasma waves driven by an external force (intended to model the beating of light waves in the Raman process) in an inhomogeneous plasma. We solve for the steady-state response and compare it with Vlasov simulations, and indicate the effects of plasma-wave advection as well as nonlinearity.

We explore inhomogeneity in the full Raman problem with ELVIS simulations in a density gradient in Chap. 5. We first present analysis of convective SRS in both the strongly damped and undamped limits. The predicted gains agree with ELVIS simulations for strong gradients, although long scale lengths display kinetic enhancement. The observed larger reflectivity when the pump propagates toward higher density is similar to the simulations of Chap. 4.

Chapter 6 summarizes the conclusions of the thesis and lays out our suggestions for future work in this area. Appendix A documents the ELVIS code, including the equations is solves, the numerical algorithm used, and some of the diagnostics. The plasma wave linearly driven by the beating of two light waves is derived via kinetic theory in Appendix B; this result is used in Chap. 3.

Chapter 2

Coupled-Mode Descriptions of SRS without Trapping

This chapter studies the linear instability and coupled-mode analyses of Raman scattering. We derive a two-dimensional fluid-PDE model of SRS that includes pump depletion and is valid for weakly-varying plasmas (in the WKB sense, e.g., scale lengths much longer than wavelengths). We cast this system in terms of slowly-varying action amplitudes. From this we find the linear (no pump depletion) SRS dispersion relation and discuss detuning. We also derive the nonlinear coupled-mode equations (CMEs) including pump evolution and medium variation, and present the resulting conservation laws for energy and action (the Manley-Rowe relations). An instability analysis of the CMEs reveals when SRS is unstable and whether it is a convective or absolute instability. We review the convective gain theory for SRS as spatial amplification.

We then consider a kinetic, three-dimensional formulation of SRS and show how to approximately obtain fluid results from the kinetic description. For moderate $k_2\lambda_D$, the two approaches compare favorably (mode 2 is the EPW). We also derive a permittivity operator for the plasma wave that includes slow space-time amplitude evolution. This fruitful approach handles fluid or kinetic descriptions, for homogeneous and inhomogeneous plasmas, with resonant or non-resonant ponderomotive drive, on the same footing. We study the limit of strongly-damped plasma waves (the so-called strong damping limit) from this viewpoint, and solve the resulting coupled-mode equations including pump depletion in steady state.

We next explore the results of linear SRS theory for ICF hohlraum plasmas. Laser intensities are usually above the instability threshold but below the absolute instability threshold. Landau damping dominates collisional damping and prevents SRS from being absolutely unstable for temperatures $\gtrsim 1$ keV. The strong damping limit (spatial gain rate $\ll$ Landau damping rate) is valid much of the time. The convective gain lengths are 10's or 100's of microns, so linear amplification is mild unless the plasmas become very large ($\sim$ mm, which is the case for ignition hohlraums). Nearly backscattered daughter light waves have the highest growth rate for small $k_2\lambda_D$, but as $k_2\lambda_D$ increases sidescatter grows faster. We nonetheless neglect sidescatter since the high-intensity speckles or "hot spots" of a laser beam are much longer than they are wide: sidescatter has much less distance over which to amplify (this is less true of the whole beam).

We also consider the validity of a 1-D collisionless model, which is the simplest one that contains electron trapping. This model neglects collisions, wavevectors transverse to the pump k (which are

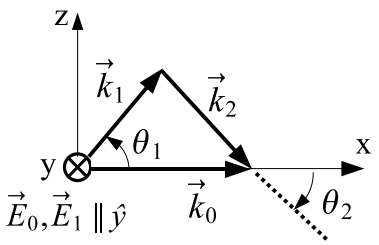

$$\vec{k}_0 = (k_0, 0, 0)$$
$$\vec{k}_1 = k_1(\cos\theta_1, 0, \sin\theta_1)$$
$$\vec{k}_2 = \vec{k}_0 - \vec{k}_1 = k_2(\cos\theta_2, 0, \sin\theta_2)$$

Figure 2-1: Fluid model geometry. Light waves polarized perpendicular to k-plane.

needed to describe sidescatter, filamentation, and TPD), and ion dynamics (which may allow for LDI, SBS, and, near the critical density, PPD). These effects may couple to SRS and be important in predicting what happens in a full hohlraum. We perform some simulations that include mobile ions and sideloss out of a speckle via a Krook operator to test the role of these effects when studying trapping in SRS. For typical hohlraum conditions, collisional damping by itself (without Landau damping) gives an absolute instability threshold which is much less than common pump laser intensities. SRS would then grow until it saturates nonlinearly and yields large reflectivities even in very small plasmas. Therefore, including collisions would not qualitatively change things. We end by discussing why TPD and PPD are not a concern for indirect-drive ICF, and why neglecting SBS and beam filamentation is acceptable for modelling SRS over speckle-sized plasmas for several-picosecond times.

As the plasma density is decreased and temperature is increased, the expected $k_2\lambda_D$ increases; its Landau damping therefore increases dramatically. Linear theory suggests large SRS gains then require long scale-length plasmas. The kinetic simulations presented in subsequent chapters show this is not the case.

2.1 Fluid-PDE SRS equations

First let us consider a fluid model of SRS only. Since SRS only involves modes with frequency $\gtrsim \omega_p$, we can treat the ions as immobile. The modes' wavevectors must match ($\vec{k}_0 = \vec{k}_1 + \vec{k}_2$), so their $\vec{k}$'s lie in a plane (which we choose to be the $x-z$ plane). We restrict both light waves to be linearly polarized along y, which we call the transverse direction. The kinetic dispersion relation given in section 2.5 allows for arbitrary polarization, and shows this choice maximizes the coupling. The scattered light wave actually has both an electromagnetic and a small electrostatic component; our geometry eliminates the electrostatic part. We let $\hat{l}$ represent the "longitudinal" (in the $x-z$ plane) component of vectors. Figure 2-1 displays the geometry. We allow the plasma to have an inhomogeneous density. We use $n_B(x)$, $\omega_p(x) = \left(n_B e^2/\epsilon_0 m_e\right)^{1/2}$ for the local background density and plasma frequency, and $n_0 = n_B(x)$, $\omega_{p0} = \omega_p(x = x_0)$ as the density and plasma frequency at a reference point x_0.

2.1.1 Nonlinear PDE model with pump depletion

We start with Maxwell's equations:

$$\begin{aligned} \nabla \cdot \vec{E} &= \epsilon_0^{-1} \rho, && (2.1)\\ \nabla \cdot \vec{B} &= 0, && (2.2)\\ \nabla \times \vec{E} &= -\partial_t \vec{B}, && (2.3)\\ \nabla \times \vec{B} &= \mu_0 \vec{J} + c^{-2} \partial_t \vec{E}. && (2.4) \end{aligned}$$

We represent $\vec{E}$ and $\vec{B}$ via potentials

$$\vec{B} = \nabla \times \vec{A}, \qquad \vec{E} = -\nabla \phi - \partial_t \vec{A}. \tag{2.5}$$

We work in the Coulomb gauge ($\nabla \cdot \vec{A} = 0$): the light waves are purely inductive (given by $\vec{A}$), while the plasma wave is electrostatic (given by ϕ). Taking $\nabla \cdot \vec{E}$ from Eq. (2.5) gives Poisson's equation

$$\nabla^2 \phi = -\epsilon_0^{-1} \rho = \frac{e}{\epsilon_0} n_1. \tag{2.6}$$

The electron number density $n_e(x,t) = n_B(x) + n_1(x,t)$ where n_B is the background profile and is balanced by the stationary ions. Beware that we use n_1 for the EPW density fluctuation, but label the SRS EPW as mode 2 and use a_2 for its action amplitude below. Both light waves are linearly polarized in the transverse (y) direction: $\vec{A} = A\hat{y}$ (although we retain the vector notation sometimes). This choice maximizes the ponderomotive drive, which goes like $\vec{E}_0 \cdot \vec{E}_1$.

Light wave equations

Putting the potential representations Eq. (2.5) into Ampere's law Eq. (2.4) gives

$$\nabla \times \nabla \times \vec{A} = \mu_0 \vec{J} - c^{-2} \partial_t \nabla \phi - c^{-2} \partial_{tt} \vec{A}. \tag{2.7}$$

A common vector identity gives $\nabla \times \nabla \times \vec{A} = \nabla(\nabla \cdot \vec{A}) - \nabla^2 \vec{A}$. The first term is zero in the Coulomb gauge. Multiplying (2.7) by c^2 and rearranging gives

$$\partial_{tt} \vec{A} - c^2 \nabla^2 \vec{A} = \epsilon_0^{-1} \vec{J} - \partial_t \nabla \phi. \tag{2.8}$$

We split $\vec{J}$ into transverse and longitudinal components:

$$\vec{J} = \vec{J}_l + \vec{J}_t, \qquad \nabla \cdot \vec{J}_t = 0, \qquad \vec{J}_t = J_y \hat{y}. \tag{2.9}$$

Taking the longitudinal component of Eq. (2.8) kills the left-hand side and yields

$$\vec{J}_l = \epsilon_0 \partial_t \nabla \phi. \tag{2.10}$$

The transverse component of Eq. (2.8) gives

$$(\partial_{tt} - c^2 \nabla^2) \vec{A} = \epsilon_0^{-1} \vec{J}_t. \tag{2.11}$$

The electrons carry the current: $\vec{J} = -en_e\vec{v}_e$. We can thus split $\vec{v}_e$ via

$$\vec{v}_e = \vec{v}_l + \vec{v}_t, \qquad \nabla \cdot \vec{v}_t = 0. \tag{2.12}$$

$\vec{v}_t$ is the electron oscillation velocity induced by the light waves. The conservation of transverse (y) canonical momentum (also known as Gabor's theorem) gives

$$\vec{v}_t = \frac{e}{m}\vec{A}. \tag{2.13}$$

The transverse wave equation (2.11) becomes

$$(\partial_{tt} - c^2\nabla^2)\vec{A} = -\frac{\omega_p^2}{n_B}n_e\vec{A}. \tag{2.14}$$

Move the linear piece $-\omega_p^2\vec{A}$ to the left-hand side to obtain

$$(\partial_{tt} - c^2\nabla^2 + \omega_p^2)\vec{A} = -\frac{\omega_p^2}{n_B}n_1\vec{A}. \tag{2.15}$$

Note ω_p^2/n_B is independent of x. We split $\vec{A}$ into the pump ($\vec{A}_0$) and scattered ($\vec{A}_1$) light waves: $\vec{A} = \vec{A}_0 + \vec{A}_1$. Each light wave is driven by the transverse current from the beating of the other light wave with the plasma wave. We arrive at a driven wave equation for each light wave:

$$(\partial_{tt} - c^2\nabla^2 + \omega_p^2)\vec{A}_0 = -\frac{\omega_p^2}{n_B}n_1\vec{A}_1, \tag{2.16}$$

$$(\partial_{tt} - c^2\nabla^2 + \omega_p^2)\vec{A}_1 = -\frac{\omega_p^2}{n_B}n_1\vec{A}_0. \tag{2.17}$$

Plasma wave equation

The plasma wave fluid equations are continuity and momentum. Continuity is

$$\partial_t n_e + \nabla \cdot (n_e\vec{v}_e) = 0. \tag{2.18}$$

Linearize continuity, neglect ∇n_B on the grounds it is much less than n_B times a typical wavenumber (this defines "slow" medium variation), and recall $\nabla \cdot \vec{v}_t = 0$ to find

$$\partial_t n_1 + n_B\nabla \cdot \vec{v}_l = 0. \tag{2.19}$$

We take ∂_t of this and rearrange (this will be used to replace $\vec{v}_l$ in the momentum equation):

$$\nabla \cdot \partial_t\vec{v}_l = -n_B^{-1}\partial_{tt}n_1. \tag{2.20}$$

The longitudinal momentum equation is

$$m_e(\partial_t\vec{v}_l + \vec{v} \cdot \nabla\vec{v}_l) = e\nabla\phi - e\vec{v}_t \times \vec{B} - n_e^{-1}\nabla p_e. \tag{2.21}$$

The advective term $\vec{v} \cdot \nabla\vec{v}_l$ does not involve the light waves, since $\vec{v}_t \cdot \nabla = 0$. Thus it only couples

different harmonics of the plasma wave. These harmonics are not essential to Raman scattering, so we drop the advective term. Similarly, the nonlinearity in the pressure term only couples plasma-wave harmonics, since light waves drive no pressure or density fluctuations. We therefore linearize the pressure force and assume adiabatic, 1-D electrons: $p_e = 3n_eT_e$. Eq. (2.21) yields

$$m_e\partial_t\vec{v}_l = e\nabla\phi - e\vec{v}_t \times \vec{B} - 3\frac{T_e}{n_B}\nabla n_1. \tag{2.22}$$

The Lorentz force $\vec{F}_{vB} = -e\vec{v}_t \times \vec{B}$ provides the resonant plasma-wave drive:

$$\vec{F}_{vB} = -e\vec{v}_t \times \vec{B} = -(e^2/m_e)\vec{A} \times (\nabla \times \vec{A}). \tag{2.23}$$

For the last form we used Eq. (2.13). By a vector identity, $\vec{A} \times (\nabla \times \vec{A}) = (\nabla\vec{A}) \cdot \vec{A} - (\vec{A} \cdot \nabla)\vec{A}$. The second term is zero since there is no transverse gradient: $\vec{A} \perp \nabla$. Thus,

$$\vec{A} \times (\nabla \times \vec{A}) = (\nabla\vec{A}) \cdot \vec{A} = \tfrac{1}{2}\nabla A^2 \tag{2.24}$$

and

$$\vec{F}_{vB} = -\frac{e^2}{2m_e}\nabla A^2. \tag{2.25}$$

In Eq. (2.22) we move linear terms (which give the dispersion relation) to the left-hand side, and find

$$m_e\partial_t\vec{v}_l - e\nabla\phi + 3\frac{T_e}{n_B}\nabla n_1 = \vec{F}_{vB} = -\frac{e^2}{2m_e}\nabla A^{2\cdot} \tag{2.26}$$

Take $\nabla\cdot$ of Eq. (2.26), and use Poisson's equation and $\nabla \cdot \partial_t\vec{v}_l$ from Eq. (2.20) to write the LHS of Eq. (2.26) in terms of n_1:

$$-\frac{m_e}{n_B}\partial_{tt}n_1 - \frac{e^2}{\epsilon_0}n_1 + 3\frac{T_e}{n_B}\nabla^2 n_1 = -\frac{e^2}{2m_e}\nabla^2 A^2. \tag{2.27}$$

The resonant term in $A^2 = (A_0 + A_1)^2$ is $2A_0A_1$. The other, non-resonant terms can be neglected since they do not contribute to SRS. Multiplying Eq. (2.27) by $-n_B/m_e$ finally gives the plasma wave equation (2.30). The three coupled nonlinear fluid PDEs which describe SRS are

$$(\partial_{tt} - c^2\nabla^2 + \omega_p^2)A_0 = -\frac{\omega_p^2}{n_B}n_1A_1, \tag{2.28}$$

$$(\partial_{tt} - c^2\nabla^2 + \omega_p^2)A_1 = -\frac{\omega_p^2}{n_B}n_1A_0, \tag{2.29}$$

$$\left(\partial_{tt} - 3v_{Te}^2\nabla^2 + \omega_p^2\right)n_1 = \frac{n_Be^2}{m_e^2}\nabla^2 A_0A_1. \tag{2.30}$$

The left-hand sides describe the natural modes, while the right-hand sides are the parametric couplings. These equations are correct for inhomogeneous plasmas with scale lengths much longer than wavelengths of interest.

2.1.2 Action amplitude envelope representation

It is useful when studying wave propagation to represent the physical fields in "envelope form," as a slowly-varying amplitude envelope times a rapid oscillation. This is similar to the WKB approximation. This subsection presents the basic ideas of this approach, along with the small-amplitude quantities associated with a wave (such as energy density). We mostly follow the treatment and conventions (including the Fourier conventions) of [67], Appendix 2 of which discusses weakly-varying media.

We write a physical field, such as the pump vector potential as $A_0 = (1/2)\tilde{A}_0 \exp i\psi_0 + cc$. We use ψ_i for the phase of mode i. For a homogeneous plasma $\psi_i = \vec{k}_i \cdot \vec{x} - \omega_i t$ with k_i and ω_i constant. When the medium has weak inhomogeneity or time dependence (weak as opposed to the mode wavelengths and periods), we have $\vec{k}_i = \nabla\psi$ and $\omega = -\partial\psi/\partial t$. Following the WKB picture, $\vec{k}$ and ω for a mode satisfy the local dispersion relation $D\left(\vec{k}, \omega, \vec{r}, t\right) = 0$ where the weak space-time dependence of D is due to variations in the medium's properties (e.g., density and temperature). The basic definitions of small-amplitude energy density, action density, and so on are the same for uniform or and weakly-varying media. The basic conservation law that holds in both cases applies to action density, Eq. (2.35) below. We also discuss at the end of this subsection how these ideas play out in a simple inhomogeneous example.

The small-amplitude energy density W in a linear wave with Fourier-space electric field amplitude $\vec{E}$ is

$$W = \frac{1}{4}\epsilon_0 \omega \ \vec{E}^* \cdot \frac{\partial \overleftrightarrow{D}^h}{\partial \omega} \cdot \vec{E}, \tag{2.31}$$

where $\overleftrightarrow{D}^h$ $\left(\overleftrightarrow{D}^a\right)$ is the Hermitian (anti-Hermitian) part of the dispersion tensor. The action density N (units: action/volume) and action amplitude a (units: (action/volume)$^{1/2}$) are

$$N = \frac{W}{\omega} = p\,|a|^2\,, \qquad \arg(a) = \arg(E). \tag{2.32}$$

$p = \text{sign}\ (W)$ is the wave parity ($p = 1$ for all Raman waves). a is chosen to be in phase with the electric field $\vec{E}$. The adiabatic invariance of action is an important concept in classical mechanics. Analogies between classical and quantum systems are frequently made by quantizing the action, and treating the number of action quanta present as the number of "particles." We associate N_i with the number of quasi-particles and see below how they evolve. For future reference, the intensity or energy flux (units: speed*energy/volume) $\vec{I}$ of a wave is related to W by the group velocity:

$$\vec{I} = \vec{v}_g W, \qquad \vec{v}_g = -\frac{\partial D/\partial \vec{k}}{\partial D/\partial \omega}. \tag{2.33}$$

The momentum density $\vec{g}$ and action flux $\vec{Z}$ are

$$\vec{g} = \vec{k} N, \qquad \vec{Z} = \vec{v}_g N. \tag{2.34}$$

$\vec{Z}$ is vectorial, and in a 1-D geometry carries the sign of v_g. The basic conservation law for action density, valid for uniform or weakly-varying media, is

$$\partial_t N + \nabla \cdot \vec{Z} + 2\nu N = 0. \tag{2.35}$$

ν is the amplitude damping rate:

$$\nu = -i\frac{\omega\epsilon_0}{4W}\vec{E}^* \cdot \frac{\partial \overleftrightarrow{D}^a}{\partial\omega} \cdot \vec{E}. \tag{2.36}$$

For light waves,

$$W_{EMW} = \frac{1}{2}\epsilon_0 |E|^2, \qquad a_{EMW} = \sqrt{\frac{\epsilon_0}{2\omega}}E. \tag{2.37}$$

The vector potential is related to action amplitude via

$$\tilde{A} \text{ (vec. pot.)} = -i\left(\frac{2}{\epsilon_0\omega}\right)^{1/2} a \text{ (act. amp.).} \qquad \text{(EMW's)} \tag{2.38}$$

The physical A_j for modes 0 and 1 is written

$$A_j = -i\left(\frac{1}{2\epsilon_0\omega_j}\right)^{1/2} a_j \exp i\psi_i + cc, \qquad j = 0, 1. \tag{2.39}$$

For plasma waves,

$$W_{EPW} = \frac{1}{2}\epsilon_0 \ |E|^2 \frac{\omega^2}{\omega_p^2}, \qquad a_{EPW} = \left(\frac{\epsilon_0\omega}{2\omega_p^2}\right)^{1/2} E, \tag{2.40}$$

where $\omega_p \sim n_B^{1/2}$ varies in space. Density is related to action amplitude by

$$n \text{ (density)} = ik\left(\frac{2n_B}{m_e\omega}\right)^{1/2} a \text{ (act. amp.).} \qquad \text{(EPW's)} \tag{2.41}$$

The mode 2 density perturbation can be written

$$n_1 = \frac{1}{2}\tilde{n}_1 \exp i\psi_2 + cc, \qquad \tilde{n}_1 = ik_2\left(\frac{2n_B}{m_e\omega_2}\right)^{1/2} a_2. \tag{2.42}$$

Note the spatially-varying n_B instead of a constant reference n_0 is used to relate $\tilde{n}_1$ and a_2.

We substitute these envelope forms into Eqs. (2.28-2.30) and retain just the terms that can resonate. They have phases $(\psi_0, \psi_1 + \psi_2)$, $(\psi_1, \psi_0 - \psi_2^*)$, or $(\psi_2, \psi_0 - \psi_1^*)$ on their (left, right) sides. The k's and ω's that appear in this system need not be solutions of the relevant dispersion relations. Usually, we treat k_i and ω_i $(i = 0, 1)$ for the light waves to be natural and k_2, ω_2 to be their beating. For varying media, k, ω, n_B, etc. in the coefficients relating A_i and n_1 to a_i can in principle vary slowly; we neglect this and pull these factors through the derivatives (valid for weak medium variation). The resulting system from Eqs. (2.28-2.30) is

$$\begin{aligned}
\left(\partial_{tt} - c^2\nabla^2 + \omega_p^2\right)\left(a_0 \exp i\psi_0\right) &= -2i\omega_0 \ Ka_1a_2 \exp i\left(\psi_1 + \psi_2\right), &(2.43)\\
\left(\partial_{tt} - c^2\nabla^2 + \omega_p^2\right)\left(a_1 \exp i\psi_1\right) &= 2i\omega_1 \ Ka_0a_2^* \exp i\left(\psi_0 - \psi_2^*\right), &(2.44)\\
\left(\partial_{tt} - 3v_{Te}^2\nabla^2 + \omega_p^2\right)\left(a_2 \exp i\psi_2\right) &= -\frac{2i\omega_2}{k_2^2} \ K\nabla^2\left[a_0a_1^* \exp i\left(\psi_0 - \psi_1^*\right)\right]. &(2.45)
\end{aligned}$$

K is the coupling constant and is real positive for SRS, and varies in non-uniform media (some

authors define K with an overall - sign):

$$K \equiv \frac{k_2}{\sqrt{\omega_0\omega_1\omega_2}} \frac{\omega_p^2}{\sqrt{8n_B m_e}}. \tag{2.46}$$

Outside of the phase exponentials (i.e., in the pre-factors and K on the RHS's) k and ω refer to their real parts. This is valid for weak growth or damping. We let k and ω be complex in the linear instability analysis of section 2.2.

To exemplify the envelope approximation, consider a light wave propagating through a plasma of varying density. The density n is underdense ($n \ll n_c$ = critical density) so there is no reflection, and varies only in x. It is flat with value n_1 on the left, smoothly ramps up to n_2, and is then flat at $n_2 > n_1$ on the right. A source emits monochromatic light waves of frequency ω far to the left. Neglect damping: $\gamma = 0$. What does the steady state ($\partial_t = 0$) look like? Since the medium is uniform in time, ω is constant. However k varies and satisfies the local dispersion relation: $k = (\omega/c)\left(1 - n\left(x\right)/n_c\right)^{1/2}$. The group velocity $\vec{v}_g = v_g\hat{x}$ where $v_g = c^2k/\omega$ varies in x as well. The action conservation equation (2.35) is simply $\partial_x Z = 0$, that is, action flux is constant. Equating Z in regions 1 and 2 and using $Z = v_g N$ gives $v_{g1}N_1 = v_{g2}N_2$. In terms of electric field amplitude, $E_2 = \left(v_{g1}/v_{g2}\right)^{1/2} E_1$. Since $n_2 > n_1$, $v_{g1} > v_{g2}$ and $E_2 > E_1$. This is the well-known electric field swelling of light propagating to higher density, which a WKB analysis of the relevant PDEs directly yields. In terms of quasi-particles ($\sim$ action density) or photons, the picture is as follows. A photon is emitted from the left and moves at the group velocity. As it propagates up the density gradient, its wavelength increases and group velocity slows. In steady state the number of photons in the region is constant, so the same number must enter and exit in a given time (equal action fluxes). Thus, there are more photons in region 2 than in region 1, although those in region 2 move more slowly. In this spatial problem action flux rather than action density remains constant.

2.2 Linear fluid dispersion relation for fixed pump

This section presents a linear analysis of the system Eqs. (2.43-2.45) with fixed pump a_0 = constant for homogeneous plasma ($n_B \to n_0$, $\omega_p \to \omega_{p0}$, $\vec{k}_i$ and ω_i constant) and the 2-D geometry of Fig. 2-1. In this section we treat the a_i's as constants and find a dispersion relation for complex ψ_1 and ψ_2, where growth due to parametric coupling is contained in $\mathrm{Im}[\psi_{1,2}]$. The a_i can be constant only if the phases match ($\psi_0 = \psi_1 + \psi_2^*$). The parametric coupling induces phase shifts so the physical fields match, although they may not be natural modes. This non-naturalness introduces a detuning term which resembles an imaginary damping. What we call detuning is also referred to as phase mismatch or dephasing.

We order a_0 as zeroth order, as opposed to the small, first-order a_1 and a_2. We neglect pump depletion as second order, so the pump satisfies the linear, collisionless (no damping) light wave dispersion relation:

$$\left(\partial_{tt} - c^2\nabla^2 + \omega_p^2\right)\exp i\psi_0 = 0 \qquad \to \qquad \Delta_0 \equiv -\omega_0^2 + c^2k_0^2 + \omega_p^2 = 0. \tag{2.47}$$

We refer to Δ_0 as the dispersion factor for mode 0. k_0 and ω_0 are real. Changes in pump amplitude due to the parametric coupling (called pump depletion) are included in the coupled-mode equations of section 2.3.

Eqs. (2.44-2.45) are the driven scattered wave and plasma wave equations, and only contain first-order terms. Consider Eq. (2.44) for a_1 constant:

$$\Delta_1 a_1 = 2i\omega_1 \; K a_0 a_2^* \exp i \; \delta\psi, \tag{2.48}$$

$$\Delta_1 \equiv -\omega_1^2 + c^2 k_1^2 + \omega_p^2, \qquad\qquad \delta\psi \equiv \psi_0 - \psi_1 - \psi_2^*. \tag{2.49}$$

Δ_1 is the mode-1 dispersion factor, and $\delta\psi$ is the phase mismatch. The RHS depends on space and time via $\delta\psi$, so it is not consistent to say all the a_i's are constant. The change of variables

$$a_2 = \tilde{a}_2 \exp i \; \delta\psi^* \tag{2.50}$$

alleviates this. The phase mismatch factor could instead be absorbed into a_1 or split between a_1 and a_2; we choose to modify a_2 since this is convenient later in studying inhomogeneity and frequency shifts in the plasma wave. The result is

$$\Delta_1 a_1 = 2i\omega_1 \; K a_0 \tilde{a}_2^*. \tag{2.51}$$

Similarly, assuming $\tilde{a}_2$ is constant, Eq. (2.45) gives

$$\tilde{\Delta}_2 \tilde{a}_2 = 2i\omega_2 \; K a_0 a_1^*, \qquad\qquad \tilde{\Delta}_2 \equiv -\tilde{\omega}_2^2 + 3v_{Te}^2 \tilde{k}_2^2 + \omega_p^2. \tag{2.52}$$

$\tilde{k}_2 \equiv k_0 - k_1^*$ and $\tilde{\omega}_2 \equiv \omega_0 - \omega_1^*$ appear instead of k_2, ω_2 due to the change of variables. Since Eq. (2.52) has no space-time dependence (unlike Eq. (2.48)), it is consistent to say $\tilde{a}_2$ is constant. Thus all three amplitudes a_0, a_1, and $\tilde{a}_2$ are constant. The physical fields have exponential space-time dependence with shifted phases that match. To show this, we calculate the physical light-wave vector potentials A_j:

$$\begin{aligned} A_j &= \frac{1}{2}\tilde{A}_j \exp i\psi_j + c.c., \qquad\qquad j = 0, 1, & (2.53)\\ &= \frac{1}{2}\tilde{A}_j \exp i\psi_{jr} \exp(-\psi_{ji}) + c.c. & (2.54) \end{aligned}$$

Recall $\psi_{0i} = 0$ (no pump damping or depletion). Similarly, the plasma-wave density fluctuation n_1 is

$$\begin{aligned} n_1 &= \frac{1}{2}\tilde{n}_1 \exp i\psi_2 + c.c. & (2.55)\\ &= \frac{1}{2}\tilde{a}_2 c_2 \exp i\,(\psi_0 - \psi_{1r}) \exp(-\psi_{1i}) + c.c. & (2.56) \end{aligned}$$

(c_2 is a constant for density-action amplitude conversion). The daughter waves thus have real phases that add to the pump phase. The two daughter waves have the same growth factor $\exp(-\psi_{1i})$. Without loss of generality, consider modes that match from the outset but may not be natural modes, that is, $\delta\psi = 0 \rightarrow \psi_2 = \psi_0 - \psi_1^*$. **We drop the tildes on the mode-2 quantities.** Growth only occurs when all three modes are nearly natural, with a bandwidth of order the growth rate. When all three modes are natural, we refer to them as "natural, matching modes." This implies all three modes satisfy their (real, no damping) dispersion relations as well as frequency and wavenumber matching.

Eliminate a_1^* from Eq. (2.52) using Eq. (2.51) and conjugate to obtain the Raman dispersion

relation

$$\Delta_1 \Delta_2^* = 4K^2 \omega_1 \omega_2^* \left|a_0^2\right| \equiv \bar{\Omega}^4. \tag{2.57}$$

Stability is analyzed by looking for complex ω_1 for real k_1. Recall that $k_2 \equiv k_0 - k_1$ and $\omega_2 \equiv \omega_0 - \omega_1^*$ since the modes match. Consider nearly-natural daughter modes with $\omega_1 = \omega_{10} + \delta\omega_1$, $\omega_{10}^2 = c^2 k_1^2 + \omega_p^2$, $|\delta\omega_1| \ll |\omega_{10}|$. Also, $\omega_2 = \omega_{20} - \delta\omega_1^*$, $\omega_{20} = \omega_0 - \omega_{10}$, $|\delta\omega_1| \ll |\omega_{20}|$. The dispersion relation becomes

$$\delta\omega_1 \left(\delta\omega_1 + \delta_2\right) \approx -\gamma_0^2, \tag{2.58}$$

$$\gamma_0 \equiv K\left|a_0\right| = \frac{1}{4} k_2 v_{os0} \frac{\omega_p}{\sqrt{\omega_{10}\omega_{20}}}, \tag{2.59}$$

$$\delta_2 \equiv \frac{\Delta_{20}}{2\omega_{20}}. \tag{2.60}$$

We call δ_2 the detuning frequency. It measures how much mode 2 (the beat of modes 0 and 1) departs from a natural plasma wave. γ_0 is the undamped temporal growth rate. $v_{os0} = e|\tilde{A}_0|/m_e$ is the non-relativistic amplitude of the electron oscillation velocity in the pump field; relativistic effects become important as $v_{os0}/c \to 1$. In terms of the pump intensity I_0 (power/area), $v_{os0}^2/c^2 = (I_{0,15}\lambda_{0v,\mu}^2 / 1370\eta_0)$. $\eta_0 = v_{g0}/c = \sqrt{1 - n_0/n_c}$ accounts for the electric-field swelling as the light wave propagates from vacuum into the plasma, and its group velocity v_{g0} slows from c to $c\eta_0$.

The shift $\delta\omega_1$ due to parametric coupling is

$$\delta\omega_1 = -\frac{\delta_2}{2} \pm \sqrt{\left(\frac{\delta_2}{2}\right) - \gamma_0^2}. \tag{2.61}$$

The real $-\delta_2$ term reflects the frequency shift induced by the coupling, which ensures the physical fields phase-match. Growth ($\gamma \equiv \mathrm{Im}\,\delta\omega_1 > 0$) occurs for the + root when $\gamma_0 > \delta_2/2$, which gives an estimate of the SRS bandwidth. The growth rate is

$$\gamma = \sqrt{\gamma_0^2 - \delta_2^2/4}. \tag{2.62}$$

For three natural, matching modes ($\delta_2 = 0$), the matching conditions and dispersion relations provide enough equations to determine the daughter waves of a specified pump wave. The resulting equation for k_2 to a good approximation is

$$\left[\rho(1 - 3g^2) + 3g^2\right] K_2^2 - \left[2g\cos\theta_2 \sqrt{1 - \rho^2}\right] K_2 + (2 - \rho)g^2 = 0. \tag{2.63}$$

$K_2 = k_2\lambda_D$, $g = v_{Te}/c$, $\rho = \sqrt{n_0/n_c}$, and θ_2 is the angle between $\vec{k}_0$ and $\vec{k}_2$ (see Fig. 2-1). Matching is only possible when real K_2 roots exist. This gives a condition on the maximum allowed θ_2:

$$\cos^2\theta_2 < \frac{2 - \rho}{1 - \rho^2}\left(\rho(1 - 3g^2) + 3g^2\right) \tag{2.64}$$

$$\approx 2(\rho + 3g^2), \qquad \rho, g \ll 1. \tag{2.65}$$

The angular dependence of SRS (forward, side, and backscatter) is discussed further on page 54.

Weak damping can be included and reduces the growth. The light waves damp via collisional inverse-bremsstrahlung. Electron-ion collisions produce a frictional drag on the electrons, which we

model by modifying the transverse momentum equation (2.13):

$$m_e \partial_t \vec{v}_t = -e\vec{E} - m_e \nu_{ei} \vec{v}_t. \tag{2.66}$$

In Fourier space, this relates the Fourier amplitude of the quiver velocity and vector potential of mode j (for $\nu_{ei} \ll \omega$)

$$\vec{V}_{tj} = \frac{e}{m_e} \frac{1}{1 + i\nu_{ei}/\omega_j} \vec{a}_j \approx \frac{e}{m_e} \left(1 - i\nu_{ei}/\omega_j\right) \vec{a}_j. \tag{2.67}$$

The light wave equation (2.11) in Fourier space, modified to include weak damping, gives for mode 1

$$\left(\Delta_1 - i\nu_{ei}\omega_p^2/\omega_1\right) a_1 = -\frac{\omega_p^2}{2n_0} a_0 a_2^*. \tag{2.68}$$

The pump (mode 0) satisfies a similar equation. The natural mode is found by neglecting the parametric coupling. Following the standard weak-damping $\omega \ll \nu$ analysis, we find the light-wave damping rate

$$\nu_{\text{emw}} = \frac{1}{2} \frac{\omega_p^2}{\omega^2} \nu_{ei}. \tag{2.69}$$

The dispersion factor Δ_1 thus gets replaced by $\Delta_1 - 2i\omega_1\nu_1$. Weak damping of the plasma wave, either collisional or Landau, is included in a similar way: $\Delta_2 \to \Delta_2 - 2i\omega_2\nu_2$ (see Sec. 2.5 for details). The dispersion relation Eq. (2.57) with damping is

$$\left(\Delta_1 - 2i\omega_1\nu_1\right)\left(\Delta_2 - 2i\omega_2\nu_2\right)^* = \bar{\Omega}^4. \tag{2.70}$$

The small $\delta\omega_1$ expansion gives

$$\left(\delta\omega_1 + i\nu_1\right)\left(\delta\omega_1 + \delta_2 + i\nu_2\right) \approx -\gamma_0^2. \tag{2.71}$$

δ_2 plays the role of an "imaginary damping" and limits the growth. The ensuing growth rate for $\delta_2 = 0$ (natural, matching modes) is the standard, oft-quoted result for linearized parametric instabilities:

$$\gamma = -\frac{1}{2}\left(\nu_1 + \nu_2\right) + \sqrt{\gamma_0^2 + \frac{1}{4}\left(\nu_1 - \nu_2\right)^2}. \tag{2.72}$$

Damping reduces the growth, and $\gamma > 0$ only for $\gamma_0 > \gamma_c \equiv \sqrt{\nu_1\nu_2}$. Note that if only one ν_i is nonzero, γ is always positive (there is always instability). We study the linear aspects of SRS, including its absolute or convective nature, via the coupled-mode equations in Sec. 2.4.

2.3 Coupled-mode equations (CMEs)

A more general way to study the PDEs (2.43-2.45) is to take the carrier-wave $\vec{k}_i$ and ω_i to be purely real and let the complex envelopes $a_i(x,t)$ evolve slowly in space and time. By "slow" we mean with respect to the carrier: $|\nabla a_i| \ll \left|\vec{k}_i a_i\right|$, $|\partial_t a_i| \ll |\omega_i a_i|$. We shall arrive at the coupled-mode equations (CMEs), where each a_i satisfies a first-order transport equation driven by the product of the other two a's. These equations allow for changes in the pump amplitude due to beating of the daughter waves (pump depletion). This aspect was neglected in Section 2.2's linear analysis and makes the equations nonlinear.

The derivation in this section applies to weakly-varying media, so $\vec{k}_i = \nabla\psi_i$ and $\omega_i = -\partial_t\psi_i$. However, we neglect derivatives of k and ω on the LHS's of Eqs. (2.43-2.45). These produce terms like $a_0\nabla\cdot\vec{v}_{g0}$ on the LHS of the CMEs, which are nonzero only for inhomogeneous plasmas. The justification for ignoring them is that the detuning length for k mismatch to be significant is much shorter than the scale lengths of these coefficients. In an inhomogeneous medium, the k's cannot be both natural modes and match over an extended region. As before, the physical fields end up phase-matching, although the resulting k's may not be natural modes. A change of variables analogous to $\tilde{a}_2$ turns the detuning from an exponential factor in the coupling to an imaginary damping.

2.3.1 Derivation of the CMEs

Let us start with the pump. With the envelope representations, Eq. (2.43) becomes

$$\begin{aligned} D_0 a_0 &= -2i\omega_0\ K a_1 a_2 \exp -i\ \delta\psi, && (2.73)\\ D_0 &\equiv \Delta_0 - 2\ i\ \omega_0(\partial_t + \vec{v}_{g0}\cdot\nabla) + \partial_{tt} - c^2\nabla^2, && (2.74)\\ \Delta_0 &\equiv -\omega_0^2 + c^2k_0^2 + \omega_p^2, \qquad \vec{v}_{g0} = c^2\frac{\vec{k}_0}{\omega_0}. && (2.75)\end{aligned}$$

As above, $\delta\psi = \psi_0 - \psi_1 - \psi_2$ is the phase mismatch. Note that Δ_i in this section is the dispersion factor for the carrier waves, not the "total" phase as in Sec. 2.2. We shall see, however, that in a linear analysis of the CMEs the slow a evolution can be absorbed into the Δ_i's, and we get the same dispersion relation as Eq. (2.71). Like before, we absorb $\delta\psi$ by working with $\tilde{a}_2 \equiv a_2 \exp -i\ \delta\psi$. Then Eq. (2.73) becomes

$$D_0 a_0 = -2i\omega_0\ K a_1 \tilde{a}_2. \tag{2.76}$$

Δ_0 measures the departure of the pump from a natural light wave. We take $\Delta_0 = 0$: small pump changes due to the parametric coupling are contained in a_0. The last two terms in D_0 that contain ∂_{tt}, ∇^2 we typically neglect, since they are much smaller than the middle terms $\sim \partial_t, \nabla$ in the envelope approximation. The result slow evolution of a_0 is

$$(\partial_t + \vec{v}_{g0}\cdot\nabla)a_0 = K a_1 \tilde{a}_2. \tag{2.77}$$

We perform a similar analysis for the daughter waves, but at first retain Δ_1, Δ_2 and $\partial_{tt}, \partial_{xx}$. The scattered light equation (2.44) produces

$$(\Delta_1 - 2i\omega_1(\partial_t + \vec{v}_{g1}\cdot\nabla) + \partial_{tt} - c^2\nabla^2)a_1 = -2i\omega_1\ K a_0 \tilde{a}_2^*, \tag{2.78}$$

$$\Delta_1 = -\omega_1^2 + c^2k_1^2 + \omega_p^2, \qquad \vec{v}_{g1} = c^2\frac{\vec{k}_1.}{\omega_1} \tag{2.79}$$

The plasma wave equation (2.45) in terms of $\tilde{a}_2$ is slightly more complicated:

$$(\Delta_{2t} - 2i\omega_{2t}(\partial_t + \vec{v}_{g2t}\cdot\nabla) + \partial_{tt} - 3v_{Te}^2\nabla^2)\tilde{a}_2 = \frac{2i\omega_2}{k_{2t}^2}\ K\left(k_{2t}^2 - 2i\vec{k}_{2t}\cdot\nabla + \nabla^2\right)a_0 a_1^*, \tag{2.80}$$

and

$$\Delta_{2t} = -\omega_{2t}^2 + 3v_{Te}^2\ k_{2t}^2 + \omega_p^2, \qquad \vec{v}_{g2t} = 3v_{Te}^2\frac{\vec{k}_{2t}}{\omega_{2t}}, \tag{2.81}$$

where $\vec{k}_{2t} \equiv \vec{k}_0 - \vec{k}_1$ and $\omega_{2t} \equiv \omega_0 - \omega_1$. For fixed pump, Eqs. (2.78, 2.80) form a linear system for a_1 and $\tilde{a}_2$. Fourier analyzing it gives the linear CME dispersion relation. It matches the linearized PDE dispersion relation Eq. (2.57), if one absorbs the slow ∂_t and ∇ into an effective $\vec{k}_1$ and ω_1 (and similarly for mode 2):

$$\Delta_{1\text{eff}} = -\omega_{1\text{eff}}^2 + c^2 k_{1\text{eff}}^2 + \omega_p^2, \qquad \omega_{1\text{eff}} = \omega_1 + i\partial_t, \qquad \vec{k}_{1\text{eff}} = \vec{k}_1 - i\nabla. \tag{2.82}$$

As before, the physical fields pick up phase shifts so that they exactly match. We henceforth consider matching modes and drop the subscript t on mode 2 quantities.

To arrive at the standard CMEs, we drop the slow ∂_{tt}, ∇^2 terms as small compared to $\omega_i(\partial_t + \vec{v}_{gi} \cdot \nabla)$. We also neglect the ∇, ∇^2 terms on the RHS of the plasma wave equation, since they are $\ll k_2^2$. Thus,

$$\begin{aligned}
(\partial_t + \vec{v}_{g0} \cdot \nabla) a_0 &= K a_1 a_2, & (2.83)\\
(\partial_t + \vec{v}_{g1} \cdot \nabla + i\delta_1)\, a_1 &= -K a_0 a_2^*, & (2.84)\\
(\partial_t + \vec{v}_{g2} \cdot \nabla + i\delta_2)\, a_2 &= -K a_0 a_1^*. & (2.85)
\end{aligned}$$

The detuning frequencies $\delta_i \equiv \Delta_i / (2\omega_i)$ represent departures of the modes from being natural, and limit the growth to a narrow band around the natural, matching modes.

Inclusion of weak damping gives rise to a term $\nu_i a_i$ on the LHS's of Eqs. (2.83-2.85). The collisional light-wave damping was presented above. The plasma wave undergoes both collisional and Landau damping; the latter usually dominates in high-temperature plasmas. See section 2.5 for a derivation of the plasma-wave CME from a kinetic description, and the relationship between ν_2 and the Landau damping rate. For brevity absorb the δ_i terms (which play the role of an imaginary damping and vanish for natural modes) into complex, effective dampings $\hat{\nu}_i$; usually we take $\delta_0 = \delta_1 = 0$ and consider detuning of mode 2. We hereby obtain from Eq. (2.83-2.85) the standard form of the CMEs:

$$\begin{aligned}
D_0 a_0 &= K a_1 a_2, & (2.86)\\
D_1 a_1 &= -K a_0 a_2^*, & (2.87)\\
D_2 a_2 &= -K a_0 a_1^*, & (2.88)
\end{aligned}$$

where $D_i \equiv \partial_t + \vec{v}_{gi} \cdot \nabla + \hat{\nu}_i$ and $\hat{\nu}_i \equiv \nu_i + i\delta_i$. The equations apply to weakly-varying plasmas. However, in this case all the modes can be natural ($\delta_i = 0$) at only one point, called the resonance or matching point.

2.3.2 CME conservation laws, Manley-Rowe relations

This section presents the conservation of energy and Manley-Rowe relations for the CMEs. These relationships allow one to view the three coupled modes as consisting of "quasi-particles" or elementary excitations that can decay into one another. This viewpoint has been adopted, e.g., in [68] to study the interaction of positive- and negative-energy modes.

The CMEs give the evolution of the action densities $N_i = a_i a_i^*$. Note that

$$\partial_t N_i = a_i^* \partial_t a_i + c.c., \qquad \nabla N_i = a_i^* \nabla a_i + c.c., \qquad 2\nu_i N_i = a_i^* \hat{\nu}_i a_i + c.c. \tag{2.89}$$

With $a_i = N_i^{1/2} \exp i\theta_i$ the CMEs give the following system for the N_i:

$$\bar{D}_0 N_0 = -\bar{D}_1 N_1 = -\bar{D}_2 N_2 = \bar{K}, \tag{2.90}$$

where

$$\bar{D}_i \equiv \partial_t + \vec{v}_{gi} \cdot \nabla + 2\nu_i, \tag{2.91}$$

$$\bar{K} \equiv 2K\sqrt{N_0 N_1 N_2} \cos \delta\theta, \tag{2.92}$$

and $\delta\theta \equiv \theta_0 - \theta_1 - \theta_2$. The phases evolve according to

$$N_i \left(\partial_t + \vec{v}_{gi} \cdot \nabla + \delta_i\right) \theta_i = \hat{K}, \qquad \hat{K} \equiv -K\sqrt{N_0 N_1 N_2} \sin \delta\theta. \tag{2.93}$$

The N equations contain the dampings ν_i, while the θ equations contain the detuning δ_i. Chow and Bers studied the chaotic behavior of the space-time CMEs including pump depletion and detuning [69]. If at $t = 0$ all $\theta_i(x)$ are constant and $\delta\theta = 0$ or π, all θ_i remain constant in space and time. Such a phase choice that gives the usual decrease of N_0 and increase of N_1 and N_2 is $\theta_0 = \pi,\ \theta_1 = \theta_2 = 0$. Then a_0 is real-negative while $a_{1,2}$ are real-positive. The action transfer from Eq. (2.90) is $-\bar{D}_0 N_0 = \bar{D}_1 N_1 = \bar{D}_2 N_2 = 2K\sqrt{N_0 N_1 N_2} > 0$ (recall K is real-positive).

We now consider $M_i \equiv \int_V N_i\, dV$, the action (or number of quasi-particles) contained in a fixed region of space V. To find the evolution of M_i, form $\int \bar{D}_i N_i\, dV$ and assume ν_i varies slowly enough that it can be pulled through the integral :

$$\int_V \bar{D}_i N_i\, dV = \frac{d}{dt}\int_V N_i\, dV + \int \vec{v}_{gi} \cdot \nabla N_i\, dV + 2\nu_i \int_V N_i\, dV \tag{2.94}$$

$$= \pm \int_V \bar{K}\, dV \tag{2.95}$$

(the + sign is for $i = 0$, while - is for $i = 1, 2$). Using $\vec{v}_{gi} \cdot \nabla N_i \approx \nabla \cdot (\vec{v}_{gi} N_i)$ (that is, neglecting $\nabla \cdot \vec{v}_{gi}$),

$$\frac{dM_i}{dt} = -\oint_{\partial V} d\vec{a} \cdot \vec{v}_{gi}\ N_i - 2\nu_i M_i \pm\ \bar{K}_M, \tag{2.96}$$

where $\bar{K}_M = \int_V \bar{K}\, dV$. The number of particles in V changes due to outflow, decay, and the parametric coupling (the first, second, and third terms on the RHS, respectively). We can view the light and plasma waves as consisting of "photons" and "plasmons" (quanta of action) that propagate, decay (with a lifetime of $1/2\nu_i$), and transform into each other. If we consider the rate of change due just to the coupling, we find

$$\left.\frac{dM_0}{dt}\right|_{coup} = -\left.\frac{dM_1}{dt}\right|_{coup} = -\left.\frac{dM_2}{dt}\right|_{coup} = \bar{K}_M. \tag{2.97}$$

This can represented in terms of quasi-particles as

$$\text{photon}_0 \rightarrow \text{photon}_1 + \text{plasmon}_2. \tag{2.98}$$

The mode energy in the region V is

$$U_i = \int_V W_i\, dV = M_i \omega_i. \tag{2.99}$$

Then Eq. (2.97) implies

$$\frac{1}{\omega_0}\frac{dU_0}{dt} = -\frac{1}{\omega_1}\frac{dU_1}{dt} = -\frac{1}{\omega_2}\frac{dU_2}{dt}. \tag{2.100}$$

Eq. (2.97) or (2.100) are known as the Manley-Rowe relations. The energy transfer to the daughters is partitioned according to $\dot{U}_1 = (\omega_1/\omega_2)\dot{U}_2$. When a pump photon decays, most of the energy is transferred to the daughter with higher frequency. This demonstrates, for instance, why SBS transfers very little energy to the plasma.

2.4 Instability analysis of the CMEs

We now study the linear behavior of Eqs. (2.87, 2.88) for fixed pump a_0 in a homogeneous medium with no detuning ($\delta_i = 0$). Detailed discussions of this analysis can be found in [67] and [70]. The latter reference provides a detailed discussion of absolute versus convective instability, the related pinch-point analysis, and applications of these ideas to coupled-mode problems. We outline the absolute-convective analysis here, and refer the reader to [71] or [70] for details.

Let D_1 act on Eq. (2.88) and obtain the linear equation

$$\left(D_1 D_2 - \gamma_0^2\right) a_2 = 0. \tag{2.101}$$

Fourier decomposing $a_2 \sim \exp i(\vec{\kappa}\cdot\vec{x} - \Omega t)$ obtains the dispersion relation

$$(\Omega - \vec{v}_{g1}\cdot\vec{\kappa} + i\nu_1)(\Omega - \vec{v}_{g2}\cdot\vec{\kappa} + i\nu_2) + \gamma_0^2 = 0. \tag{2.102}$$

We determine stability by looking for roots with $\gamma \equiv \mathrm{Im}\,\Omega > 0$ for $\vec{\kappa}$ real. γ maximizes when $\vec{\kappa} = 0$, for which $\Omega = i\gamma$ and γ is the usual growth rate with damping from Eq. (2.72). Instability ($\gamma > 0$) occurs when $\gamma_0 > \gamma_c \equiv \sqrt{\nu_1\nu_2}$. For simplicity, we consider 1-dimensional propagation in what follows. All $\vec{k}$'s point in the x direction: $\vec{k}_i = k_i\hat{x}$. We choose $k_0 > 0$. For SRS with ω_0 the largest frequency, we must have $k_2 > 0$ to satisfy matching (or else we'd need $|k_1| > k_0 + k_2$, which would require $\omega_1 > \omega_0$). The only "free sign" is $s_1 = \mathrm{sign}(k_1)$, with k_1 positive (negative) corresponding to forward (back) scatter. Note that $v_{pi},\ v_{gi}$ has the sign of k_i for all SRS modes.

An instability can either be convective or absolute. The difference refers to the time-asymptotic evolution of a local impulse $\sim \delta(t)\,\delta(\vec{x})$. If every observer at rest in the medium (the "lab frame") sees the signal grow in time without bound, the instability is absolute; otherwise it is convective. For a convectively unstable system, there exists a moving frame (the "pulse frame") in which the signal grows without bound. In this case, a lab observer sees the signal grow as the unstable pulse approaches and then decay as it passes by. A convective instability may leave a finite amplifying region before reaching an amplitude where nonlinearity is important. An absolute instability, however, grows at every point until nonlinear effects saturate it.

We work in the Fourier-Laplace domain (k and ω) rather than the physical domain (x and t). To construct the space-time signal from the Fourier-Laplace results requires choosing Fourier (k) and Laplace (ω) integration contours (F and L, respectively). The dispersion relation $D(k,\omega) = 0$ relates these contours. Given F, $D = 0$ gives frequency roots $\omega(k)$. Instability occurs when $\mathrm{Im}[\omega(k_r)] > 0$ for F along the real-k axis. Causality requires L lies above the largest ω_i. Refer to such an L as L_0.

One can deform F to lower the corresponding ω_i's. The dispersion relation, however, associates

k roots with an ω: $D(k(\omega),\omega)=0$. For ω on L, the corresponding $k(\omega)$ roots cannot cross F. Subject to this restriction, there is no absolute instability if one can choose F such that $\omega_i(k)<0$ for all frequency branches. One cannot deform past a point where two $k(\omega)$ branches "pinch," or touch the F contour at the same point. If such a pinch point occurs for an F that yields $\omega_i(k)>0$, then there *may* be an absolute instability. The caveat is the pinching k roots must be continuous deformations of "upper" ($k_i>0$) and "lower" ($k_i<0$) branches of $k(\omega)=0$ for $L=L_0$. The algebraic condition for ω to be a pinch point is $D(k,\omega)=\partial D/\partial k=0$.

For the CME dispersion relation Eq. (2.102), this analysis plays out as follows. κ and Ω play the role of k and ω in the preceding general discussion. $\Omega_i(\kappa_r)>0$ when $\gamma_0>\gamma_c$, as mentioned above. Let us choose $L_0:\Omega=\Omega_r+i\Omega_i,\ \Omega_r=(-\infty,\infty)$ and $\Omega_i\to+\infty$. The dispersion relation Eq. (2.102) is quadratic in κ and gives two κ roots for each Ω. As $\Omega_i\to+\infty$ we see the two κ branches lie on opposite sides of the real κ axis if and only if $k_1<0$. Therefore, absolute instability is only possible for oppositely-propagating daughter waves. We can solve the two pinch-point equations $D(\kappa,\Omega)=\partial D/\partial\kappa=0$ for Eq. (2.102). The solution gives the time-asymptotic growth rate $\gamma_{A\infty}=\operatorname{Im}\Omega$ once the absolute instability is full developed:

$$(|v_{g1}|+v_{g2})\,\gamma_{A\infty}=2\gamma_0\sqrt{|v_{g1}v_{g2}|}-(|v_{g1}|\,\nu_2+v_{g2}\nu_1)\,. \tag{2.103}$$

Since $2\sqrt{|v_{g1}v_{g2}|}<(|v_{g1}|+v_{g2})$, $\gamma_{A\infty}<\gamma_0$ even for $\nu_1=\nu_2=0$. Under typical BSRS conditions $v_{g2}\ll|v_{g1}|\,,\nu_1\ll\nu_2$ we have approximately $\gamma_{A\infty}\approx2\gamma_0\sqrt{|v_{g1}|\,/v_{g2}}-\nu_2$. The condition $\gamma_{A\infty}>0$ gives the threshold pump strength γ_a for absolute instability

$$\gamma_0>\gamma_a=\frac{1}{2}\sqrt{|v_{g1}v_{g2}|}\,(\sigma_1+\sigma_2)\,, \tag{2.104}$$

with $\sigma_i\equiv\nu_i/\,|v_{gi}|$ the spatial damping rate of mode i in the direction of propagation (σ_i is always positive). For $\nu_1=0$ the absolute instability condition becomes

$$\gamma_0>\gamma_{a,\nu_2}\equiv\left|\frac{v_{g1}}{v_{g2}}\right|^{1/2}\nu_2\qquad\qquad(\nu_1=0). \tag{2.105}$$

The instability and absolute instability conditions can be expressed as threshold pump amplitudes. For SRS, we write these as threshold pump laser intensities. γ_0 and the pump intensity I_0 are related by

$$I_0=h\gamma_0^2,\qquad\qquad h\equiv8\frac{\omega_0^2\omega_1\omega_2}{\omega_p^2k_2^2}\frac{P_{em}}{c^4}\eta_0. \tag{2.106}$$

Thus, the pump thresholds are

$$\gamma_0>\gamma_{c,a}\qquad\leftrightarrow\qquad I_0>I_{c,a}\equiv h\,\gamma_{c,a}^2. \tag{2.107}$$

I_c and I_a in typical hohlraum conditions are shown below in Fig. 2-6.

When SRS is unstable ($\gamma_0>\gamma_c$) but below the absolute threshold, it is a convective instability. In this case, the early-time evolution of the instability consists of exponential growth in time from small amplitudes at the rate γ. However, after the scattered light wave (the faster daughter wave) traverses the interaction region several times, the system approaches a temporal steady state (this behavior is seen, e.g., in [39]).

In the convective steady state, the daughter amplitudes grow exponentially in space from one side of the interaction region to the other. The direction of growth is determined as follows. For a convective instability, one can deform F without pinching to one with $\Omega_i(\kappa) < 0$ for all branches. However, if the system is unstable ($\Omega_i(\kappa_r) > 0$), then one of the upper or lower $\kappa(\Omega)$ roots will cross the real κ axis in the deformation process. It is sufficient to consider an L contour just below the real Ω axis, that is, $\Omega = \Omega_r$. The region where $\kappa(\Omega_r)$ has crossed indicates spatial amplification. The region's endpoints satisfy $\kappa(\Omega_r) = 0$.

Let us determine what crossings are possible. Eq. (2.102) gives a complex quadratic equation for the two branches $\kappa_\pm$. The solutions for $\Omega_i = 0$ (an L contour just below the real Ω axis) are

$$\kappa_{\pm i} = \sigma_+ \pm s_1 \kappa_{si}, \tag{2.108}$$

$$\kappa_{si}^2 = \frac{1}{2}\left(-\kappa_{Tr} + \sqrt{\kappa_{Tr}^2 + \kappa_{Ti}^2}\right) \tag{2.109}$$

with $\alpha_0 = \gamma_0/\sqrt{|v_{g1}v_{g2}|}$, $\kappa_{Tr} \equiv -\sigma_-^2 + u_-^2\omega_r^2 - s_1\alpha_0^2$, $\kappa_{Ti} \equiv 2u_-\sigma_-\omega_r$, $\sigma_\pm \equiv (\sigma_2 \pm s_1\sigma_1)/2$, and $u_\pm \equiv (1/v_{g2} \pm 1/v_{g1})/2$. We choose κ_{si} to be the positive branch of κ_{si}^2. Recall s_1 =sign(k_1). We treat the two directions of scattered-light propagation separately:

$\mathbf{k}_1 > 0$: $\sigma_+ > 0$ and κ_+ always describes an upper branch. We know from the absolute instability discussion that both κ branches are on the same side of the real κ axis for Ω on the L_0 contour described there. Thus κ_- is initially an upper branch as well. Spatial growth then occurs when a different L contour gives a κ_- that has a segment with $\kappa_{-i} < 0$. Growth is then in the positive x direction (forward scatter, in the direction of k_0). κ_- can cross the real κ axis only if $\sigma_+ < \kappa_{si}$. This condition for $\Omega_i = 0$ becomes, after some algebra,

$$\gamma_0^2 > \gamma_c^2 + P\Omega_r^2, \qquad P \equiv \nu_1\nu_2\left(\frac{u_-}{\sigma_+}\right)^2 > 0. \tag{2.110}$$

As long as $\gamma_0 > \gamma_c$, there is a window around $\Omega_r = 0$ where spatial amplification occurs.

$\mathbf{k}_1 < 0$: σ_+ can in principle be negative, but under typical SRS conditions $\sigma_1 < \sigma_2$ and $\sigma_+ > 0$. κ_+ is thus an upper branch (it is the sum of two positive quantities). We know that $k_1 < 0$ allows for absolute instability, so κ_- must start as a lower branch. Instability occurs if $\sigma_+ > \kappa_{si}$ so that $\kappa_{-i} > 0$ for some $\Omega = \Omega_r$. This leads to growth in the $x < 0$ direction, i.e. backscatter. The instability condition again is Eq. (2.110). We can only deform L below the real Ω axis if $\gamma_0 < \gamma_a$, so that we are below the absolute instability threshold. There is a range $\gamma_c < \gamma_0 < \gamma_a$ for which $k_1 < 0$ gives convective instability.

Another way to study the direction of pulse propagation is via the asymptotic unstable pulse shape ([67], p. 204). This tells us the growth rate γ_V in a frame moving with velocity V. γ_V is positive only for some range of V. The edge velocities V_1, V_2 are the points where $\gamma_V = 0$. If V_1, V_2 are on opposite sides of $V = 0$, the instability is absolute. Otherwise, the pulse grows in the direction where $\gamma_V > 0$. For the coupled-mode problem,

$$V_{1,2} = \frac{1}{1+\Gamma^2}\left(V_0 \pm \frac{1}{4}(v_{g2} - v_{g1})\frac{2\gamma\Gamma}{\nu_1+\nu_2}\right), \qquad V_0 \equiv v_{thr} + \frac{1}{4}(v_{g1}+v_{g2})^2\Gamma^2. \tag{2.111}$$

$\Gamma^2 \equiv 4(\gamma^2 - \gamma_c^2)/(\nu_1+\nu_2)^2$ and $v_{thr} = (\nu_1 v_{g2} + \nu_2 v_{g1})/(\nu_1+\nu_2)$. For $k_1 > 0$, $V_{1,2}$ cannot enclose zero (there is no absolute instability). Since $V_0 > 0$, both edge velocities are positive, and the pulse

propagates in the $+x$ direction. However, for $k_1 < 0$ in the convectively unstable case $\gamma_c < \gamma < \gamma_a$, V_0 is negative when

$$|v_{g1}| > \frac{1+\gamma_1\rho}{1+\gamma_2\rho} v_{g2}, \qquad \rho \equiv \frac{\nu_1+\nu_2}{2\left(\gamma^2-\gamma_c^2\right)}. \tag{2.112}$$

When collisional damping is included, γ_2 is always greater than γ_1. Both edge velocities are negative as long as $|v_{g1}| > v_{g2}$. Since v_{g1} is near c and $v_{g2} < 1.3 v_{Te}$ (from solving the kinetic EPW dispersion relation), this is always true. The pulse propagates toward $-x$ for $k_1 < 0$.

To find the spatial gain rate $\alpha = \kappa_i$, we solve the dispersion relation Eq. (2.102) for complex κ given real Ω. Note that α is positive or negative, and must have the correct sign deduced above for growth. The gain rate maximizes for $\Omega = 0$. For $k_1 > 0$, we find

$$\alpha = \frac{\sigma_1+\sigma_2}{2} - \sqrt{\alpha_0^2 + \frac{1}{4}\left(\sigma_1-\sigma_2\right)^2}, \qquad \alpha < 0 \text{ for growth} \qquad (k_1 > 0). \tag{2.113}$$

Instability clearly occurs for $\gamma_0 > \gamma_c$. Similarly, for $k_1 < 0$ the gain is

$$\alpha = \frac{\sigma_2-\sigma_1}{2} - \sqrt{-\alpha_0^2 + \frac{1}{4}\left(\sigma_1+\sigma_2\right)^2}, \qquad \alpha > 0 \text{ for growth} \qquad (k_1 < 0). \tag{2.114}$$

This formula is somewhat opaque. Growth happens for a restricted range of α_0, which corresponds to $\gamma_c < \gamma_0 < \gamma_a$. However, $\partial\alpha/\partial\alpha_0 > 0$ as long as convective growth occurs - increasing the pump increases the gain. The maximum $\alpha = (\sigma_2 - \sigma_1)/2$ occurs at the absolute threshold, namely $\alpha_0 = (\sigma_1+\sigma_2)/2$. Note that $\alpha \neq \alpha_0$ when there is no damping: the instability is not convective in that case! Calling α_0 the undamped gain rate is incorrect.

2.5 Kinetic description of SRS

Our analysis so far has used a fluid description. When $k_2\lambda_D$ is not small, kinetic effects become important in plasma waves. We can replace the fluid plasma-wave equations with the electron Vlasov equation in the direction of $\hat{x} = \vec{k_2}/|\vec{k_2}|$:

$$\partial_t f + v\partial_x f + F_x \partial_p f = 0. \tag{2.115}$$

The longitudinal force $F_x = -eE_x - ev_y(B_{0z} + B_{1z})$ contains the self-consistent plasma electric field as well as the longitudinal component of the $\vec{v}\times\vec{B}$ force from the light waves ($\vec{v}$ comes from the electron quiver motion). In this thesis we restrict ourselves to a nonrelativistic treatment, so $p = m_e v$. For natural plasma waves we drop the $\vec{v}\times\vec{B}$ force and find the kinetic dispersion relation $\hat{\varepsilon}\left(k\,,\omega\right) = 1 + \chi(k,\omega) = 0$. $\hat{\varepsilon}$ is the unitless permittivity (in SI units, the dielectric function is $\varepsilon_0\hat{\varepsilon}$) and χ is the kinetic electron susceptibility:

$$\chi(k,\omega) = -\frac{\omega_p^2}{k^2 n_0}\frac{d}{dv_p}\int_{-\infty}^{\infty} dv\,\frac{f_0(v)}{v-v_p}, \qquad v_p = \omega/k. \tag{2.116}$$

The integral is understood in the Landau sense. For a Maxwellian plasma $f_0 = n_0/(v_T\sqrt{2\pi})$ $\exp(-v^2/2v_T^2)$, χ is expressed in terms of the usual plasma dispersion or Z function:

$$\chi = -\frac{1}{2k^2\lambda_D^2} Z'\left(\zeta\right), \qquad \zeta \equiv \frac{v_p}{v_{Te}\sqrt{2}}. \tag{2.117}$$

In terms of complex errors functions, $Z(\zeta) = i\sqrt{\pi}w(\zeta)$ where $w(\zeta) = \exp(-\zeta^2)\ \mathrm{erfc}(-i\zeta)$ ([2], p. 297). This information is included in the thesis preamble. The reader may refer to appendix B, which derives the amplitude of a plasma wave driven by two light waves, to become acquainted with the kinetic description.

In laser-heated plasmas the equilibrium f is not a Maxwellian but a super-Gaussian DLM (Dum Langdon Matte) distribution [72]. This alters the plasma-wave dispersion relation, and can dramatically reduce the Landau damping rate of plasma waves [73]. We neglect this effect in this thesis, and do all calculations for a Maxwellian f. Also, in our kinetic simulations the initial f is Maxwellian. Large-amplitude high-frequency ($\omega \gg \omega_p$) waves, such as light waves, are known to alter the equilibrium f due to ponderomotive effects [74]. Since we do not resolve the velocity dependence in the direction of light-wave propagation (the transverse y direction) this effect is also excluded.

In this section we first analyze the kinetic linear SRS dispersion relation and compare it to our fluid theory. We then show how to include weak plasma-wave amplitude variation in a kinetic permittivity operator $\hat{\varepsilon}$. The CMEs are derived by expanding $\hat{\varepsilon}$ for weak variation. We solve the steady-state CMEs including inhomogeneity and pump depletion in the strong damping limit, where plasma-wave advection can be ignored compared to damping.

2.5.1 Kinetic linear dispersion relation

A linear instability analysis of the resulting system was carried out by Drake *et al.* [24]. They derive a general dispersion relation for arbitrary wave geometry, including ion motion, that accounts for both the electromagnetic and electrostatic components of the scattered light wave. SRS, SBS, Compton scatter, and filamentation are included in this dispersion relation. Recently, Salcedo *et al.* attempted to explain stimulated electron acoustic scatter by using this dispersion relation for a bi-Maxwellian electron distribution (bulk and beam) [40].

Drake's approach is analogous to the linear fluid approach above. That is, we take matching modes, so that $\vec{k}_0 = \vec{k}_1 + \vec{k}_2^*,\ \omega_0 = \omega_1 + \omega_2^*$. Neglecting the nonresonant anti-Stokes wave and the electrostatic part of the Stokes wave, the kinetic Raman dispersion relation is

$$\Delta_1^* \hat{\varepsilon} = \bar{\Omega}^4 \frac{\chi}{\omega_p^2} \sin^2 \beta. \tag{2.118}$$

β is the angle between the pump polarization $\vec{E}_0$ and $\vec{k}_1$. It is clear that the coupling is largest for $\beta = \pi/2$, which is the the choice we made for the fluid model geometry (see Fig. 2-1). From now on we take $\beta = \pi/2$. $\Delta_1 = -\omega_1^2 + c^2 k_1^2 + \omega_p^2$ is the usual scattered-wave dispersion factor. $\bar{\Omega}^4$ is defined in Eq. (2.57). $\hat{\varepsilon} = 0$ for a natural plasma wave, so $\hat{\varepsilon}$ plays the role of Δ_2. Since χ is a complicated function, we write the mode 1 quantities in terms of modes 0 and 2: $\vec{k}_1 = \vec{k}_0 - \vec{k}_2^*$, $\omega_1 = \omega_0 - \omega_2^*$. Eq. (2.118) in more familiar form is

$$\left[-(\omega_0 - \omega_2)^2 + c^2 (k_0 - k_2)^2 + \omega_p^2 \right] \hat{\varepsilon}(k_2, \omega_2) = \frac{1}{4} k_2^2 v_{os0}^2 \chi(k_2, \omega_2) \tag{2.119}$$

$$= 4\gamma_0^2 \frac{\omega_1 \omega_2}{\omega_p^2} \chi. \tag{2.120}$$

We now show, under certain conditions, how to obtain the coupled-mode dispersion relation

Eq. (2.102) from the kinetic dispersion relation Eq. (2.118). The approach will be useful in studying inhomogeneous plasmas and the nonlinear plasma-wave frequency shift. As is usual for weakly damped (or growing) modes, we write $\hat{\varepsilon}(k,\omega) = \hat{\varepsilon}_r + i\hat{\varepsilon}_i$ where $\hat{\varepsilon}_r$ ($\hat{\varepsilon}_i$) is real (imaginary) for real k and ω and $|\hat{\varepsilon}_i| \ll |\hat{\varepsilon}_r|$. Let the real variables k_U and ω_U describe the "undamped" mode satisfying $\hat{\varepsilon}_r(k_U, \omega_{2U}) = 0$. The undamped mode in general differs from the natural mode k_N, ω_N which satisfies $\hat{\varepsilon}(k_N, \omega_N) = 0$. Consider k_N real. Not only is ω_N complex, but $\mathrm{Re}[\omega_N] \neq \omega_U$ for $k_U = k_N$. The difference vanishes as damping become weaker ($|\hat{\varepsilon}_i/\hat{\varepsilon}_r| \to 0$). In fact, there are two ω_U roots for each k_U, one $> \omega_p$ (the EPW branch) and one that is approximately acoustic for small k; they merge for $k\lambda_D \approx 0.53$, while there are no real roots for larger k. There are still EPW roots to the full dispersion relation for $k > 0.53$, although it is not permissible to neglect $\hat{\varepsilon}_i$. This is further discussed in Sec. 4.4.

The usual coupled-mode results follow from assuming the damping is weak. Write $k_2 = k_N + \delta k$, $\omega_2 = \omega_U + \delta\omega$ and δk, $\delta\omega$ are small. Expanding $\hat{\varepsilon}$ gives

$$\hat{\varepsilon}(k_2, \omega_2) \approx \underbrace{\hat{\varepsilon}_r}_{=0} + \delta k \frac{\partial \hat{\varepsilon}_r}{\partial k} + \delta\omega \frac{\partial \hat{\varepsilon}_r}{\partial \omega} + i\hat{\varepsilon}_i. \tag{2.121}$$

Quantities on the RHS are evaluated at (k_U, ω_U). Standard results from linear theory for weakly-damped modes give

$$v_{g2} = -\frac{\partial \hat{\varepsilon}_r/\partial k}{\partial \hat{\varepsilon}_r/\partial \omega}, \qquad \nu_2 = \frac{\hat{\varepsilon}_i}{\partial \hat{\varepsilon}_r/\partial \omega}. \tag{2.122}$$

Eq. (2.121) yields

$$\hat{\varepsilon} = \frac{\partial \hat{\varepsilon}_r}{\partial \omega} \left(\delta\omega - v_{g2}\delta k + i\nu_2\right). \tag{2.123}$$

Expanding Eq. (2.118) for natural matching modes, and taking the fluid approximation $\partial\hat{\varepsilon}_r/\partial\omega \approx 2\omega_{2lr}/\omega_p^2$, we find

$$\left(\delta\omega - v_{g1}\delta k\right)\left(\delta\omega - v_{g2}\delta k + i\nu_2\right) = \gamma_0^2 \chi. \tag{2.124}$$

$\chi \approx -1$ (equality holds for the complex natural mode) gives the coupled-mode dispersion relation Eq. (2.102) with $\nu_1 = 0$.

We stress that v_{g2} and ν_2 are evaluated at k_U, ω_U and are not the natural-mode quantities. In numerical examples below we shall nonetheless use the natural-mode values, since they are close as long as damping is not too strong. To correctly include kinetic effects one should resort to Eq. (2.118). This gives a region in ω_2, usually including both ω_U and ω_N, where SRS is unstable for a given k_2. One can then evaluate $\hat{\varepsilon}$ and its derivatives at an ω_2 where growth occurs and expand $\hat{\varepsilon}$ to arrive at a coupled-mode type expression. The quantities expressions involving $\hat{\varepsilon}$ which we call v_{g2} and ν_2 would be complex instead of real, and may differ substantially from their natural-mode values. Our approach of finding three natural, matching modes and then computing the SRS growth rate using the natural-mode v_{g2} and ν_2 is vindicated by the excellent agreement, both in k_2 and γ, of the natural, matching mode point with the maximum growth rate point from Eq. (2.118) in Fig. 2-2.

We compare the fluid and kinetic Raman dispersion relations in Fig. 2-2. This is for a reference set of parameters (called the "standard parameters") defined in the thesis preamble. This figure is calculated for a "collisionless plasma" (no collisional damping is included, but mode 2 is Landau damped). The dashed and solid curves are the roots of the fluid and kinetic dispersion relations, Eqs. (2.70) and (2.118), respectively. The $\circ$ and $\times$ are the natural, matching modes from the fluid

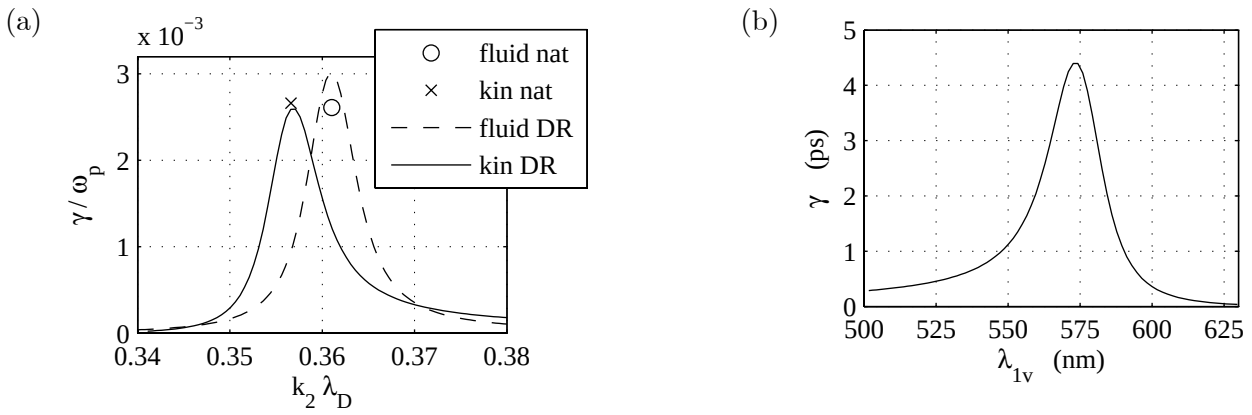

Figure 2-2: (a) BSRS growth rate using the fluid and kinetic dispersion relations, as well as the fluid and kinetic natural matching modes, for the collisionless standard parameters (the only damping is plasma-wave Landau damping). (b) Growth rate from kinetic dispersion relation vs. scattered light vacuum wavelength.

and kinetic real dispersion relations, with γ given by the standard linear result Eq. (2.72). We see that the natural, matching modes are very close to the fastest-growing mode.

The downshift of the kinetic compared to the fluid k_2 is explained by the different EPW dispersion relations. The natural, matching modes are found by using the matching conditions and dispersion relations to write a single equation for $\bar{k}_2$ with $\bar{k}_i \equiv k_i \lambda_D$:

$$\omega_2(\bar{k}_2) = \omega_0 - \omega_p \sqrt{1 + \left(c^2/v_{Te}^2\right)\left(\bar{k}_0 - \bar{k}_2\right)^2}. \tag{2.125}$$

$\omega_2(\bar{k}_2)$ is the EPW dispersion relation, and differs for the kinetic and fluid treatments. $\omega_2(\bar{k}_2)$ is always larger for the kinetic than for the fluid dispersion relation, as numerically solving the kinetic dispersion relation shows. We also note the kinetic dispersion relation to fourth order in $\bar{k}_2 \ll 1$ gives $\omega_2/\omega_p \approx 1 + (3/2)\bar{k}_2^2 + (15/8)\bar{k}_2^4$. The first two terms is the fluid result. This shows that the kinetic ω_2 is larger. Eq. (2.125) has two roots for k_2, one less than k_0 (forward scatter) and one greater than k_0 (back scatter). The LHS monotonically increases with $\bar{k}_2$. The RHS is zero for $\bar{k}_2 = 0$, increases until it maximizes at $\bar{k}_2 = \bar{k}_0$, and then decreases with $\bar{k}_2$. The $\bar{k}_2$ roots are where the LHS and RHS cross. The BSRS root for $\bar{k}_2$ occurs when the decreasing RHS meets the increasing LHS. When we move from the fluid to kinetic ω_2, we increase the LHS. This lowers the intersection $\bar{k}_2$ and explains why the fluid matching k_2 (the circle in Fig. 2-2(a)) is to the right of the kinetic k_2 (the x).

2.5.2 CMEs from kinetic description

We can derive the CMEs from a general description of the plasma wave in terms of a permittivity operator that includes slow evolution of the wave envelope, as in [25]. We begin by relating the plasma-wave electric displacement $\vec{D}$ to the total electric field $\vec{E}$. Recall that in electrodynamics the macroscopic fields $\vec{D}$ and $\vec{B}$ are defined in terms of the "free" or external charge and current densities ρ_{ex} and $\vec{J}_{ex}$, as opposed to the "bound" or internal to the medium excitations ρ_{in} and $\vec{J}_{in}$. In particular, $\nabla \cdot \vec{D} = \rho_{ex}$. For SRS, we treat the plasma wave as the internal response and the ponderomotive force from the beating of the light waves as the external drive, which gives rise to an effective ρ_{ex}. We restrict ourselves to 1-dimensional electrostatic plasma waves.

The general linear relation between D and E for nearly homogeneous media is a space-time convolution [67]

$$D(x,t) = \epsilon_0 \int dx' dt' \bar{\epsilon}\left(x', t', x, t\right) E\left(x - x', t - t'\right). \tag{2.126}$$

$\bar{\epsilon}$ is the unitless space-time permittivity kernel. The dependence of $\bar{\epsilon}$ on x and t allows for medium variation; for uniform media we have $\bar{\epsilon}(x', t')$. The total electric field $E = E_{in} + E_{ex}$ where $\partial_x E_{in,ex} = \epsilon_0^{-1} \rho_{in,ex}$. We represent all fields as a slowly-varying envelope times a carrier wave, e.g., $E = (1/2)\tilde{E} \exp i\psi + cc$, $\psi = kx - \omega t$. k and ω are determined by the external driver E_{ex}. For the SRS problem, the beating of the two light waves acts as an external drive of plasma waves. In principle k and ω can vary, but we ignore this for SRS. The reason is the scale length $L_i = 1/\left|\partial_x \log k_i\right|$ of the light-wave k's is much longer than for the k_2 corresponding to a given ω_2. Consider a static plasma (uniform in time) with a density gradient. The fluid dispersion relations give $L_i = (2n/n')\left(\omega_i^2/\omega_p^2 - 1\right)$. The plasma wave has a much smaller ω than the light waves, so $L_2 \ll L_{0,1}$. For the standard parameters, $L_2/L_0 = 0.0567$ and $L_2/L_1 = 0.187$. Our analysis of inhomogeneity therefore focuses on variations in the plasma-wave permittivity rather than the light-wave k's.

Treating the $\exp i\psi$ and $\exp -i\psi$ terms in Eq. (2.126) as independent, we find

$$\tilde{D} = \epsilon_0 \int dx' dt' \bar{\epsilon} \exp\left(-i\psi'\right) \tilde{E}\left(x - x', t - t'\right) \tag{2.127}$$

where $\psi' = kx' - \omega t'$. The slowly-varying Fourier-space permittivity $\hat{\varepsilon}(k, \omega, x, t)$ is

$$\hat{\varepsilon}(k, \omega, x, t) \equiv \int dx' dt' \bar{\epsilon} \exp\left(-i\psi'\right). \tag{2.128}$$

For a pure Fourier mode of constant amplitude, $\tilde{E}$ is constant and we have $\tilde{D} = \epsilon_0 \hat{\varepsilon} \tilde{E}$. However, we wish to account for slow amplitude evolution. We can absorb this evolution into $\hat{\varepsilon}$ by Taylor expanding $\tilde{E}$:

$$\tilde{E}\left(x - x', t - t'\right) = \sum_{i,j=0}^{\infty} \frac{\left(-x'\partial_x\right)^i}{i!} \frac{\left(-t'\partial_t\right)^j}{j!} \tilde{E}(x,t) = \exp\left(-x'\partial_x - t'\partial_t\right) \tilde{E}(x,t). \tag{2.129}$$

Thus

$$\tilde{D} = \epsilon_0 \left\{ \int dx' dt' \bar{\epsilon} \exp -i\left[x'\left(k - i\partial_x\right) - t'\left(\omega + i\partial_t\right)\right] \right\} \tilde{E}(x,t). \tag{2.130}$$

The braced quantity is an operator $\hat{\varepsilon}$ with a wavenumber and frequency that include slow amplitude evolution:

$$\tilde{D} = \hat{\varepsilon}\left(k - i\partial_x, \omega + i\partial_t\right) \epsilon_0 \tilde{E}(x,t). \tag{2.131}$$

Using $\epsilon_0 ik\tilde{E} = ik\tilde{D} + \tilde{\rho}_{in} = \tilde{\rho}_{in} + \tilde{\rho}_{ex}$, we obtain

$$\hat{\varepsilon}\tilde{\rho}_{in} = -\chi\tilde{\rho}_{ex}, \tag{2.132}$$

where $\chi = \hat{\varepsilon} - 1$ was used. This expression is valid regardless of what plasma model (e.g., fluid or kinetic) we use for $\hat{\varepsilon}$. In addition, it is valid when the drive is not a natural mode ($\hat{\varepsilon}_r(k, \omega) \neq 0$) and for weakly inhomogeneous plasmas.

Let us write Eq. (2.132) for the SRS plasma wave. In terms of action amplitudes, $\tilde{\rho}_{in} \propto a_2$

and $\tilde{\rho}_{ex} \propto a_0 a_1^*$ (the $v \times B$ force from the beating of the light waves with phase $\psi_0 - \psi_1$). Also, $(k, \omega) \to (k_2, \omega_2)$. The relation of the a's to charge-density and electric-field amplitudes is given in subsection 2.1.2. Using those definitions, Eq. (2.132) gives

$$\hat{\varepsilon}\left(k_2 - i\partial_x, \omega_2 + i\partial_t\right) a_2 = 2i\frac{\omega_2}{\omega_p^2}\chi \; K a_0 a_1^*. \tag{2.133}$$

The plasma wave CME Eq. (2.88) is recovered by expanding $\hat{\varepsilon}$ for small ∂_x and ∂_t: $\hat{\varepsilon}\left(k_2 - i\partial_x, \omega_2 + i\partial_t\right)$ $\approx \hat{\varepsilon}_r + i\hat{\varepsilon}_i - i\left(\partial\hat{\varepsilon}_r/\partial k_2\right)\partial_x + i\left(\partial\hat{\varepsilon}_r/\partial\omega_2\right)\partial_t$. $\hat{\varepsilon}$ and its derivatives are evaluated at (k_2, ω_2). Using the group velocity v_{g2} and damping ν_2 from Eq. (2.122), Eq. (2.133) becomes

$$\left(\partial_t + v_{g2}\partial_x + \nu_2 + i\delta_2\right) a_2 = \left[2\frac{\omega_2}{\omega_p^2}\frac{\chi\left(k_2, \omega_2\right)}{\partial\hat{\varepsilon}_r/\partial\omega_2}\right] \; K a_0 a_1^*. \tag{2.134}$$

$\delta_2 \equiv -\hat{\varepsilon}_r/\left(\partial\hat{\varepsilon}_r/\partial\omega_2\right)$ is the kinetic detuning frequency and equals zero at the resonance point. In the fluid limit the bracketed factor becomes -1, and we recover the CME $D_2 a_2 = K a_0 a_1^*$.

2.5.3 Strong damping limit (SDL): steady-state solution

When Landau damping is strong enough, BSRS ($k_1 < 0$) enters what is called the strong damping limit (SDL), which has been applied to parametric coupling since at least Ref. [75]. In this limit, the advection term in the plasma wave CME Eq. (2.88) is much less than the damping term: $|v_{g2}\partial_x a_2| \ll |\hat{\nu}_2 a_2|$. For a homogeneous plasma in the convective steady state with gain rate α from Eq. (2.114), the SDL condition is $|\alpha| \ll \sigma_2$. α increases with α_0 until α reaches its maximum of $\sigma_2/2$ at $\gamma_0 = \gamma_a$. To keep α/σ_2 small we need α_0/σ_2 small. This gives

$$\alpha_0 \ll \sigma_2 \qquad \to \qquad \gamma_0 \ll \gamma_{a,CL} \qquad \text{(SDL condition)}. \tag{2.135}$$

$\gamma_{a,CL}$ is the collisionless absolute instability threshold defined in Eq. (2.105). The SDL can be thought of as meaning SRS is "well below absolute." In the SDL, α is approximately

$$\alpha \approx \alpha_{SDL} \equiv \frac{\gamma_0^2}{|v_{g1}|\,\nu_2} \qquad \text{(SDL)}. \tag{2.136}$$

The SDL is convenient since it allows us to write the plasma wave amplitude as an algebraic function of the local in x and t light-wave amplitudes. We can then analytically solve the steady-state CMEs, including pump depletion. Consider the steady-state ($\partial_t = 0$) 1-D CME's with undamped light waves (this is good for the weak damping limit where $|v_{gi}\partial_x a_i| \gg |\nu_i a_i|$ for the light waves). We use the kinetic description Eq. (2.133) for the plasma wave. In the steady-state SDL, we neglect derivatives of a_2. We can simply set $\partial_t = \partial_x = 0$ in the operator $\hat{\varepsilon}$ and arrive at the CME system (f' denotes df/dx)

$$v_{g0} a_0' = K a_1 a_2, \tag{2.137}$$

$$v_{g1} a_1' = -K a_0 a_2^*, \tag{2.138}$$

$$\hat{\varepsilon}\left(k_2, \omega_2\right) a_2 = 2i\frac{\omega_2}{\omega_p^2}\chi \; K a_0 a_1^*. \tag{2.139}$$

These equations and the following derivation are valid for homogeneous and inhomogeneous plas-

mas, except we neglect spatial variation of the light-wave group velocities v_{g0}, v_{g1}. As discussed on p. 48, this is valid since the plasma-wave scale length is much shorter than those of the light waves. Spatial variations in the EPW permittivity $\hat{\varepsilon}$ are kept. We immediately solve for a_2 in terms of the local light-wave amplitudes:

$$a_2 = \tau\ K a_0 a_1^*, \qquad \tau \equiv 2i\frac{\omega_2}{\omega_p^2}\frac{\chi}{\hat{\varepsilon}}. \tag{2.140}$$

The complex τ has units of time. As usual for steady-state problems, it is convenient to work with the action fluxes $Z_i = v_{gi} a_i a_i^*$ defined in Eq. (2.34). Eqs. (2.137 - 2.138) then become, neglecting $\partial_x v_{gi}$,

$$Z_0' = -Z_1', \qquad Z_1' = -\frac{2K^2\tau_r}{v_{g0}v_{g1}} Z_0 Z_1. \tag{2.141}$$

We specialize to backscatter geometry. The pump Z_0 and scattered light Z_1 propagate to the right ($v_{g0} > 0$) and left ($v_{g1} < 0$), respectively. Let the subscripts L and R denote quantities at the left and right edges x_L and x_R, respectively. The appropriate boundary conditions we must specify are $Z_0(x_L) \equiv Z_{0L}$ and $Z_1(x_R) \equiv Z_{1R}$. We normalize to Z_{0L}: $z_i \equiv |Z_i| / Z_{0L}$ (note $Z_{0,2}$ are positive but Z_1 is negative; all z_i are positive) and find

$$z_0' = z_1', \qquad z_1' = -2\alpha_k z_0 z_1 \tag{2.142}$$

where

$$\alpha_k = \frac{\tau_r \gamma_0^2}{v_{g1}} = \frac{2\gamma_0^2\omega_2}{|v_{g1}|\,\omega_p^2} \operatorname{Im}\left[\frac{\chi}{\hat{\varepsilon}}\right]. \tag{2.143}$$

$\alpha_k(x)$ is the kinetic spatially-varying SDL amplitude (as opposed to energy) gain rate. It is positive and has units of 1/length. $\gamma_0 = K a_{0L}$ is the undamped temporal growth rate in the undepleted pump. The plasma-wave action flux z_2 is

$$z_2 = \left|\tau^2\right| \gamma_0^2 \frac{v_{g2}}{|v_{g1}|} z_0 z_1. \tag{2.144}$$

The Manley-Rowe relation for the SDL system is $z_0 - z_1 = \text{const.}$ and does not involve the plasma wave. This yields $z_0 = \hat{z} + z_1$ where $\hat{z} \equiv 1 - z_{1L} > 0$.

We can separate the z_1' equation (2.142) to find

$$\frac{dz_1}{z_1(\hat{z} + z_1)} = -2\alpha_k(x)\,dx. \tag{2.145}$$

Integrating from x to x_R and using the method of partial fractions, we find

$$\log\left[\frac{z_1(\hat{z} + z_{1R})}{z_{1R}(\hat{z} + z_1)}\right] = \hat{z} G(x), \qquad G(x) \equiv \int_x^{x_R} dx'\, 2\alpha_k(x'). \tag{2.146}$$

G is the SRS intensity gain exponent. For a homogeneous plasma, α_k is constant and $G = 2\alpha_k(x_R - x)$. We solve Eq. (2.146) for z_1:

$$z_1 = \left[\frac{\hat{z}}{1 + \hat{z}/z_{1R} - e^{\hat{z}G}}\right] e^{\hat{z}G}. \tag{2.147}$$

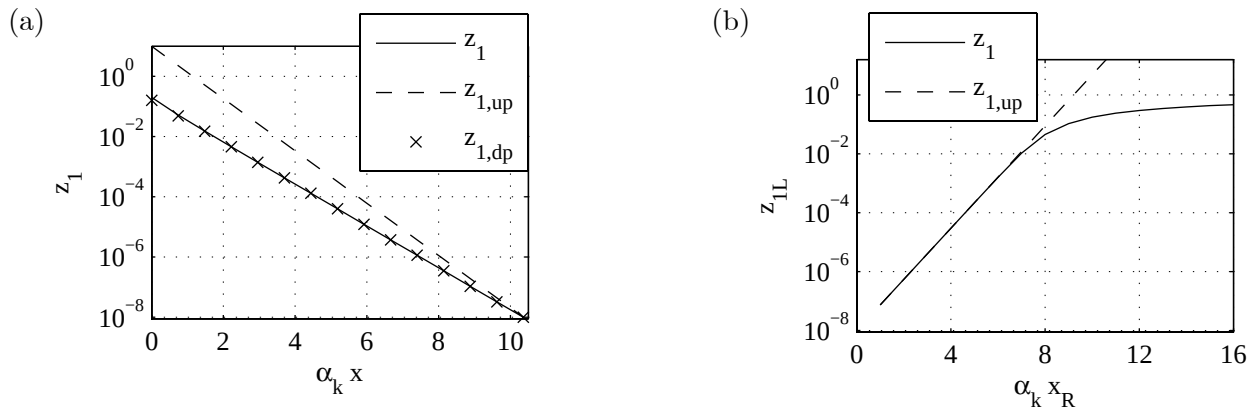

Figure 2-3: (a) scattered light z_1 from Eq. (2.147), the undepleted pump result $z_{1,\mathrm{up}} = z_{1R} \exp G$, and $z_{1,\mathrm{dp}} = z_{1R} \exp \hat{z} G$ for the homogeneous example of p. 51. (b) z_{1L} vs. x_R.

Evaluating Eq. (2.146) at $x = x_L$ gives

$$z_{1L} \left(1 + z_{1R} - z_{1L}\right) = e^{\hat{z} G_L}. \tag{2.148}$$

Solving for z_{1L} in terms of z_{1R} gives $z_1(x)$ and the reflectivity $R \equiv I_{1L}/I_{0L} = (\omega_1/\omega_0)\,|z_{1L}|$. For weak reflectivity $z_{1R}, z_{1L} \ll 1$ we recover the undepleted-pump results $z_{1,\mathrm{up}}(x) = z_{1R} \exp G(x)$ and $R_{\mathrm{up}} = (I_{1R}/I_{0L}) \exp G_L$.

Let us take a numerical example to see the effects of pump depletion. Choose a homogeneous plasma (α_k constant) and a seed level $z_{1R} = 10^{-8}$, which is small enough that pump depletion does not occur unless the scattered light undergoes large amplification. We set $x_L = 0$ and choose $\alpha_k x_R = 4.5 \log 10 = 10.36$ so that the undepleted-pump result is $z_{1L,\mathrm{up}} = 10$. Since we always have $z_{1L} < 1$ this case shows depletion effects. Figure 2-3(a) portrays z_1 from Eq. (2.147) as well as the undepleted pump result $z_{1,\mathrm{up}}$. In both cases z_1 grows exponentially to the left. In the steady state, the pump drops off most rapidly near the left edge. Farther to the right, the effective pump strength driving SRS is lower. This is reflected by the $\hat{z}$ factor in $\exp \hat{z} G$. The points marked with an 'x' in the figure are for $z_{1,\mathrm{dp}} = z_{1R} \exp \hat{z} G$ ("exponential with depleted pump") and are almost identical to the full z_1 solution. The effective lowering of G is thus the main difference when pump depletion is included; the bracketed factor in Eq. (2.147) changes things very little from z_{1R}. Fig. 2-3(b) displays the saturation of the left-edge signal z_{1L} with system length x_R due to pump depletion.

2.6 SRS in ICF hohlraums

2.6.1 Plasma conditions and electron-ion collisions

This section acquaints us with the physical scales relevant to ICF hohlraum plasmas, and explores the predictions of linear theory for SRS in these conditions. We fix the pump vacuum wavelength at $\lambda_0 = 351$ nm, appropriate to frequency-tripled Nd:glass light (which will be used on NIF and LMJ). This introduces a timescale $\tau_0 = \lambda_0/c = 1.17$ fs and a density scale (the critical density) $n_c = 9.05 \times 10^{27}$ m^{-3}, where $\omega_0^2 = n_c e^2/(\epsilon_0 m_e)$. For SRS, we are interested in underdense coronal plasmas with $n_0 < n_c/4$ (required to satisfy frequency matching). For very low n_0 the Landau

damping of the plasma wave becomes very large, and SRS cannot occur. In this study (if not in experiments), we also want to avoid the interaction between SRS and TPD which occurs near $n_0 = n_c/4$. These factors limit us to a density range of, say $0.05 \lesssim n_0/n_c \lesssim 0.2$, which gives plasma frequencies $\omega_p = \omega_0\sqrt{n_0/n_c}$ in the range $0.22 \lesssim \omega_p/\omega_0 \lesssim 0.45$. One should use the approximation $\omega_p \ll \omega_0$ with caution. Typical electron temperatures are in the keV, and $v_{Te} = \sqrt{T_e/m_e}$, $v_{Te}/c = 0.044\sqrt{T_{e,keV}}$.

First, we consider collisions. The electron-ion collision frequency for a single ion species j is [76]

$$\frac{\nu_{ej}}{\omega_p} = \frac{1}{3\,(2\pi)^{3/2}}\frac{1}{N_\lambda} f_j Z_j^2 \lambda_{ej}. \tag{2.149}$$

$N_\lambda = n_0\lambda_D^3$ is the number of particles in a Debye cube, $n_j = f_j n_0$, $Z_j = q_j/e$ is the ion charge state, $\lambda_{ej} = \log\Lambda_{ej}$ is the Coulomb logarithm, and $\Lambda_{ej} = r_{\max}/r_{\min}$. For the typical case $T_{j,eV} m_e/m_j < 10Z_j^2 < T_{e,eV}$, $r_{\max} = \lambda_D$ and $r_{\min}$ = the electron deBroglie wavelength. The standard parameters include a 50-50 H-He ion mixture with $T_i = T_e/3$ and satisfy this inequality. The resulting $\Lambda_{ej} \equiv \Lambda$ is independent of ion species and $\ln\Lambda = 30.9 - \ln(n_0^{1/2}/T_{e,eV})$. For the standard parameters,, $N_\lambda = 2244$ and $\ln\Lambda = 7.88$.

For multiple ion species, the probability that an electron suffers a collision with any ion in a time interval is the sum of the probabilities it collides with each species: $\nu_{ei} = \sum_j \nu_{ej}$. For a quasi-neutral plasma, $\sum_j f_j Z_j = 1$. Figure 2-4 shows ν_{ei} for our standard parameters and various n_0, T_e. For standard parameters, $\nu_{ei} = 2.10$ ps^{-1} $= 1/(4.76$ ps), or $\nu_{ei}/\omega_p = 1.24 \times 10^{-4}$. The electron mean free path $\lambda_{mfp} = v_{Te}/\nu_{ei} = 109$ μm. The spatial damping rate of light waves in a plasma ($\sigma_{0,1}$ from above) is

$$\sigma = \left|\frac{\nu}{v_g}\right| = \frac{1}{2}\frac{\nu_{ei}}{\omega}\frac{1}{d_e^2 k} \qquad \text{(EMW)}. \tag{2.150}$$

$d_e \equiv c/\omega_p$ is the (collisionless) electron skin depth. For mode 0 under standard parameters, this works out to a damping length of $1/\sigma_0 = 2.71$ cm. This is larger than the typical distance the lasers propagate between the LEH and hohlraum walls (see Fig. 1-1 in Chap. 1). Collisional damping can thus be safely neglected in the low-Z gas-fill plasma (but of course not near the hohlraum walls, where the light damps via collisions due to the much larger Z).

In typical hohlraums, the ion temperature lags that of the electrons, but not vastly. The lasers deposits energy in the coronal plasma primarily via electron quiver motion, randomized by collisions. This ionizes the gas, and collisions slowly transfer the energy to ions as the shot proceeds. The ion temperature equilibration rate is [76]

$$\nu_{eq,j} = 2.1\frac{m_e}{m_j}\frac{1}{f_j}\nu_{ej}. \tag{2.151}$$

For the H species in our standard parameters, we find $1/\nu_{eq,H} = 6.93$ ns. An ICF shot lasts for $\sim 10 - 20$ ns, so there is time for energy to transfer from electrons to ions. LASNEX simulations indicate T_i is usually around half of T_e for much of an implosion. We take $T_i = T_e/3$ for our sample calculations in this section.

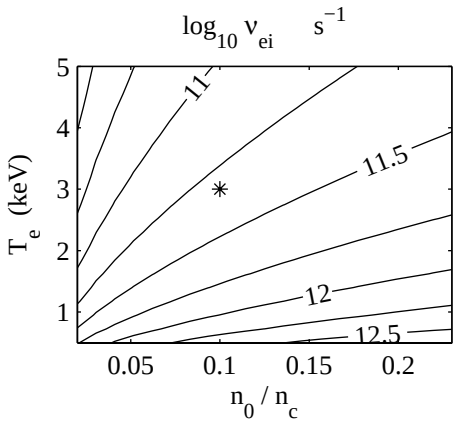

Figure 2-4: ν_{ei} for standard parameters (50-50 hydrogen-helium mixture). Star indicates the density and temperature in the "complete" standard parameters.

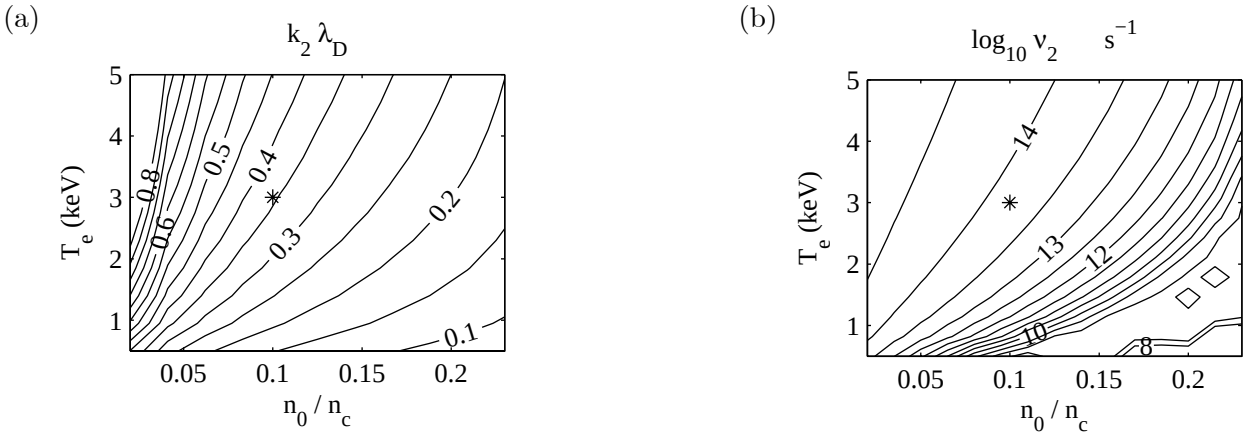

Figure 2-5: (a) $k_2\lambda_D$ and (b) ν_2 (Landau damping) for collisionless standard parameters.

2.6.2 Linear predictions for SRS growth

To get a feel for SRS in ICF, we consider all three modes to match and be natural. For given plasma conditions, this gives a unique set of modes. As seen in Fig. 2-2, they turn out to be very near the maximum growth rate of the dispersion relation. We use a kinetic description of the plasma wave to find $\omega_{2r}(k_2)$. Figure 2-5 shows the resulting $k_2\lambda_D$ and ν_2 (Landau damping rate) of the collisionless standard parameters for various n_0, T_e . Note that $k_2\lambda_D$, and therefore the Landau damping, increases with T_e and decreases with n_0. In the area of prime interest for ICF, where $T_e \sim$ several keV, $\nu_2 \gg \nu_{ei}$. For our standard parameters, $k_2\lambda_D = 0.357$, $\nu_2 = 0.0380\omega_p$, and $\nu_{ei}/\nu_2 = 0.0033$. The SRS growth rate from Eq. (2.72) is $\gamma = 4.28$ ps^{-1}, giving a growth time of $\gamma^{-1} = 0.234$ ps.

We display the threshold pump intensities I_c, I_a from Eq. (2.107) for instability and absolute instability in Fig. 2-6. Typical ICF lasers have beam-averaged intensities of $\lesssim 10^{15}$ W/cm^2 with speckles of up to 10^{16} W/cm^2. In these conditions, SRS will be unstable but not absolutely so. Fig. 2-7(a) shows the BSRS growth rate. This controls how quickly SRS develops initially, even if it is convective and approaches a steady state. We characterize the strength of convective SRS by

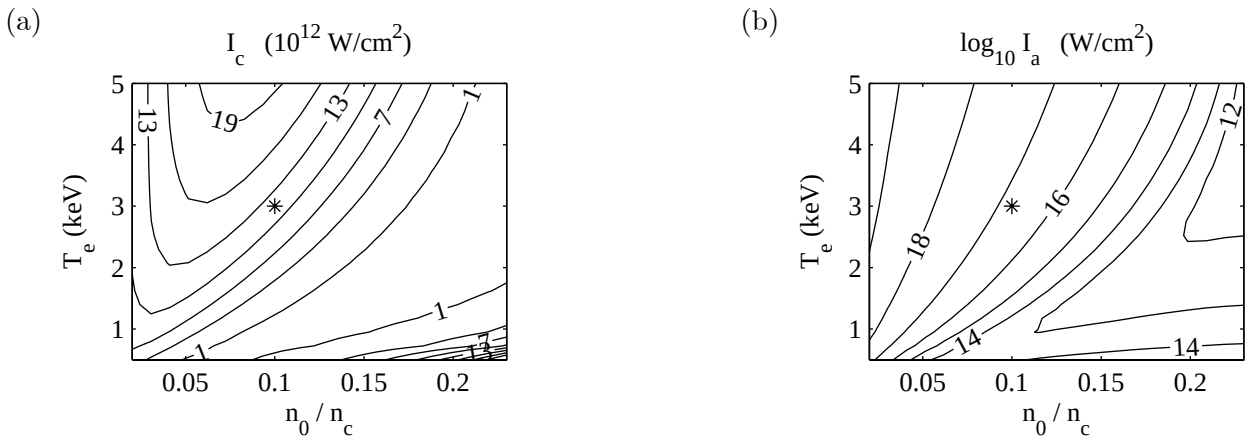

Figure 2-6: Threshold pump intensity for instability I_c (a) and absolute instability I_a (b) for collisional standard parameters.

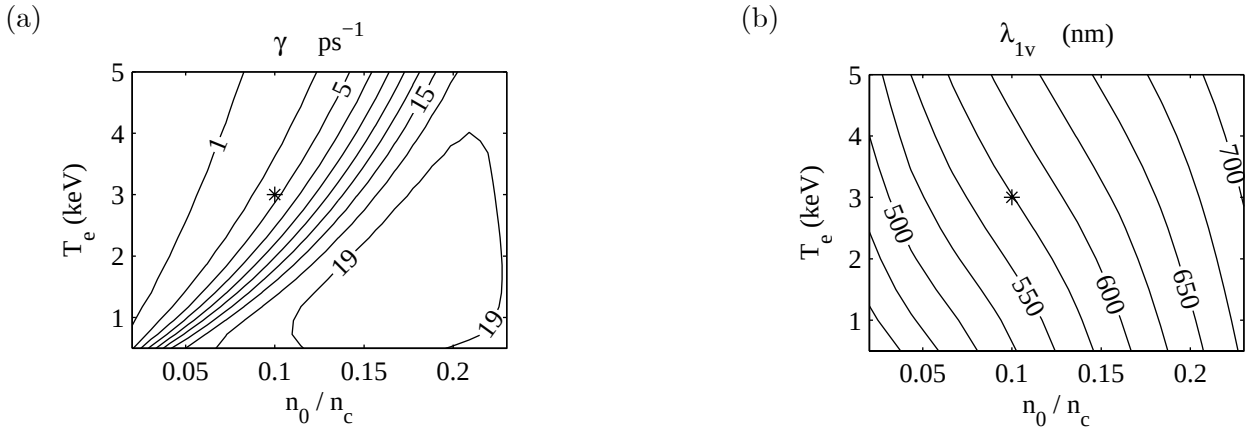

Figure 2-7: (a) SRS growth rate γ for kinetic natural matching modes using collisional standard parameters. (b) Vacuum λ_1 from kinetic matching.

the steady-state spatial gain rate α, from Eq. (2.114). As discussed above, BSRS is frequently in the strong damping limit (SDL): $\gamma_0 \ll \gamma_{a,CL}$ and $\alpha \approx \alpha_{SDL}$ from Eq. (2.136). Figure 2-8 shows α and α_{SDL}/α for collisionless standard parameters. The SDL gain rate is very accurate except near the convective-absolute boundary. We also present the vacuum λ_1 from kinetic matching in Fig. 2-7(b).

The SRS growth rate depends on the angles between the $\vec{k}$'s (recall the geometry from Fig. 2-1). Eq. (2.65) indicates there is a critical $\theta_{2c} \approx \arccos\left[(2\sqrt{n_0/n_c} + 6v_{Te}^2/c^2)^{1/2}\right]$ beyond which matching is impossible. There are two k_2 roots for each $\theta_2 < \theta_{2c}$, corresponding to forward (lower k_2) and back (higher k_2) scatter. We plot the roots using the kinetic dispersion relation for standard parameters in Fig. 2-9. The approximate formula Eq. (2.65) gives $\theta_{2c} = 36.3°$, which is close to the actual cutoff. This thesis focuses on kinetic effects, which are more important for backscatter since the plasma-wave phase velocity is lower. We therefore mainly concern ourselves with backscatter in what follows.

The scattered light can emerge with $\vec{k}_1$ at any angle to $\vec{k}_0$. The matching conditions give $\vec{k}_1$ as a function of k_2 and θ_2. For $\theta_2 = 0$, the larger and smaller k_2 give back ($\theta_1 = \pi$) and forward ($\theta_1 = 0$)

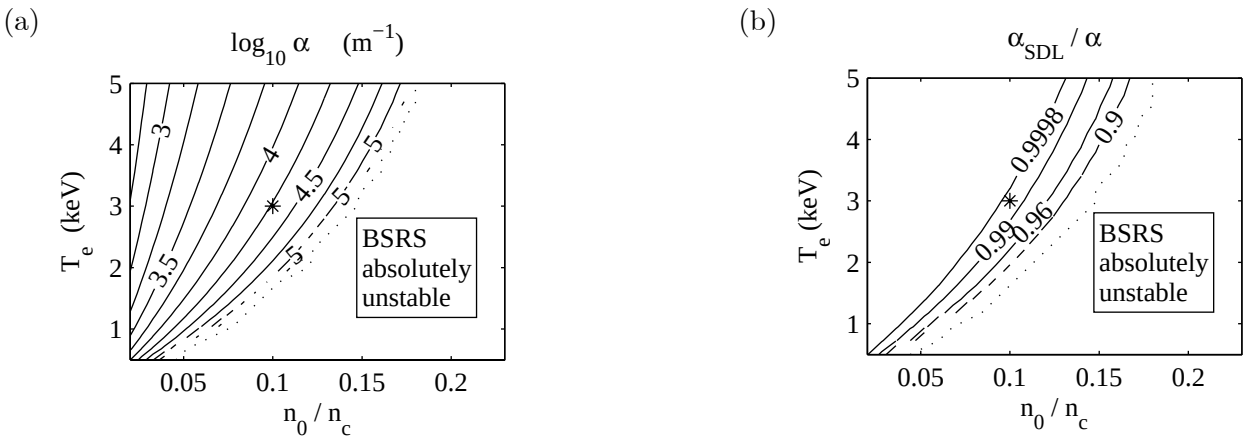

Figure 2-8: BSRS spatial gain rate α (a) and α_{SDL}/α (b) for collisionless standard parameters.

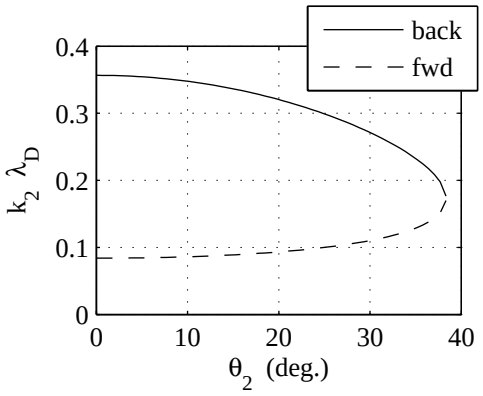

Figure 2-9: $k_2\lambda_D$ vs. θ_2 for collisional standard parameters.

scatter, respectively. In the fluid limit ($k_2\lambda_D \ll 1$, weak damping), the growth rate $\gamma \approx \gamma_0 \sim k_2$ peaks for the largest k_2, i. e. backscatter ($\theta_1 = \pi \rightarrow \theta_2 = 0,\ k_2 = k_0 + |k_1|$). This is not so when $k_2\lambda_D$ increases and Landau damping becomes appreciable [64]. ν_2 grows with k_2, so there is an optimal θ_1 for growth. We display γ vs. θ_1 for standard parameters and various T_e and n_0 in Fig. 2-10. These plots include collisional damping but are virtually unchanged if only Landau damping is used. For low T_e and high n_0, $k_2\lambda_D$ and Landau damping are small, γ is controlled by the k_2 effect, and backscatter dominates. However, Landau damping is important for high T_e, low n_0 plasmas, where sidescatter has the largest γ.

For convective SRS, the direction where most laser energy is scattered depends on the spatial gain in steady state (which roughly increases with γ) as well as the size of the amplifying region. The pump beam is generally much longer in its direction of propagation than it is wide. The aspect ratio is severe for a diffraction-limited speckle but much less so for a whole beam. Even though sidescatter has a higher growth rate than backscatter, it amplifies over a much shorter distance. We therefore neglect sidescatter and consider a 1-D SRS model below.

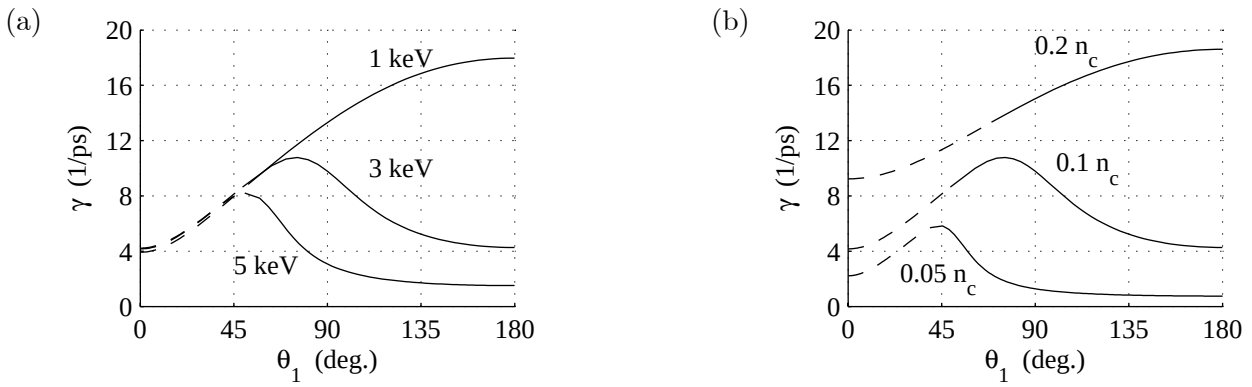

Figure 2-10: γ vs. θ_1 for collisional standard parameters but for several T_e (a) and several n_0 (b). The solid and dashed segments are for the high ("back") and low ("forward") $k_2\lambda_D$ roots, respectively.

2.6.3 Comparison with other LPI

A laser propagating through a plasma undergoes many nonlinear interactions besides SRS, discussed in Chap. 1. Stimulated Brillouin Scattering (SBS) couples the laser to a daughter light wave and an ion acoustic wave, and is discussed more in Sec. 3.6. An anti-correlation of the times when SRS and SBS levels are high is observed in many experiments. In the fluid limit, the SBS undamped growth rate is [77]

$$\gamma_{0,\mathrm{SBS}} = \frac{1}{\sqrt{8}} v_{os0}\omega_{pi}\sqrt{\frac{k_0}{\omega_0 c_s}}. \tag{2.152}$$

ω_{pi} is the ion plasma frequency, which for a single ion species is $\omega_{pi} = \omega_p\sqrt{Z_i m_e/m_i}$. $c_s = \sqrt{Z_i T_e/m_i}$ is the sound speed. Using the kinetic description of [24], which includes daughter wave damping, gives for the standard parameters $\gamma_{\mathrm{SBS}} = 0.618$ ps^{-1}. This is much less than the SRS growth rate $\gamma_{\mathrm{SRS}} = 4.28$ ps^{-1}, so over short times we may neglect SBS's effects on SRS.

A process related to SBS is the filamentation instability or self-focusing, which amplifies laser beam intensity ripples perpendicular to its propagation direction. An estimate of the filamentation growth rate can be found by solving the dispersion relation given in Eq. (8.21) on p. 93 of [77] (the later approximations made there are invalid for our case). The result for the standard parameters with just helium ions is $\gamma_{\mathrm{fil}} = 0.22$ ps^{-1}, which is much lass than γ_{SRS} and allows only one or two growth times over the duration of most simulations we perform. Filamentation primarily affects SRS by creating regions of high intensity within the laser beam, which gives a larger pump for SRS. We cannot study filamentation (a 2-D process) with the 1-D code ELVIS.

Two-plasmon decay (TPD, EMW→EPW+EPW), requires $n_0 \approx n_c/4$ to satisfy frequency matching and has the highest growth rates for plasmon k's roughly 45° from the pump. In hohlraums, the density reaches this level near the walls, where sharp gradients and high-Z gold suppress TPD. It is therefore a concern for direct but not indirect drive. We can prevent TPD from being a concern by considering densities sufficiently below quarter-critical. Plasmon-phonon decay (PPD) refers to the decay of a light wave to a plasma and ion-acoustic wave. Frequency matching requires $n_0 \approx n_c$ since IAWs have very low frequencies. This decay is suppressed for the same reasons TPD is but even more so, since gradients and high-Z concentrations are even higher at the required densities.

This thesis focuses on how electron trapping and inhomogeneity affect SRS when the plasma

wave has strong linear Landau damping. It is known that trapping can greatly reduce the Landau damping and greatly increase SRS over linear theory. To study this, we adopt a 1-D, kinetic, collisionless model. Neglecting light-wave damping ($\nu_0 = \nu_1 = 0$) makes SRS at least convectively unstable: $\gamma_c = 0$. For parameters of interest, plasma-wave Landau damping is usually much greater than collisional damping. SRS is therefore unstable but not absolutely unstable with or without collisional damping, and the SRS gain rates are comparable. The rest of this thesis demonstrates that this simple model entails a vast array of rich physics.

Chapter 3

Simulations of Raman Scattering from Homogeneous Plasmas

This chapter shows kinetic simulations of Raman scattering from finite, homogeneous plasmas, performed with the 1-D Vlasov-Maxwell solver ELVIS. Section 3.1 presents a run (labeled `BC1`) for our standard parameters where SRS is heavily Landau damped ($k_2\lambda_D = 0.357$, $\nu_2/\omega_2 = 0.0309$), which shows reflectivities far in excess of coupled-mode convective gain levels. We call the increase "kinetic enhancement" and attribute it to the reduction of Landau damping by electron trapping (dubbed "kinetic inflation" by some) [58]. The reflected light comes in sub-picosecond temporal bursts, and no steady state is reached. Forward SRS and the anti-Stokes line of the pump are also evident, as well as forward Raman re-scatter of the BSRS light. The electron distribution f_e shows phase-space vortices, and the space-averaged f_e is locally flattened at the EPW phase velocity. The $k-\omega$ spectrum of the longitudinal (plasma wave) electric field shows most of the activity occurs near or below the expected SRS k but downshifted in ω from the linear EPW dispersion curve. As the EPW builds to large amplitude, its instantaneous frequency decreases, in qualitative agreement with the trapping-induced frequency downshift. The plasma waves occur in a series of several pulses that propagate away from the laser entrance at the group velocity of the downshifted plasma waves. We do not attempt to determine which saturation mechanism - such as pump depletion, the nonlinear frequency shift, or the trapped particle instability - dominates.

We study the scattering for `BC1` conditions but various pump strengths I_0 and electron temperatures in Sec. 3.2. Trapping can only play a role if trapped electrons complete enough bounce motion to exchange energy with the plasma wave (and thereby reduce Landau damping) before they cross the finite box. The distance required for an electron to complete a bounce period decreases with wave amplitude, so kinetic enhancement occurs for pump strength above a threshold (which numerically is about $I_0 \approx 8 \times 10^{14}$ W/cm^2). Sufficiently below this level the reflectivity is near the coupled-mode steady-state value. Above this level SRS is bursty but does not increase much with I_0 - saturation has taken place.

The role of noise levels and seeding is discussed in Sec. 3.4. We first estimate the background level of thermal radiation noise in hohlraum plasmas, from the viewpoint of Kirchoff's law and the fluctuation-dissipation theorem. We find these plasmas are somewhat optically thick (optical depths near unity) *at the frequencies of Raman backscattered light* (that is, several eV), although they certainly do not radiate as blackbodies - they are optically thin to photons at the electron temperature of several keV. The SRS noise levels are much less than the numerical seeds we use.

Simulations with lower seed levels than BC1 have the same qualitative behavior (large, bursty reflectivity). We also examine the effects of the Krook operator we use for numerical purposes at the box edges, and the SRS that develops in the absence of a seed.

Section 3.6 discusses the role of ion dynamics, particularly LDI and SBS. The BSRS EPW in the immobile-ion run `BC1` exceeds the LDI threshold for only a few sub-picosecond periods. We present a run called `iBC` identical to `BC1` but with mobile helium ions. The reflectivity is large and chaotic, as for fixed ions, until a large "blob" of electrostatic activity develops near the laser entrance around 5 ps. After this time the reflectivity is very low. We analyze the dynamics in terms of parametric processes, and see several decays and cascades occur. However, we see very few signs of SBS of the pump laser or LDI of the BSRS EPW, two mechanisms thought to limit SRS in some regimes.

The chapter concludes with a consideration of loss mechanisms and their effect on trapping in Sec. 3.7. We analyze transverse sideloss from a laser speckle, 1-D collisional velocity diffusion, and pitch-angle scattering and find the threshold wave amplitude $\hat{n} = n_1/n_0$ needed for trapped electrons to bounce before becoming detrapped by each process. $\hat{n}$ for sideloss and 1-D diffusion are similar, but $\hat{n}$ for pitch-angle scattering is typically much less than for 1-D diffusion (trapping overcomes pitch-angle scattering at much smaller amplitudes). Reruns of `BC1` with a sideloss rate ν_{sl} (a nonzero value of the Krook relaxation rate ν_{Ke} in the central part of the box) show a sharp cutoff in the reflectivity for $\nu_{sl} \gtrsim 2 \times 10^{-3}\omega_p$ (much less than the Landau damping rate of $0.038\omega_p$). Below this value the reflectivity is large and bursty, while above this value it approaches the coupled-mode steady-state level.

3.1 The base case run `BC1`

In this section we analyze in detail the run `BC1`, for a homogeneous plasma with fixed ions, a monochromatic scattered-light seed, and no sideloss. The physical parameters are those of our "standard parameters" given in the thesis preamble ($n_0/n_c = 0.1$, $T_e = 3$ keV, $\lambda_{0v} = 351$ nm, $I_{0,15} = 2$ where I_{15} denotes intensity in units of 10^{15} W/cm^2). The reflectivity is found to be orders of magnitude larger than the predictions of coupled-mode theory, which we attribute to electron trapping. See Chap. 4 for a detailed discussion of trapping in EPWs. Table 3.1 contains k and ω for the natural matching modes of several parametric processes of interest, for the standard parameters with the helium ions used in Sec. 3.6. We use a shorthand for the different modes, explained in the table caption, which facilitates the discussion in Sec. 3.6. **Unless otherwise stated, all wavenumbers and frequencies in this chapter are given with respect to λ_D^{-1} and ω_p, respectively.**

3.1.1 Run parameters and setup

All simulations in this thesis were done with the Eulerian Vlasov-Maxwell code ELVIS [65], [66], described in detail in Appendix A. The code's transverse dynamics are collisionless, so $\nu_0 = \nu_1 = 0$ (no light-wave damping) and there is no instability threshold ($\gamma_c = 0$). ELVIS includes an optional Krook operator to mimic sideloss, prevent plasma-wave reflections from plasma edges, and remove kinetic energy from the finite plasma. ν_2 contains Landau damping and sometimes Krook damping. Landau damping provides an absolute instability threshold $I_{a,15} = 58.7$.

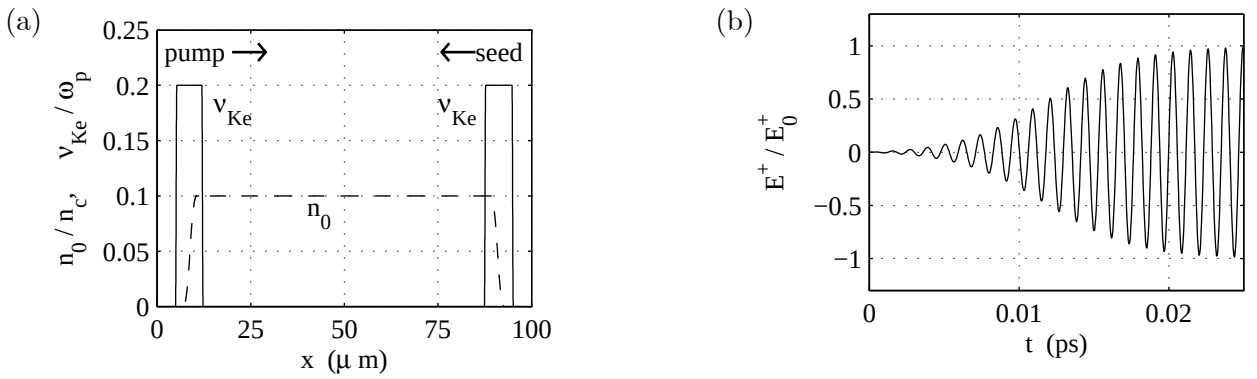

Figure 3-1: (a) Initial density (dashed) and ν_{Ke} profiles (solid, for Krook relaxation) for run `BC1`. (b) $E^+(t)$ at left edge.

The plasma spatial profile is shown in Fig. 3-1(a). The simulation domain extends from $x = 0$ to $x = L = 284\lambda_0 = 99.68$ μm. The left- and right-most 2.81 μm are "moats" where $f_e \equiv 0$ throughout the run but light waves can propagate. The light that reaches the edges is thus not due to edge plasma currents. Immediately inward of the moats are vacuum regions, where f_e is initially zero but allowed to evolve. Next we encounter two regions where the density ramps up, consisting of two parabolas with matching slopes at the ramp midpoint. We then have the central flattop region. After several plasma periods the electron density adjusts itself to a sheath-like pattern near the ramp-ups. The spatial grid is periodic for particles (but not for e/m fields) with the endpoints of the vacuum regions (not the moat regions) identified. That is, left-moving particles at the left edge appear at the right edge and vice versa. While this doesn't happen in a finite plasma, this approach conserves well the particle number and thus overall charge. We tried other boundary conditions, such as an open plasma (particles leaving were lost) and absorbing plates (particles leaving accumulate on charged boundary plates), none of which were as satisfactory. The large Krook relaxation operator in the edge regions prevents any structure (such as beams) from crossing from one side to the other: the particles crossing the edges have a Maxwellian distribution. For practical purposes the plasma is finite and not periodic.

We include a spatially-varying Krook relaxation rate $\nu_{Ke}(x)$, also plotted in Fig. 3-1(a). This function is zero for this run in the flattop region of length 75.1 μm, and is *not* intended to mimic sideloss. Instead, it is used to prevent plasma waves produced in the flattop from being reflected when they propagate to the ramps, and to stop oscillations generated near the ramps from propagating inward. Also, the Krook term removes kinetic energy from the electrons when waves damp at the edges; otherwise the finite plasma would gain energy via SRS indefinitely. Since the Krook term is used for numerical purposes, we give it a very large value $\nu_{Ke} = 0.2\omega_p$. In runs with a Krook term, SRS does not (or takes a long time to) occur without a seed due to the low numerical noise of continuum kinetic codes such as ELVIS. Without a Krook term, however, some SRS develops without any seed after long times. See Sec. 3.4 for further discussion.

The pump laser, which we label mode 0, impinges on the plasma from the laser entrance (here, the left edge). ELVIS represents the transverse e/m fields via the right- and left-moving combinations $E^\pm \equiv E_y \pm cB_z$. They satisfy the 1-D advection equations $(\partial_t \pm c\partial_x)\, E^\pm = -\varepsilon_0^{-1} J_y$, which imply the vacuum ($J_y = 0$) propagation $E^\pm(x, t + dt) = E^\pm(x \mp c\, dt, t)$. E^+ (E^-) advects to the right (left). In general, for $E^\pm$ we must specify the boundary conditions at the appropriate

mode	$\mathbf{k\lambda}_D$	$\boldsymbol{\omega/\omega}_p$	**comment**	**shorthand**
0	0.2299	3.162	pump	
*** PUMP DECAYS ***				
1	-0.1267	1.933	EMW in BSRS of 0	BR_{0m}
1u	-0.1355	2.031	upshifted mode 1 (approx.)	BR_{0m}
2	0.3566	1.229	EPW in BSRS of 0	BR_{0p}
3	0.146	2.15	EMW in FSRS of 0	FR_{0m}
4	0.0839	1.01	EPW in FSRS of 0	FR_{0p}
5	-0.229	3.15	EMW in SBS of 0	B_{0m}
6	0.459	8.76×10^{-3}	IAW in SBS of 0	B_{0i}
*** 1u (BSRS upshifted light) DECAYS (approximate) ***				
7	3.7×10^{-3}	≈ 1	EMW in BSRS of 1u	BR_{1m}
8	-0.14	1.03	EPW in BSRS of 1u	BR_{1p}
9	-8.68×10^{-3}	≈ 1	EMW in FSRS of 1u	FR_{1m}
10	-0.13	1.03	EPW in FSRS of 1u	BR_{1p}
11	0.135	2.03	EMW in SBS of 1u	B_{1m}
12	-0.27	5.36×10^{-3}	IAW in SBS of 1u	B_{1i}
*** 3 (FSRS light) DECAYS ***				
13	-0.0351	1.10	EMW in BSRS of 3	BR_{3m}
14	0.181	1.05	EPW in BSRS of 3	BR_{3p}
15	0.0411	1.14	EMW in FSRS of 3	FR_{3m}
16	0.105	1.02	EPW in FSRS of 3	FR_{3p}
17	-0.146	2.15	EMW in SBS of 3	B_{3m}
18	0.291	5.75×10^{-3}	IAW in SBS of 3	B_{3i}
*** 2 (BSRS EPW) DECAYS ***				
19	-0.338	1.21	EPW in LDI of 2	L_{2p}
20	0.695	0.0125	IAW in LDI of 2	L_{2i}
*** MODE 8/10 DECAYS				
21	0.13	1.02	EPW in LDI of 8/10	$L_{8/10p}$
22	-0.27	5.3×10^{-3}	IAW in LDI of 8/10	$L_{8/10i}$

Table 3.1: Parametric processes for standard parameters with helium. Mode 1u is chosen to allow the listed decays and reflects the upshift in Fig. 3-3. It and its decays thus have approximate values. The capital letters in a mode's shortand indicate it is a daughter wave of FSRS (FR), BSRS (BR), SBS (B), or LDI (L) process. The number subscript is the decay parent mode (1 means 1u). The letter subcript is the mode type: (m, p, i) for (EMW, EPW, IAW). For instance, B_{3m} is the daughter EMW in Brillouin scatter of mode 3. Since modes 8 and 10 are so close we treat their LDI as one process.

edges. We do this via

$$E^{\pm}(x_{0\pm},t) = \sum_i E_{0i}^{\pm}\sin(\omega_i^{\pm}t + \phi_i^{\pm})g_i^{\pm}(t) \tag{3.1}$$

where $x_{0\pm} = 0, L$ for $+,-$. $g_i^{\pm}(t)$ ramps from 0 to 1 over several wave periods (suddenly turning on the lasers can produce unwanted effects). For `BC1` we impose a single wave on each boundary and choose $\phi_i^{\pm} = 0$. E^+ contains the pump and other transmitted light, while E^- contains the reflected and backscattered light. We apply a scattered light seed to give SRS a level to grow from. Figure 3-1(b) depicts the pump turn-on for `BC1`.

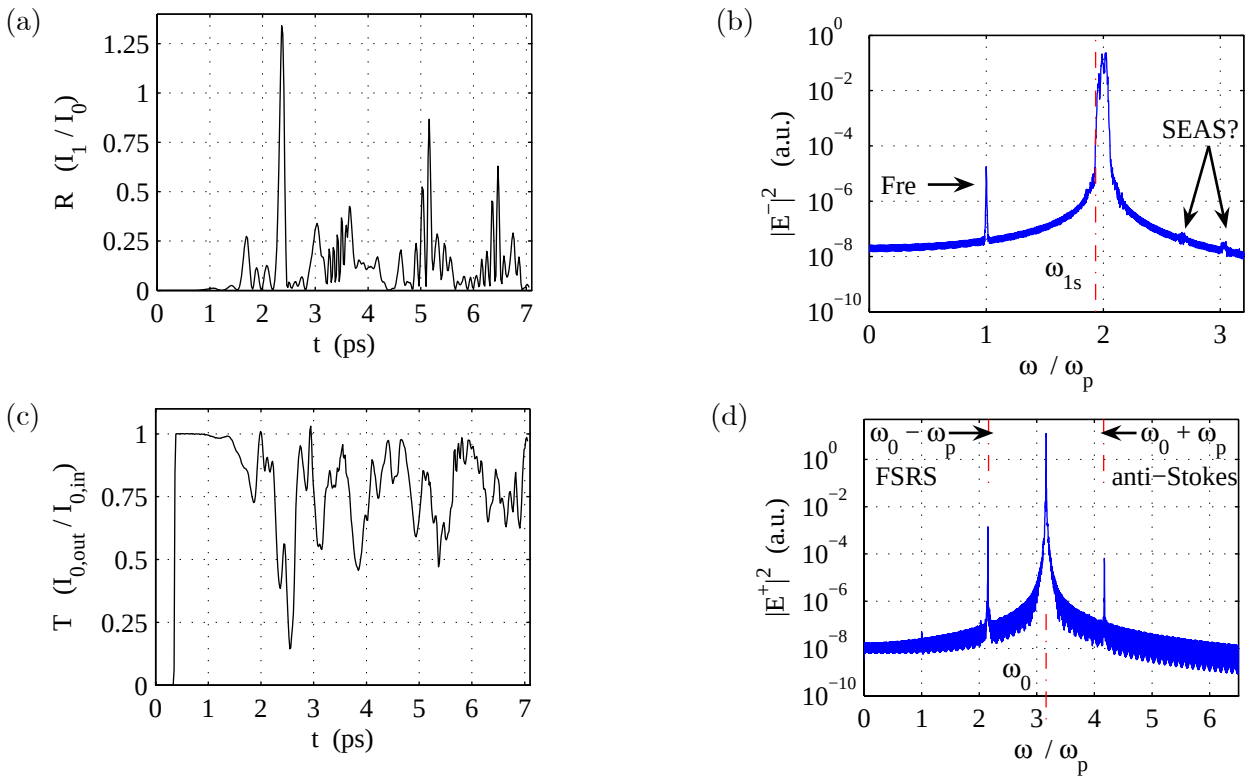

Figure 3-2: (a) Reflectivity R and (b) gated $E^-(x=0)$ spectrum over the whole run `BC1`. "Fre" and "SEAS?" denote forward re-scatter of BSRS light and possible stimulated electron acoustic scatter, respectively. ω_{1s} is the seed scattered light frequency. (c) Transmitted fraction T and (d) gated $E^+(x=L)$ spectrum over whole run at right edge.

3.1.2 Reflected and transmitted light

The instantaneous reflectivity $R \equiv \langle I_1(x=0)\rangle \,/\, \langle I_0(x=0)\rangle$ ($\langle\rangle$ denotes time average over several wave periods) is displayed in Fig. 3-2(a). Coupled-mode theory gives an amplitude gain rate for run `BC1` of $\alpha = 0.0190\ \mu\text{m}^{-1}$, or $\alpha^{-1} = 52.6\ \mu$m. Over the $\nu_{Ke} = 0$ flattop of 75.1 μm, this yields an intensity gain of $I_{1,\text{out}}$ =$17.2 I_{1,\text{in}}$. "Coupled-mode theory" refers to the linear theory of Sec. 2.4 or the nonlinear strong-damping-limit theory of subsection 2.5.3 when pump depletion is important. We seed the scattered light $E^-(L,t)$ with a vacuum wavelength $\lambda_{1s} = 574$ nm $\rightarrow$ $\omega_{1s}/\omega_p = 1.933$ (the linearly most unstable mode) and an intensity of $I_{1R} = 10^{-5} I_{0L} = 2\times 10^{10}$ W/cm^2. The coupled-mode steady-state $R = 1.72\times 10^{-4}$ is far below the numerically observed R. The numerical time-averaged R from $t = 1$ ps to the run end is $R_{\text{av}} = 13.8\%$. In addition, the reflectivity comes in temporal bursts, showing the system does not reach a steady state. Fig. 3-2(c) contains the transmitted fraction $T = I_{0,\text{out}}/I_{0,\text{in}}$ at the right edge, and reveals periods of strong pump depletion. The time-averaged T from 1 ps to the run end is $T_{\text{av}} = 78.4\%$. We discuss below how the reflected and transmitted fractions compare with Manley-Rowe estimates.

The "gated" (time-integrated, or averaged over a time interval) frequency spectrum of the backscattered light $E^-(x=0,t)$ for the whole run is shown in Fig. 3-2(b). Most of the power is confined to a narrow band slightly upshifted from the seed SRS frequency ω_{1s}. There is also a feature at ω_p, which we identify as forward Raman re-scatter of the primary BSRS light (mode 9 in table 3.1) and label "Fre." We shall see below the matching EPW activity. The seed SRS light

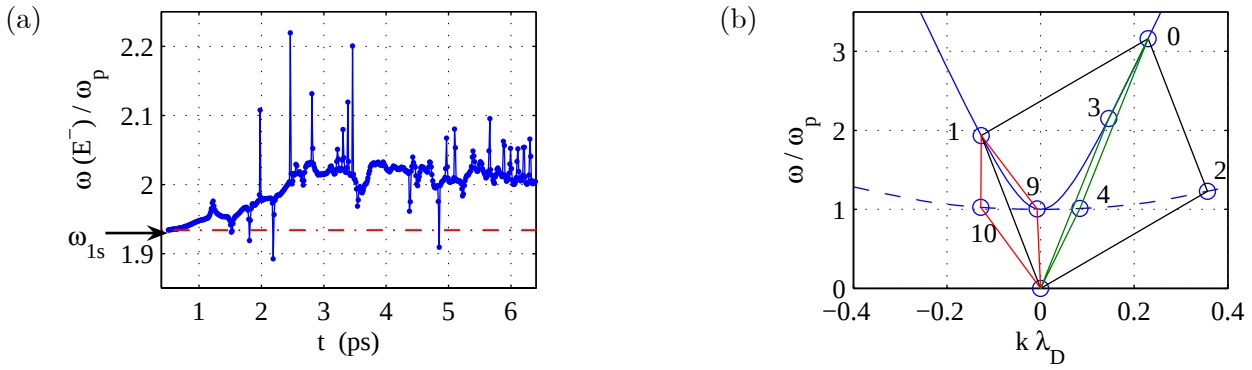

Figure 3-3: (a) Instantaneous frequency of $E^-(x=0,t)$ for run `BC1`. (b) Dispersion diagram of BSRS (black, modes 0, 1, 2), FSRS (green, modes 0, 3, 4) and forward re-scatter of BSRS (red, modes 1, 9, 10) for run `BC1`. The solid and dashed curves are the EMW and EPW dispersion relations. Mode numbers follow table 3.1.

cannot be the pump for a Raman process, since ω_{1s} is too low for frequency matching: $\omega_{1s} = 1.933 < 2$. Figure 3-3(a) is a time series of the "instantaneous frequency" of $E^-(x=0,t)$ (the definition and method of computing the "instantaneous frequency" is described on p. 144 of Appendix A). The scattered light begins at ω_{1s} but drifts upward over time and exceeds $2\omega_p$ after about 2.5 ps, thus allowing for forward re-scatter. We show the primary BSRS, primary FSRS, and forward re-scatter modes on the dispersion diagram in Fig. 3-3(b). Table 3.1 lists the corresponding natural, matching modes. Since ω_{1s} cannot undergo SRS, we calculate the "Fre" daughter waves based on the unshifted pump $\omega_{1u} = 2.031$. There are also a few wiggles labeled "SEAS?" which may be stimulated electron acoustic scattering (SEAS) off the longitudinal acoustic activity discussed below [52], [54], [53]. These feature are more clearly seen in the streaked E^- spectrum of Fig. 3-4(a).

The spectrum of transmitted light, displayed in Fig. 3-2(d), shows features at several frequencies besides the pump ω_0. The peak near $\omega_0 - \omega_p = 2.16$ is probably due to FSRS of the pump ($\omega_3 = 2.15$; see table 3.1), while the one at $\omega_0 + \omega_p$ is likely the anti-Stokes upshifted light. There is also a very small feature at ω_p, potentially mode 7 of table 3.1 (backward Raman re-scatter of mode 1). We analyze the plasma wave in the next subsection and find the corresponding EPWs that are part of FSRS and re-scatter of BSRS. As seen in Chap. 2, when plasma conditions give strong Landau damping of BSRS, FSRS can compete with it (see, for instance, Fig. 2-10). FSRS is always convective, and here has an undamped temporal growthrate $\gamma_{0F} = 4.34$ ps^{-1} and spatial amplitude gain rate $\alpha_F = 0.111$ μm^{-1}. γ_{0F} is comparable to the BSRS value $\gamma_{0B} = 4.52$ ps^{-1} and α_F is significantly greater than the BSRS $\alpha_B = 0.0190$ μm^{-1}. However, FSRS is not susceptible to kinetic enhancement due to damping reduction, since the EPW has a very low $k_4\lambda_D$ and essentially no Landau damping. In addition, it can never become an absolute instability since both daughter waves propagate in the same direction. For these reasons we do not focus on FSRS in this thesis, which concentrates on electron trapping and other kinetic effects. We also do not seed FSRS as we do BSRS, so FSRS must develop from fluctuations generated during the simulation.

We can see the time evolution of the light waves via a "streaked" spectrum, computed over successive time windows. Figure 3-4(a) presents the streaked spectrum of $E^-(x=0,t)$ for `BC1`. The BSRS signal develops before 1 ps, and upshifts and broadens at later times. The forward re-scatter signal near ω_p, also seen in Fig. 3-2(b), begins around $t = 3.5$ ps. The E^- streaked

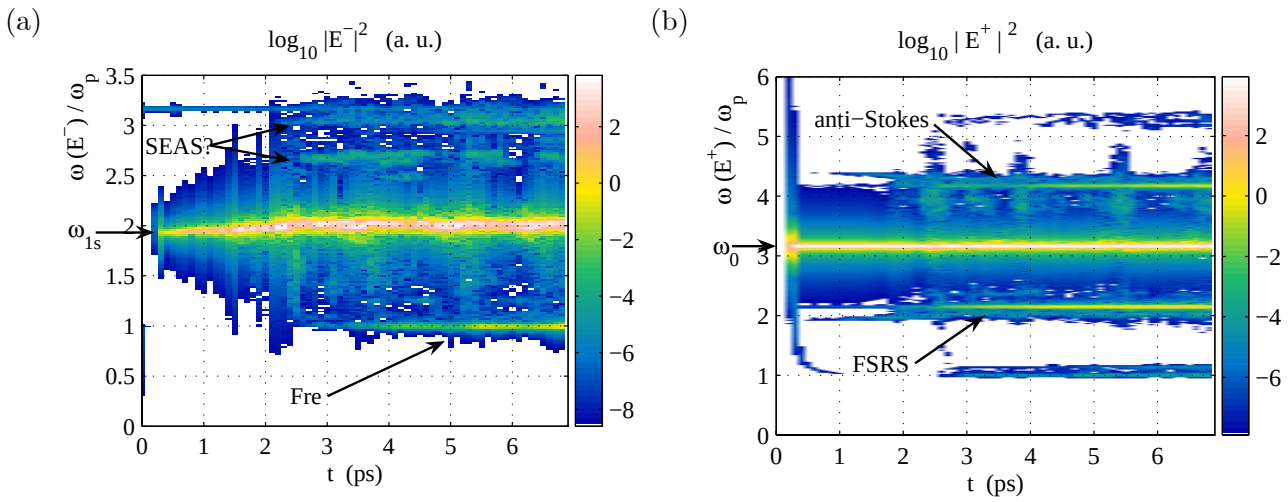

Figure 3-4: Streaked frequency spectrum of (a) $E^-(x=0,t)$ and (b) $E^+(x=L,t)$ for run `BC1`. "Fre" and "SEAS?" indicate forward re-scatter of BSRS light and possible SEAS, respectively.

spectrum also contains possible SEAS signals slightly above $2.5\omega_p$ and near $\omega_0 = 3.16$, which appear as wiggles about the background level in Fig. 3-2(b). The transmitted light streaked spectrum is shown in Fig. 3-4(b). The pump and sidebands at $\omega_0 \pm \omega_p$ (anti-Stokes and FSRS) are clearly visible, along with fainter signals at $\approx \omega_0 \pm 2\omega_p$. As expected, these lines develop after BSRS is large-amplitude and has generated enough noise from which they can grow.

The Manley-Rowe relations, derived in subsection 2.3.2, state that the energy gains ΔW_i of the two daughter waves in a three-wave interaction satisfy $\Delta W_1/\Delta W_2 = \omega_1/\omega_2$. Let us take the time-averaged $R = 0.138$ calculated above to measure ΔW_1, and assume the rest of the energy lost from the pump is transferred to the plasma wave. Since the transmitted fraction $T = 0.784$, the fraction of incident pump energy transferred to mode 2 is $1 - 0.784 - 0.138 = 0.078$. Therefore, $\Delta W_1/\Delta W_2 = 13.8/7.8 = 1.77$. We compare this to the frequency ratio. For the linear matching modes we have $\omega_1 = 1.93$, $\omega_2 = 1.23$, and thus $\omega_1/\omega_2 = 1.57$. This is smaller than the energy transfer ratio. However, we know that ω_1 upshifts during the run, and we shall see in the next section (e.g., Fig. 3-6(c)) that ω_2 downshifts. The numerically observed dominant frequencies $\omega_1 \approx 2$ and $\omega_2 \approx 1.15$ (in ω_p units) give $\omega_1/\omega_2 = 1.74$, which is very close to $\Delta W_1/\Delta W_2$. The Manley-Rowe relations hold fairly well for this simulation, further indicating a three-wave process dominates the physics.

3.1.3 Plasma waves

The longitudinal, plasma-wave dynamics provide a better picture of SRS in this kinetic simulation and show clear signs of strong electron trapping. We present the streaked spectrum of the electrostatic field $E_x(t)$ at $x = 49.84$ μm (the box center) in Fig. 3-5. The spectrum consists of a dominant EPW that extends in frequency from $\omega_2 = 1.229$ (the linear matching value) downward slightly, as well as several harmonics of this wave. The relatively constant signal at $2\omega_0 = 6.32$ is an electrostatic second harmonic of the pump. The electron v_y driven by the laser interacts with the laser B_z to give a longitudinal Lorentz force $\sim v_y B_z$ with a component at $2(k_0 x - \omega_0 t)$. This wave is not involved in any parametric coupling and does not grow, but initially takes a small amount of energy from the pump to be set up (since it is undamped, in steady state it does not absorb energy).

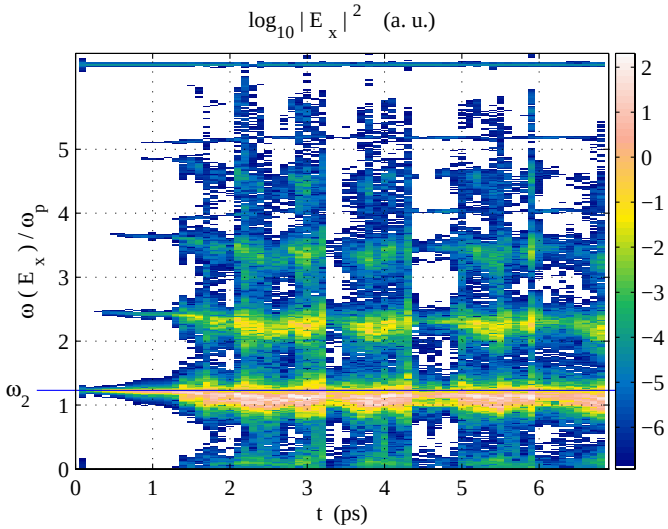

Figure 3-5: Streaked frequency spectrum of $E_x(t)$ at $x = 49.84$ μm (box center) for run `BC1`.

Fig. 3-6(a) zooms in on Fig. 3-5 near ω_2. It is evident that the EPW initially develops at the ω_2 from matching; it broadens and downshifts in frequency at later times. Fig. 3-6(b) graphs the rms of the perturbed electron density $\delta n/n_0$ ($\delta n \equiv n_e - n_B$), and panel (c) displays the instantaneous frequency of E_x at the box center (see p. 144). The frequency downshift roughly correlates with large wave amplitude; the temporal burstiness in amplitude is reminiscent of the bursty reflectivity.

It is well-established [26] that the frequency of a plasma wave is downshifted when the wave traps electrons near its phase velocity in its potential well. This phenomenon, and trapping in general, is further discussed in Chap. 4. For a wave of amplitude n_1 ($\delta n = n_1 \cos(kx - \omega t)$), deeply trapped electrons have a bounce frequency $\omega_B \equiv \omega_p \hat{n}^{1/2}$ where $\hat{n}_1 = n_1/n_0$. The shift $\delta\omega/\omega_p$ is proportional to ω_B and a unitless function of $k\lambda_D$: $\delta\omega/\omega_p = \hat{n}^{1/2} H(k\lambda_D)$ (for a Maxwellian equilibrium, $H < 0$.). The correlation of large downshift with large amplitude is in keeping with this. As a rough estimate, using the H calculated by Morales [26], for the SRS EPW $k_2 = 0.357$ and $\hat{n} = 0.05$ we find $\delta\omega/\omega_p = -0.0416$. We also depict the space-averaged electron distribution $\langle f_e \rangle$, taken over the central region of the box, from 43.5 to 49.1 μm, in Fig. 3-6(d). As the right-moving ($v_p > 0$) plasma wave amplitude grows, electrons are trapped in it. This appears as the flattening of $\langle f_e \rangle$ around the phase velocity v_{p2}. There is very little distortion of f_e for $p_e < 0$, indicating very few left-moving plasmons (which would trap electrons with $p_e < 0$). A wave traps electrons within $\pm v_{tr}$ of v_p where the island half-width $v_{tr} = 2(\omega_p/k)\hat{n}^{1/2}$ is called the trapping width. The observed trapping width varies with the wave amplitude, but f_e never returns to a Maxwellian. The SRS EPWs see a locally flat f_e at their phase velocities, and do not undergo Landau damping. This greatly increases the scatter and is the basis for the kinetic enhancement.

We can further appreciate the trapping dynamics by examining f_e over the full $x - p$ phase space. Fig. 3-7(a) shows f_e at $t = 1.41$ ps, shortly before the plasmon amplitude maximizes near $t = 1.7$ ps (see Fig. 3-6(b)). Coherent phase-space vortices centered on v_{p2} are visible, which gives rise to a flattened $\langle f_e \rangle$ on space-averaging. The vortices become irregular and smear into each other during the turn-over, as seen at $t = 1.77$ ps in Fig. 3-7(b). These plots demonstrate the capability of continuum kinetic numerical methods to capture fine phase-space structures. We present in Fig. 3-8(a) the space-averaged $\langle f_e \rangle$ over the central region $x = 43.5$ to 49.1 μm. The flattening

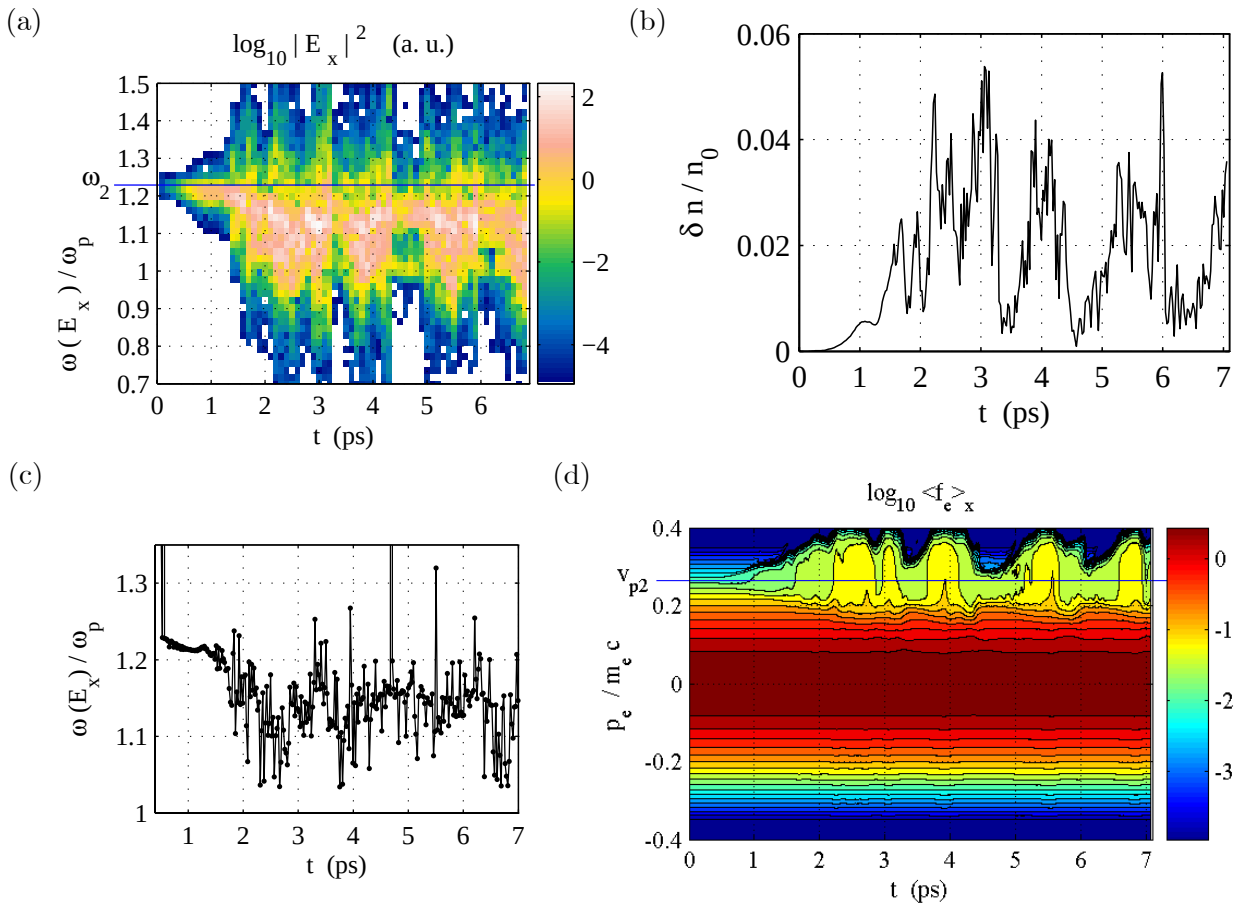

Figure 3-6: (a) Frequency zoom-in of Fig. 3-5 for run `BC1`. (b) rms electron density perturbation at box center. (c) Instantaneous frequency of E_x at box center $x = 49.84$ μm. (d) space-averaged electron distribution over $x = 43.5 - 49.1$ μm.

around v_{p2}, is clearly seen. The chosen times are typical, in that $\langle f_e \rangle$ is usually very flat when a significant plasma is present. There are only brief periods ($\sim$0.1 ps) when $\langle f_e \rangle$ displays a small bump ($\partial \langle f_e \rangle / \partial p_e > 0$) slightly above v_{p2}. Significant beams are thus not generated. Outside the trapping region there is little departure from a Maxwellian and no distortion for $p_e < 0$.

One way to determine if trapping can enhance SRS is to consider whether a resonant electron ($v \approx v_{p2}$), emerging from the Maxwellian plasma near the "Krook edges," undergoes a bounce period $\tau_B \equiv 2\pi/\omega_B$ before crossing the plasma. As discussed in chapter 4, the resonant electrons start to give energy back to the wave, rather than Landau damp the wave, once they complete about half a bounce period. Given the EPW amplitude we can compute ω_B and the "bounce length" $L_B \equiv v_{p2}\tau_B \sim \hat{n}_1^{-1/2}$, or how far a resonant electron travels before bouncing. If it crosses the box before it bounces ($L_B > L$), it cannot return energy to the wave, and Landau damping is not reduced. $L_B(x)$ calculated from the numerical density fluctuation at $t = 0.85$ ps is displayed in Fig. 3-8(b). This time is during the smooth growth of δn (see Fig. 3-6(b)), before erratic bursting occurs. We first filter δn in k space to only include $0.29 \leq k\lambda_D \leq 0.43$; almost all the energy is near $k_2\lambda_D = 0.357$, and L_B computed from the unfiltered δn is very similar. The bounce length varies between 4 and 10 μm, so resonant electrons undergo several bounces as they cross the 75 μm box. The coupled-mode convective growth is from right to left for BSRS, so the smaller L_B on the

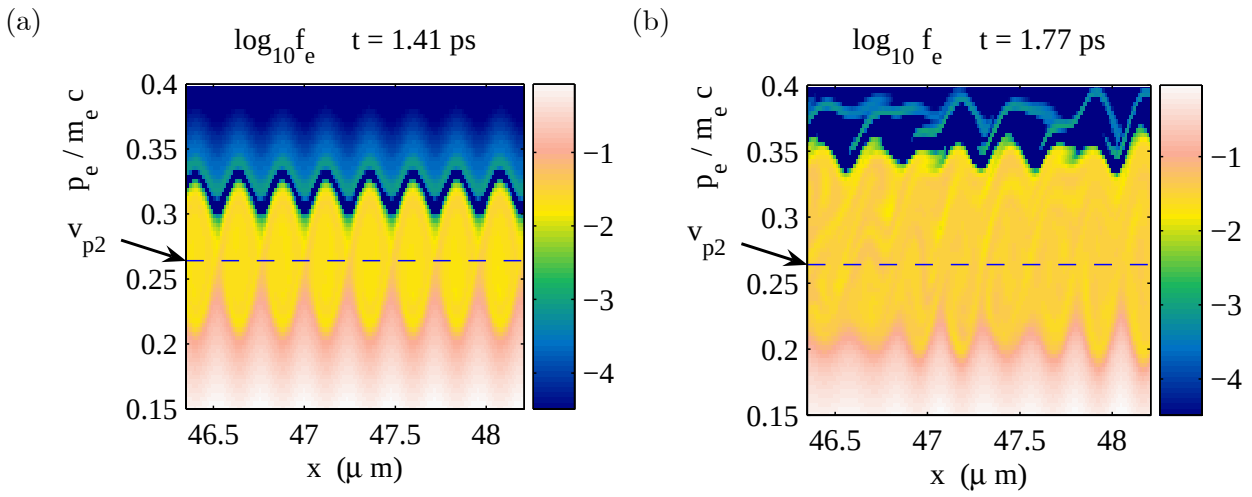

Figure 3-7: f_e near box center for (a) $t = 1.41$ ps and (b) $t = 1.77$ ps for run `BC1`.

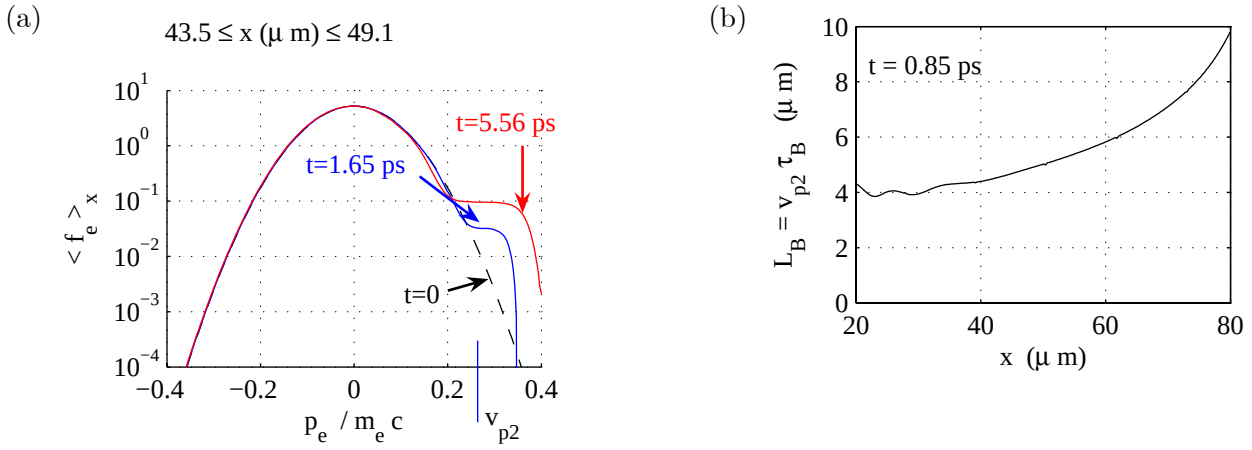

Figure 3-8: (a) $\langle f_e \rangle$ over $x = 43.5 - 49.1$ μm for run `BC1`. (b) Bounce length L_B at $t = 0.85$ ps, computed from δn filtered to include only $0.29 < k\lambda_D < 0.43$.

left corresponds to larger EPWs there.

The importance of trapping and the concomitant frequency downshift appears in the $k - \omega$ spectrum of E_x. Fig. 3-9(a-c) show $|E_x(k,\omega)|^2$ for $t =$ 1-3 ps, 3-5 ps, and 5-7 ps, respectively. The spectra are all dominated by plasmons from BSRS, which are seen to extend between $k_2 \approx 0.3 - 0.4$. Several harmonics of this feature appear at higher k and ω (beyond axes limits in figures). A "shadow" of the physical $k > 0$ SRS EPW appears for $k < 0$ since the numerical diagnostic cannot perfectly distinguish right- and left-moving signal. There is very little $k < 0$ activity, especially at early times, indicating plasmons are absorbed by the Krook operator at the edges and not reflected by the density ramps. We superpose the kinetic, linear EPW dispersion relation as the black dotted curve. The Raman plasma waves consistently fall below this curve due to the trapping-induced frequency downshift. This is easier to see in Fig. 3-10(a-b), which contain a zoomed subset of the early (1-3 ps) and late (5-7 ps) spectra from Fig. 3-9. The downshifted plasma wave has a group velocity $d\omega/dk \approx 0.12c$. In addition, there are two "acoustic-like" modes ($\omega \propto k$), one of which extends to the BSRS plasma wave and another one with a lower slope. The signals labeled "SEAS?"

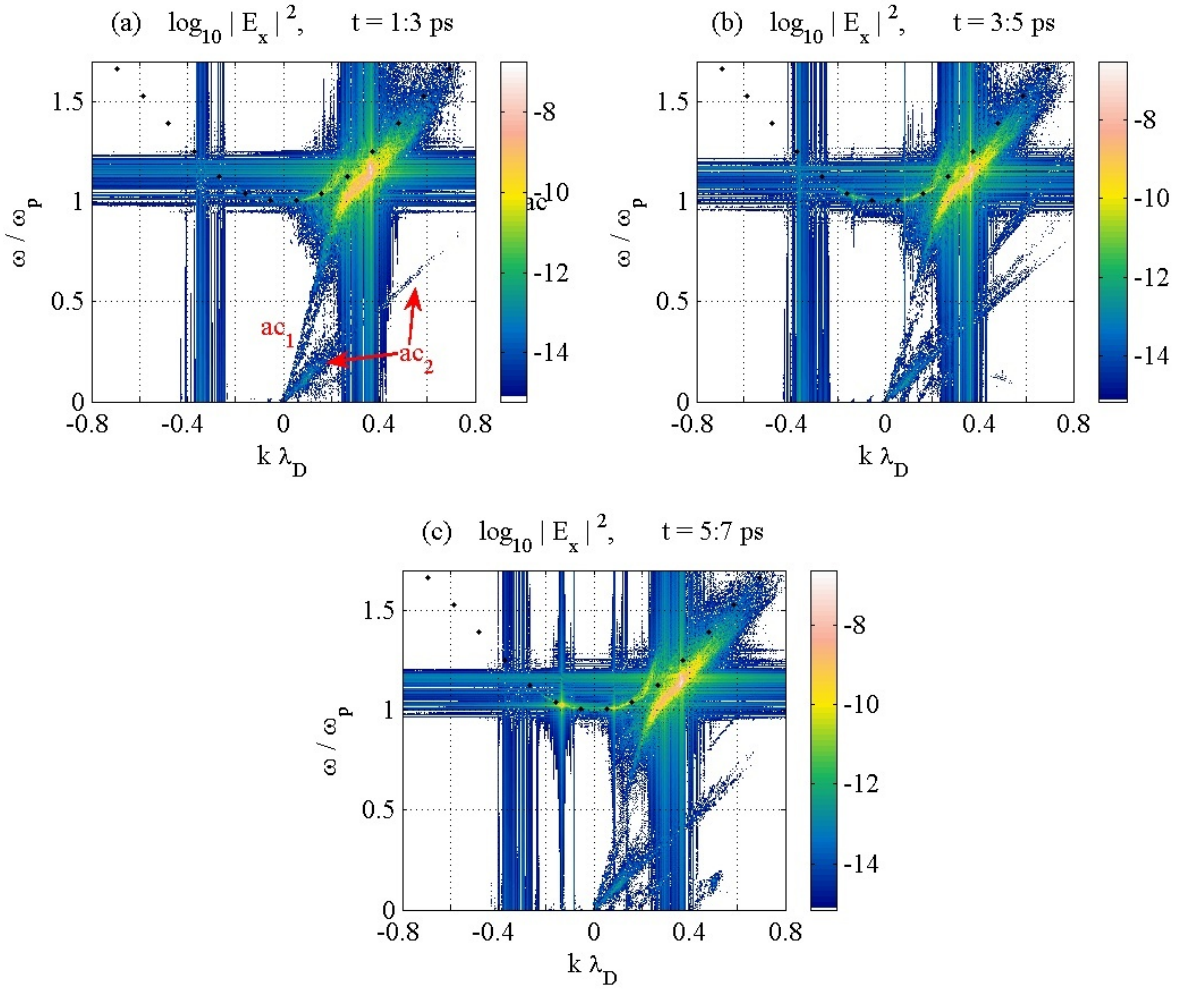

Figure 3-9: $\log_{10}|E_x(k,\omega)|^2$ over $x = 20 - 80$ μm for t = (1-3, 3-5, 5-7) ps for (a-c). "ac1" and "ac2" label the two acoustic features.

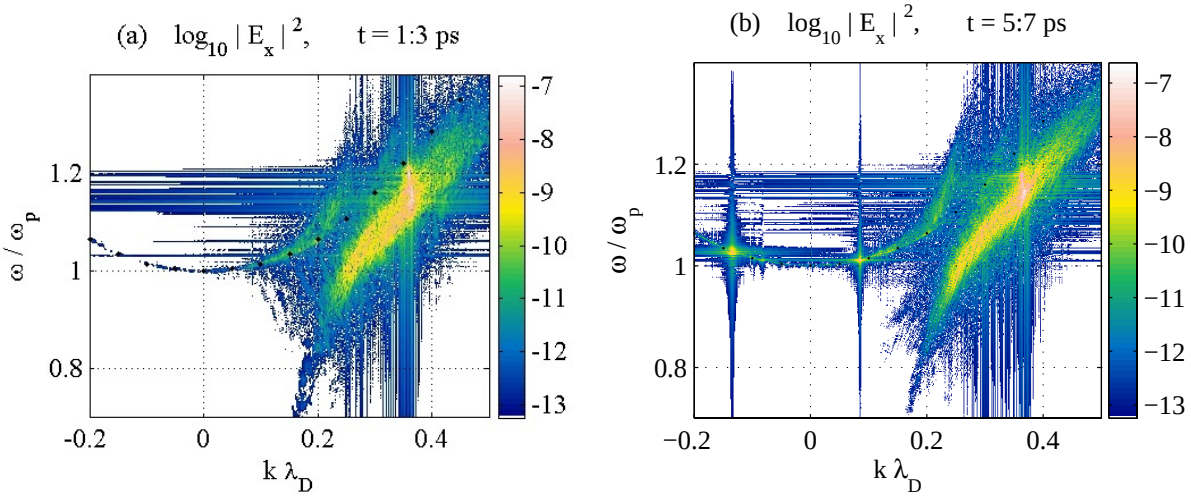

Figure 3-10: $\log_{10}|E_x(k,\omega)|^2$ over $x = 20 - 80$ μm for t = (1-3, 5-7) ps for (a,b). Zoom of Fig. 3-9(a,c).

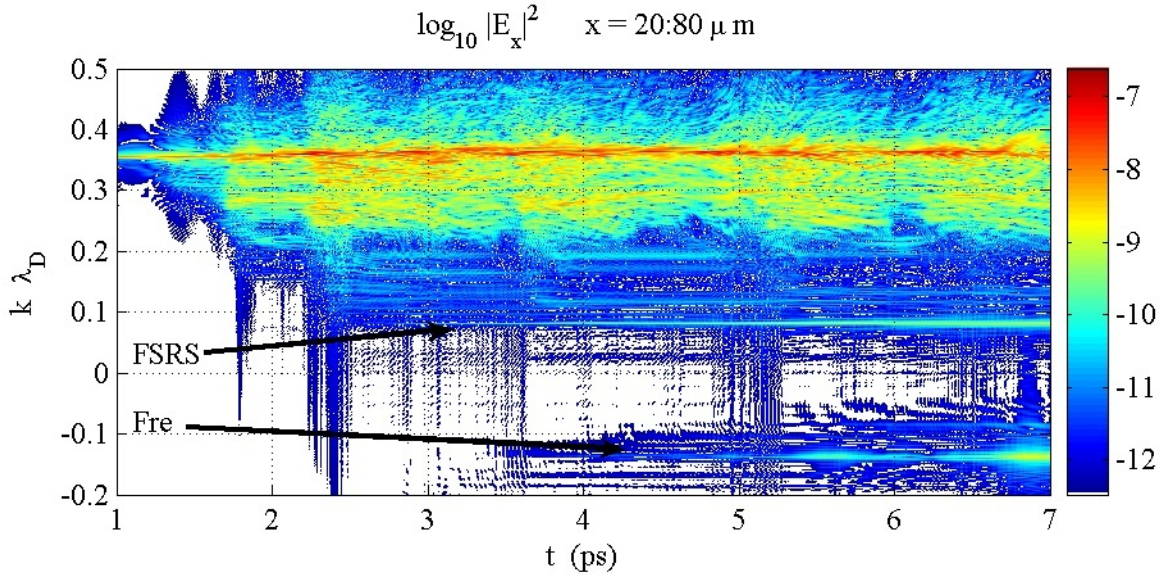

Figure 3-11: Streaked spectrum $|E_x(k,t)|^2$ over $x = 20 - 80$ μm for $t = 1 - 7$ ps for run `BC1`. FSRS and Fre label forward SRS and forward re-scatter of BSRS.

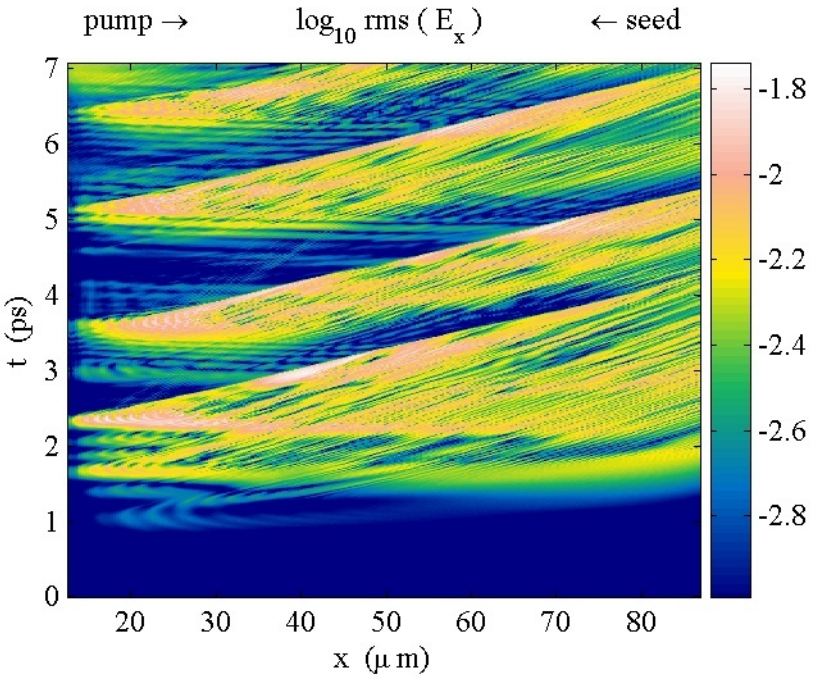

Figure 3-12: rms of $E_x(x,t)$ for run `BC1` ($\log_{10}$ scale).

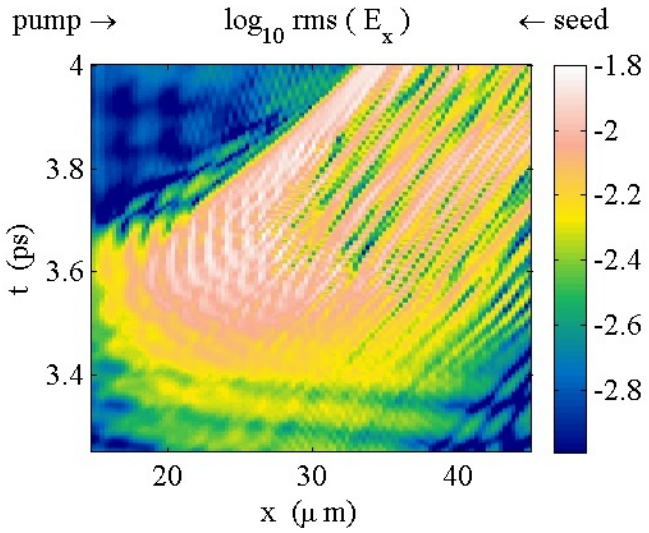

Figure 3-13: rms of $E_x(x,t)$ for run `BC1`, zoom of one pulse from Fig. 3-12. Left-moving structure is visible.

in the reflected light spectra may be SEAS off these waves.

Besides the downshifted Raman plasmon, the late-time spectrum has two points of localized activity at $k \approx 0.08$ and -0.13 that fall on the linear EPW dispersion curve. We claimed above these are, respectively, due to FSRS of the laser pump and the forward Raman re-scatter of BSRS. The EPW activity is at the correct k for these modes, as given in table 3.1. We can better see the time evolution of the plasma waves by looking at the streaked (time-resolved) k spectrum, depicted in Fig. 3-11. The FSRS and re-scatter of BSRS plasma waves develop late in time at the required k to satisfy matching. This figure also shows persistent and broad activity for a range of k near but below the primary BSRS value of $k = 0.357$.

The EPW evolution in space and time is shown in Fig. 3-12, which plots the rms amplitude of E_x. The plasma waves occur as a series of four or five pulses that develop on the left side (the laser entrance) and then propagate to the right. There is clearly a dominant group velocity, or slope to the trajectories or "rays" of high intensity, which ranges from $(0.09 - 0.13)c$. The downshifted SRS plasma waves in the $k - \omega$ diagram Fig. 3-10 has a group velocity $(d\omega/dk)$ of roughly $0.12c$, which agrees with the observed $E_x(x,t)$ pulse propagation speed. The pulses are not uniform but have detailed structure. In particular, the waves do not merely propagate and decay, but their amplitudes grow and decay along the rays. Thus, there are regions of high intensity within a pulse that develop from low-intensity regions earlier along the ray. However, there are well-defined "valleys" between the pulses, where no significant waves occur. Figure 3-13 zooms in on one pulse from Fig. 3-12. Near the laser entrance one can see features moving with negative group velocity, particularly at the start of pulses. Since they are present in all pulses we do not associate them with BSRS re-scatter, which only occurs after 3 ps.

3.2 Pump strength I_0 scan

This section explores the effects of changing the pump intensity I_0. Trapping can reduce the Landau damping only if a trapped particle bounces before crossing the finite interaction region.

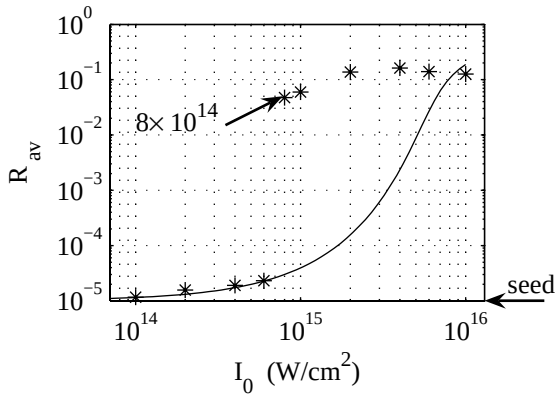

Figure 3-14: Average R for reruns of `BC1` for varying I_0. Solid curve is steady-state coupled-mode R.

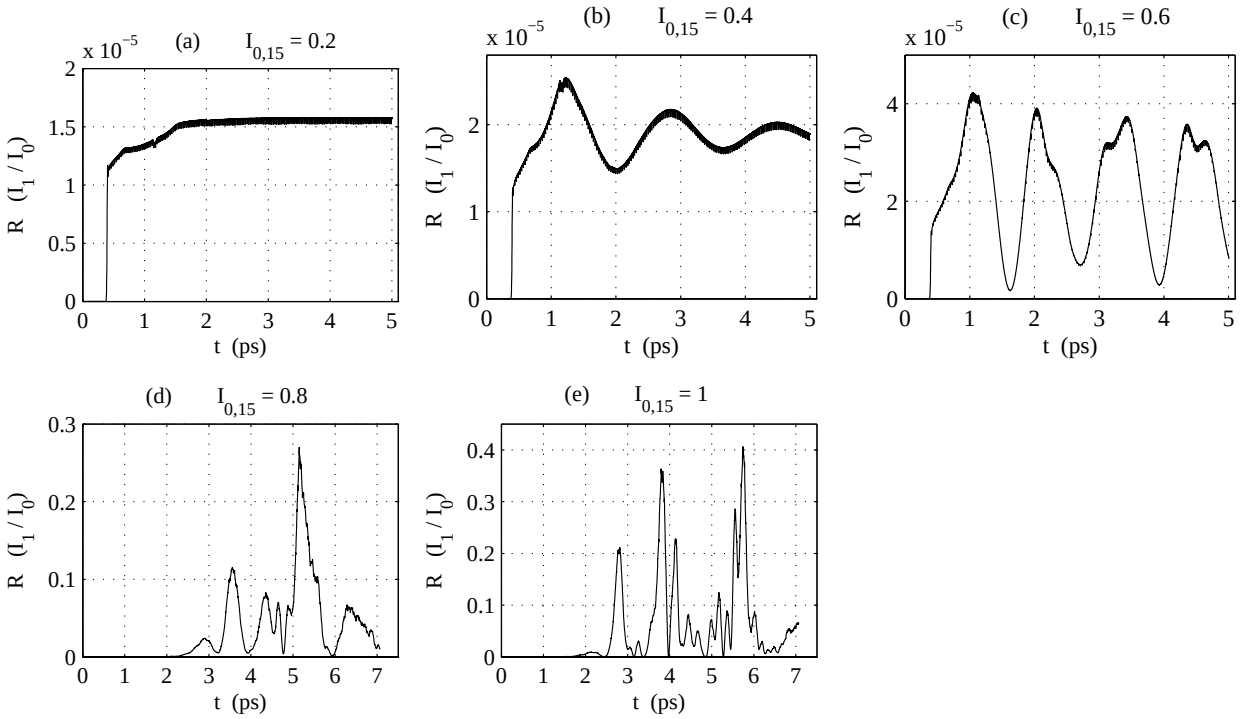

Figure 3-15: R vs. t for reruns of `BC1` with several I_0.

The linearized Vlasov equation yields the amplitude of a plasma wave (mode 2) driven by the beating of two imposed light waves (for SRS, the pump and seed, modes 0 and 1):

$$\hat{n} = \frac{1}{2}\left(k_2\lambda_D\right)^2 \frac{\chi}{1+\chi}\frac{v_{os0}v_{os1}}{v_{Te}^2} \approx \frac{1}{4}\left(k_2\lambda_D\right)^2 \frac{\omega_p}{\nu_2}\frac{v_{os0}v_{os1}}{v_{Te}^2}. \tag{3.2}$$

$\hat{n} = |n_1|/n_0 = (\omega_B/\omega_p)^2$, $n_e - n_0 = n_1 e^{i\psi_2} + cc$ is the perturbed electron density, χ is the kinetic susceptibility, and v_{osi} is the electron oscillation speed for mode i. This result is derived in appendix B. The parameters for `BC1`, with the oscillation speeds taken from the imposed pump and seed, give $\hat{n} = 1.18 \times 10^{-4}$. SRS amplifies the daughter light wave, and thus the plasma wave, above this value. To estimate when trapping becomes significant, we neglect the amplification and find

T_e, **keV**	$\mathbf{k_2\lambda_D}$	I_a, $\mathbf{W/cm^2}$	$\boldsymbol{\nu_2/\omega_2}$	γ, $\mathbf{ps^{-1}}$	α, $\boldsymbol{\mu m^{-1}}$	R, **SS**	R, **num**	L_B, $\boldsymbol{\mu m}$
1	0.214	4.6×10^{12}	1.95×10^{-4}	18.7	no SS	no SS	0.301	no SS
2	0.297	6.9×10^{15}	0.0100	10.9	0.071	0.051	0.214	13.6
3	0.357	5.9×10^{16}	0.0309	4.52	0.019	1.6×10^{-4}	0.138	27.0
4	0.405	1.8×10^{17}	0.0542	2.45	0.0099	4.5×10^{-5}	0.0624	38.8
5	0.447	3.5×10^{17}	0.0769	1.61	0.0065	2.8×10^{-5}	1.85×10^{-5}	49.3

Table 3.2: Parameters for reruns of `BC1` with different T_e. Steady-state R is computed from the SDL including pump depletion. I_a, R, SS, num, and L_B indicate respectively the absolute instability threshold, reflectivity, steady state, numerical run result, and bounce length. "No SS" indicates no steady state is reached since I_0 is above the absolute instability threshold.

the pump strength for which trapped electrons bounce before crossing the flat region. Trapping reduces Landau damping once electrons have undergone about one bouncing cycle, which requires them to travel a bounce length $L_B = \tau_B v_{p2}$ (see p. 66).

We performed a set of runs where all parameters match `BC1` except for I_0, and choose the seed intensity $I_1 = 10^{-5} I_0$. We varied the momentum resolution dp_e to test convergence. L_B for these runs is

$$L_B = 38.2\ \mu\text{m}\ I_{0,15}^{-1/2} \qquad \text{(for BC1 parameters)}. \tag{3.3}$$

L_B equals the flattop length 75.1 μm for $I_{0\text{cr},15} = 0.26$ and 37.6 μm (half the flattop length) for $I_{0,15} = 1.0$. We expect trapping will have no effect on SRS for $I_0 < I_{0\text{cr}}$, and that the reflectivity R should approach the coupled-mode value. Since the gain is very small for I_0 near $I_{0\text{cr}}$ (R_{av} in Fig. 3-14 close to the seed value), this estimate changes little if we use the SRS amplified instead of the imposed seed I_1. The numerically observed time-averaged R vs. I_0 (stars) is plotted in Fig. 3-14, along with the steady-state coupled-mode R (solid curve) in the strong damping limit. This calculation is done in subsection 2.5.3 and includes pump depletion. For the higher intensities in the figure pump depletion significantly lowers R: the undepleted, linear R exceeds unity. It is reassuring that R agrees with the coupled-mode theory for low I_0. The numerical R exhibits a sharp increase for $I_{0,15} = 0.8$, which we attribute to kinetic enhancement effects. SRS saturates at slightly more than 10% and does not increase with $I_{0,15}$ above 2.

Figure 3-15 displays R vs. t for several values of I_0 near the onset of the kinetic enhancement. The lowest pump strength $I_{0,15} = 0.2$ reaches a steady state where the seed $I_1 = 10^{-5} I_0$ is barely amplified. For $I_{0,15} = (0.4, 0.6)$, R remains small but temporally oscillates; for the 0.4 case the oscillations decay, while they seem to be persistent and not completely periodic for 0.6. The largest values $I_{0,15} = (0.8, 1)$ demonstrate bursty reflectivities orders of magnitude above the coupled-mode result. R is qualitatively similar (that is, bursty and large) for the higher I_0 values shown in Fig. 3-14. These runs establish that the bursty nature of SRS and the kinetic enhancement is generic to the plasma conditions studied for sufficiently strong pump lasers.

3.3 Dependence on electron temperature

It is commonly believed that $k_2\lambda_D$ strongly controls what mechanisms dominate SRS saturation. Trapping is thought to be important when $k_2\lambda_D$ is large: v_{p2}/v_{Te} decreases with $k_2\lambda_D$, so there are more resonant electrons which may become trapped. To test the role of $k_2\lambda_D$ we performed a

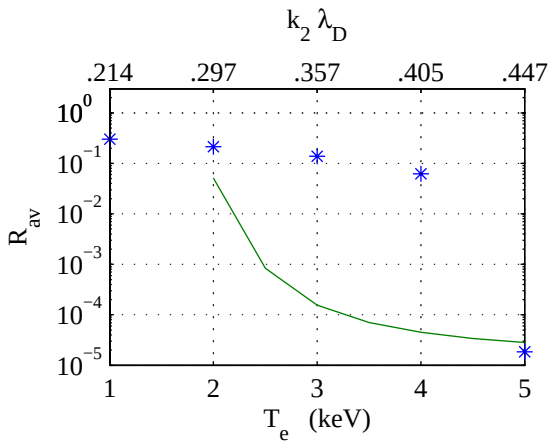

Figure 3-16: Average R for reruns of `BC1` for varying T_e. Solid curve is steady-state coupled-mode R.

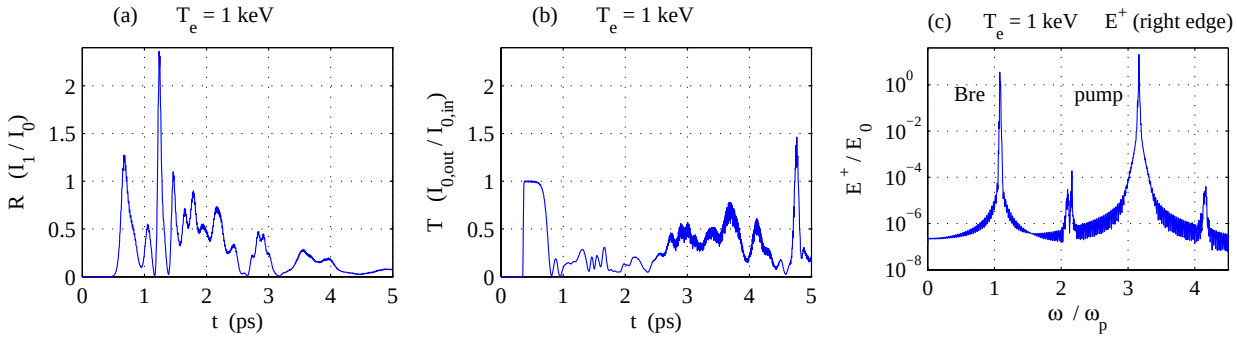

Figure 3-17: (a) Instantaneous reflectivity, (b) instantaneous transmitted fraction, and (c) spectrum of transmitted light E^+ at right edge, all for rerun of `BC1` with $T_{e,kV} = 1$. "Bre" in panel (c) indicates back Raman re-scatter of primary BSRS light.

series of reruns of `BC1` keeping all physical parameters the same except the electron temperature $T_e = 1$, 2, 4, and 5 keV (recall $T_e = 3$ keV in `BC1`). The ions are immobile, as in `BC1`. The SRS seed wavelength satisfies the linear matching conditions, and the seed intensity is $I_1 = 10^{-5} I_0$. The momentum grid spacing dp_e is chosen to assure there are several grid points in the trapping region of the plasma wave generated by the beating of the two unamplified light waves (given by Eq. (3.2)).

Table 3.2 gives selected parameters for the values of T_e used in the reruns and `BC1`. Higher T_e yields higher $k_2\lambda_D$ and thus stronger Landau damping. The reflectivity is therefore expected to decrease with temperature. Figure 3-16 displays the time-averaged reflectivity for different T_e, as well as the coupled-mode steady-state level when SRS is not absolutely unstable.

SRS is absolute for $T_{e,kV} = 1$ so highly nonlinear behavior should result even in the absence of trapping effects. The instantaneous reflectivity and transmitted fraction for $T_{e,kV} = 1$ is graphed in Fig. 3-17(a,b), respectively. SRS is high early on but is lower for later times, while the transmitted fraction recovers and briefly exceeds unity late in the run. This is due to strong back SRS re-scatter of the back SRS light, analogous to modes 7 and 8 in table 3.1. The transmitted light spectrum in Fig. 3-17(c) demonstrates that a substantial portion of the energy is contained in re-scatter.

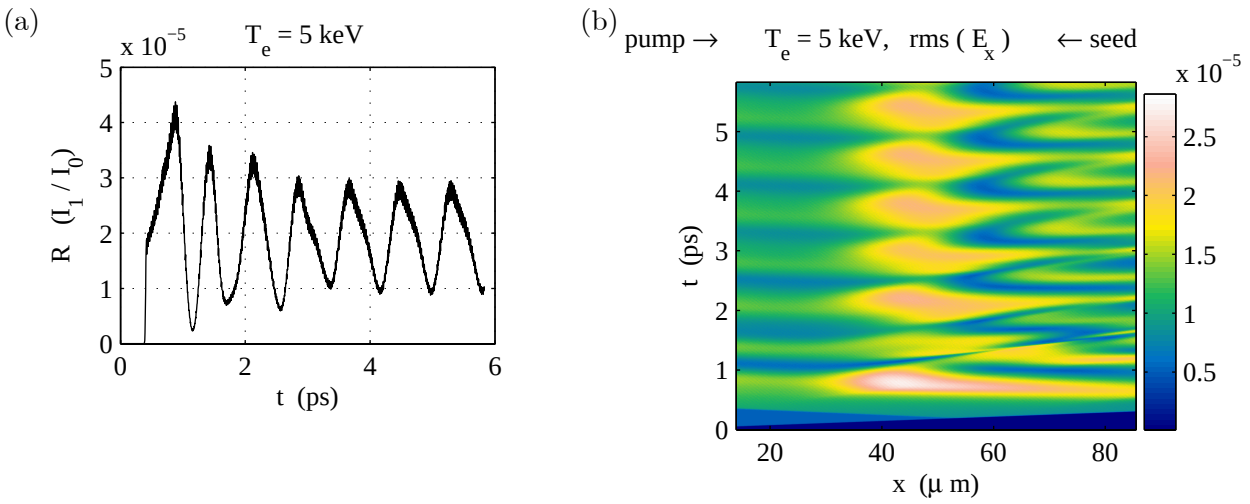

Figure 3-18: (a) Average R and (b) E_x for rerun of `BC1` with $T_{e,kV} = 5$.

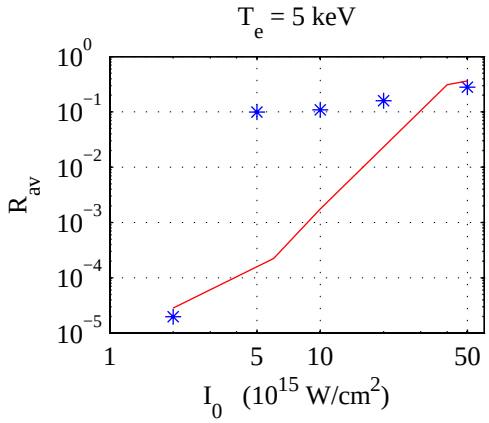

Figure 3-19: Average R for reruns of of `BC1` with $T_{e,kV} = 5$ and various pump strengths I_0. Solid red curve is the SDL with pump depletion calculation, and the stars are simulation results.

The BSRS scattered light wave from matching has $\omega_1 = 2.09\omega_p$. The plasma density n_0 is below $n_{c1}/4$ where n_{c1} is the critical density for ω_1. The scattered light from matching can itself undergo Raman scattering. In `BC1`, $\omega_1 < \omega_p/2$ and Raman re-scatter only occurs once the SRS light is frequency-upshifted due to electron trapping and the EPW frequency downshift. The $T_{e,kV} = 1$ run should be viewed as a study of the electron dynamics in SRS at low temperature since the ions are fixed. It is known that processes involving mobile ions, such as the Langmuir decay instability, interaction with Brillouin scatter, and Langmuir-wave collapse, are important in SRS saturation at low $k_2\lambda_D$. Ions are considered in Sec. 3.6.

The backscatter is kinetically enhanced for $T_{e,kV} = 2$, 3, and 4, but is not for $T_{e,kV} = 5$. There are signs of acoustic longitudinal activity and SEAS for $T_{e,kV} = 4$. Figure 3-18(a) presents the instantaneous reflectivity for $T_{e,kV} = 5$. Pulsations are evident, and a totally steady state is not reached. The longitudinal field E_x is depicted in Fig. 3-18(b). The largest response occurs near the box center, and oscillates in time. This is in contrast to the coupled-mode steady state, where both daughter waves grow exponentially toward the laser entrance. Note that the color scheme in

panel (b) may suggest a deceptively large variation; the color bar which relates colors to amplitudes clarifies this. To see if kinetic enhancement can occur for this high $k_2\lambda_D = 0.45$ scenario, we reran the $T_{e,kV} = 5$ case but varied the pump strength up to $I_0 = 5 \times 10^{16}$ W/cm^2 (still well below the absolute threshold of 3.5×10^{17} W/cm^2) with a seed $I_1 = 10^{-5} I_0$. Figure 3-19 shows the time-averaged reflectivities and demonstrates kinetic enhancement develops for $I_0 \gtrsim 5 \times 10^{15}$ W/cm^2 and then saturates with intensity. The behavior is qualitatively similar to the I_0 scan for $T_{e,kV} = 3$ in Sec. 3.2.

3.4 Noise levels and seeding

SRS, like all parametric processes, requires some initial amplitude in at least one daughter wave to grow. Here we estimate the thermal noise levels due to fluctuations in the hohlraum plasma via thermodynamic arguments. We first estimate the background radiation level via Kirchoff's law, and then by the fluctuation-dissipation theorem. We follow the book by Bekefi [78] and refer the reader there for background. Detailed calculations of stimulated scattering from noise using the "dressed" or test particle approach are contained in [79] and [80]. Next, we show the reflectivity of run `BC1` is qualitatively similar for a weaker seed intensity, and that there is no SRS without a seed. However, removing the boundary Krook operator allows SRS with or without a seed, and is examined in Sec. 3.4.4.

3.4.1 Thermal radiation via Kirchoff's law

A given mode of oscillation (such as photons, phonons, or plasmons) may have several excitation mechanisms. Each entails spontaneous and stimulated emission, as well as absorption (which is "stimulated" since it only occurs when excitations are present). These processes are connected via the Einstein relations, first derived for the so-called "A and B" coefficients [81]. For photons in hohlraum plasmas, the dominant emission mechanism is electron-ion bremsstrahlung, while the corresponding absorption process is collisional damping or inverse-bremsstrahlung. Čerenkov radiation is the excitation of waves in a medium by a discrete source moving faster than the wave's phase velocity. This cannot occur for light waves, whose phase velocity is $\geq c$ in an unmagnetized plasma. However, super-thermal electrons moving above the EPW phase speed $\approx \omega_p/k = v_{Te}/(k\lambda_D)$ can Čerenkov radiate plasmons which in turn suffer Landau and collisional damping.

We analyze fluctuations of weakly damped modes, so the mode energy, group velocity, etc. are well-defined. Although we use language common to light waves, the logic also applies to plasma waves. When geometrical optics is valid, conservation of energy gives rise to the equation of transfer ([78], Secs. 1.6-1.7)

$$\eta_r^2 \frac{d}{ds}\left(\frac{I_\omega}{\eta_r^2}\right) = j_\omega - \alpha_\omega I_\omega. \tag{3.4}$$

s is distance along the ray path. η_r is the "ray refractive index," which for isotropic media (such as the unmagnetized plasma we are considering) is the usual refractive index $\eta = ck/\omega$. I_ω is the "specific intensity," or power dP per area da of radiation per solid angle $d\Omega$ per angular frequency interval $d\omega$, in one polarization: $I_\omega = dP/(da\ d\omega\ d\Omega)$. The net absorption coefficient α_ω (units length^{-1}) accounts for both stimulated emission and absorption and is given by

$$\alpha_\omega = 2|\operatorname{Im} k| \cos\beta \tag{3.5}$$

where β is the angle between the group velocity and wavevector. j_ω is the emission coefficient and equals the power radiated per medium volume per frequency per solid angle ($j_\omega = dP/(dV\ d\omega\ d\Omega)$). All of these quantities refer to radiation at one frequency ω, and there is a separate transfer equation for each ω. In terms of $\iota_\omega = I_\omega/\eta^2$ Eq. (3.4) becomes

$$\frac{d\iota_\omega}{d\tau} = \iota_\omega - S_\omega, \qquad\qquad S_\omega \equiv \frac{j_\omega}{\eta^2 \alpha_\omega}. \tag{3.6}$$

$d\tau = -\alpha_\omega ds$ defines the unitless optical depth τ, which *decreases* along the direction of ray propagation.

The "source function" S_ω and the rate of spontaneous emission $\eta_\omega(\vec{p}) = dP/(d\omega\ d\Omega)$ from electrons with momentum $\vec{p}$ ([78] Sec. 2.2) are related by Kirchoff's law:

$$S_\omega = \frac{\hbar\omega^3}{8\pi^3 c^2} \frac{\int \eta_\omega(\vec{p}\,') f(\vec{p}\,') d^3p'}{\int \eta_\omega(\vec{p}\,') \left[f(\vec{p}) - f(\vec{p}\,')\right] d^3p'}. \tag{3.7}$$

$\vec{p} = \vec{p}\,' + \vec{p}_\gamma$ is the final electron momentum after absorbing a photon with momentum $\vec{p}_\gamma$. Kirchoff's law holds whether or not the radiation or electrons are in equilibrium with themselves or each other. The effective "radiation temperature" of the plasma ([78] Sec. 2.3), is defined by

$$S_\omega = B_0(\omega, T_r). \tag{3.8}$$

B_0 is the blackbody intensity distribution $dP/(da\ d\omega\ d\Omega)$ in one polarization:

$$B_0(\omega, T) = \frac{\hbar\omega^3}{8\pi^3 c^2} \frac{1}{\exp[\hbar\omega/T] - 1} \tag{3.9}$$

$$\approx \frac{\omega^2 T}{8\pi^3 c^2}, \qquad \hbar\omega \ll T. \tag{3.10}$$

The low-frequency approximation is the classical, Rayleigh-Jeans limit. Whatever S_ω is at a given ω, we choose T_r such that $S_\omega = B_0(\omega, T_r)$. If the electron distribution is Maxwellian, then $T_r = T_e$, the electron temperature. In experiments, it is common that T_r peaks above T_e in the vicinity of a resonance, such as the cyclotron resonance in a magnetized plasma ([78], pp. 56-58). This reveals the distribution is slightly non-Maxwellian, perhaps because the method of plasma generation preferentially put energy into cyclotron waves.

Hohlraum plasmas are thought to be nearly Maxwellian, so we take $T_r = T_e$. Although the source function $S_\omega = B_0(\omega, T_e)$, this does *not* mean we have blackbody emission. We must solve the equation of transfer Eq. (3.6) to find the radiation present. For a homogeneous medium where S_ω does not vary along the ray path, the solution is

$$\iota_\omega = \iota_{\omega 0} e^\tau + S_\omega (1 - e^\tau). \tag{3.11}$$

Choose $\tau = 0$ at the ray origin, at which point $\iota_\omega = \iota_{\omega 0}$. Recall τ decreases along the ray. Any initial radiation is absorbed (damped) as it propagates, so that very little survives for optically thick plasmas ($-\tau \gg 1$). However, along the ray the medium emits and absorbs via S_ω. Perhaps counter-intuitively, for optically *thick* plasmas $1 - e^\tau \approx 1$, and the net emission approaches the full source function. Conversely, the fluctuations in optically thin plasmas are a very small fraction of S_ω, and may be dominated by boundary effects via $\iota_{\omega 0}$.

We need to know the optical depth at a given ω to know the level of light-wave fluctuations in the plasma. The temporal amplitude damping rate of light waves due to electron-ion collisions is given in Eq. (2.69): $\nu = (1/2)(\omega_p/\omega)^2\nu_{ei}$. The spatial damping rate $k_i = \nu/v_g$ where $v_g = c(1-n_0/n_c)^{1/2}$ is the group velocity and n_c is the light wave's critical density. For the BSRS daughter light wave in the standard parameters ($\lambda_1 = 574$ nm), $\nu_1 = 28.1$ ns^{-1} and $k_i = 110$ m^{-1}. Using α_ω from Eq. (3.5) with $\beta = 0$, we find the optical depth $d\tau = -ds/(4.6\text{ mm})$. Since the hohlraum radius is typically several millimeters, much of the blowoff plasma is somewhat optically thick ($-\tau \geq 1$). Thus, the light-wave fluctuations at ω_1 will be on the order of $B_0(\omega, T_e)$. The "optical depth" for plasma waves depends on the Landau and collisional damping. The daughter EPW in BSRS from the standard parameters has $d\tau = -ds/(0.226\ \mu\text{m})$, so the plasma is much more optically thick for these plasmons: their fluctuation level is very nearly $B_0(\omega, T_e)$.

The fluctuation intensity at λ_1, in one linear polarization over a half-sky (2π) of solid angle, is

$$\iota_{1,\text{fl}} = 2\pi f_c \int_{\omega_{1a}}^{\omega_{1b}} \mathrm{d}\omega \quad B_0(\omega, T_e). \tag{3.12}$$

f_c is the fractional cone of wavevectors included in the backscatter. A cone of half-angle θ has $f_c = (1/4\pi)\int_0^\theta \mathrm{d}\theta' 2\pi \sin\theta' = (1-\cos\theta)/2 \approx \theta^2/4$ for $\theta \ll 1$. For a speckle, we can take this to be all k's that stay within the speckle. A lens with optic f/# F produces diffraction-limited speckles with transverse radius $r = 1.028F\lambda_0$ and axial length $l = 7.08F^2\lambda_0$ ([52], p. 25). For $F = 8$ (being considered for NIF) and $\lambda_0 = 351$ nm, we have $r = 2.89\ \mu$m and $l = 159\ \mu$m. $\theta = \arcsin(r/l) = 1.04^\circ$ and $f_c = 8.24 \times 10^{-5}$. We take frequency range [ω_{1a}, ω_{1b}] as that for which there is appreciable BSRS growth. From Fig. 2-2, we use $\lambda_{1a}, \lambda_{1b} = 600$, 540 nm. Note that 574 nm corresponds to an energy of 2.16 eV, so for keV plasmas this is well into the low-frequency Rayleigh-Jeans portion of the spectrum. Folding in all these numbers, we find $\iota_{1,\text{fl}} = 4280$ W/cm^2. The refractive index $\eta_1 = 0.856$ finally gives $I_{1,\text{fl}} = 3140$ W/cm^2. This is much lower than our simulation seed levels (usually $I_1 = 10^{-5}I_0 \sim 10^{10}$ W/cm^2), which are in turn lower than the numerical noise of PIC simulations.

We can similarly estimate the plasma wave fluctuation power. Since the plasma is optically quite thick to EPWs (more so than the light waves), we can relate $\iota_{2,\text{fl}}$ to B_0 as with light waves above. However, the frequency interval is narrower, since the EPW bandwidth for growth is smaller (plasma-wave frequencies do not depart much from ω_p). On the other hand, the refractive index η is much larger than for light waves. These two effects tend to cancel each other. The resulting $I_{2,\text{fl}}$ is of the same order as $I_{1,\text{fl}}$ (although note we do not seed the EPW in our simulations). Perhaps more important, the action density fluctuations will be roughly comparable (the EPW has a lower frequency than the EMW but typically by only a factor of 2 or 3). Imagine we initially have energy in the pump and just one daughter. From Eq. (2.90) it is easy to show that, for early times, the rate of pump energy loss goes like the square root of the initial daughter action density. Thus, if we have similar action densities in each daughter, the amount scattering from fluctuations in each channel is similar.

3.4.2 Thermal radiation via the fluctuation-dissipation theorem

Insight into thermal fluctuations can also be gained from the fluctuation-dissipation theorem. We follow closely Bekefi chapter 4 here. Accordingly, in this section we use the Fourier representation $f(t) = \int d\omega\ \exp[i\omega t]\tilde{f}(\omega)$ rather than the $\exp[-i\omega t]$ convention used in the rest of this thesis.

Consider a system which exchanges energy with an external source via the Hamiltonian $H_1 = -\vec{A}\cdot\vec{F}$ where $\vec{A}$ and $\vec{F}$ are a generalized displacement and the corresponding force. In Fourier space, the two are related by a "generalized susceptibility" (not to be confused with the plasma susceptibility $\overleftrightarrow{\chi}$) $\overleftrightarrow{\chi}_g$: $\vec{A}(\vec{k},\omega) = \overleftrightarrow{\chi}_g(\vec{k},\omega)\cdot\vec{F}(\vec{k},\omega)$. The fluctuation-dissipation theorem states the average fluctuation amplitude of the $j^{\rm th}$ component of $\vec{A}$ is

$$\left\langle A_j^2 \right\rangle = \int \frac{d^3k}{(2\pi)^3}\, d\omega\; P, \qquad\qquad P = -\frac{T}{\pi\omega}\,\mathrm{Im}\,\chi_{g,jj}. \tag{3.13}$$

T is the system temperature. To identify $\vec{A}$ and $\vec{F}$ for a specific problem, write the time-averaged dissipated power density

$$\langle \partial_t W\rangle = \int_{-\infty}^{\infty} d\omega\; G(\omega) \tag{3.14}$$

where

$$\mathrm{Re}\,G(\omega) = \lim_{T_0\to\infty}\frac{1}{T_0}\int_{-T_0/2}^{T_0/2} dt\;\vec{A}\cdot\partial_t\vec{F} \tag{3.15}$$

$$= \lim_{T_0\to\infty}\frac{1}{T_0}\left(\frac{-\omega}{2\pi}\right)\mathrm{Im}\left[\vec{F}^*\cdot\overleftrightarrow{\chi}\cdot\vec{F}\right] \qquad (k-\omega \text{ space}). \tag{3.16}$$

Consider a plasma, which we take to be the "system." Thermal fluctuations ultimately arise from particle discreteness. In the spirit of the test-particle method, we imagine the plasma medium to interact with a single particle as the external source. Linear waves in a plasma, with an external current source $\vec{J}_s$, satisfy

$$\overleftrightarrow{D}\cdot\vec{E} = i\frac{1}{\omega\varepsilon_0}\vec{J}_s, \qquad\qquad \overleftrightarrow{D} = \vec{\eta}\vec{\eta} - \eta^2 + 1 + \overleftrightarrow{\chi}. \tag{3.17}$$

$\overleftrightarrow{D}$ is the dispersion tensor, $\vec{\eta} = c\vec{k}/\omega$ is the index of refraction, and $\overleftrightarrow{\chi}$ is the plasma susceptibility. Since $\partial_t W = -\vec{J}_s\cdot\vec{E}$ is the rate of energy density gain by the plasma, we can make the associations

$$\vec{F} = \vec{E}, \qquad\qquad \overleftrightarrow{\chi} = \varepsilon_0\overleftrightarrow{D}, \qquad\qquad \vec{A} = \frac{i}{\omega}\vec{J}_s. \tag{3.18}$$

We now know the fluctuation spectrum of $\vec{J}_s$ from Eq. (3.13) and can use Eq. (3.17) to find the spectrum of E fluctuations. Let us specialize to transverse electromagnetic waves ($\vec{k} = k\hat{x}$, $\vec{E} = E\hat{y}$), for which $\chi_{g,yy} = \varepsilon_0 D$ where $D = D_{yy}$. For an unmagnetized plasma with weak damping from electron-ion collisions,

$$D = -\eta^2 + 1 - \frac{\omega_p^2}{\omega^2} - i\frac{\omega_p^2\nu}{\omega^3}. \tag{3.19}$$

The electric field fluctuation spectrum is

$$\left\langle E^2\right\rangle = \int \frac{d^3k}{(2\pi)^3}\, d\omega\; P_E, \qquad\qquad P_E = \frac{T}{\pi\varepsilon_0\omega}\frac{D_i}{|D|^2}. \tag{3.20}$$

This tells us the fluctuation power contained in every $\vec{k}$ and ω. However, $|D|^2 = D_r^2 + D_i^2$ in P_E is very large when $\vec{k}$ and ω are far from the natural-mode dispersion relation $D_r = 0$. Therefore, most

of the power for a given ω is concentrated in a narrow band around the corresponding natural-mode $\vec{k}$. We can perform the k integrals using residue techniques and deduce

$$\frac{\varepsilon_0}{2}\left\langle E^2\right\rangle = \int d\omega\ \frac{T\omega^2\eta}{8\pi^2c^3}. \tag{3.21}$$

This spectral energy density is precisely the Rayleigh-Jeans limit of the blackbody distribution $B_0(\omega, T)$, modified by the index of refraction η. Similarly, we saw in the prior subsection the source function $S_\omega = B_0(\omega, T_r)$ where the radiation temperature $T_r = T$ if the plasma is in thermal equilibrium (that is, the particles have a Maxwellian distribution). The fluctuation level thus equals that given by Kirchoff's law (over the same frequency interval). The fluctuation-dissipation theorem reveals how the power is partitioned among the different k's, and shows most of it is contained near the appropriate natural mode.

The EPW noise is calculated similarly, only using the EPW instead of the EMW dispersion relation. The resulting energy density for the kinetic, collisionless dispersion relation is ([78], p. 125)

$$\frac{1}{2}\varepsilon_0\left\langle E^2\right\rangle = \frac{T}{2}\int \frac{d^3k}{(2\pi)^3}\frac{1}{1+(k\lambda_D)^2}. \tag{3.22}$$

The fluctutation-dissipation theorem tells us most of the energy in each k is concentrated around the natural plasma wave. We thus find the standard classical "T per mode" energy density, attenuated by $(1+(k\lambda_D)^2)$ for short wavelengths. The EPW fluctuations thus also have approximately the same level as the EMWs, namely $B_0(\omega, T)$.

3.4.3 Role of seed strength

This subsection examines how ELVIS simulations of SRS are affected by different seed levels. Unlike PIC codes, Vlasov codes such as ELVIS have very low intrinsic numerical noise. Frequently, noise or seed sources are added when laser-plasma interactions are studied with Vlasov codes. We provide this via a back-propagating seed light wave imposed at the boundary with a wavelength that has a large linear SRS growth rate. Such coherent seeding at a single frequency is of course quite different from the thermal, incoherent noise present in all frequencies in a real plasma. One drawback of our technique is other parametric instabilities that are not seeded, such as FSRS, SRS re-scatter and, in kinetic ion runs, SBS and LDI, only develop if the system evolution produces sufficient noise in their daughter waves. Nonetheless, the run `BC1` shows both FSRS and re-scatter of BSRS even though we do not seed them. A more noise-like seeding should be tried in the future, perhaps by adding externally-controlled charge and current densities with the desired noise spectrum. To partly address this Sec. 3.5 presents the results of a simulation with ten seed frequencies, which shows reflectivities similar to the case of a monochromatic seed.

Typically we choose a seed intensity $I_1 = 10^{-5}I_0$, which is many orders of magnitude above the thermal noise estimate of subsection 3.4.1. Our justification is that ignition hohlraums are expected to have large regions of homogeneous plasma, in which the linear SRS gain amplifies noise to order unity reflectivities. This is not observed in experiment, implying nonlinear effects become important. However, linear theory should hold for large portions of a laser beam's path, until SRS reaches a threshold amplitude for nonlinearity to become important. This linearly-amplified SRS light acts as a seed impinging on a small region, such as a focused speckle, which we simulate. We thereby eliminate the "uninteresting" linear region and only perform an expensive, kinetic

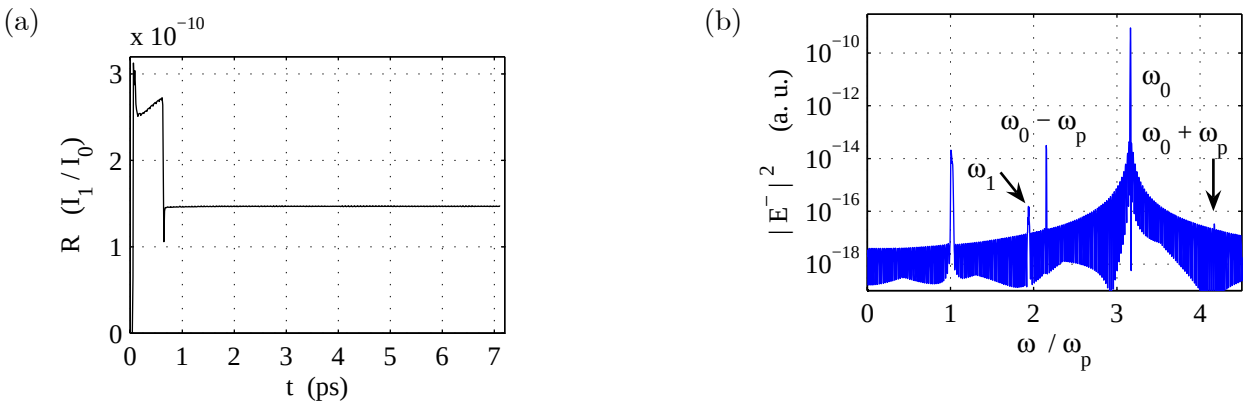

Figure 3-20: (a) R vs. t for rerun of `BC1` with $I_1 = 0$. (b) $|E^-(\omega)|^2$ from time 2 ps to run end.

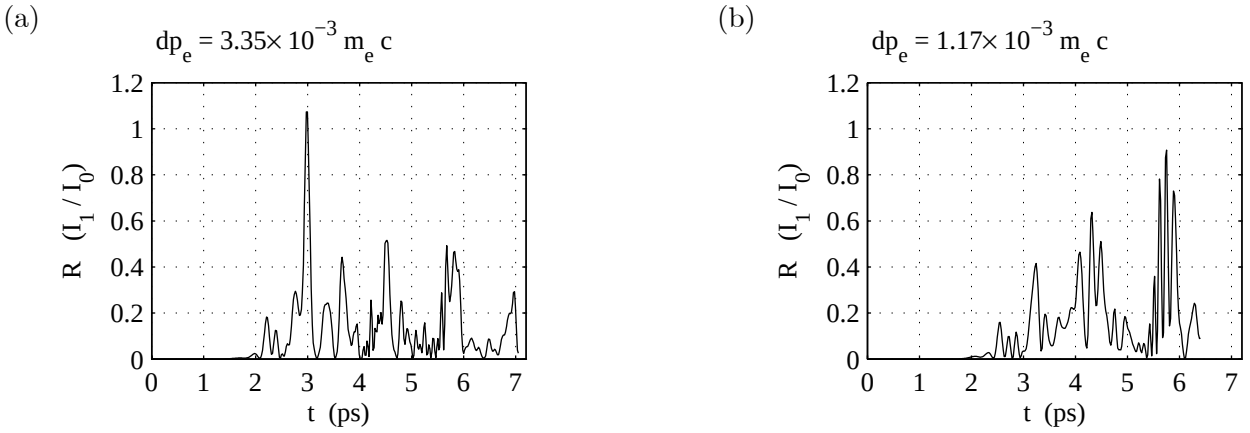

Figure 3-21: R vs. t for rerun of `BC1` with $I_1 = 10^{-7} I_0$ and $dp_e = (3.35, 1.17) \times 10^{-3} m_e c$ for panels (a,b).

simulation on the "interesting" part. The validity of this should be explored in the future with a few simulations of long plasmas, to see how the linear and nonlinear regions connect.

Let us consider the effect of varying the seed intensity I_1 while keeping all other parameters the same as the run `BC1`. In Fig. 3-20 we present (a) R and (b) the reflected light spectrum for no seed: $I_1 = 0$. We also use a smaller $dp_e = 1.95 \times 10^{-3}$ than in `BC1`. The reflectivity approaches the tiny constant value 1.5×10^{-10}, indicating there is very little noise in the code from which SRS can grow. The spectrum reveals most of the reflected light is at ω_0 and is due to the reflection of the pump when it encounters the density ramp-up (and is thus a "true" reflection and not the result of parametric coupling). There are also clear features at ω_p and $\omega_0 - \omega_p$, as well as weaker signals at ω_1 and $\omega_0 + \omega_p$ where ω_1 is the linear SRS matching frequency.

We next choose a seed $I_1 = 10^{-7} I_0$ and find reflectivity similar to `BC1` (where $I_1 = 10^{-5} I_0$). Figure 3-21 plots R for two different values of dp_e, showing qualitatively similar results. There is very little SRS before 2 ps, but after this point SRS comes in large, chaotic bursts. We vary dp_e to test convergence since Landau damping of small-amplitude EPW is not correctly reproduced for insufficient momentum resolution (namely, if the trapping width is unresolved); some runs in this chapter show very large reflectivity with one dp_e only to approach linear reflectivity levels with a smaller dp_e. The time-averaged R from 1 ps to the run end is $\langle R \rangle$ = (12.5%, 13.8%) for dp_e = $(3.53, 1.17) \times 10^{-3} m_e c$, respectively. The scattered light spectrum for the smaller dp_e choice,

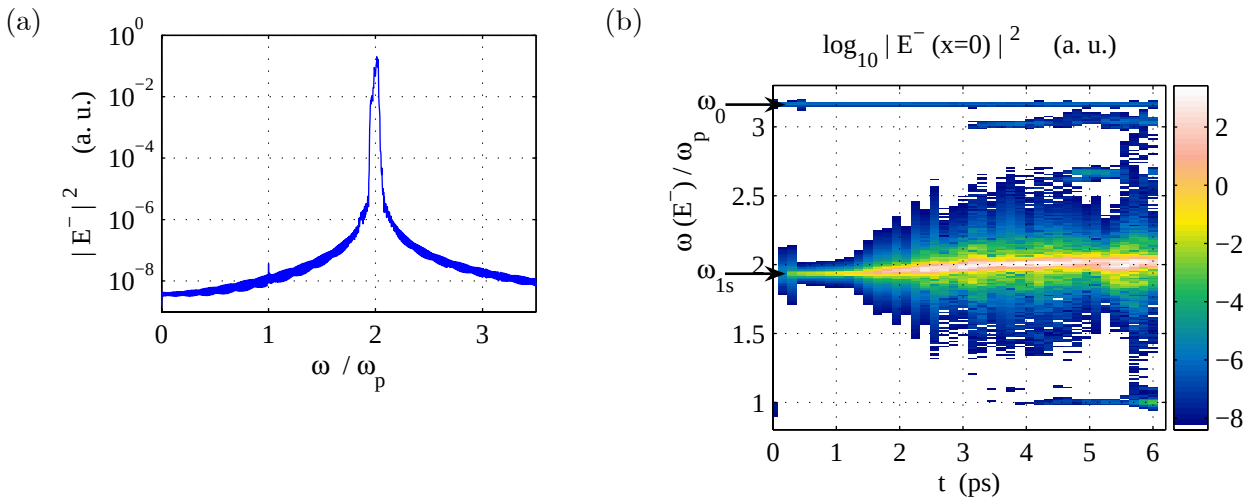

Figure 3-22: (a) Gated over entire run and (b) streaked spectrum of $E^-(\omega)$ for rerun of `BC1` with $I_1 = 10^{-7} I_0$ and $dp_e = 1.17 \times 10^{-3} m_e c$.

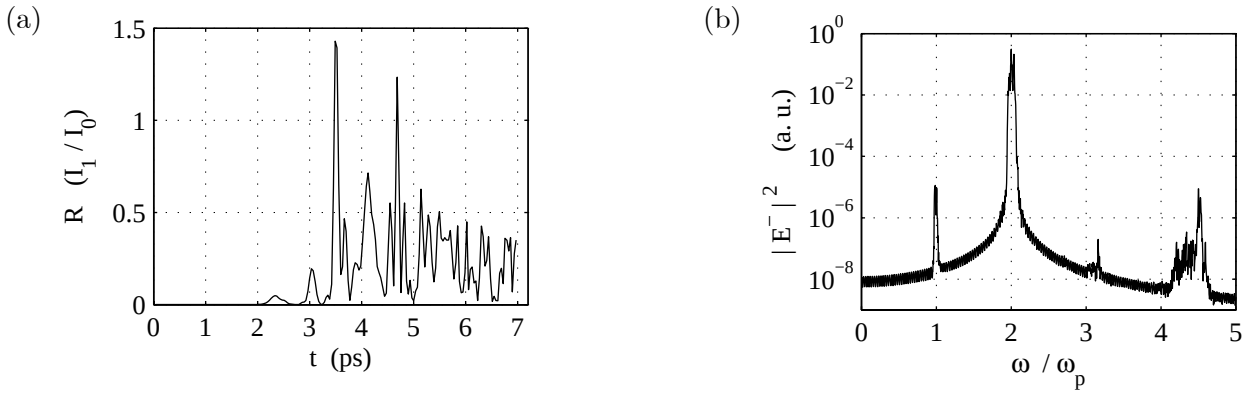

Figure 3-23: (a) Reflectivity and (b) whole-run $E^-(\omega)$ spectrum for rerun of `BC1` with $I_1 = 0$ and no Krook operator.

displayed in Fig. 3-22, is similar to the spectrum for `BC1`. Note that the possible SEAS (the two features with $\omega \approx 2.5\omega_p$, $3\omega_p$) and re-scatter of BSRS occur later in time and appear weaker than for `BC1`. The $E_x(k, \omega)$ spectrum (not shown) agrees qualitatively with `BC1`: the EPW is downshifted from the linear dispersion relation, there are two acoustic streaks at low frequency, and the BSRS re-scatter plasmon is visible.

3.4.4 Role of edge Krook operator

We include a Krook operator at the domain edges to absorb plasma waves generated by SRS and prevent them from being reflected at the boundaries. The run `BC1`, therefore, shows very little left-moving plasma waves, except for those generated by BSRS re-scatter: there is no activity with k equal to the negative of the SRS EPWs. The Krook operator also damps plasma waves produced by the adjustment of the electron density to a sheath-like pattern early in time. These waves can provide enough noise for SRS to develop. Figure 3-23 shows (a) the reflectivity and (b) the scattered light spectrum for a rerun of `BC1` with no Krook operator and no seed ($I_1 = 0$). The

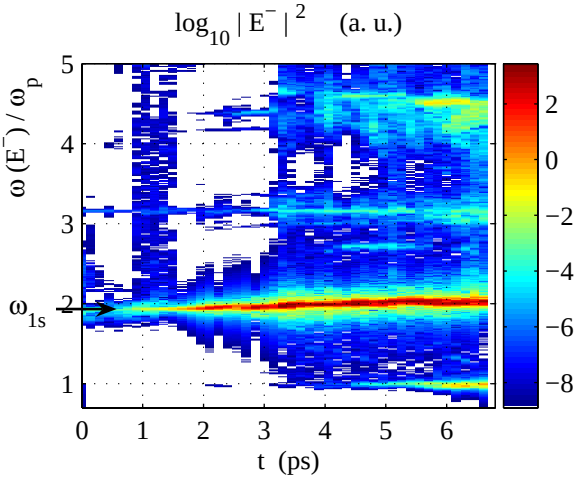

Figure 3-24: Streaked E^- spectrum for rerun of `BC1` with $I_1 = 0$ and no Krook operator.

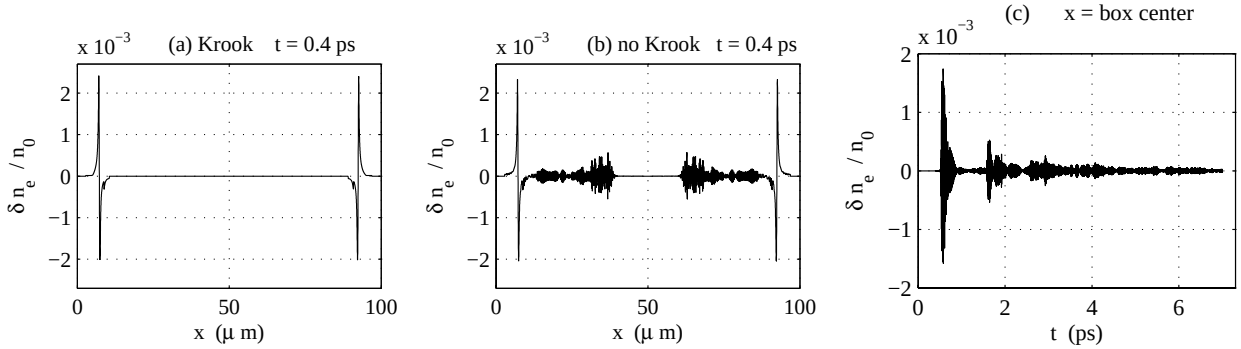

Figure 3-25: Density perturbation for electrostatic reruns of `BC1` (a) with and (b) without the edge Krook operator.

typical large, bursty R occurs, with an average from 1 ps to the run end $R_{\rm av} = 18.7\%$. The usual BSRS, BSRS re-scatter, and $\omega \lesssim \omega_0$ signals are present, with most of the energy in BSRS. There is also activity at $\approx \omega_0 + \omega_p$ that is not present in the prior spectra with a seed and an edge Krook operator. The streaked spectrum in Fig. 3-24 is similar to BC1, even showing the possible SEAS below $3\omega_p$, except for the additional signal at $\omega_0 + \omega_p$. This feature requires further exploration in the future.

We now present the electrostatic evolution (no transverse e/m fields) of a finite density profile with and without an edge Krook operator. The ELVIS model equations are such that if $E^{\pm}$ and v_{ys} are initially zero, and the boundary values of $E^{\pm}$ are zero for all times, then $E^{\pm}$ and v_{ys} remain zero. We can therefore neglect these fields entirely, and call this the "electrostatic" mode of simulation. We perform two electrostatic runs that otherwise match BC1, except one has the BC1 edge Krook operator and the other has none. In both cases the density stays flat in the center, but evolves at the edges into a sheath-like pattern. The resulting change in the density profile $\delta n = n_e - n_B$ after the sheath becomes steady in time is shown in Fig. 3-25. The difference between these cases stems from the electrostatic fluctuations generated by the edge evolution. Plasma waves are generated by this motion and propagate inwards, giving the noise for that SRS grows from in the prior example. A Krook operator greatly suppresses them: the δn for the Krook case at the box center is always

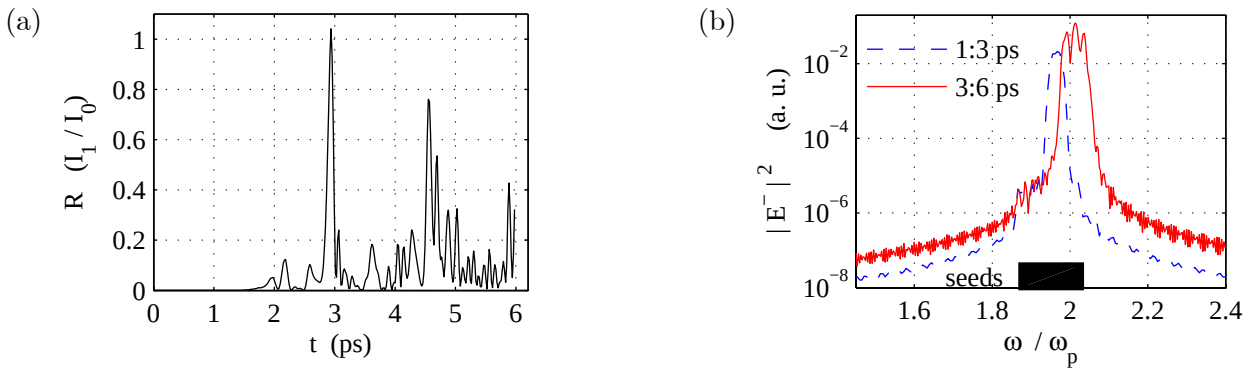

Figure 3-26: (a) Reflectivity and (b) whole-run $E^-(\omega)$ spectrum for rerun of `BC1` with multiple seeds.

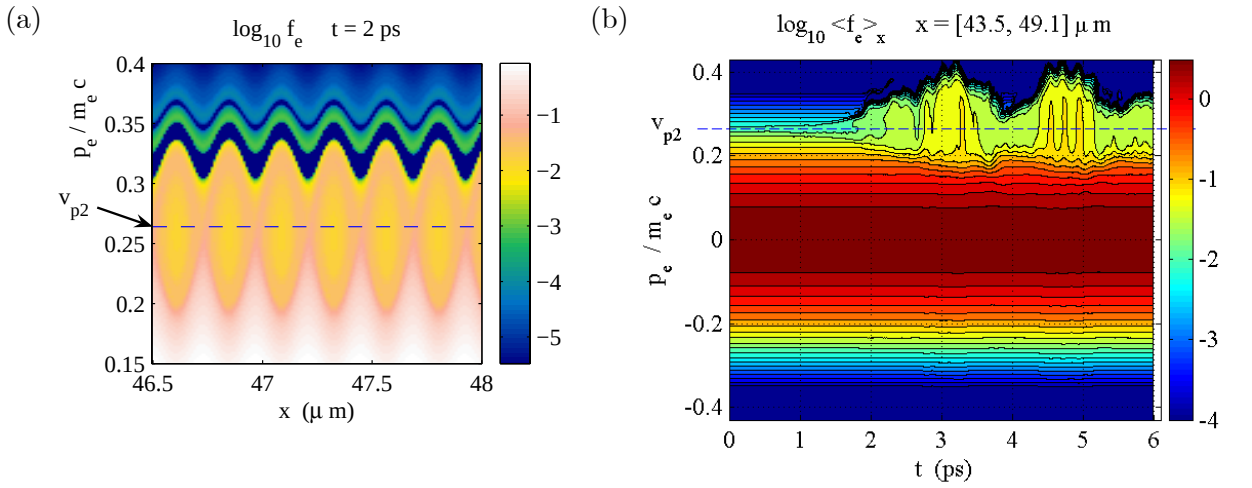

Figure 3-27: (a) f_e near box center at $t = 2$ ps and (b) space-averaged $\langle f_e \rangle$ for rerun of `BC1` with multiple seeds.

less than 10^{-7}.

3.5 Seed bandwidth and possible SEAS

This section considers a run with seeds of several wavelengths to mimic the bandwidth present in the physical noise spectrum. Trapping and large reflectivity still result, with the faster-growing modes producing coherent phase-space vortices early in time. The physical noise from which SRS grows is of course not monochromatic. How can a finite seed bandwidth affect Raman scattering? Linearly, each SRS daughter wave acquires a bandwidth of the order of the growth rate γ. Waves separated in frequency by more than this should amplify independently of each other. When trapping is important, however, the waves can nonlinearly interact. If several plasma waves reach sufficient amplitude, their trapping regions in phase space may overlap. Resonant electrons will not be trapped in a single wave and will not undergo coherent bounce motion. A quasi-linear velocity diffusion and flattening of the distribution may still result and reduce the Landau damping.

`BC1` utilizes a single scattered-light seed wavelength ($I_1 = 10^{-5} I_0$, $\lambda_{1v} = 574$ nm). As seen in Fig. 2-2, SRS has a substantial growth rate for a range of λ_{1v} around the peak. We performed a run

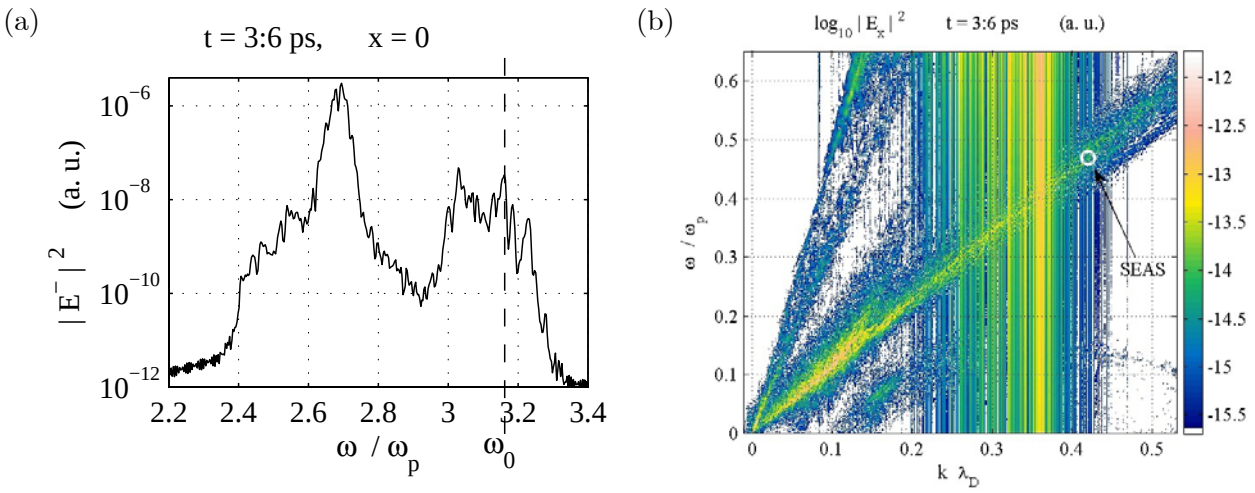

Figure 3-28: (a) Spectrum of reflected light (E^-) pre-filtered to pass the band $\omega/\omega_p = [2.4, 3.3]$. (b) $E_x(k,\omega)$ spectrum showing acoustic activity. The EPW matching the possible SEAS light is marked by a white ring.

identical to `BC1`, except using ten seed light waves with λ_{1v} evenly spaced between 549 nm and 594 nm. Each has an intensity $I_1 = 10^{-6} I_0$ and a random, constant phase (ϕ_{1i}^- in Eq. (3.1) between 0 and 2π). The reflectivity, displayed in Fig. 3-26(a), is qualitatively similar to the monochromatic seed case. It occurs in temporal bursts, and has an average value of 13.5% from 1 ps to the run end. The scattered light spectrum is depicted in Fig. 3-26(b) for early (1:3 ps) and late (3:7 ps) times, and is also similar to `BC1`. The black box indicates the range of seed frequencies, although its height is unrelated to their amplitudes. Early in the run, a subset of the seeds are amplified by SRS; however, at later times the spectrum upshifts and broadens. Figure 3-27(a) displays f_e at an early time when coherent vortices are produced by a few of the faster-growing SRS modes; shortly after 2 ps the vortices become irregular and "washed out" as in Fig. 3-7(b) for `BC1`. The space-averaged f_e is shown in Fig. 3-27(b) and indicates the flattening remains later in time when there is large EPW activity.

This multiple-seed run also has scattered light between the SRS and pump frequencies, which we speculate may be stimulated electron acoustic scatter (SEAS). The streaked $E^-(\omega,t)$ spectrum (not shown) is very much like that for `BC1` only it seems the BSRS re-scatter is weaker and SEAS is stronger. We want to isolate the SEAS signal. As in experiments, it is hard to detect a signal's component at one frequency if most of the energy is in another one. Some energy from the dominant frequency appears in the measured level at the weaker frequency. This produces, for instance, the long tails of frequency spectra away from the dominant mode, and the vertical and horizontal streaks extending from the SRS EPWs throughout our $E_x(k,\omega)$ spectra. To mitigate this numerically we pass $E^-(t)$ at the left edge through a Matlab filter whose effect is to eliminate signal outside a specified frequency band. We then apply the usual Fourier transform diagnostics to the filtered $E^-(t)$. Figure 3-28(a) contains the "filtered" E^- spectrum for the band $\omega = 2.4$ to 3.3 and only after 3 ps. There is always some reflected light at the pump ω_0 that begins very early in the run; this is the reflection from the density gradient observed in the no-seed run above. However, the spectrum reveals two distinct regions of activity below ω_0, a stronger one around $\omega_s = 2.7$ and a weaker one slightly below ω_0.

The reflected light at ω_s maybe be scattering of the pump laser off a low phase-velocity acoustic longitudinal mode present in the electric field E_x. Such a three-wave process must satisfy k and

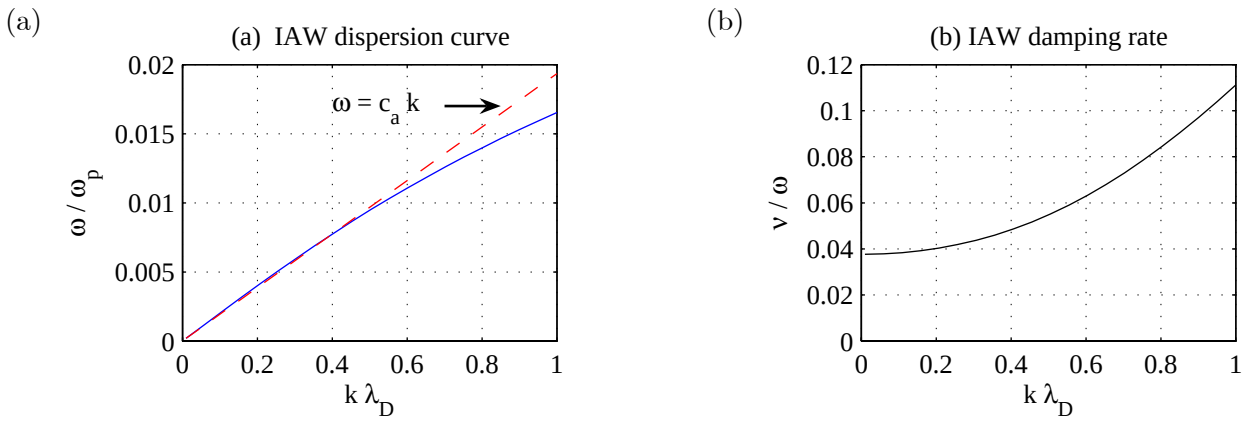

Figure 3-29: IAW kinetic (a) dispersion relation and (b) damping rate for the standard parameters with helium. The dashed red line in (a) is $\omega = c_a k$ with $c_a = 0.0194 v_{Te}$ from Eq. (3.23).

ω matching. The pump and backscattered light of frequency ω_s match with a third wave having $k_2 = 0.42$, $\omega_2 = 0.47$ and a phase velocity $v_{p2} = 1.1 v_{Te}$. There is indeed an acoustic mode $\omega = v_a k$ in the E_x spectrum with $v_a \approx v_{p2}$. Figure 3-28(b) shows $E_x(k, \omega)$ taken from 3 ps to the end run (the time during which SEAS occurs) and zoomed on the two acoustic features. The full spectrum contains SRS EPWs downshifted from the linear dispersion curve as for `BC1`, which connect to the acoustic feature with the higher slope shown. The point (ω_2, k_2) from matching is shown as a white circle and clearly falls on the lower-slope acoustic mode. The circle may obscure the fact that the intensity of E_x near the SEAS point is not enhanced compared to neighboring regions of the beam; in fact, there is "nothing special" about the beam near SEAS. The vertical stripes from $k = 0.2$ to 0.4 and strongest near 0.35 are artifacts of the SRS EPWs due to the numerical Fourier transform, as discussed in the prior paragraph. It would be illuminating to filter the 2-D $E_x(x, t)$ as described above and more clearly see the acoustic activity. The largest activity on the low-slope acoustic branch occurs for $\omega \approx 0.05$ to 0.15, very far from the SEAS point. Although this activity has the right frequency to account for the scattered light around $3\omega_p$, it would need a much higher $k \approx 0.45$ to satisfy wavenumber matching; $E_x(k, \omega)$ has no power there.

3.6 Kinetic ions

Ion motion introduces new effects to LPI. For underdense plasmas in our 1-D geometry, these include stimulated Brillouin scattering (SBS) and ion-based SRS saturation mechanisms (in higher dimensions laser filamentation also takes place). For small $k_2 \lambda_D \lesssim 0.15$, mobile ions allow Langmuir collapse and cavitation to occur [82–84]. At higher $k_2 \lambda_D$ ion motion can saturate SRS via the Langmuir decay instability (LDI) of the plasma wave [42, 45]. An anti-correlation of SRS and SBS has also been observed in some experiments [85–87]. In this section we explore LDI and SBS for the standard parameters, and present a rerun of BC1 with kinetic ions. SRS proceeds as with immobile ions for early times, but is suppressed toward the run end when a large number of parametric decays appear to occur.

The examples of this section are for the standard parameters with helium ions, given in the thesis preamble: $Z_i = 2$, $m_i = 4 m_p$, $T_i = T_e/4 = 750$ eV (ion conditions are discussed in Sec. 2.6). We present results of an ELVIS simulation of this case below. The ion acoustic wave (IAW)

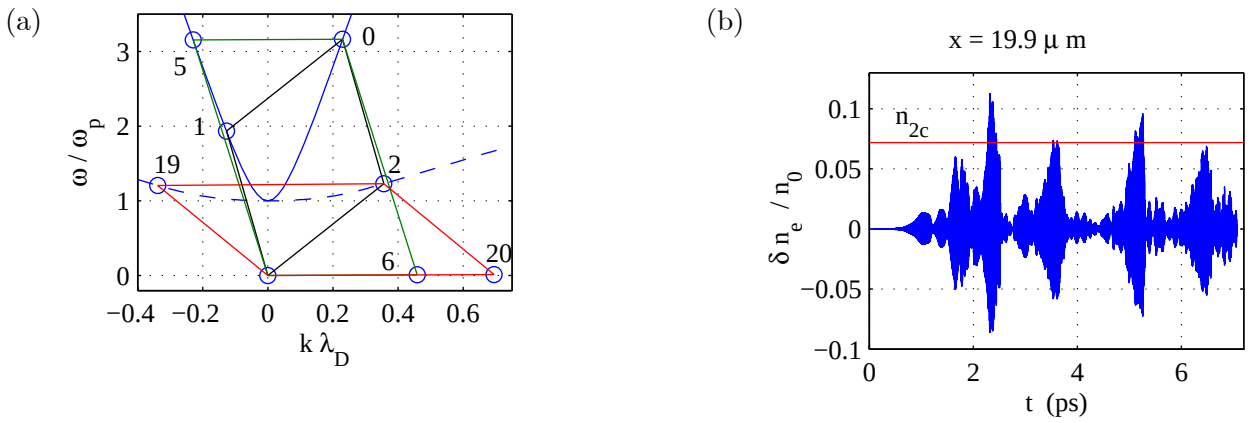

Figure 3-30: (a) Dispersion diagram showing BSRS (modes 0, 1, 2), LDI (2, 19, 20), and BSBS (0, 5, 6) for the standard parameters with helium. Mode numbers follow table 3.1. Solid and dashed curves are the EMW and EPW dispersion curves. (b) $\delta n = n_e - n_0$ for run `BC1`. The solid red line is the LDI threshold $\delta n = \hat{n}_{2c}$ for the SRS EPW.

approximately satisfies $\omega = c_a k$ where the acoustic speed c_a is given by

$$c_a^2 = v_{Te}^2 Z_i \frac{m_e}{m_i}\left(1 + \frac{3T_i}{Z_i T_e}\right). \tag{3.23}$$

For our example parameters $c_a = 0.0194 v_{Te}$. The real and imaginary parts of the solution to the kinetic IAW dispersion relation $1+\chi_e+\chi_i = 0$ are displayed in Fig. 3-29. The collisionless damping of these modes is fairly strong.

3.6.1 LDI

LDI is the parametric coupling of a pump EPW (labeled mode 2) to a daughter EPW (mode 19) and a daughter IAW (mode 20). Our labelling follows table 3.1, although of course any EPW can undergo LDI. Some experiments show an increase in SRS with an increase in ion wave damping, which was taken to mean LDI was saturating SRS [49], [48]. More recently the EPWs associated with LDI cascades have been directly observed with Thomson scattering [52, 53]. In our 1-D geometry the matching conditions can only be satisfied for back LDI ($k_{19} < 0$) and not forward LDI ($k_{19} > 0$); by LDI we always mean back LDI. This is equivalent to the fact that completely forward SBS cannot exist. We use the kinetic EPW and IAW dispersion relations to find the natural, matching modes for LDI of mode 2. The results are shown in the dispersion diagram in Fig. 3-30(a) and in table 3.3. $\gamma_c = (\nu_{19}\nu_{20})^{1/2}$ is the threshold pump strength for LDI. The undamped growthrate for LDI $\gamma_{0,\mathrm{LDI}}$ is ([39], p. 38)

$$\gamma_{0,\mathrm{LDI}} = \frac{1}{4}\frac{v_{os2}}{v_{Te}}\sqrt{\omega_{19}\omega_{20}} = \frac{\omega_p/\omega_2}{4k_2\lambda_D}\hat{n}_2\sqrt{\omega_{19}\omega_{20}}. \tag{3.24}$$

$v_{os2} = eE_2/(m_e\omega_2) = \hat{n}_2 v_{Te}(\omega_p/\omega_2)/(k_2\lambda_D)$ is the electron oscillation speed in the pump EPW and $\hat{n}_2 = n_2/n_0$ is the pump density perturbation. The threshold pump strength n_{2c} for growth ($\gamma_{0,\mathrm{LDI}} > \gamma_c$) is

$$\hat{n}_{2c} = 4k_2\lambda_D\frac{\omega_2}{\omega_p}\left(\frac{\nu_{19}\nu_{20}}{\omega_{19}\omega_{20}}\right)^{1/2}. \tag{3.25}$$

ν_{19}/ω_{19}	0.0233		$\hat{n}_{2c}$	0.0719
ν_{20}/ω_{20}	0.0722		γ_0	$119\hat{n}_2$ ps^{-1}
$2\pi/\omega_{20}$	0.296 ps		γ_c	8.58 ps^{-1}

Table 3.3: LDI of mode 2 for the standard parameters with helium, and neglecting collisional damping.

γ_0	1.71 ps^{-1}		$2\pi/\omega_6$	0.423 ps
γ_c	0.0989 ps^{-1}		γ	1.36 ps^{-1}
γ_a	10.4 ps^{-1}		$I_{a,15}$	74.1

Table 3.4: Pump SBS quantities for the standard parameters with helium.

Figure 3-30(b) depicts $\delta n = n_e - n_B$ for `BC1` toward the left side of the central flattop (δn is comparable at points to the right, but with slightly lower amplitudes early in time). The density fluctuations just briefly exceed the LDI threshold. In addition, for $\hat{n}_2 = 0.15$ (above the largest observed δn) the undamped growth time $1/\gamma_0 = 0.056$ ps, which is comparable to the bursting time. The plasmons are thus not above threshold long enough for LDI grow significantly. We do not expect LDI to seriously affect SRS in a run with kinetic ions. Note that the numerical δn is not completely symmetric for $\delta n > 0$ and $\delta n < 0$. This indicates harmonic generation (as seen in Fig. 3-5) and wave steepening, which tend to increase the positive part of an EPW density fluctuation. Wave-breaking is a limit on the amplitude below which a plasma wave can attain and still be described by fluid theory [88], [89], [90]. The warm-fluid wave-breaking upper bound is $\hat{n}_2 = 0.2$, almost twice the largest δn observed in the run. It is unclear how wave-breaking applies to low phase-velocity waves, when Landau damping and kinetic effects are important. This applies even more to our simulations, where the SRS EPW lies below the linear dispersion curve and displays strong nonlinearity.

3.6.2 SBS

Brillouin scattering, or the decay of a pump EMW (mode 0) to a daughter EMW (mode 5) and IAW (mode 6), is a major concern for both direct- and indirect-drive ICF. Several theories have been advanced to explain the experimentally observed lower SRS levels during periods of high SBS. This may be due to the modification of the EPW dispersion relation by ion-wave density fluctuations [15, 16, 91], which introduces a detuning that varies in time with ion wave amplitude. Moreover, SRS saturation by Langmuir collapse provides enhanced ion fluctuations from which SBS can develop. Unlike with Raman scattering, there is no totally forward SBS ($\vec{k}_0 \,||\, \vec{k}_5$): matching cannot be satisfied for a purely acoustic ion wave $\omega_6 \propto k_6$. Filamentation can be thought of as the $\vec{k}_0$ almost parallel to $\vec{k}_5$ limit of SBS, but the ion wave $\vec{k}_6$ is perpendicular to $\vec{k}_0$. Our 1-D geometry cannot model this. We are only concerned then with back SBS, and by SBS we mean back SBS. For the standard parameters with helium, the SBS natural matching modes (calculated with the kinetic IAW dispersion relation) are given in table 3.4 and diagrammed in Fig. 3-30(a). SBS is convective with a growth time $\gamma^{-1} = 0.753$ ps. We do not observe pump SBS in our simulations, even though our several-picosecond runs last for several growth times. This is probably because we do not seed it.

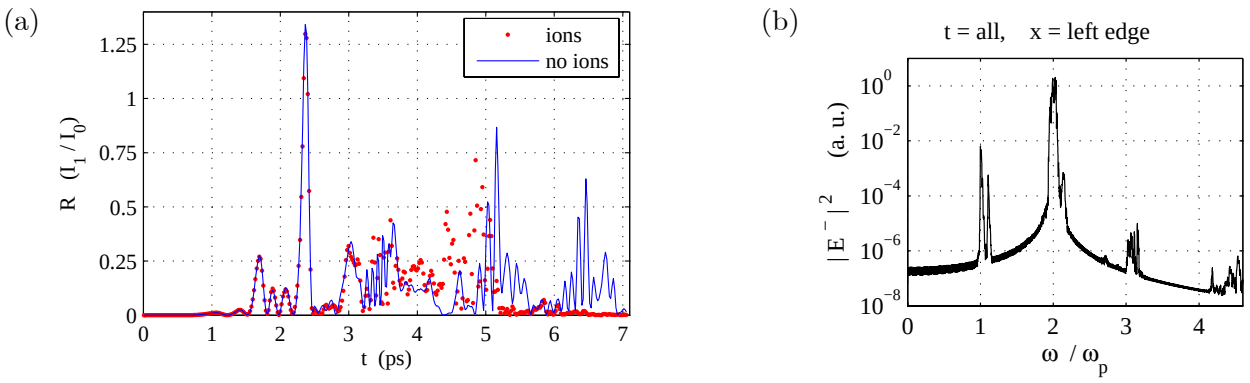

Figure 3-31: (a) Reflectivity for runs `iBC` (red dots) and `BC1` (solid blue). (b) Gated E^- spectrum over whole run `iBC`.

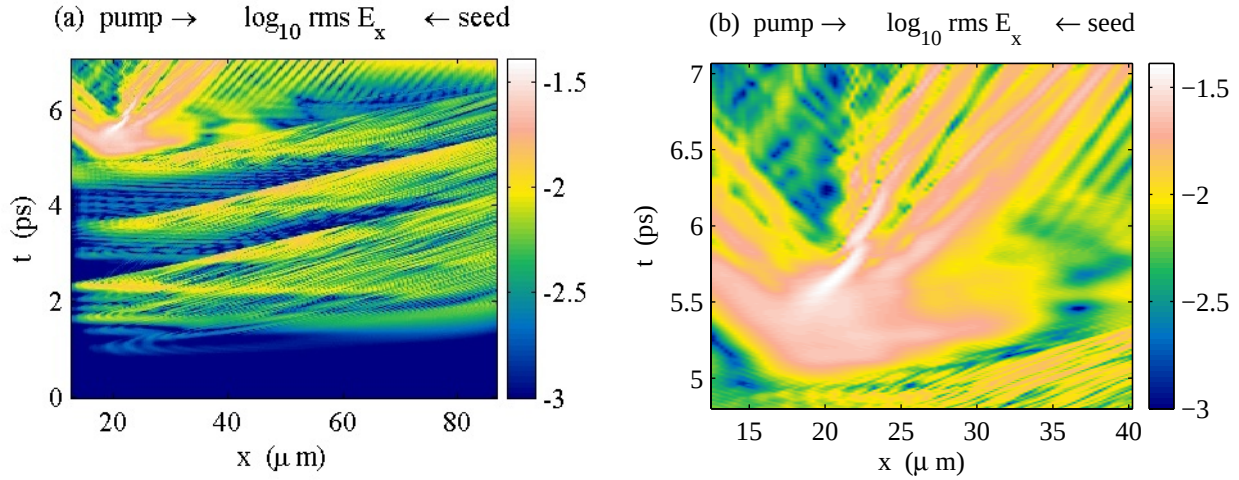

Figure 3-32: rms E_x for run `iBC`. (b) zooms on the "blob" in the upper left of (a).

3.6.3 Simulation with kinetic ions

The run `iBC` explores the role of ions in SRS, and matches `BC1` except with kinetic helium ions as described above. In this thesis we use at most one kinetic ion species, although ELVIS can easily be extended to handle any number. Our basic finding is that kinetic enhancement can still occur, but can also be inhibited by the interplay of several parametric processes. We do not see evidence of pump SBS or LDI of the BSRS plasmon. Many of the parametric processes listed in table 3.1 occur, including decays or re-scatter of daughters from decays if the pump. We extensively use the shorthand of table 3.1, explained in its caption. We trust this won't create confusion once the reader understands how a mode's label is constructed. Many of these modes are close in k or ω and can provide enhanced noise for each other. If the mismatch is comparable to the mode bandwidth, either due to the parametric coupling or bandwidth in the appropriate pump, one cannot treat the modes as distinct an analysis like [24] may be needed. Coupled-mode simulations, with no kinetic effects, allowing SRS cascades and SRS coupling to LDI show a chaotic region near the laser entrance, a bursty reflectivity, and SRS saturation [39], [40]. Recent PIC simulations of Raman scatter from high-temperature plasmas ($T_e \approx 10$ keV) indicate Raman and Brillouin re-scatter are both important [92].

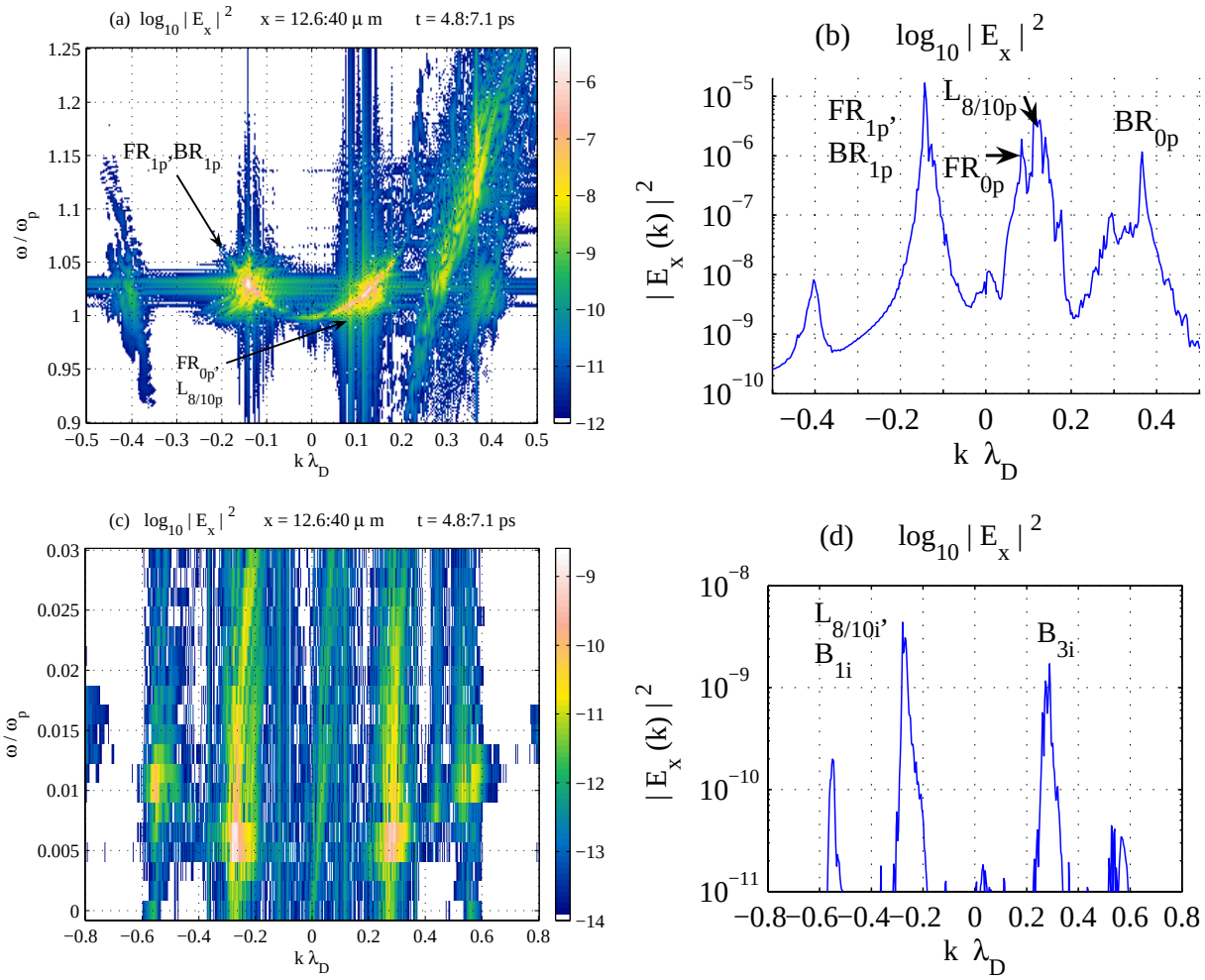

Figure 3-33: E_x power spectrum for run iBC for (a, b) high and (c, d) low frequencies. Panels (b, d) are sums over the power contained in the frequencies of panels (a, c).

Figure 3-31(a) plots the reflectivity for `iBC` and `BC1`. The R's agree very well until 3 ps, after which they diverge due to the chaotic nature of the dynamics. However, after 5 ps the `iBC` reflectivity stays low. The rms electrostatic field E_x is shown in Fig. 3-32. Early in time pulses form at the laser entrance and propagate to the right, as for fixed ions. At 5 ps a "blob" of activity develops, after which R is very low. The $k-\omega$ spectrum of this blob is plotted in Fig. 3-33 for the high-frequency, EPW range (panels a and b) and the low-frequency, IAW range (panels c and d).

First we analyze the EPW features in Fig. 3-33(a, c). The plasmon BR_{0p} (mode 2) is downshifted from the linear dispersion relation, as for immobile ions; $E_x(k,\omega)$ for the whole run (not shown) demonstrates this for all times. Panels b and d plot the total power in k summed over all frequencies in the corresponding panels a and c. Most left-moving EPW activity occurs at $k=-0.143$. This corresponds to Raman re-scatter of mode 1, labeled BR_{1p} and FR_{1p}, which practically coincide in k and ω. Recall ω_1 fluctuates in time with the downshift in ω_2, so the numbers in table 3.1 are approximate for mode 1's decays. For $k>0$, besides mode 2 there is a plasmon cluster around $k\approx 0.1$. The strongest peak has $k\approx 0.125$, and the two others are at 0.084 and 0.14. The lowest-k peak is FR_{0p}, while the strongest peak may be LDI of mode 8 or 10 ($L_{8/10p}$).

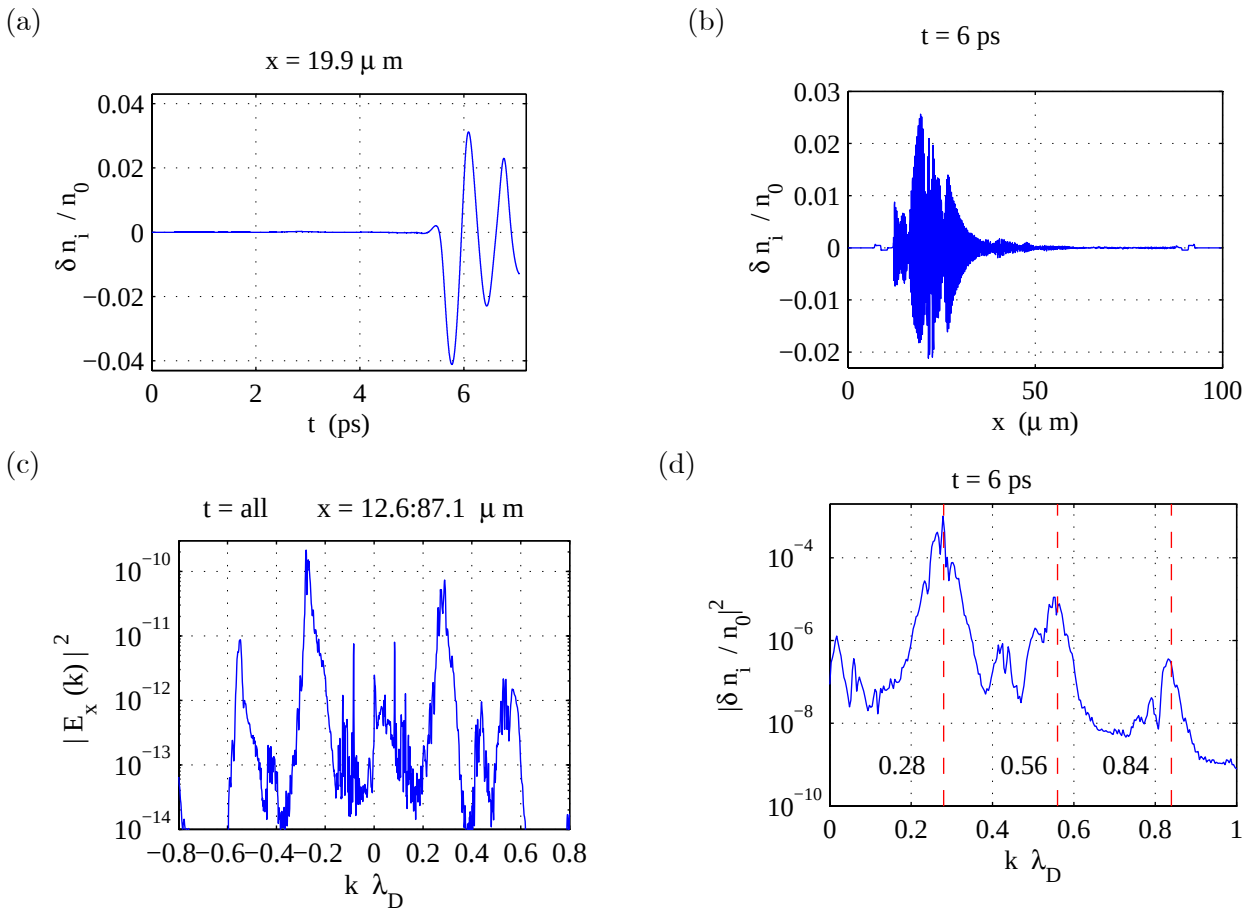

Figure 3-34: δn_i (a) vs. t near the left edge and (b) vs. x shortly after the blob. (c) E_x power spectrum over whole run, summed over frequencies $\omega = 0 : 0.03\omega_p$ to show ion motion. (d) k spectrum of panel b.

The low-frequency, ion-mode spectra (Fig. 3-33(b, d) shows several points lying on the IAW dispersion curve, with $k \approx -0.28$ being the largest. Besides matching $L_{8/10i}$, this k also corresponds to the Brillouin re-scatter mode B_{1i}; B_{1m} is observed in the transmitted spectrum below. Several harmonics of $k = -0.28$ appear, as well as a signal at $k = +0.28$. The reflected light (see below) shows a small blip of Brillouin light for B_{3m}, which corresponds to the IAW B_{3i} with $k = 0.29$ and may explain the signal there. If a mode described by (k, ω) is an acoustic mode ($\omega \propto k$), then its harmonics $(2k, 2\omega)$, $(3k, 3\omega)$, and so on, are also natural modes. It is unclear if the features at multiples of $k = \pm 0.28$ are due to parametric couplings or harmonics of the fundamentals.

The ion density fluctuation $\delta n_i = n_i - n_i(t = 0)$ is presented in Fig. 3-34. Most of the ion activity occurs during or after the blob in time, and near the left edge. The period between the two minima near 6 ps in panel (a) corresponds to $\omega = 5.6 \times 10^{-3}$, which agrees well with B_{1i} and $L_{8/10i}$. Moreover, the k spectrum in panel (c) of the spatial profile shown in panel (b) is peaked at $k = 0.28$ (positive and negative k are not distinguished). The low-frequency $E_x(k, \omega)$ spectrum for the whole run is plotted in panel (d) and also shows activity mainly at $k = \pm 0.28$ and their harmonics. Note that pump SBS and LDI of the pump BSRS EPW (modes B_{0i} and L_{2i}) are absent from all the spectra.

Now consider the transmitted light. We show the spectrum of E^+ in Fig. 3-35, filtered to

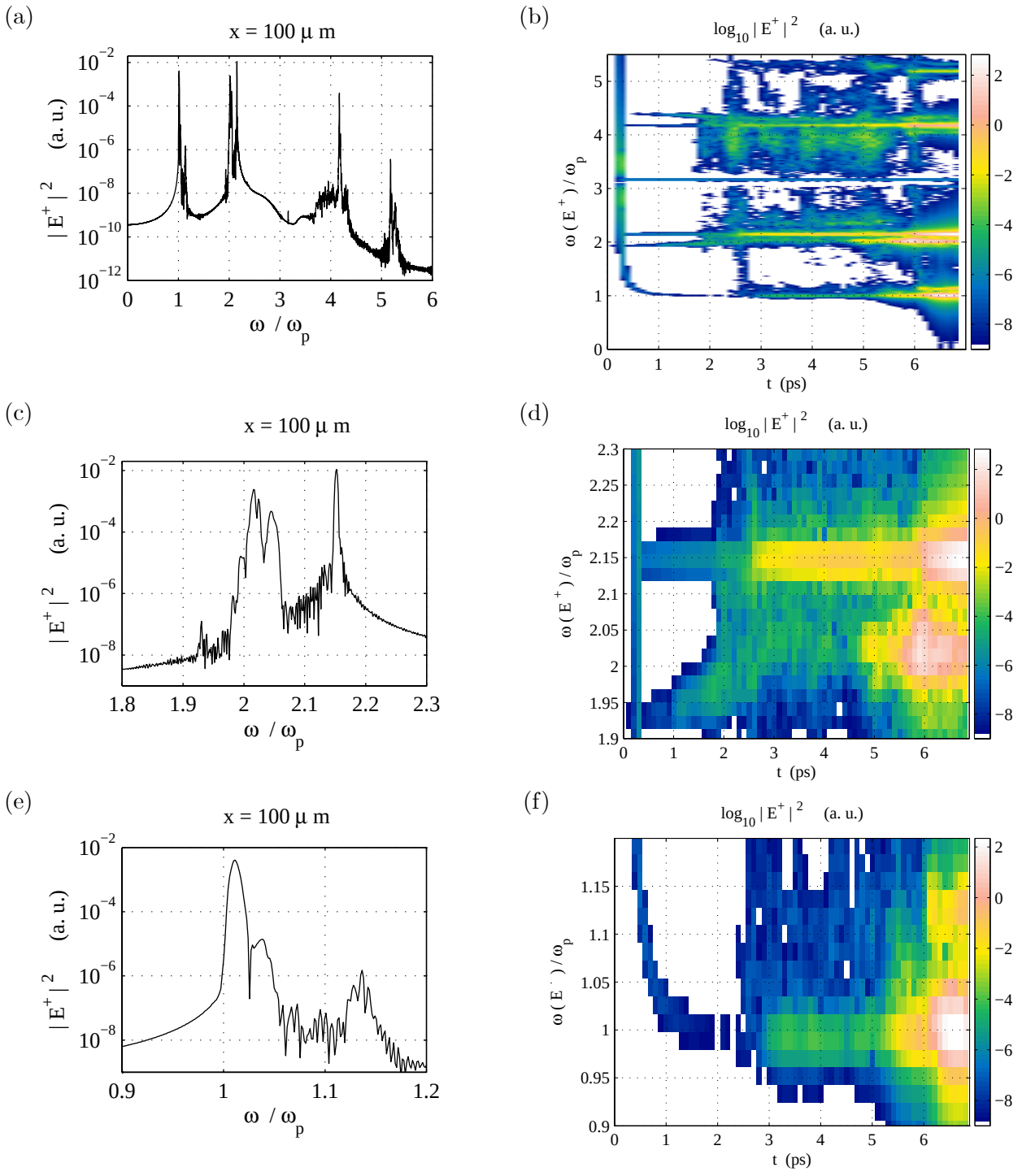

Figure 3-35: Sepctra of transmitted light E^+ for run `iBC` at the right edge ($x = 100$ μm). Signal is filtered to suppress the pump near $\omega/\omega_p = 3.16$.

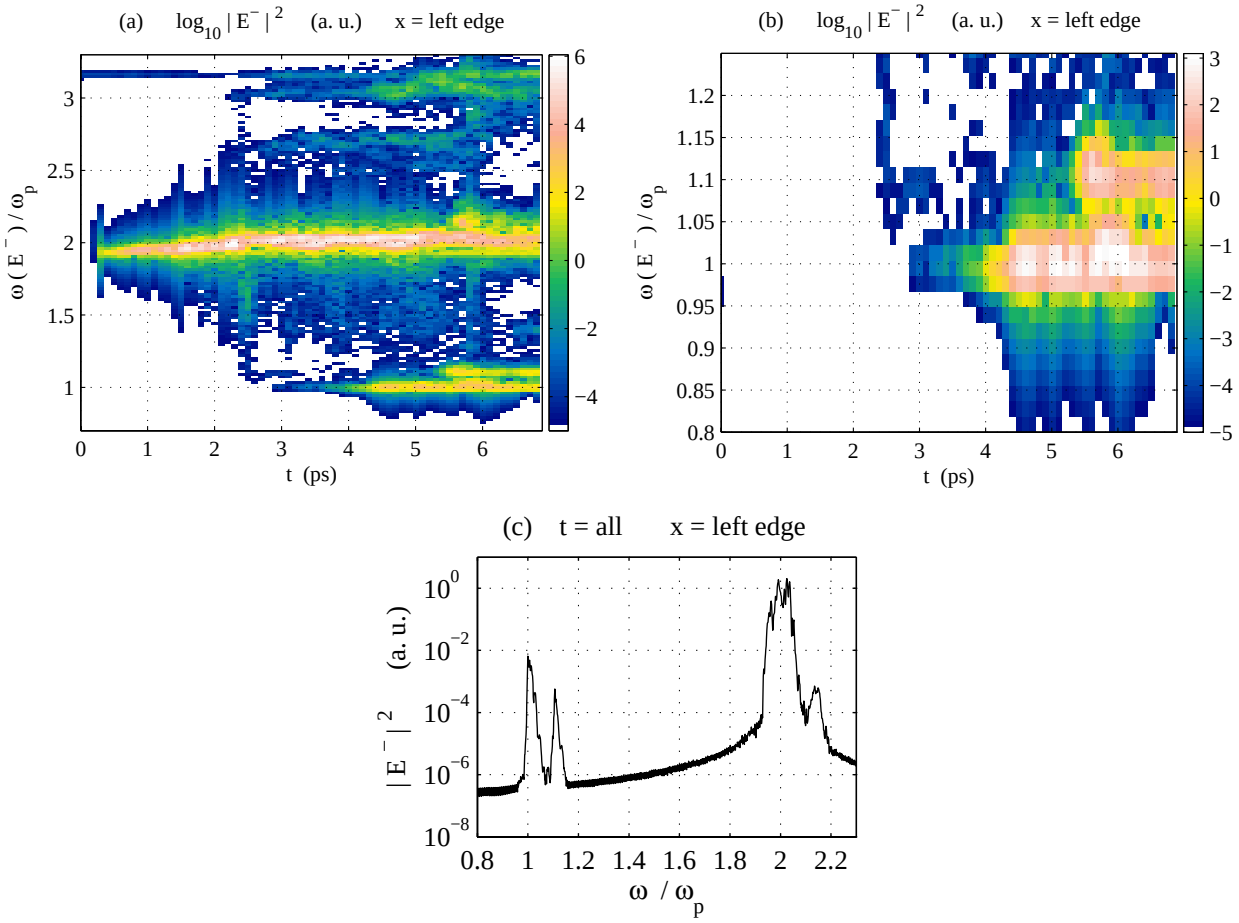

Figure 3-36: Spectra of reflected light E^- for run `iBC`.

eliminate the pump. As for immobile ions, anti-Stokes upshifted light of the pump is seen ($\omega \approx 4.16$, 5.16). The weak signal at $\omega = 3.16$ is the pump light that survives filtration. Near $2\omega_p$ there are two features: pump FSRS (FR_{0m}, $\omega_3 = 2.15$), also present with immobile ions, as well as SBS re-scatter of mode 1 (B_{1m}, $\omega \approx 2.03$). The spectra show that these two signals are separated in both frequency and the time they are strong (their group velocities in the plasma are similar). Shortly after B_{1m} develops at 5.5 ps, FR_{0m} intensifies. These modes are so close in frequency that one may act as an enhanced seed for the other. Inspection of the E_x and light-wave signals outside the blob (not shown) clearly reveal the plasmons FR_{0p} (mode 3) and FR_{3p} (the FSRS decay of mode 3). Continuing to lower frequency, there are two signals near ω_p: BR_{1m} ($\omega \approx 1$), and a weak FR_{3m} ($\omega = 1.15$). Both these last features are visible in run `BC1` with fixed ions, which strengthens our identification of them as Raman modes.

We complete our analysis with the reflected light spectra in Fig. 3-36. In accord with the reflectivity plot, BSRS in panel (a) is strong until about 5ps. FR_{1m} ($\omega \approx 1$) is evident starting around 4 ps and reaches its maximum before and during the blob in E_x. For clarity panel (b) zooms on the $\omega \approx \omega_p$ portion of panel (a). The light waves FR_{1m} and BR_{1m} are very close, have $\omega \approx \omega_p$ and thus very slow group velocities; they almost form a "standing light wave" in the plasma. From 5.5 ps onward there is a weaker signal at $1.1\omega_p$ which we identify as BR_{3m}; of course, this signal cannot occur until mode 3 (FR_{0m}) is appreciable. There is a short blip at $\omega \approx 2.15$ matching B_{3m}

which occurs just before 6 ps, and is visible in the time-integrate spectrum Fig. 3-36(c). Higher in frequency, we see the weak signal above $2.5\omega_p$ which we argued earlier may be SEAS. Near $3\omega_p$ there is also some activity roughly at two frequencies. Although pump SBS (B_{0m}) falls in this range, fixed ion runs also reveal light at this frequency; moreover, we do not see ion activity for B_{0i}. Pump SBS, if it occurs at all, is weak.

Let us suggest why the reflectivity becomes low and the longitudinal blob forms late in time, and in particular how ions may enhance this. We focus on processes BR_1, FR_1, $L_{8/10}$, B_1, and FR_0. BR_1 and FR_1 occur in the fixed ion run but at lower levels. Most of the blob electrostatic activity, which terminates the high reflectivity, is in the BR_{1p} and/or FR_{1p} plasmons, as well as $L_{8/10p}$. Moreover, the ion activity is dominated by $k \approx -0.28$, which is either $L_{8/10i}$ or B_{1i}. The light waves B_{1m} and FR_{0m}, as well as the IAWs B_{1i} and $L_{8/10i}$, are close in k and ω, and can provide noise for each other. These processes appear to grow in tandem within the blob. The EPW $L_{8/10p}$ constitutes a substantial part of the E_x blob energy in Fig. 3-33(b). These LDI decays remove energy from BR_1 and FR_1 and may give rise to the chaotic dynamics observed in coupled-mode simulations [39], [40].

We stress our ion study is preliminary. Performing more and longer runs, with and without mobile ions, for different conditions, will show if the electrostatic "blob" requires ion motion, or can be generated by the electron dynamics themselves via Raman re-scattering. The run `iBC` reveals many parametric decays take place. This suggests a broadband source of noise, in both the electrostatic and electromagnetic channels, should be added to ELVIS in the future, rather than preferentially seeding just BSRS of the pump. The lack of seeding may also explain why we see no pump SBS or LDI of mode 2. LDI of mode 2 is also suppressed because the daughters L_{2p} and L_{2i} are strongly Landau damped, giving a high threshold (discussed above). The LDI daughters of modes 8 and 10, however, all have much lower k's and therefore lower damping rates. We conclude that ion dynamics do not inherently suppress kinetic enhancement of SRS for at least short (several picosecond) intervals in these plasma conditions, and that the nonlinear interplay of several parametric processes may be important. We leave much work on ions for the future.

3.7 Loss mechanisms

Various relaxation or loss mechanisms, such as collisions and sideloss out of a laser speckle, interfere with electron trapping. If a resonant electron is removed from the trapping region before it undergoes bouncing, it will not give energy back to the wave; as a result, Landau damping will not be affected by trapping. The space-averaged f_e must have a nonzero slope at the phase velocity v_p for Landau damping to occur; trapping tries to flatten f_e, while the loss mechanisms try to restore f_e to an equilibrium distribution (e.g., a Maxwellian) and thereby restore the slope. We consider in this section de-trapping due to speckle sideloss ("sl"), 1-D collisional diffusion ("diff"), and pitch-angle scattering ("pa"). Each process imposes a minimum wave amplitude $\hat{n} = n_1/n_0$ for the trapping-induced damping reduction to happen. For typical ICF conditions $\hat{n}_{\rm sl}$ is greater than or not much smaller than $\hat{n}_{\rm diff}$, while $\hat{n}_{\rm diff} \gg \hat{n}_{\rm pa}$. We show ELVIS simulations with a Krook relaxation operator, intended to model sideloss. The reflectivity R approaches its linear value when ν_{sl} exceeds a threshold ($\approx 2 \times 10^3 \omega_p$ for the chosen parameters), while R is large and chaotic for lower ν_{sl}.

3.7.1 Speckle sideloss

A laser beam has a finite transverse extent (perpendicular to the propagation direction). Electrons eventually cross the beam transversely and stop interacting with it due to their thermal motion. This is called sideloss. Once a trapped electron is lost, it cannot bounce or affect Landau damping. Sideloss is particularly potent for diffraction-limited speckles or "hot spots," which have a transverse half-width (radius) $L_\perp = 1.028F\lambda_0$ where F is the optic f/# ([52], p. 25). For NIF, $F = 8$ and λ_0 =351 nm, giving $L_\perp = 2.81$ μm. Using the thermal speed v_{Te} as a typical transverse speed, the time for electron to leave the speckle by sideloss is $t_{sl} = L_\perp/v_{Te}$. For the standard parameters ($T_e = 3$ keV), this gives $t_{sl} = 0.12$ ps. Since the damping reduction happens for $t \gtrsim \tau_B$, sideloss will not disrupt the damping reduction if $\tau_B < t_{sl}$.

Sideloss is a multi-dimensional effect, which can be mimicked in a 1-D model (such as that used in ELVIS) with a Krook relaxation operator $[\partial f_e/dt]_{\rm Krook} = K_e[f_e]$:

$$K_e[f_e] = \nu_{Ke}(x)\left(n_e\tilde{f}_{0Ke} - f_e\right). \tag{3.26}$$

This operator, its effect on linear plasma waves, and how it is implemented in ELVIS, is discussed in the appendix on ELVIS (p. 132). We imagine electrons in the speckle are replaced by thermal electrons from the surrounding "bath" of Maxwellian plasma at a rate $\nu_{Ke} = \nu_{sl} = v_{Te}/L_\perp$. The wave amplitude $\hat{n}$ needed for trapping to overcome sideloss is determined by $\tau_B > t_{sl}$, which gives

$$\hat{n} > \hat{n}_{\rm sl} = \left(2\pi\frac{\nu_{sl}}{\omega_p}\right)^2 = \left(2\pi\frac{\lambda_D}{L_\perp}\right)^2. \tag{3.27}$$

For the standard parameters and the NIF speckle $L_\perp$ mentioned above, we find $\hat{n}_{\rm sl} = 9.23\times10^{-4}$.

A detailed solution of the evolution of a finite-amplitude plasma wave with a Krook operator, including the effects of trapping, is given in [21]. They find the linear damping occurs, unimpeded by trapping, when $\nu_{Ke} \gg \omega_B$; in this case the relaxation is strong enough to maintain a slope of f_e at v_p. For $\omega_B \gg \nu_{Ke}$ the damping is reduced but there is a residual, amplitude-dependent damping rate $\nu_{\rm res}$ for late times ($t \gg \tau_B$)

$$\frac{\nu_{\rm res}}{\nu_L} = \frac{1}{1+(\omega_B/\nu_{Ke})^2}, \tag{3.28}$$

where ν_L is the linear damping rate (Landau plus Krook). More recent discussions of large-amplitude plasma waves in the presence of a Krook operator, and the relevance to SRS, can be found in [60], [61].

3.7.2 1-D collisions

1-D electron-ion Coulomb collisions also limit the trapping process. The effect we consider here is velocity-space diffusion $[\partial f_e/dt]_{\rm diff} = D_e\partial_{vv}f_e$ where $D_e = \nu_e v_{Te}^2$ is the velocity diffusion coefficient and ν_e is appropriate for a Vedenov operator with a single ion species:

$$\nu_e = (2+Z_i)\nu_0\frac{v_{Te}^3}{v_p^3}, \qquad \nu_0 = \frac{\ln\Lambda}{4\pi}\frac{\omega_p}{N_\lambda}. \tag{3.29}$$

$N_\lambda = n_0\lambda_D^3$ is the number of particles in a Debye cube. The interaction of trapping with this 1-D diffusion operator was studied analytically in [20]. They find linear damping takes place for $\hat{n} \ll (\nu_e/\omega_p)k\lambda_D$, while in the opposite limit the damping rate approaches a residual, amplitude-dependent value $\nu_{\rm res}$ for $t \gg \tau_B$ given by

$$\frac{\nu_{\rm res}}{\nu_L} = 4\pi\frac{\nu_e}{\omega_p}(k\lambda_D)^2\hat{n}^{-3/2}. \tag{3.30}$$

As a trapped electron bounces it follows a closed, elliptical orbit in phase space. A collision puts it on another orbit. If this new orbit is also trapped, it continues the bouncing motion, albeit at a new distance from the elliptic fixed point. Once the electron is moved outside the trapping region, however, it moves on a passing orbit and no longer bounces. This suggests collisional diffusion disrupts the damping reduction if an electron diffuses out of the trapping region before it bounces. The time to diffuse from the center of the trapping region (located at $v = v_p$) to the edge ($v = v_p + v_{tr}$) is

$$t_{\rm diff} = \frac{v_{tr}^2}{2D_e} = \frac{2}{(k\lambda_D)^2}\frac{1}{\nu_e}\hat{n}. \tag{3.31}$$

Requiring $\tau_B < t_{\rm diff}$ gives

$$\hat{n} > \hat{n}_{\rm diff} = \left[\pi\frac{\nu_e}{\omega_p}(k\lambda_D)^2\right]^{2/3}. \tag{3.32}$$

This makes qualitative sense: the stronger collisions are, the larger the wave amplitude must be to overcome diffusion.

For the standard parameters with $Z_i = 1$, we have $\nu_e = 2.04\times10^{-5}\omega_p$ and $\hat{n}_{\rm diff} = 4.06\times10^{-4}$ $= 0.44\hat{n}_{\rm sl}$. It is difficult to say in general whether $\hat{n}_{\rm diff}$ or $\hat{n}_{\rm sl}$ is larger; both are rough estimates, and $\hat{n}_{\rm sl}$ depends strongly on how we choose $L_\perp$. However, for reasonable ICF parameters it is hard to make $\hat{n}_{\rm diff}$ significantly larger than $\hat{n}_{\rm sl}$; retaining sideloss and neglecting diffusion is therefore not unreasonable.

3.7.3 pitch-angle scattering

Collisions also rotate an electron's velocity vector $\vec{v}_e$, and can move the longitudinal component v_{ex} out of the trapping region. For elastic collisions of fast electrons with both electrons and ions ($v_{ex} \gg v_{Te}$, v_{Ti}), the scattering rate $\nu(\Delta\theta)$ for an angular change $\Delta\theta$ in $\vec{v}_e$ is [93]

$$\nu(\Delta\theta) = \frac{\nu_\perp}{\Delta\theta^2}; \qquad \frac{\nu_\perp}{\omega_p} = \frac{1+Z_i}{2\pi}\frac{\ln\Lambda}{N_\lambda}\left(\frac{v_{Te}}{v_e}\right)^3. \tag{3.33}$$

$\nu_\perp$ is the rate for 90° scatter and $v_e = |\vec{v}_e|$. Using Eq. (3.29), $\nu_\perp = 2(1+Z_i)\nu_0(v_{Te}/v_e)^3$. The time $t_{\rm pa} = 1/\nu(\Delta\theta)$ for a deeply-trapped particle to pitch-angle scatter out of the trapping region can be estimated by setting $v_e = v_p$ and $\cos\Delta\theta = (v_p - v_{tr})/v_p$, giving $\Delta\theta \approx (2v_{tr}/v_p)^{1/2}$:

$$t_{\rm pa} = \frac{2v_{tr}}{v_p\nu_\perp} = \frac{1}{(1+Z_i)\nu_0}\frac{v_{tr}v_p^2}{v_{Te}^3}. \tag{3.34}$$

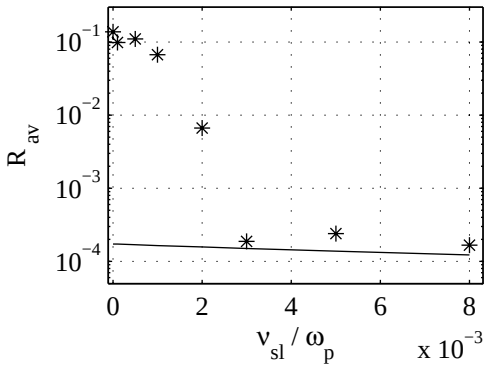

Figure 3-37: Time-averaged reflectivity R_{av} for re-runs of `BC1` with sideloss rate ν_{sl} ($\nu_{Ke}(x)$ in the central region). The solid curve is the steady-state R calculated including sideloss.

$\tau_B < t_{\rm pa}$ when

$$\hat{n} > \hat{n}_{\rm pa} = \pi(1+Z_i)\frac{\nu_0}{\omega_p}\frac{(k\lambda_D)^3}{(\omega/\omega_p)^2}. \tag{3.35}$$

We can compare this to $\hat{n}_{\rm diff}$:

$$\frac{\hat{n}_{\rm pa}}{\hat{n}_{\rm diff}} = \left(\frac{\pi\nu_0}{(k\lambda_D)\omega_p}\right)^{1/3}\frac{1+Z_i}{(2+Z_i)^{2/3}} \tag{3.36}$$

$$= \left(\frac{\ln\Lambda}{4(k\lambda_D)N_\lambda}\right)^{1/3}\frac{1+Z_i}{(2+Z_i)^{2/3}}. \tag{3.37}$$

Typically $\hat{n}_{\rm pa} \ll \hat{n}_{\rm diff}$, meaning that 1-D diffusion is a more important de-trapping mechanism than pitch-angle scattering. For the standard parameters with $Z_i = 1$, $\hat{n}_{\rm pa}/\hat{n}_{\rm diff} = 0.130$.

3.7.4 Simulations with sideloss

We can estimate the value of ν_{sl} needed to prevent trapping from enhancing SRS using Eq. (3.27). Recall Eq. (3.2) gives the plasma wave amplitude driven by the beating of two light waves. For the parameters of run `BC1` and $\nu_{sl} = 0$, the imposed pump and seed amplitudes (that is, neglecting any parametric amplification of the seed) yield $\hat{n}_0 = 1.18 \times 10^{-4}$. SRS raises the amplitude above this value. The amplitude gain rate $\alpha = 0.0190\ \mu\text{m}^{-1}$ over the 75.1 μm flattop gives an amplitude gain of 4.17, and a steady-state amplified plasma wave with $\hat{n}_a = 4.92 \times 10^{-4}$. The sideloss rates ν_{sl} that give $\hat{n}_{\rm sl} = \hat{n}_0$ and $\hat{n}_{\rm sl} = \hat{n}_a$ are $\nu_{sl,0} = 1.73 \times 10^{-3}\omega_p$ and $\nu_{sl,{\rm a}} = 3.53 \times 10^{-3}\omega_p$, respectively. We expect sideloss to start interfering with trapping for ν_{sl} somewhere in this range. The reference NIF values discussed above entail $\nu_{sl} = 4.8 \times 10^{-3}\omega_p$. Thus in a NIF speckle sideloss may limit the effects of trapping, especially in regions where the scattered light has not been amplified from thermal noise up to the seed levels we use in simulations.

To explore the role of sideloss, we reran the base case `BC1` including a Krook operator in the central region ν_{sl} to replicate sideloss. Recall the Krook relaxation rate ν_{Ke} varies with x and still has a large value near the edges to prevent plasma-wave reflections. Whereas in `BC1` we set $v_{Ke} = 0$ in the central region, we now set it to a nonzero value ν_{sl}. Figure 3.7.4 displays for different ν_{sl} the time-averaged R_{av} from shortly before SRS begins until the run end, while Fig. 3-38 shows $R(t)$ for ν_{sl} near the cutoff in R_{av}. The reflectivity R remains temporally erratic and high up to the

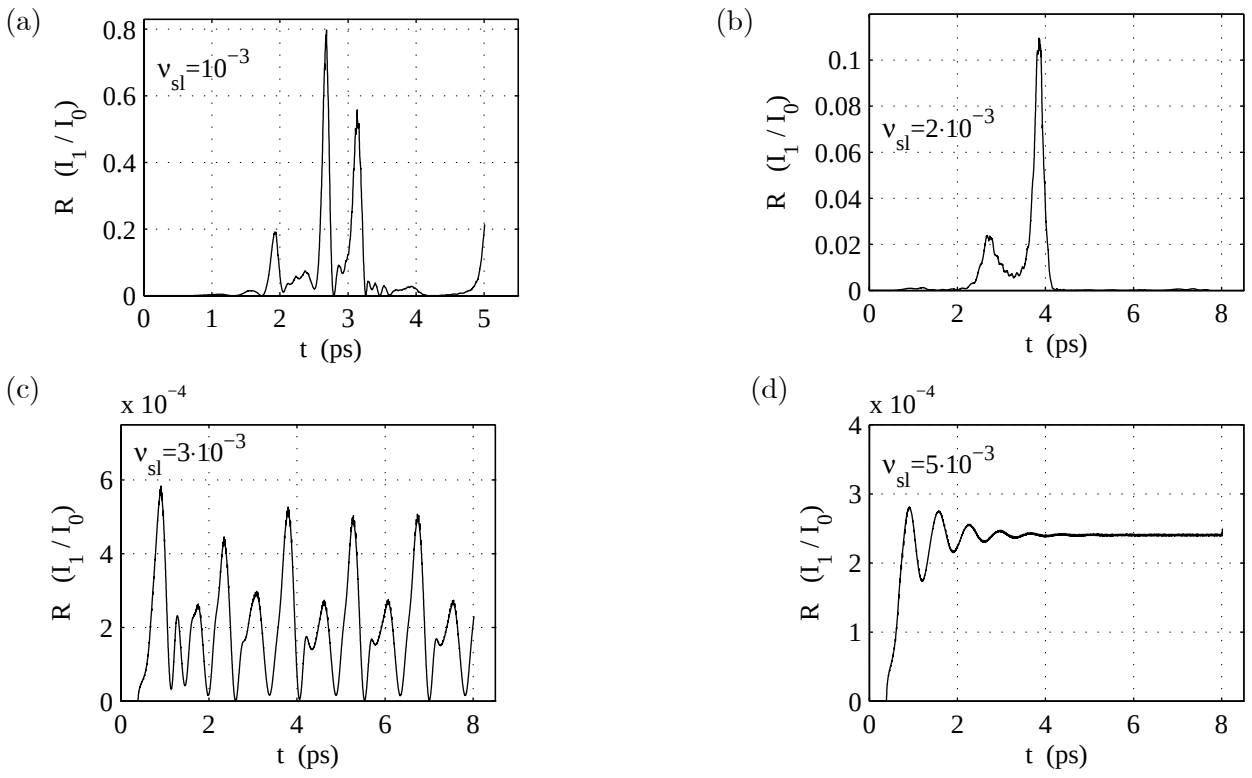

Figure 3-38: Reflectivity for reruns of `BC1` with various sideloss rates ν_{sl}.

cutoff $\nu_{sl} \approx 2 \times 10^{-3}\omega_p$, within the range of $\nu_{sl,0}$ and $\nu_{sl,\mathrm{a}}$ calculated above. The solid curve in Fig. 3.7.4 is R from the steady-state coupled-mode gain rate. The damping rate $\nu \approx \nu_{LD} + \nu_{sl}/2$ (ν_{LD} is the Landau damping rate) is calculated from the linearized kinetic equation including a Krook operator (see p. A.2.1). Since $\nu_{sl} \ll \nu_2 = 0.0380\omega_p$ for the simulations performed, sideloss minorly reduces R. It is reassuring that R approaches the coupled-mode value for strong sideloss. In principle sideloss decreases the resulting steady-sate $\hat{n}$ and lowers the ν_{sl} needed to interfere with trapping; for these parameters this effect is small and we neglect it.

Chapter 4

Trapping Effects in Electron Plasma Waves

We turn our attention to the behavior of electron plasma waves (EPWs) without collisions when electrons are trapped in the wave's potential well. Trapping greatly reduces the Landau damping of EPWs, and can give rise to undamped modes if no other relaxation (e.g., collisions or sideloss) is included. This leads to a steady-state Berstein-Greene-Kruskal (BGK) mode [94] where the space-averaged distribution has zero slope at the EPW phase velocity. The details of the damping reduction due to trapping were studied as an initial value problem for a free (that is, undriven) wave by O'Neil [18]. Subsequently, Morales and he analyzed the downshift in the wave frequency due to trapping with a similar approach [26].

These effects are crucial to understanding stimulated Raman scattering (SRS). The Landau damping of the EPW in SRS is the main source of damping in ICF hohlraum conditions. As Chap. 3 shows, when trapping reduces Landau damping, the reflectivity increases dramatically. Moreover, the amplitude-dependent frequency downshift introduces a nonlinear detuning into the coupled-mode description of SRS, and can produce temporal oscillations in the reflectivity.

This chapter reviews trapping, and explores the damping reduction and frequency shift with ELVIS simulations. We also consider the plasma waves in a density gradient driven by a fixed external force, which is more appropriate to SRS than free plasma waves. We derive an envelope equation for the steady-state amplitude of driven EPWs, and compare it with ELVIS runs. This allows one to see the role of nonlinear changes in the wave dielectric properties, for instance due to trapping. This work is somewhat a spatial analog to the study of time evolution of plasma waves driven in a homogeneous plasma done in [25]. We include inhomogeneity so that contact can be made in Chap. 5 with simulations of SRS in a density gradient.

4.1 Trapping overview

Let us first orient ourselves to the physics of trapping. Consider a monochromatic traveling wave, described in the lab frame by an electric field $E = E_0 \sin(kx_L - \omega t)$. The electron density perturbation associated with E is $n_1 = -(\varepsilon_0 k/e)E_0 \cos(kx_L - \omega t)$, and the total electron density $n_e = n_0(1 - \hat{n}\cos(kx_L - \omega t))$ where $\hat{n} \equiv (\varepsilon_0 k/n_0 e)E_0$ is the unitless amplitude. In the wave frame

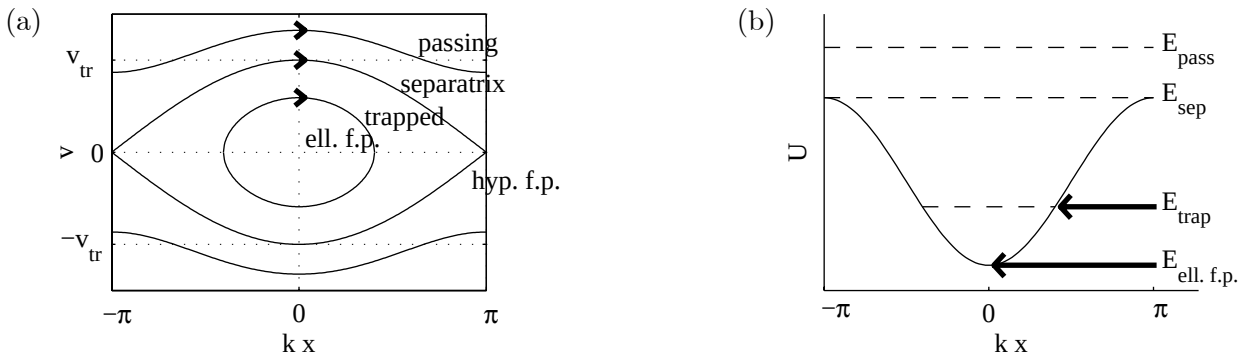

Figure 4-1: Wave-frame (a) phase space and (b) potential energy for electrons in a sinusoidal electric field.

moving with the phase velocity $v_p = \omega/k$, particles experience a sinusoidal force similar to the nonlinear pendulum: $m\ddot{x} = qE_0 \sin(kx)$ (x is the particle's wave frame position). The pendulum is an archetypal nonlinear oscillator and is reviewed in many books on classical mechanics and dynamical systems (such as [95] p. 25 or [96]). The phase space divides into *trapped* particles, which lack enough energy to escape the potential well, and *untrapped* or *passing* particles which have enough energy. Trapped and passing orbits correspond to oscillatory and rotary ("over-the-top") motion of the pendulum, respectively. The two populations are separated by the separatrix orbits corresponding to a pendulum started from almost the vertical position with an arbitrarily small push. We use the term "resonant" for particles which interact strong with the wave and whose orbits differ significantly from straight lines. The set of resonant particles contains all the trapped particles, as well as the barely passing ones near the separatrix.

All orbits are periodic, although the periods vary. Every orbit crosses the point of minimum potential energy, so we can characterize an orbit by its velocity there, v_0. The deeply trapped particles, for which the linearization $m\ddot{x} \approx qE_0kx$ is valid, oscillate with the *bounce frequency* ω_B, which is independent of v_0:

$$\omega_B \equiv \left|\frac{qE_0k}{m}\right|^{1/2} = \omega_p\hat{n}^{1/2}. \tag{4.1}$$

We also use the bounce period $\tau_B \equiv 2\pi/\omega_B$. Some EPW and trapping formulas are given in the thesis preamble. Note that ω_B is typically much smaller than ω_p and that $\omega_B = \omega_p$ corresponds to $\hat{n} = 1$, Dawson's cold nonrelativistic wavebreaking limit [90]. As we increase $|v_0|$, the oscillations become larger and the frequency nonlinearly decreases. Particles on the separatrix take an infinite amount of time to complete one orbit, so their frequency is formally zero. Passing particles outside the separatrix have periods which decrease with $|v_0|$, ultimately approaching $\lambda/|v_0|$ for highly-passing particles that have approximately straight-line orbits.

Consider electrons in particular: $q = -e < 0$ and take $E_0 > 0$. The potential energy $U = -(eE_0/k)\cos kx$ has its minimum at $x = 0$. $(x, v) = (0, 0)$ is the stable elliptic fixed point. The other fixed point, the unstable hyperbolic one, is at $(x, v) = (\pi/k, 0)$. Conservation of energy states $W(x, v) = (m/2)v^2 - (eE_0/k)\cos kx$ is constant. The separatrix connects $(x, v) = (0, v_{tr})$ with $(\pi/k, 0)$ where v_{tr} is the phase-space island half-width. Equating $W(0, v_{tr}) = W(\pi/k, 0)$ gives

$$v_{tr} = 2\left|\frac{eE_0}{mk}\right|^{1/2} = 2\left|\frac{\omega_p}{k}\right|\hat{n}^{1/2}. \tag{4.2}$$

Note that it is defined with a factor of 2 and is *half* the width of full phase-space island. Figure 4-1 displays the wave-frame phase space and potential energy for electrons in the sinusoidal electric field described above.

4.2 Landau damping reduction by trapping

O'Neil [18] solved for the amplitude evolution of an EPW when trapping is important, and found that the linear Landau damping shuts off as the resonant particles undergo bounce motion. This analysis is valid as long as $\omega_B \gg \nu_L$ where ν_L is the linear Landau damping rate. In addition the wave amplitude cannot be so large that the trapping region extends into the bulk and $f(v)$ cannot be linearized about v_p. O'Neil considered the initial value problem of a homogeneous, Maxwellian plasma with a sinusoidal density perturbation. The plasma is then left to evolve by itself, with no external forces acting on it. We call such a wave a "free" wave. O'Neil solves for the evolution of f along characteristics (that is, the particle orbits), assuming that the wave amplitude remains constant. This is valid as long as trapping eliminates Landau damping before the wave has damped appreciably, which we quantify below. Given $f(t)$ one can find the plasma kinetic energy. By invoking conservation of total (kinetic plus electric) energy we determine the instantaneous damping rate $\nu(t)$, which is defined by

$$\hat{n} = \hat{n}_I \exp[-\int_0^t dt\ \nu(t)], \tag{4.3}$$

where $\hat{n}_I$ is the initial wave amplitude.

This calculation yields the contributions to $\nu(t) = \nu_U(t) + \nu_T(t)$ from the trapped (ν_T) and barely untrapped (ν_U) particles [18], Eq. (31):

$$\nu_U = \sum_{n=0}^{\infty} \nu_{Un}, \qquad \nu_{Un}/\nu_L = 128n\pi \int_0^1 d\kappa \frac{\sin\left(\frac{\pi n}{\kappa K}\omega_B t\right)}{\kappa^5 K^2 \cdot (1+q^{2n})(1+q^{-2n})}; \tag{4.4}$$

$$\nu_T = \sum_{n=0}^{\infty} \nu_{Tn}, \qquad \nu_{Tn}/\nu_L = 64\pi(2n+1) \int_0^1 d\kappa \frac{\kappa \sin\left(\frac{\pi(2n+1)}{2K}\omega_B t\right)}{K^2 \cdot (1+q^{2n+1})(1+q^{-2n-1})}. \tag{4.5}$$

ν_L is the linear Landau damping rate. $K = K(\kappa^2)$ is the complete elliptic integral of the first kind (using the notation of [2], Chap. 17). $q = \exp(\pi K'/K)$ and $K' = K(1-\kappa^2)$ and κ is the modulus (referred to as k in [2]). In the above equations κ is a unitless integration variable. Each ν_{Tn} and ν_{Un} phase mixes to zero after $\omega_B t$ goes through a few periods (ν_{U1} diverges at $\kappa = 0$ and must be numerically handled with care). Figure 4-2 shows ν_T, ν_U, and the total ν versus t/τ_B. The untrapped particles provide the damping early in time, but ν_U rapidly phase-mixes to zero after a bounce period. The trapped contribution oscillates around zero and switches between damping to growth before phase-mixing away. For $t \gg \tau_B$ the theory predicts the wave amplitude becomes constant. The specific background distribution enters only in determining the linear damping ν_L, which may be positive (damping) or negative (growth) if $f_0'(v_p)$ is negative or positive, respectively. Note that ν/ν_L depends only on t/τ_B. We can form time-integral of ν in Eq. (4.3) to find $\hat{n}(t)$,

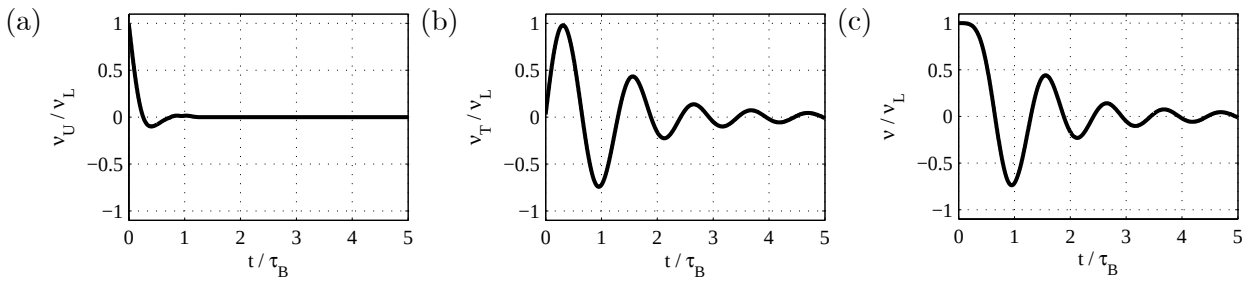

Figure 4-2: ν_U (a), ν_T (b), and ν (c) from O'Neil's calculation.

also given in [18], Eq. (32):

$$\hat{n} = \hat{n}_I \exp\left[-\nu_L \tau_B \beta(\omega_B t)\right], \tag{4.6}$$

$$\beta \equiv \sum_n (\beta_{Un} + \beta_{Tn}), \tag{4.7}$$

where β is a unitless function and

$$\beta_{Un} = \int_0^t dt' \, \frac{\nu_{Un}(t')}{\tau_B \nu_L} = \frac{64}{\pi} \tau_B \int_0^1 d\kappa \frac{1 - \cos\left(\frac{\pi n}{\kappa K} \omega_B t\right)}{\kappa^4 K \cdot (1 + q^{2n})(1 + q^{-2n})}; \tag{4.8}$$

$$\beta_{Tn} = \int_0^t dt' \, \frac{\nu_{Un}(t')}{\tau_B \nu_L} = \frac{64}{\pi} \tau_B \int_0^1 d\kappa \frac{1 - \cos\left(\frac{\pi(2n+1)}{2K} \omega_B t\right)}{K \cdot (1 + q^{2n+1})(1 + q^{-2n-1})}. \tag{4.9}$$

The amplitude depends on not just the scaled time $\omega_B t$ but also on $\nu_L \tau_B$.

The physical picture of the time-dependent damping for $f_0'(v_p) < 0$ is as follows. Initially, the passing particles gain kinetic energy due to the wave field, and ν_U dominates the total damping rate ν. After $t = \tau_B$, the passing particles' kinetic energy is roughly constant, and they make no contribution to the damping: $\nu_U \to 0$. Consider now the trapped particles of a given energy, which in the wave frame form an ellipse in phase space centered on the elliptic fixed point. This "Ferris wheel" rotates at ω_B and carries particles with low lab-frame speeds to high speed, and vice-versa. If $f_0'(v_p) < 0$, there are initially more low-speed than high-speed particles. The rotation gives a net increase to the trapped particles' lab-frame kinetic energy. It takes a time of order τ_B for this process to start, and thus ν_T is zero for $t \ll \tau_B$. Once the low-energy particles reach the top, they begin to lose kinetic energy, which is given back to the wave. Because trapped particles of different energy have different rotation frequencies, eventually the energy exchange ceases due to phase mixing, and the wave reaches a steady state. The space-averaged f near v_p is flat, so that Landau damping no longer occurs.

O'Neil's calculation assumes the wave amplitude is constant for solving the orbits, and is only valid if the wave amplitude changes very little. As the wave damps, ω_B decreases, and it takes longer for resonant particles to bounce. If the damping is strong enough, the resonant particles never bounce before the wave decays. We roughly quantify this by observing in Fig. 4-2(c) that ν decreases to about $\nu_L/2$ when $t \approx \tau_B/2$. Since the damping is provided mainly by trapped particles at this time, we interpret this to mean the damping is significantly reduced once trapped particles have gone through half a bounce cycle, or a "bounce phase" of $\omega_B t = \pi$. The time T when this

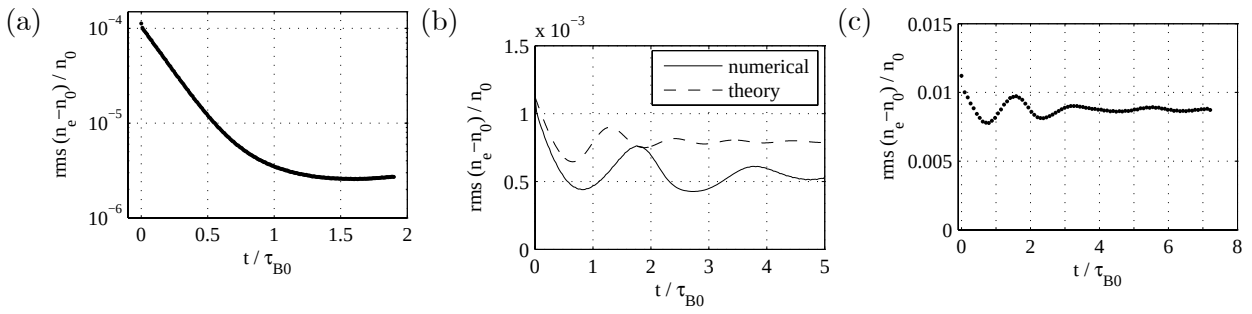

Figure 4-3: rms($\hat{n}$) at one gridpoint for $k\lambda_D = 0.28$ and (a) $\hat{n}_0 = 10^{-4}$, (b) $\hat{n}_{10} = 10^{-3}$ including calculation from Eq. (4.6), and (c) $\hat{n}_{10} = 0.01$.

happens can be found in terms of the instantaneous ω_B:

$$\int_0^T dt\ \omega_B\left(\hat{n}(t)\right) = \pi. \tag{4.10}$$

The wave amplitude decays as $\hat{n} = \hat{n}_I \exp(-\nu_L t)$ during the linear phase, giving

$$T = -\frac{1}{\nu_L}\log\left(1 - \frac{\pi\nu_L}{\omega_{B0}}\right). \tag{4.11}$$

$T = \infty$ if $\omega_{B0} = \pi\nu_L$, giving $\hat{n} < \hat{n}_{\rm thr} \equiv \pi^2(\nu_L/\omega_p)^2$ as the condition for trapping to not affect Landau damping. $\hat{n}_{\rm thr} = 0$ for $k\lambda_D = 0$ and increases rapidly with $k\lambda_D$. For $\omega_{B0} \gg \gamma_L$ we expand the log and find $T \approx \tau_B/2$, as expected.

Sugihara and Kamimura performed a more detailed calculation of the amplitude evolution of an EPW, including simulations of the distribution of resonant particles [97]. Their analysis covers values of $q \equiv \nu_L/\omega_B$ ranging from large (linear Landau damping) to small (O'Neil's theory). They show that for $q < 0.77$ the trapping causes the amplitude to rebound to at least a fraction of its initial level after a period of damping. For $q \approx 0.77$, the wave damps until it reaches a small, constant amplitude; there is no rebounding, although Landau damping stops. For $q > 0.77$ the wave damps continually, although the damping rate is less than the Landau value until $q \gtrsim 3$. Our rough estimate above gives the transition for when trapping occurs as $q = 1/\pi = 0.32$, which is somewhat less than the 0.77 from the Sugihara analysis.

ELVIS simulations of a periodic, electrostatic plasma (no light waves) validate the O'Neil theory. The plasma initially has a Maxwellian f_0,and a density $n = n_0(1+\hat{n}\sin kx)$ with a wavelength equal to the box size. This produces a standing wave, or right- and left-traveling waves at the same ω and $|k|$. As long as the trapping regions of the two waves do not overlap they should not substantially interfere with each other. Figure 4-3 presents results for $k\lambda_D = 0.28$ (which has $\nu_L/\omega_p = 7.11\times10^{-3}$ and $\hat{n}_{\rm thr} = 4.99 \times 10^{-4}$). Panel (a) shows the rms density perturbation amplitude for $\hat{n} = 10^{-4}$ ($q = 0.711$) decaying exponentially in time until it reaches a low level. Since this is near the critical $q = 0.77$ we do not expect, trapping to give a substantial rebound. A generic feature of this type of simulation is a rapid loss of wave energy during the first wave period or two due to phase-mixing of initial conditions. This appears as a slightly enhanced drop-off in the wave amplitude for the first two points of Fig. 4-3(a) and especially (c). The wave amplitudes for $\hat{n} = 10^{-3}$ and 0.01 ($q = 0.225, 0.0711$) shown in Fig. 4-3(b, c) demonstrate the predicted rebounding and approach to steady state. In both cases the wave loses some energy before rebounding. Panel (b) includes

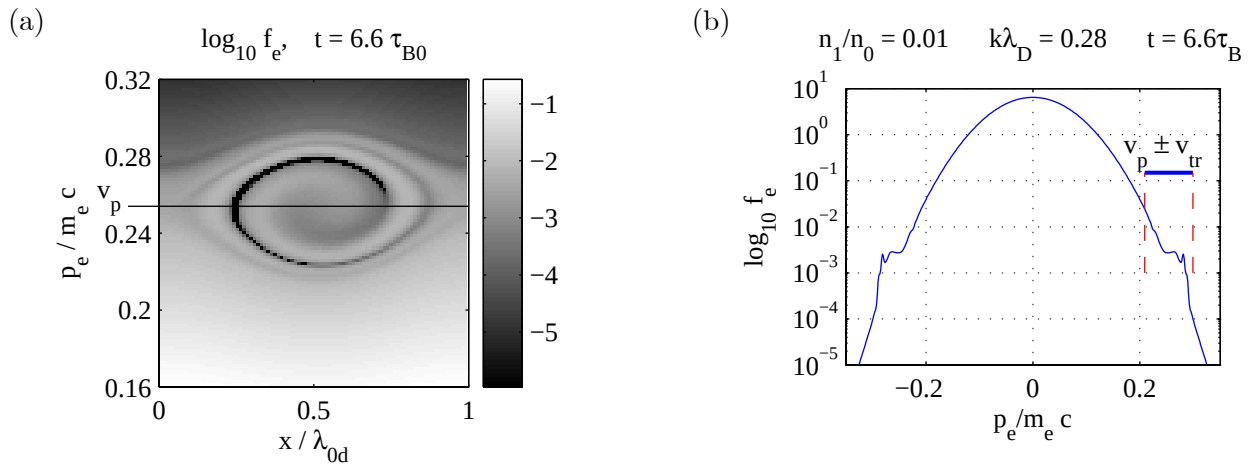

Figure 4-4: (a) f_e at $t = 6.6\tau_B$ for $k\lambda_D = 0.28$, $n_1/n_0 = 0.01$ run. (b) space-averaged f_e.

the theoretical amplitude from Eq. (4.6). This is higher than the numerical result since it was calculated for particle orbits in a constant $\hat{n}$. The electron distribution f shows a phase-space vortex and flattening of the space-averaged f. Figure 4-4 depicts this for the $\hat{n} = 0.01$ case when the wave has gone through several bounce periods ($t = 6.6\tau_B$).

Several experiments corroborate O'Neil's calculation of the amplitude oscillation. For a review of these papers, as well as other work on large-amplitude plasma waves (and other parametric processes) see [98]. Rather than mimic the initial value problem, most experiments study the boundary value problem and excite the wave at a specific location for all time. One observes the wave amplitude and thereby the spatial damping rate σ as a function of $k_B x$. This relates to the initial value problem calculation by $\sigma(k_B x) = |\nu(\omega_B t)/v_g|$ where the bounce wavenumber $k_B \equiv \omega_B/v_p$. The first experiments by Malmberg and Wharton [99] excited an EPW traveling along the background B field in a magnetized plasma column and found oscillation of the amplitude with $k_B x$ instead of linear damping. Later work by the same group [100] measured sidebands of the main EPW at $\omega_p \pm \omega_B$ and found the resonant electrons' kinetic energy profile in space was 180° out of phase in space with the wave amplitude, indicating energy exchange between the trapped particles and wave.

The damping rate calculation of this section, as well as the following one of the frequency shift, neglect collisions. As discussed in Sec. 3.7, collision terms, such as a Krook or Vedenov operator, provide a residual, amplitude-dependent damping rate if the collisions are "weak" compared to bouncing (the precise conditions are given in Sec. 3.7). If collisions (or other relaxation mechanisms such as speckle sideloss) distort the trapped particle motion before they can complete a bounce orbit, then collisions are "strong" compared to trapping. Linear theory including collisions then applies, with a small correction due to trapping.

4.3 Nonlinear frequency shift

When resonant electrons get trapped in a plasma wave, the normal-mode frequency is reduced. There are numerous calculations of the downshift [26, 60, 101–104]. Although they differ in their details, they share some general features. For instance, the downshift scales as the square root

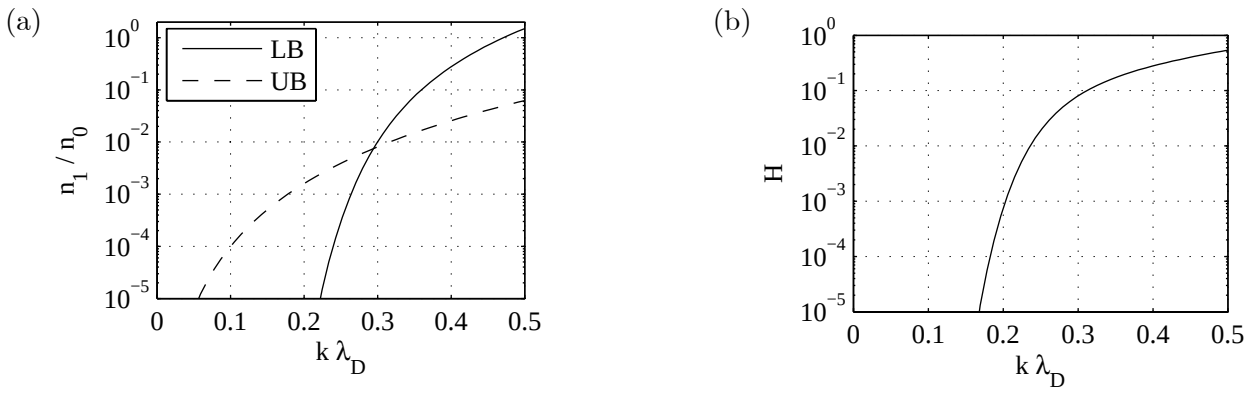

Figure 4-5: (a) Lower bound ($\omega_{B0} > 7.98\nu$) for trapping to occur and upper bound ($n_1/n_0 \ll (k\lambda_D)^4$) for validity of Morales' frequency shift. (b) $H(k\lambda_{De})$ showing $k\lambda_{De}$ dependence of Morales' result.

of the wave amplitude and is proportional to $f_0''(v_p)$. For a Maxwellian f_0 this entails a negative frequency shift. This section compares these scalings with the results of ELVIS simulations of a "free" plasma wave.

There is an upper bound on the wave amplitude for which analytic theories of the frequency shift applies. Calculations such as that of Morales [26] expand $f_0(v)$ about v_p in a Taylor series over the resonant region, given by $v = v_p \pm v_{tr}$. This expansion is valid if the first term $\sim f'$ is much greater than the second term $\sim f''$. This is the case as long as $|f_0'| \gg (v_{tr}/2)\ |f_0''|$. For a Maxwellian with $v_p \gg v_T$ this holds if $v_{tr}v_p \ll 2v_T^2$, or equivalently if $\hat{n} \ll (k\lambda_D)^4$. This bounds $\hat{n}$ from above, while the $T < 1/\nu$ criterion (electrons bounce before wave damps) bounds it from below. We thus have a range of $\hat{n}$ for each $k\lambda_D$ where there is a downshift, and the analytic theory applies. In practice, the lower bound is more stringent: there is no frequency shift, and indeed no steady-state wave, if the damping is too strong. The upper bound merely shows where the analytic estimates start to fail, although the downshift still occurs at these amplitudes. Figure 4-5 presents the lower bound for trapping to set in and the upper bound for the Taylor expansion to be valid.

Morales' result for the frequency shift $\delta\omega(t) = \omega(t) - \omega_L$ is

$$\frac{\delta\omega\,(t)}{\omega_p} = \hat{n}^{1/2} H\,(k\lambda_D)\, g\,(\omega_B t)\,, \tag{4.12}$$

$$H\,(k\lambda_D) = -N_H \left(\frac{\omega_p}{k}\right)^3 \frac{\hat{f}_0''}{\omega_L \partial\varepsilon_r/\partial\omega_L}. \tag{4.13}$$

$g(\omega_B t)$ oscillates with a period roughly half τ_B; $g(0) = 0$ and $g(\omega_B t \gg 1) = 1$. N_H is a pure number, which Morales finds to be an integral over elliptic functions with the value 1.645 (1.411 of which comes from trapped particles, 0.235 of which from nearly-trapped but passing particles). These numerical values were computed by the author and are very slightly different from Morales. Other workers have found different values of N_H, of order unity. For a Maxwellian,

$$H_{\rm mxw}\,(k\lambda_D) = \frac{2N_H}{\sqrt{\pi}} \frac{2\zeta^2 - 1}{Z_r''\,(\zeta)} e^{-\zeta^2} \qquad (f_0 \text{ Maxwellian}). \tag{4.14}$$

Note H is negative, so ω downshifts from its linear value over time.

A frequency shift is appropriate to an initial-value problem, while a boundary-value problem

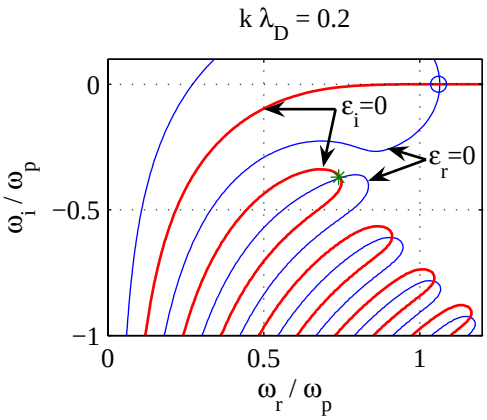

Figure 4-6: Zero contours $\epsilon_r = 0$ (thin blue) and $\epsilon_i = 0$ (thick red) for Vlasov dispersion relation and $K = 0.2$.

entails a wavenumber shift. The permittivity $\hat{\varepsilon}$ can be expressed as a linear part ε_L plus a small nonlinear correction $\delta\varepsilon$: $\hat{\varepsilon} = \varepsilon_L + \delta\varepsilon$. The linear frequency ω_L satisfies $\varepsilon_L(\omega_L) = 0$. Setting $\hat{\varepsilon}(\omega_L + \delta\omega) = 0$ and Taylor expanding gives $\delta\omega = -\delta\varepsilon/(\partial\varepsilon_L/\partial\omega_L)$. An analogous calculation for the nonlinear wavenumber $k = k_L + \delta k$ yields $\delta k = -\delta\varepsilon/(\partial\varepsilon_L/\partial k_L)$. We can relate the two shifts by $\delta k = -\delta\omega/v_g$ where the group velocity $v_g = -(\partial\varepsilon_L/\partial k_L)/(\partial\varepsilon_L/\partial\omega_L)$.

4.4 Natural and $\varepsilon_r = 0$ EPWs

This section discusses some aspects of linear EPWs. The linear dispersion relation, as calculated by Landau for the initial value problem [105], is $\varepsilon = 1 + \chi = 0$ where χ is given in the preamble and Sec. 2.5 for a Vlasov (kinetic, collisionless) description. It is common for weakly-damped modes to write $\varepsilon = \varepsilon_r + i\varepsilon_i$ where (ε_r, ε_i) are (real, imaginary) for real arguments. With a Maxwellian background f_e, we have $\chi = -1/(2K^2)Z'(\zeta)$. $K = k\lambda_D$, $\Omega = \omega/\omega_p$, $\zeta = \Omega/(K\sqrt{2})$, and Z is the plasma dispersion function. There has been recent discussion about the small-amplitude or "linear" limits of nonlinear theories of plasma waves which include trapping [7] and also a Krook relaxation term [60]. The first paper (without Krook) finds that the linear limit gives undamped waves with real k and ω that satisfy the real part of the dispersion relation, $\varepsilon_r = 0$. Phase-space "holes" form in the perturbed distribution near the phase velocity due to trapped particles, eliminating the damping. The second paper (with Krook) carefully considers the joint limit of small wave amplitude $\hat{n}$ and small relaxation ν ([60], p. 4789). The authors expand ε in powers of ν for finite $\hat{n}$, retain the leading-order term in ν, and then take the limit $\hat{n} \to 0$. This gives $\varepsilon_r(k,\omega) = 0$, as in [7], while ε_i and thus the damping vanish linearly with $\hat{n}$. The opposite procedure of expanding $\varepsilon(\hat{n} = 0)$ for small ν is shown to yield the usual Landau damping.

Here we study the results of these two approaches, and compare them to the acoustic features seen in SRS simulations from Chap. 3. We distinguish between a "natural mode," for which $\varepsilon(k,\omega) = 0$ where k and ω may be complex, and what we term an "$\varepsilon_r = 0$ mode," where $\varepsilon_r(k,\omega) = 0$, and k and ω are real. First we take natural modes. One can either find complex ω for real k, appropriate to an initial-value problem, or complex k for real ω, appropriate to a boundary-value or steady-state problem (such as the steady-state response to a drive). For illustrative purposes we find complex ω for real k. There are an infinite number of natural modes satisfying $\varepsilon = 0$; for a

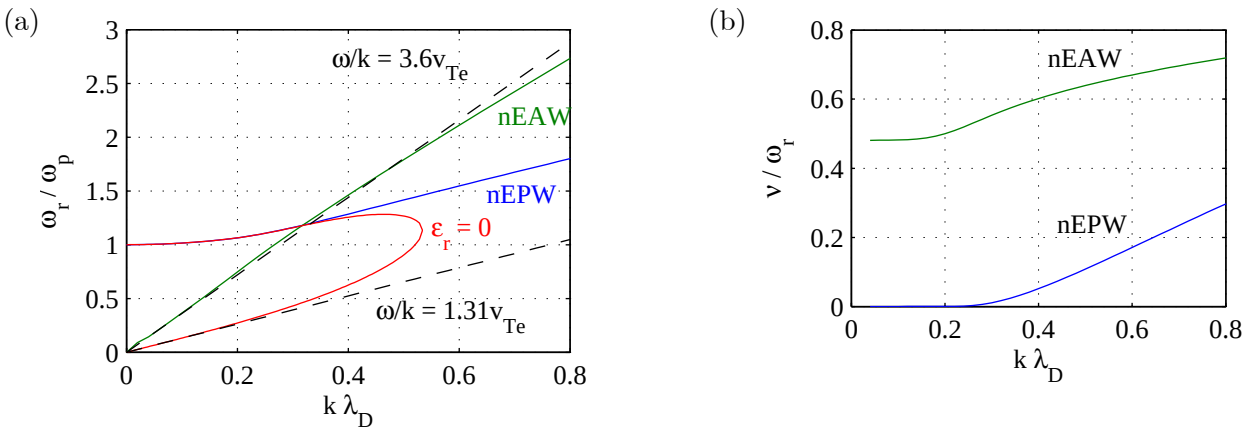

Figure 4-7: (a) Dispersion curves for the real parts of the natural modes $\epsilon = 0$, and the $\epsilon_r = 0$ modes. The solid blue, dashed green, and solid red curves are for the natural EPWs ("nEPW"), natural electron acoustic waves ("nEAW"), and the $\varepsilon_r = 0$ modes, respectively. (b) Relative damping rates for nEPW and nEAW natural modes.

Maxwellian f_e all modes are stable, with $\omega_i < 0$. The most weakly-damped root is the traditional EPW, while the rest are strongly damped [3]. Figure 4-6 displays the contours of $\varepsilon_r = 0$ and $\varepsilon_i = 0$ in the complex ω plane for $K = 0.2$. The intersections are the roots of $\varepsilon = 0$. We see the weakly-damped EPW, indicated by the circle at $\Omega = 1.06$, and a series of strongly-damped roots. We call the least damped of this series the natural electron acoustic wave (EAW) and mark it with a star. This natural EAW has an acoustic dispersion $\Omega = 3.6K$ (calculated numerically) and is still heavily damped.

Following the standard logic for weakly-damped natural modes, we assume $|\omega_i| \ll |\omega_r|$ and $|\varepsilon_i| \ll |\varepsilon_r|$. A weakly-damped natural mode thus approximately satisfies $\varepsilon_r(k_r, \omega_r) = 0$ (the $\varepsilon_r = 0$ dispersion relation) and has a damping rate $\nu = -\omega_i \approx \varepsilon_i / \varepsilon_{r\omega}$ where $\varepsilon_{r\omega} = \partial\varepsilon_r/\partial\omega$. However, the nonlinear calculations of the $\varepsilon_r = 0$ mode described above are not simply the weak-damping limit of linear theory. Figure 4-7(a) displays the natural and $\varepsilon_r = 0$ electrostatic dispersion curves. There are two $\varepsilon_r = 0$ roots for K less than the cutoff $K_c = 0.5337$ and none for $K > K_c$. We cannot use the weakly-damped natural mode approach at all above K_c. The upper root for $K \ll K_c$ corresponds to the traditional EPW ($\Omega^2 \approx 1 + 3K^2$) and is quite close to the natural EPW away from K_c. The lower root is the "$\varepsilon_r = 0$ EAW" ($\omega \approx 1.31K$ for $K \ll 1$) and has a slope less than half that of the natural EAW. This substantial difference is not surprising, since ε_i is not much less than ε_r for the natural EAW but ε_i is neglected when finding the $\varepsilon_r = 0$ EAW. The relative damping rates ν/ω_r are shown in Fig. 4-7(b) for the natural EPWs and natural EAWs. The EAW damping rate is always roughly half its real frequency, making it strongly damped. In periodic, electrostatic ELVIS simulations with an initial density perturbation, designed to produce free plasma waves, it is very difficult to see any spectral content other than the natural EPW, such as either natural or $\varepsilon_r = 0$ EAWs. In this undriven problem, all the heavily Landau damped roots phase-mix away in the first several plasma periods.

The SRS simulations of Chap. 3 with large-amplitude EPWs show acoustic ($k \propto \omega$) features in the $E_x(k, \omega)$ spectra, which are close to the natural and $\varepsilon_r = 0$ EAWs of this section. Figure 4-8 presents the E_x spectrum for run `BC1`, along with the natural ($V_p \equiv \Omega/K = 3.6$) and $\varepsilon_r = 0$ ($V_p = 1.31$) EAW dispersion curves. As in Chap. 3, the acoustic activity is partially masked over by the strong SRS EPWs for $K = 0.2$ to 0.4; this leads to the vertical streaks for these k, and is

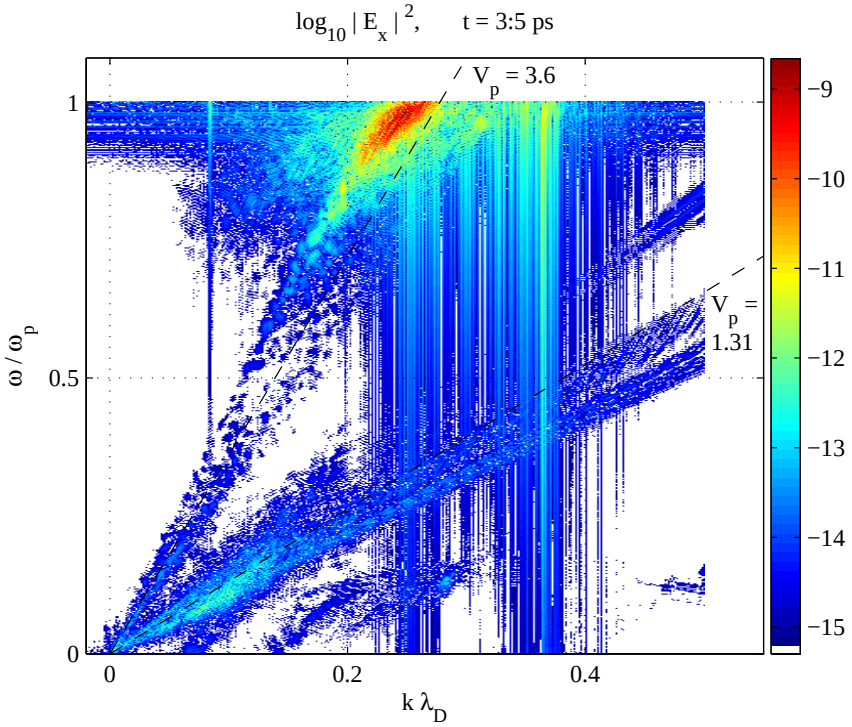

Figure 4-8: $E_x(k,\omega)$ spectrum for run `BC1`. The black dashed lines indicate the natural and $\varepsilon_r = 0$ EAW phase velocities. $V_p = \omega/(kv_{Te})$.

due to the method we use to compute Fourier transforms. To mitigate this, in this section we first pass $E_x(t,x)$ through a low-pass filter designed to eliminate signal with $\omega > \omega_p$. Filtering only somewhat reduces the vertical streaks. The low-V_p acoustic activity falls slightly below the $\varepsilon_r = 0$ EAW line, especially where it is strongest around $K \approx 0.1$. The longitudinal mode involved in the possible SEAS from Chap. 3 falls on this curve (see Sec. 3.5). The high-V_p acoustic features roughly coincide with the natural EAW. Both of these EAW dispersion relations apply in the limit of small wave amplitude and near-Maxwellian f_e. Since trapping and flattening occur in these simulations, a linear analysis utilizing the actual f_e instead of a Maxwellian would provide useful insight. This has not yet been carried out.

4.5 Driven plasma waves in a density gradient

Nonlinearity in EPWs can be studied by considering the plasma waves driven by a fixed, external force. This allows one to extract the nonlinear dielectric properties of the plasma due to, for instance, trapping. In this section we derive an envelope equation for a driven plasma wave, that has reached a temporal steady state, in a density gradient. The drive wave is resonant, or matches the local $\varepsilon_r = 0$ plasma wave (in the parlance of the prior section), at one point in space, called the resonance point. Cohen and Kaufman studied the time-evolution analog of this problem [25]. They consider a uniform plasma subject to a non-resonant driving force. The plasma response oscillates as trapping reduces the damping rate and introduces an amplitude-dependent frequency shift. No steady state is reached. With regard to SRS, a model of the nonlinear effects is needed to make analytic progress in understanding the role of trapping. In Chap. 5 we present simulations

of Raman scattering in a density gradient, and use these results to interpret them.

4.5.1 Derivation of the envelope equation

We take a plasma with uniform temperature and background electron density n_B that varies linearly in x: $n_B = n_0(1+X)$, $X = x/L_n$ (X is unitless) and L_n is the density scale length. Without loss of generality, we choose $L_n > 0$. Quantities evaluated at $X = 0$ are denoted with a subscript 0: ω_{p0}, λ_{D0} are the plasma frequency and Debye length at $X = 0$, and let $\Omega \equiv \omega/\omega_{p0}$ and $K \equiv k\lambda_{D0}$. The plasma feels an harmonic driving external force $\tilde{F}_d = F_d \exp i\psi_d + cc$ with phase $\psi_d = (k_d x - \omega_d t)$ which we imagine arises from a driving electron density perturbation: $\tilde{F}_d = -e\nabla\tilde{\phi}_d$, $\nabla^2\tilde{\phi}_d = e\varepsilon_0^{-1} n_d \exp i\psi_d + cc$. For the SRS problem the drive is the ponderomotive force from the beating of two light waves. In principle one could allow k_d to vary slowly in space, but we treat it as constant here. To account for drives propagating up or down the gradient, we allow k_d to have either sign: $k_d = p|k_d|$, $p = \pm 1$.

The internal electron density (excluding the external drive) is $n_e = n_B(x) + [n_1(x,t)\exp i\psi_d + cc]$. We envelope the perturbation with the drive as the carrier wave, but n_d is not included in n_1. We assume the variation of n_1 is slow with respect to the driver k_d and ω_d. Subsection 2.5.2 describes the plasma response in terms of a dielectric operator containing slow space and time evolution of the envelope. Eq. (2.132) with n_1, n_d analogous to n_{in}, n_{ex} yields

$$\varepsilon\left(k_d - i\partial_x, \omega_d + i\partial_t\right) n_1 = -\chi(k_d, \omega_d) n_d. \tag{4.15}$$

$\varepsilon = (1+\chi)$ is the unitless permittivity operator, referred to as $\hat{\varepsilon}$ previously. This equation applies for weakly inhomogeneous plasmas, where the background density varies slowly compared to the driver wavelength. For a collisionless, 1-D Vlasov description, with a density gradient,

$$\chi = (1+X)\chi_0, \qquad \chi_0 = \frac{1}{2K^2} Z'(\zeta). \tag{4.16}$$

$\zeta = \Omega/(K\sqrt{2})$. Note that χ_0 and ζ have no explicit dependence on x, although they may have implicit dependence if K varies with x (this is not the case in this section, but it is in the full SRS problem discussed in Chap. 5).

We now find the steady state solution to Eq. (4.15). ELVIS simulations below show the driven plasma wave amplitude becomes relatively steady. We drop the slow ∂_t evolution from ε. As in the derivation of the CMEs in Subsec. 2.5.2, we expand ε for slow ∂_x:

$$\varepsilon\left(k_d - id_x\right) n_1 \approx \left[\varepsilon - i\varepsilon_k d_x\right] n_1. \tag{4.17}$$

Subscripts on ε denote differentiation: $\varepsilon_k \equiv \partial\varepsilon/\partial k$, $\varepsilon_x \equiv \partial\varepsilon/\partial x$, and so on. A subscript r or i indicates the real part; for instance $\varepsilon_{\omega r} = \partial_\omega \mathrm{Re}[\varepsilon]$. All functions of ε are evaluated at (k_d, ω_d). Plasma-wave nonlinearity can be incorporated through a nonlinear, amplitude-dependent term in ε. For the present ε is the linear, complex, kinetic permittivity. Dividing Eq. (4.15) by $-i\varepsilon_k$ and using the expansion Eq. (4.17) yields

$$\left[d_x + i\varepsilon/\varepsilon_k\right] n_1 = -i\frac{\chi}{\varepsilon_k} n_d. \tag{4.18}$$

Plasma inhomogeneity leads to a spatial variation in ε, which explicitly depends on the density. Assume the drive is resonant at the point $x = 0$, that is, $\varepsilon_r(x = 0) = 0$ and the drive is the $\varepsilon_r = 0$ EPW at that point. The dominant effects of inhomogeneity can be understood if we simplify the spatial dependence of the coefficients following what we call the "linearized spatial variation" (LSV). Inhomogeneity most dramatically affects ε_r (appearing in the second term of Eq. (4.19)) since $\varepsilon_r(x = 0) = 0$, so the linear term in a Taylor series of ε_r about $x = 0$ is not a small correction. However, χ, ε_i, and ε_K are nonzero at $x = 0$ so their spatial variation can be neglected to leading order. The LSV consists of linearizing ε_r about $x = 0$: $\varepsilon \approx \varepsilon_{xr}x + i\varepsilon$; all other coefficients are evaluated at $x = 0$. Letting ε_i vary for long profiles can lead to the unphysical result that ε_i and the damping rate $\nu \sim \varepsilon_i$ become negative. Care must also be used with $\mathrm{Im}[\varepsilon_k]$. For weakly-damped modes $|\varepsilon_{ki}/\varepsilon_{kr}| \ll 1$ and one frequently keeps just ε_{kr}, for instance when finding the wave's group velocity. We shall see below that for $K \gtrsim 0.3$, $\varepsilon_{ki}/\varepsilon_{kr}$ can be significant even though the damping is weak. Including ε_{ki} can lead to unphysical behavior, such as a blow-up of the resulting n_1. The physical significance of ε_{ki} should be explored more in the future. One should be aware of the physical consequences of using the full, complex ε and not simply assume it is more "exact." The ultimate vindication is agreement with numerical solutions of the full Vlasov-Poisson system.

4.5.2 Analytic ODE solution

Define the unitless variables $\hat{n}_1 \equiv n_1/n_{d0}$, $\hat{n}_d = n_d/n_{d0}$ (n_{d0} is a scale for the drive strength), $\bar{L}_n \equiv L_n/\lambda_{D0}$, $\varepsilon_K = \varepsilon_k/\lambda_{D0}$ (note uppercase, unitless K vs. lowercase, dimensional k) and recall $X = x/L_n$. Equation (4.18) becomes

$$\frac{d\hat{n}_1}{dX} + i\bar{L}_n\frac{\varepsilon}{\varepsilon_K}\hat{n}_1 = -i\bar{L}_n\frac{\chi}{\varepsilon_K}\hat{n}_d. \tag{4.19}$$

We can solve the envelope equation Eq. (4.18) by using the LSV approximation. We keep ε complex for now and drop the undesired imaginary terms later. From Eq. (4.16), $\varepsilon_X = \chi$. Equation (4.19) becomes

$$\frac{d\hat{n}_1}{dX} + a(X)\hat{n}_1 = -iC\hat{n}_d, \tag{4.20}$$

where

$$a(X) \equiv iCX - C_I, \tag{4.21}$$

$$C \equiv \bar{L}_n\frac{\chi}{\varepsilon_K}, \qquad C_I \equiv \bar{L}_n\frac{\chi_i}{\varepsilon_K}. \tag{4.22}$$

Note that $C_I \neq \mathrm{Im}[C]$ if $\mathrm{Im}[\varepsilon_K]$ is retained.

Let the drive amplitude n_d have a step function form $\hat{n}_d = \theta(p(X - X_s))$ where $\theta(X) = 0$ for $X < 0$ and $\theta(X) = 1$ otherwise. $X_s = -p|X_s|$ is the "drive start," or point where the drive turns on. Recall $p =$sign(k_d). This representation turns the drive on "upstream" of the resonance point, that is, $X_s < 0$ ($X_s > 0$) for $k_d > 0$ ($k_d < 0$). The boundary condition is that n_1 is zero upstream of where the drive turns on, or $n_1(pX < pX_s) = 0$. Equation (4.20) yields

$$\frac{d\hat{n}_1}{dX} + a(X)\hat{n}_1 = -iC\theta(p(X - X_s)). \tag{4.23}$$

This driven, first-order linear ODE has the solution downstream of X_s (formally, for $pX > pX_2$)

$$\hat{n}_1 = -iCe^{-A(X)} \int_{X_s}^{X} dX' e^{A(X')}; \tag{4.24}$$

$$A(X) = \int^{X} dX'\, a(X') = i\frac{C}{2}X^2 - C_I X. \tag{4.25}$$

Change variables to complete the square in the exponential:

$$\hat{n}_1 = -iqC \left(\frac{2i}{C}\right)^{1/2} e^{u^2(X)} \int_{u_s}^{u(X)} du'\, e^{-u'^2}, \tag{4.26}$$

$$u(X) = q\left(\frac{iC}{2}\right)^{1/2} \left(X + i\frac{\chi_i}{\chi}\right). \tag{4.27}$$

and $u_s = u(X_s)$. $A(X) = u(X)^2$. $q = \pm 1$ and we choose the value that gives a well-behaved $\hat{n}_1$. We can write $\hat{n}_1$ in terms of error functions and ultimately the Faddeeva function (discussed in the thesis preamble):

$$\hat{n}_1 = N_1 w\left(iu\right)\left(1 - g_s\left[u\left(X\right)\right]\right)$$

with

$$N_1 = iqC\left(\frac{i\pi}{2C}\right)^{1/2}, \tag{4.28}$$

$$g_s(u) = e^{u^2 - u_s^2} \frac{w\left(iu_s\right)}{w\left(iu\right)}. \tag{4.29}$$

We now make the usual "weakly-damped wave" approximations. Namely, we replace the complex ε_K with the real ε_{Kr} in C and C_I, and replace the total χ with just χ_r. At the resonance point $x = 0$ we have $\chi_r = -1$ to make $\varepsilon_r = 0$. With these replacements,

$$C = -\frac{L_n}{\varepsilon_K}, \tag{4.30}$$

$$u(X) = q\left(\frac{iC}{2}\right)^{1/2} \left(X - i\chi_i\right). \tag{4.31}$$

The definitions of N_1 and g, and $\hat{n}_1$ in terms of them, are unchanged. To further connect with existing literature, consider the $K(X)$ which locally satisfies $\varepsilon_r(K, X) = 0$. Put $K = K_d + \delta K$ and expand

$$\varepsilon_r(K_d + \delta K, X) \approx \varepsilon_r(K_d, 0) + \varepsilon_{Kr}\delta K + \varepsilon_{Xr} X = 0. \tag{4.32}$$

Solving for δK, we find the unitless detuning or wavenumber mismatch parameter

$$\bar{\kappa}' \equiv \partial_X(\delta K) = -\frac{\varepsilon_{Xr}}{\varepsilon_{Kr}} = -\frac{\chi_r}{\bar{L}_n \varepsilon_{Kr}} = \frac{1}{\bar{L}_n \varepsilon_{Kr}}. \tag{4.33}$$

The dimensional $\kappa' \equiv -\varepsilon_{xr}/\varepsilon_{kr}$ and $\bar{\kappa}' = \lambda_{D0} L_n \kappa'$. Using the fluid limit of ε_r (see the preamble) we approximately have $\varepsilon_{Kr} \approx -6K/\Omega^4$. Although this formula is not quantitatively good, it correctly shows $\mathrm{sign}(\varepsilon_{Kr}) = -p$ (computation of the full derivative, using Z functions, confirms

this). Therefore $\bar{\kappa}' = -p|\bar{\kappa}'|$ and $|\bar{\kappa}'| = 1/(\bar{L}_n|\varepsilon_{Kr}|)$. With all this, we find

$$\hat{n}_1 = N_1 w(iu)\left(1 - g_s\left[u(X)\right]\right), \tag{4.34}$$

$$N_1 = ipq(ip)^{1/2}\left(\frac{\pi}{2}\right)^{1/2}\Lambda, \tag{4.35}$$

$$u(x) = q(-ip)^{1/2}\frac{1}{\sqrt{2}}\Lambda\left(X - i\chi_i\right), \tag{4.36}$$

$$\Lambda \equiv \bar{L}_n\left|\bar{\kappa}'\right|^{1/2} = \left(\frac{\bar{L}_n}{\varepsilon_{Kr}}\right)^{1/2}. \tag{4.37}$$

The unitless parameters Λ and χ_i and choices for p and q completely characterize the solution.

g_s is only important near $X = X_s$. Let $X = -X_s\tau$ where τ varies from -1 to 1 over the region of interest. $\mathrm{Re}[u^2 - u_s^2] = -\Lambda^2\chi_i|X_s|(1+\tau)$. This quantity is ≤ 0 and decreases as τ increases. Therefore, g_s is rapidly attenuated away from the drive start X_s. Numerical examples show the only effect of g_s is to take $\hat{n}_1$ to zero at X_s, since g itself is nonzero there. We can safely drop g_s away from X_s.

4.5.3 The strong damping limit (SDL)

Commonly, the plasma-wave advection is weak compared to its damping: $|dn_1/dx| \ll \sigma|n_1|$. $\sigma = |\,\mathrm{Im}\,k| \approx |\varepsilon_i/\varepsilon_{kr}|$ is the mode's spatial damping rate. In this strong damping limit (SDL), we can drop plasma-wave advection ∂_x from the outset. The original envelope Eq. (4.15) in steady state ($\partial_t = 0$) gives an algebraic equation for n_1 in terms of the local drive:

$$n_1 = -\frac{\chi}{\varepsilon}n_d \qquad \text{(SDL-F)}. \tag{4.38}$$

χ and ε both vary in space, and can be evaluated for arbitrary spatial profiles. We call this solution the "full SDL" (SDL-F). For a linear density gradient, In terms of unitless variables, for a constant n_d, this gives

$$|\hat{n}_1|^2 = \frac{1+\chi_i^2}{\frac{X^2}{(1+X)^2} + \chi_i^2} \qquad \text{(SDL-F)}. \tag{4.39}$$

To compare with the analytic solution Eq. (4.34), calculated for the LSV, we evaluate χ at $x = 0$ and neglect χ_i in the RHS numerator of Eq. (4.38) : $\chi \to -1$. Linearizing ε about the resonance point $\varepsilon \approx \chi_i + \varepsilon_{xr}x$ gives the "linearized SDL" (SDL-L)

$$\hat{n}_1 = \frac{1}{i\chi_i - X} \qquad \text{(SDL-L)}. \tag{4.40}$$

We recover the SDL from the analytic solution when $|u|$ is large. u minimizes at $x = 0$, where $|u| = |\Lambda\chi_i|/\sqrt{2}$. The SDL applies if damping, represented by χ_i, is sufficiently strong. If so, then we can expand $g(u)$ for large u. As discussed above, g_s is negligible away from the drive start. The Faddeeva function $w(z)$ decreases for large z only for certain phases of z; this requirement dictates the choice of q. The leading-order asymptotic expansion for $w(z) \sim i\pi^{-1/2}/z$ holds provided $\arg z$ is outside the interval $[-3\pi/4,\ \pi/4]$. $u = -iz$ gives z outside this interval for $q = -p$. With this choice, expanding $g(u)$ for large u gives Eq. (4.40), the result we obtained by dropping ∂_x from the

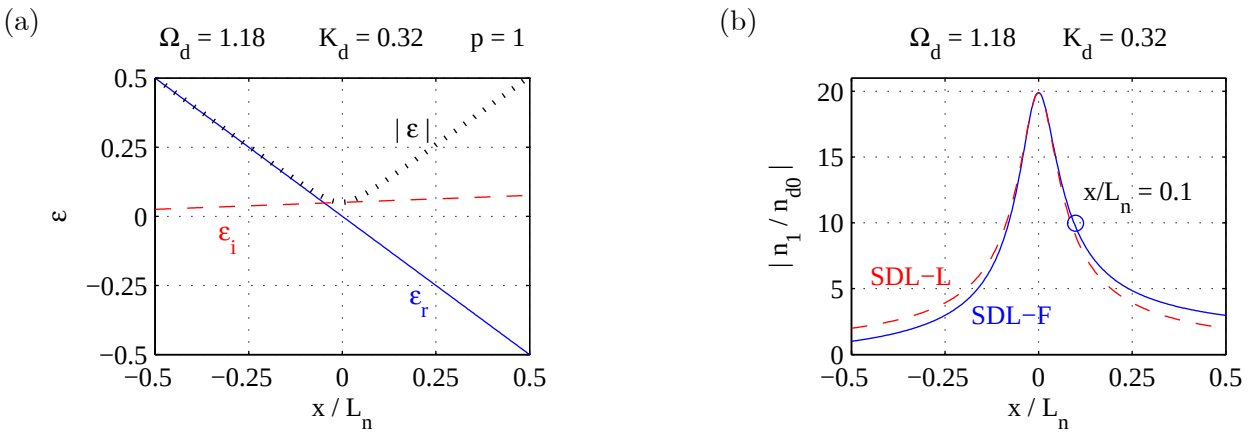

Figure 4-9: (a) Permittivity ϵ vs. x for linear density gradient for $(K_d, \Omega_d, p) = (0.32, 1.18, 1)$. Minimum $\epsilon_i \approx 0.05$. (b) Driven response $|n_1/n_{d0}|$ from the full SDL Eq. (4.38) and linearized SDL Eq. (4.40). Cirlce indicates width at half maximum value ($x/L_n \approx 0.1$).

outset. The amplitude can be expressed in terms of the dimensional x as

$$|\hat{n}_1|^2 = \frac{1}{\chi_i^2} \frac{1}{1 + (x/L_d)^2} \qquad \text{(SDL-L)}. \tag{4.41}$$

$L_d \equiv \chi_i L_n$ is the detuning length over which the amplitude decays, and is much shorter than L_n. This is equivalent to Eq. (4.39) if the $(1 + X)$ factor in the denominator is replaced with 1 and χ_i is neglected in the numerator.

4.5.4 Numerical examples

Let us take a numerical example: $\Omega_d = 1.18$, $|K_d| = 0.32$, $p = 1$, $q = -1$, and $\bar{L}_n = 2000$. $\varepsilon_r(K_d, \Omega_d, x = 0) = 0$, as required at the resonance point (K_d is the "$\varepsilon_r = 0$ mode" for Ω_d). The corresponding natural mode $\varepsilon(K_{dn}, \Omega_d) = 0$ has $K_{dn} = 0.313 + 0.0138i$. K_d and $\mathrm{Re}[K_{dn}]$ are close, as expected for weakly-damped modes. $\varepsilon_i = 0.0503$, $|\bar{\kappa}'| = 1.92 \times 10^{-4}$, and $\Lambda = 27.7$. From the analytic solution above, we found the SDL is valid for all x when $|\Lambda\chi_i|/\sqrt{2} \gg 1$. For these parameters $|\Lambda\chi_i|/\sqrt{2} = 0.986$, indicating the SDL should be somewhat off for $X < \chi_i$. $\varepsilon_{Kr} = -2.61$ and $\varepsilon_{Ki}/\varepsilon_{Kr} = -0.639$. As mentioned above, ε_{Ki} is not much less than ε_{Kr} when K is not small. The permittivity ε is shown in Fig. 4-9(a). ε_i varies weakly with x. Figure 4-9(b) plots the driven response amplitude in both the full and linearized SDL, Eqs. (4.38) and (4.40), respectively. The peak response occurs at $x = 0$ and is $1/\varepsilon_i(x = 0) = 19.9$, while the drop-off away from resonance is due to inhomogeneity: the drive departs more and more from a natural mode at larger x. The width of the response L_d is much less than L_n, as indicated by the half-width in Fig. 4-9(b) and in Eq. (4.41). The linearized SDL result is higher (lower) than for the full SDL on the (left, right) of the resonance due to the $(1 + X)$ denominator in Eq. (4.39).

The analytic solution Eq. (4.34) departs from the linearized SDL as Λ or χ_i decreases. The intuition is that spatial variation and thus advection become more important relative to damping as the scale length $\bar{L}_n$ (and thereby $\Lambda = |L_n/\varepsilon_{Kr}|^{1/2}$) becomes shorter or as the damping (proportional to χ_i) becomes weaker. Figure 4-10 portrays both solutions for the parameters discussed above. They are close except the peak is shifted slightly away from resonance in the direction of wave

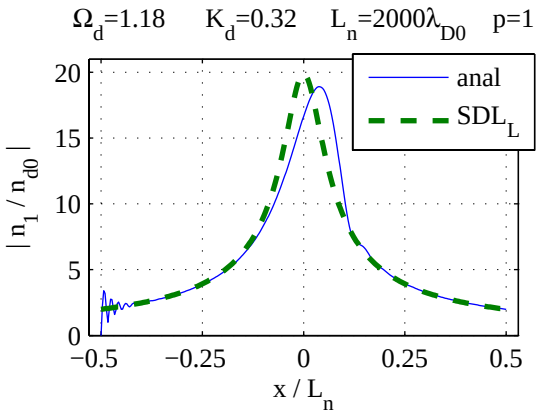

Figure 4-10: Linearized SDL solution Eq. (4.40) and analytic solution Eq. (4.34) for $(\Omega,\ K,\ \bar{L}_n,\ p,\ q) = (1.18,\ 0.32,\ 2000,\ 1,\ -1)$, which give $\chi_i = 0.0503$, $\Lambda = 27.7$.

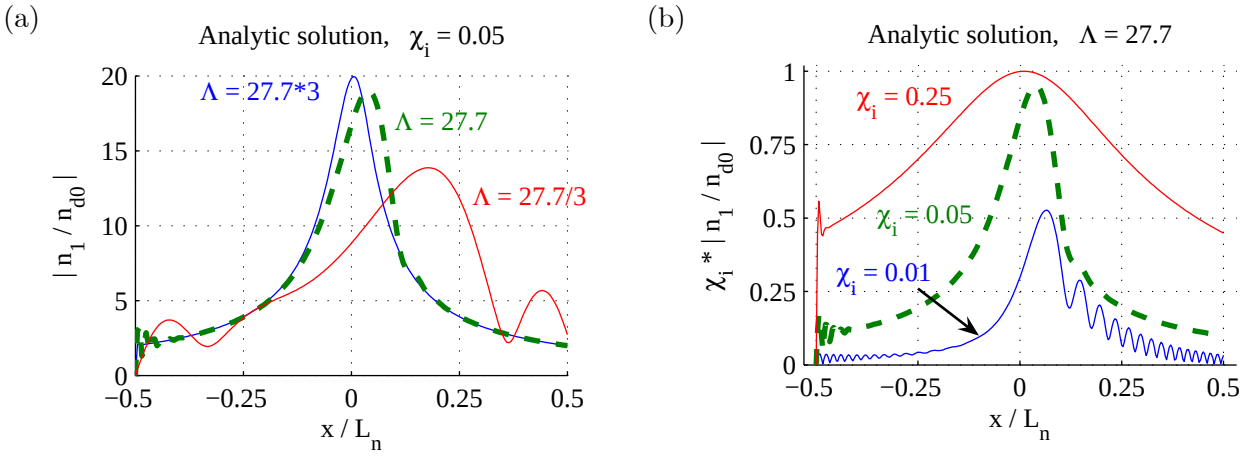

Figure 4-11: Analytic solution Eq.(4.34) for $p = -q = 1$. (a) $|n_1|$ for $\chi_i = 0.05$ and several Λ values, and (b) $\chi_i|n_1|$ for $\Lambda = 51.8$ and several χ_i values.

propagation. The analytic solution drops to zero near the drive start $X_s = -0.5$ due to g_s; without it the analytic solution would match the linearized SDL in this region. Figure (4-11) graphs the driven amplitude for varying Λ and χ_i. The analytic solution develops more oscillations, a lower peak value compared to $1/\chi_i$, and a greater shift of the peak in the direction of wave propagation for lower Λ or χ_i.

To test the goodness of the simplified spatial variation used in the analytic solution, we compare with numerical solutions to the original ODE Eq. (4.19). We retain the full spatial variation of all parameters, except we omit $\mathrm{Im}[\varepsilon_K]$ entirely. As discussed above, this leads to unphysical blow-up of the driven amplitude. Figure 4-12(a) displays the analytic as well as numerical solutions. The main difference is the numerical solution behaves like the full SDL far from resonance, since it accounts for variations in χ_i and ε_{Kr}. The numerical solution for $K = 0.32$ and $K = -0.32$ is shown in Fig. 4-12(b). The peak is always shifted from $x = 0$ in the direction of drive propagation. However, the solution far to the right is always greater than that far to the left, as seen in the full SDL solution Eq. (4.39) which is insensitive to the sign of K.

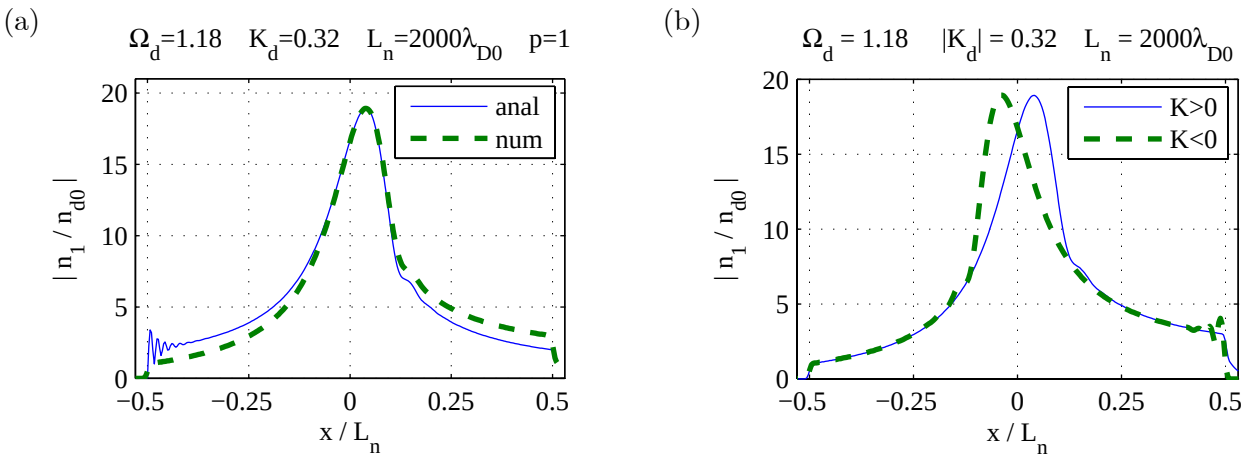

Figure 4-12: (a) Analytic solution Eq. (4.34), and numerical solution to Eq. (4.19) with $\mathrm{Im}[\varepsilon_K] = 0$. (b) Numerical solution for $K = 0.32$ and $K = -0.32$.

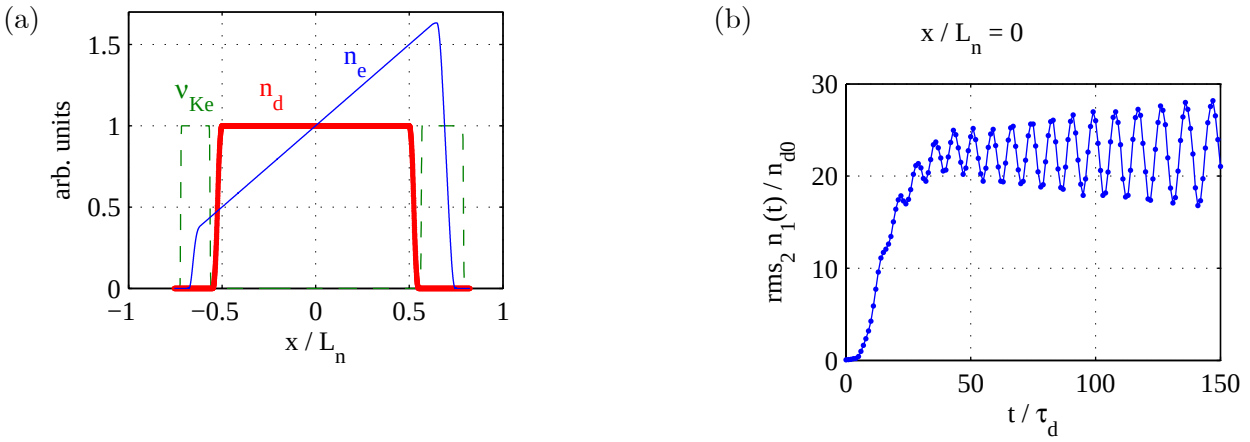

Figure 4-13: (a) Spatial profile of density, driving force, and Krook relaxation rate for run `DRV`. (b) $n_1(t)$ at box center for run `DRV`. $\tau_d \equiv 2\pi/\omega_d$. rms_2 denotes $\sqrt{2}\times$rms.

4.5.5 Vlasov simulations

This subsection examines electrostatic ELVIS simulations of driven plasmons in a density gradient. The plasma conditions are $T_e = 2$ keV and $n_0 = 5 \times 10^{26}$ m^{-3}. As in the prior section, the drive satisfies $\Omega_d = 1.18$ and $|K_d| = 0.32$. The normalized scale length $\bar{L}_n = 2000$. The drive is not quite a step function in space but ramps from zero to one over a few wavelengths. A Krook relaxation operator is included near the profile edges to prevent wave reflection, with a peak relaxation rate $\nu_{Ke} = 0.2\omega_p$. Figure 4-13(a) depicts the spatial profiles.

The run `DRV` utilizes the above-mentioned parameters, a drive strength $n_{d0} = 10^{-5} n_0$ and a drive propagating up the gradient ($p = 1$). $n_1(t)$ at the resonance point is shown in Fig. 4-13(b). It oscillates on a time scale of roughly $8\tau_d$ where $\tau_d \equiv 2\pi/\omega_d$ is the driver period. The response amplitude is centered on a value slightly higher than the steady-state result of $1/\chi_i \approx 20$. "rms_2" denotes the usual rms value is multiplied by $\sqrt{2}$, so that $\mathrm{rms}_2 \sin\omega t = 1$. Figure 4-14 presents the spatial rms of $n_1(x)$ late in time for DRV run with various drive strengths and both directions of drive propagation. For the smallest value of n_{d0} the profile is similar to the numerical ODE

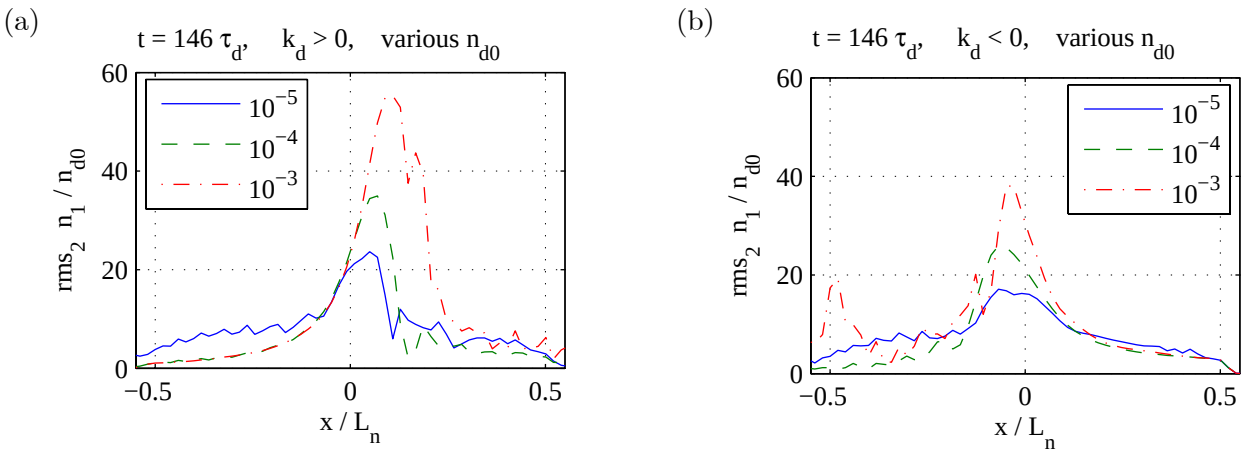

Figure 4-14: Driven EPW amplitude for reruns of `DRV` with various drive strengths n_{d0} and (a, b) $K_d = (0.32, -0.32)$.

solution to Eq. (4.19). As n_{d0} increases, the response level rises above linear theory and becomes more offset in the direction the drive propagates. The rise is greater for $K_d > 0$ than for $K_d < 0$. The trapping-induced nonlinear damping reduction may account for the rise, while the nonlinear shift in the natural k could lead to the directional asymmetry. The differences from linear theory can be interpreted as a nonlinear correction $\delta\varepsilon$ to the dielectric. Given the numerical solution to Eq. (4.19), $\delta\varepsilon$ can be numerically backed out and compared with calculations of Morales-O'Neil or others. This is in the same spirit as Cohen and Kaufman's work [25]. We leave further work along these lines to the future.

Chapter 5

Simulations of SRS from Inhomogeneous Plasmas

This chapter presents simulations and analysis of Raman scattering from an inhomogeneous plasma. As plasma conditions vary, so do the wavenumbers of the natural modes at specified frequencies. This detunes the interaction from resonance, since wavenumber matching can only be satisfied at a point. ELVIS simulations of SRS in a density gradient show that for short enough scale lengths a convective steady state is reached, with SRS gains similar to coupled-mode theory. For longer scale lengths, kinetic enhancement occurs.

There are several sources of inhomogeneity in ICF hohlraums. The density, temperature, and plasma flow speeds vary on length scales of order a millimeter. In addition, the intensity of a laser speckle or hot spot varies in space. The length (along beam propagation) of a diffraction-limited spot is $7.08F^2\lambda_0$, which for $\lambda_0 = 351$ nm and $F = 8$ (considered for NIF) gives 159 μm ([52], p. 25). This gives rise to a spatial variation in the pump strength γ_0. This chapter focuses on a inhomogeneity via a density gradient. In a finite density profile, which goes to zero away from a region of interest, the SRS pump strength goes to zero as well.

5.1 Coupled-mode equations in a density gradient

This section investigates coupled-mode equations (CMEs) for SRS in a density gradient. We first derive the CMEs in one spatial dimension, and then solve them in the strong damping limit (SDL) for linearized spatial variation (the LSV from Sec. 4.5). The SDL solution from Chap. 2 is equivalent. We find the SRS steady-state gain and envelope profiles. We then compare these results to Rosenbluth's calculation with no damping [31].

5.1.1 Derivation of inhomogeneous CMEs

The background density profile $n_B(x) = n_0(1 + h(x))$ where $h(0) = 0$. The density scale length $L_n \equiv n_0(dn/dx)^{-1}$ at $x = 0$, or $L_n = 1/h'(x = 0)$. For a linear gradient, $h = x/L_n$. The resonance or matching point $x = 0$ is where the light waves beat to give a "$\varepsilon_r = 0$" plasma wave (defined precisely below). ω_p and λ_D are the plasma frequency and Debye length in terms of the local

density, while $\omega_{p0} = \omega_p(x=0)$ and $\lambda_{D0} = \lambda_D(x=0)$. In particular, $\omega_p = \omega_{p0}(1+h)^{1/2}$ and $\lambda_D = \lambda_{D0}(1+h)^{-1/2}$. The EMW k's satisfy the local, natural EMW dispersion relation with the corresponding ω, that is, $k_i(x) = (p_i/c)(\omega_i^2 - \omega_p^2)^{1/2}$ for $i = 0, 1$. p_i is the sign of k_i. Following the conventions of Chap. 2, the EPW is driven by the beating of the light waves, and $k_2 = (k_0 - k_1)$. Thus k_2 is not the local EPW corresponding to ω_2.

The SRS coupled-mode equations (CMEs) in one dimension follow from Eqs. (2.86, 2.87) with no damping ($\nu_0 = \nu_1 = 0$) for the EMWs and the kinetic operator Eq. (2.133) for the EPW:

$$\begin{aligned} (\partial_t + v_{g0}\partial_x)\, a_0 &= K a_1 a_2; & (5.1)\\ (\partial_t + v_{g1}\partial_x)\, a_1 &= -K a_0 a_2^*; & (5.2)\\ \varepsilon\,(k_2 - i\partial_x, \omega_2 + i\partial_t, x)\, a_2 &= 2i\frac{\omega_2}{\omega_p^2}\chi\; K a_0 a_1^*. & (5.3) \end{aligned}$$

ε is the unitless permittivity and is called $\hat{\varepsilon}$ elsewhere. We adopt the linearized spatial variation (LSV) to make analytic progress, as described on p. 109. All coefficients in Eqs. (5.1-5.3), besides ε on the LHS of Eq. (5.3), are evaluated at $x = 0$. We seek steady-state solutions ($\partial_t = 0$) and expand ε for slow envelope variation, with $d_x f \equiv df/dx$:

$$\begin{aligned} v_{g0} d_x a_0 &= K a_1 a_2; & (5.4)\\ v_{g1} d_x a_1 &= -K a_0 a_2^*; & (5.5)\\ (\varepsilon - i\varepsilon_k d_x)\, a_2 &= 2i\frac{\omega_2}{\omega_p^2}\chi\; K a_0 a_1^*. & (5.6) \end{aligned}$$

ε and its derivatives $\varepsilon_k \equiv \partial_k \varepsilon$, $\varepsilon_\omega \equiv \partial_\omega \varepsilon$, and $\varepsilon_x \equiv \partial_x \varepsilon$ are evaluated at (k_2, ω_2). A second subscript r or i denotes real or imaginary part: e. g., $\varepsilon_{kr} = \partial_k \varepsilon_r$.

Inhomogeneity enters via ε. We choose $x = 0$ to be the resonance or matching point, where $\varepsilon_r(k_2, \omega_2, 0) = 0$. Taylor expanding about $x = 0$ and neglecting ε_{xi} yields $\varepsilon \approx \varepsilon_i + \varepsilon_{xr} x$. Inserting this into Eq. (5.4) and dividing by $i\varepsilon_{\omega r}$ gives

$$\begin{aligned} \left(v_{g2} d_x + \nu_2 - i\frac{\varepsilon_{xr}}{\varepsilon_{\omega r}} x\right) a_2 &= \left[2\frac{\omega_2}{\omega_p^2}\frac{\chi}{\varepsilon_{\omega r}}\right]\; K a_0 a_1^* & (5.7)\\ &\approx -K a_0 a_1^*. & (5.8) \end{aligned}$$

As defined in the preamble, $\nu_2 = \varepsilon_i/\varepsilon_{\omega r}$ is the time damping rate and $v_{g2} = -\varepsilon_{kr}/\varepsilon_{\omega r}$ is the group velocity. The approximation of the bracketed factor holds for $k_2\lambda_D \ll 1$. It is customary to work with the mismatch parameter $\kappa'(x) \equiv d_x(k_0 - k_1 - k_{2R})$ where k_{2R} is the x-dependent natural EPW that corresponds to ω_2: $\varepsilon_r(k_{2R}, \omega_2, x) = 0$. Let $k_{2R} = k_2 + \delta k$ and expand about $\delta k = x = 0$ to find $\delta k \approx -(\varepsilon_{xr}/\varepsilon_{kr})x$. Since $k_0 - k_1 - k_2 = 0$ by matching, $\kappa' \approx -\varepsilon_{xr}/\varepsilon_{kr}$ and Eq. (5.7) becomes

$$\left(v_{g2} d_x + \nu_2 - i v_{g2}\kappa' x\right) a_2 = -K a_0 a_1^*. \qquad (5.9)$$

As in Chap. 4, we work with normalized wavenumbers $K_i \equiv k_i \lambda_{D0}$ and $\Omega_i \equiv \omega_i/\omega_{p0}$. For the

light waves,

$$K_i = K_{im}\left(1-\frac{\delta_T^2}{K_{im}^2}h\right)^{1/2}, \qquad i=0,1 \text{ (EMW)} \tag{5.10}$$

$$\approx K_{im}\left(1-\frac{\delta_T^2}{2K_{im}^2}h\right), \qquad h \ll 1, \tag{5.11}$$

with

$$K_{im} \equiv p_i \delta_T \left(\Omega_i^2 - 1\right)^{1/2}. \tag{5.12}$$

$\delta_T \equiv v_{Te}/c$. The resulting K_2 is approximately for $h \ll 1$

$$K_2 \approx K_{2m}\left(1+\frac{\delta_T^2}{2K_{0m}K_{1m}}h\right). \tag{5.13}$$

The second term is usually quite small. The EPW susceptibility $\chi = (1-\varepsilon)$ is

$$\chi = -\frac{1+h}{2K_2^2}Z'(\zeta), \qquad \zeta \equiv \frac{\Omega_2}{K_2\sqrt{2}}. \tag{5.14}$$

χ depends on x not just through h but also K_2. Thus, using subscripts on χ to denote derivatives as for ε,

$$\chi_x = \frac{\chi}{L_n} + (1+h)\chi_K \partial_x K_2. \tag{5.15}$$

Evaluating this at $x=0$ for small h,

$$\chi_x(x=0) = \frac{1}{L_n}\left(\chi + \frac{\delta_T^2}{2}\chi_K \frac{K_{2m}}{K_{0m}K_{1m}}\right). \tag{5.16}$$

By comparison with Sec. 4.5, the first term is present even if k_0 and k_1 are constants, while the second term is due to their variation. It is easy to track the "electromagnetic" contribution by the δ_T factor. κ' is given by

$$\kappa' = -\frac{\varepsilon_{xr}}{\varepsilon_{kr}} = \frac{1}{L_n\chi_{Kr}}\left(1-\frac{\delta_T^2}{2}\frac{\chi_{Kr}K_{2m}}{K_{0m}K_{1m}}\right). \tag{5.17}$$

The second term is typically small. For the standard parameters (see thesis preamble), its magnitude is 0.0324. This justifies the frequent neglect of the spatial variation in quantities besides ε, and in sometimes dropping the EMW k variation altogether (that is, from κ' as well).

5.1.2 The strong damping limit

When plasmon damping is strong, it is useful to work in the strong damping limit (SDL). This entails neglecting the EPW advection term $\sim d_x a_2$ in Eq. (5.9). The formal validity condition is $|v_{g2}d_x a_2| \ll |(\nu_2 - iv_{g2}\kappa' x)a_2|$. Even if damping is weak, far enough from resonance the κ' term can make the SDL condition hold. The SDL is convenient since the EPW equation becomes algebraic rather than differential, so that a_2 is a local function of a_0 and a_1:

$$a_2 = -\frac{K a_0 a_1^*}{\nu_2 - iv_{g2}\kappa' x}. \tag{5.18}$$

$|a_2|$ can be expressed in terms of a "detuning length" $L_d \equiv |v_{g2}\kappa'/\nu_2| = \varepsilon_i L_n$, analogous to the one defined in Sec. 4.5:

$$|a_2| = \frac{|Ka_0 a_1^*|}{\nu_2}\left(1+\left(\frac{x}{L_d}\right)^2\right)^{-1/2}. \tag{5.19}$$

ε_i is related to the damping rate and is usually $\ll 1$, so that $L_d \ll L_n$. As seen in Chap. 4, the EPW envelope drops off much faster in x than the density scale length. Note that a_0 and a_1 vary in space due to the parametric coupling, so that the maximum $|a_2|$ may not occur at $x = 0$.

The steady-state CMEs were solved in the SDL, for arbitrary spatial variation and including pump depletion, in Subsec. 2.5.3. There the geometry was chosen for backscatter such that the pump and plasmon propagate to the right ($k_0, k_2 > 0$) and the scattered light to the left ($k_1 < 0$). Subscript L and R denote quantities at the left and right edges. Recall the definitions made there for normalized action flux $z_i \sim |a_i|^2$, $\tau \equiv 2i(\omega_2/\omega_p^2)\chi/\varepsilon$, and the kinetic gain rate $\alpha_k \equiv \tau_r\gamma_0^2/v_{g1}$. The solution for z_2 is

$$z_2 = \rho z_0 z_1, \qquad \rho \equiv |\tau|^2\gamma_0^2\left|\frac{v_{g2}}{v_{g1}}\right|. \tag{5.20}$$

The Manley-Rowe relation for the SDL is $z_0 = z_1$, and z_1 satisfies $z_1' = -2\alpha_k z_0 z_1$. The complete solution for z_1 is given in Eq. (2.147), but a more comprehensible and very accurate approximation (derived in Subsec. 2.5.3) is

$$z_1 = z_{1R}\exp\left[\hat{z}G(x)\right], \tag{5.21}$$

$$G(x) \equiv \int_x^{x_R} dx'\, 2\alpha_k(x'), \tag{5.22}$$

where $\hat{z} = 1 - z_{1L}$.

G can be integrated analytically for the LSV, whence τ becomes

$$\tau \approx -\frac{2i}{\omega_p\left(\varepsilon_{xr}x + \varepsilon_i\right)} \tag{5.23}$$

$$= \frac{1}{\nu_2\left(-1 + ix/L_d\right)}. \tag{5.24}$$

In this limit Eq. (5.20) gives the same z_2 as Eq. (5.19) does. The resulting G is

$$G(x) = G_0\frac{1}{\pi}\left(\arctan u_R - \arctan u\right); \tag{5.25}$$

$$G_0 \equiv \frac{2\pi\gamma_0^2}{|v_{g1}v_{g2}\kappa'|}, \qquad u(x) \equiv x/L_d. \tag{5.26}$$

$u_R = u(x_R)$. For a profile much wider than L_d, so that $u \ll -1$ and $u_R \gg 1$, G approaches G_0.

To illustrate, Fig. 5-1 shows the spatial profiles of z_1 and z_2 for the LSV profile variation. We choose $G_0 = 8$, $u_R = 15$, and $u_L = -15$. This covers the region where the majority of the spatial growth occurs. The total amplification to z_1 is small, so that $z_{1L} \ll 1$ and we neglect pump depletion entirely: $\hat{z} \to 1$. The EPW z_2 peak is shifted to the left, since it is determined by both the Lorentzian $1/(1+(x/L_d)^2)$ factor as well as the scattered EMW intensity $z_1(x)$. The light wave grows most rapidly near $x = 0$, although it takes many detuning lengths to realize most of the full e^{G_0} amplification.

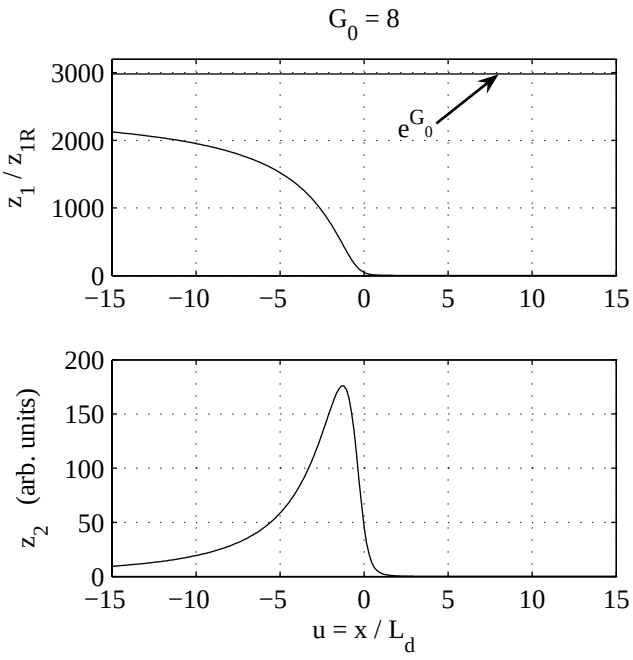

Figure 5-1: Solutions for LSV with $G_0 = 8$ and no pump depletion $\hat{z} \to 1$.

5.1.3 Comparison with undamped solution

Rosenbluth et al. solved for the steady-state convective amplification of a parametric instability with no damping but with detuning due to inhomogeneity, for an infinitely extended profile [31], [106]. When boundary effects are neglected the instability can never be absolute, and the maximum amplitude always approaches a steady value. Late in time the amplified signal is roughly constant over a spreading region bordered by two sharp edges. However, if the interaction region is of finite extent, then wave reflections from the boundaries can lead to unstable normal modes [107], [32]. In the absence of damping the detuning scale $L_d = |\kappa'|^{-1/2} \sim (L_n/k)^{1/2}$ and is usually much shorter than the inhomogeneity scale L_n: $L_d/L_n \sim (\lambda/L_n)^{1/2}$ which must be small for a WKB-type analysis to hold. Therefore it is permissible to keep detuning as the dominant inhomogeneity effect and neglect variations of the group velocity and other parameters, which vary on the scale L_n. The total undamped gain exponent is calculated to be the G_0 found above for strong damping. Therefore, the amplification for a sufficiently wide interaction region is the same in both limits. It can be shown that as long as the pump exceeds the instability threshold $\gamma_0 > \gamma_c$ then the total amplification is given by G_0. Damping slows how rapid in space the amplification is.

5.2 SRS simulations in a density gradient

This section shows results of ELVIS runs with a background density gradient. Besides the spatial profile, the parameters unless noted agree with the run `iBC` and thus the standard parameters with helium of the thesis preamble. In particular, the plasma conditions are $T_e = 3$ keV, $n_0 = 0.1 n_{c0}$, and kinetic helium ions with $T_i = 700$ eV are included. The pump satisfies $I_{0,15} = 2$ and $\lambda_{0v} = 351$ nm, and BSRS is seeded with $I_1 = 10^{-5} I_0$ and $\lambda_{1v} = 574$ nm. This seed has the largest SRS temporal

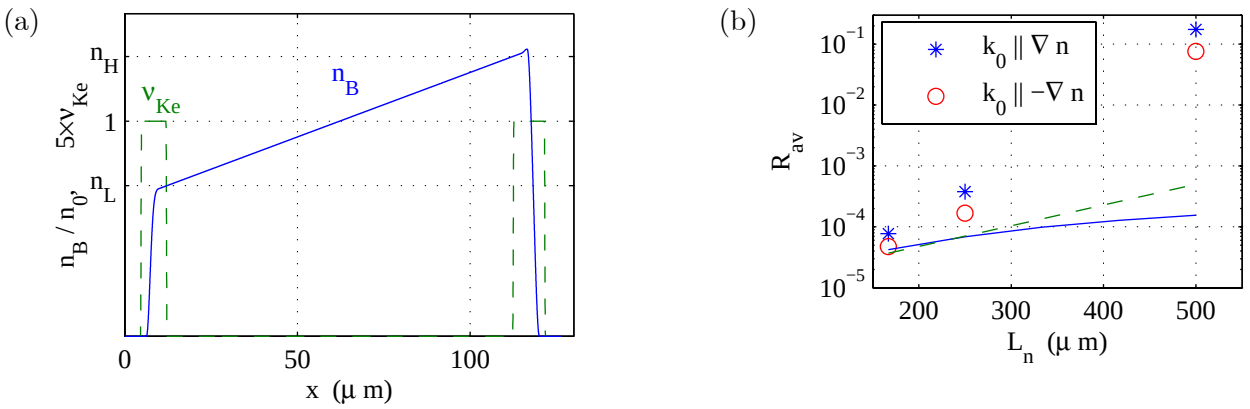

Figure 5-2: (a) Spatial profiles of n_B and ν_{Ke} for inhomogeneous SRS runs. n_L and n_H are the densities at the ends of the linear region and are different for each run. (b) Time-averaged reflectivity for different L_n and both directions of pump propagation. The solid and dashed curves, respectively, are the SDL and undamped steady state values.

growth rate γ for a homogeneous plasma of density n_0. The spatial profiles of the background density n_B and Krook relaxation operator (used only at the edges for numerical purposes) are displayed in Fig. 5-2(a). n_B is linear in the central region. The scale length $L_n = [(1/n_0)dn_B/dx]^{-1}$ (evaluated at $n_B = n_0$) is varied by changing the values of the low and high densities $n_B(x_L) = n_L$ and $n_B(x_H) = n_H$. $x_L = 12.3$ μm and $x_H = 112.3$ μm and the profile is otherwise identical for all runs. The role of pump propagation direction, either along ($\vec{k}_0||\nabla n$) or against ($\vec{k}_0|| - \nabla n$) the gradient is examined by changing which side of the box the pump and seed are incident from, rather than reversing the density profile. The runs lasted for 7 ps.

A series of runs was performed with $n_L = (0.7, 0.8, 0.9)$ and $n_H = 2 - n_L$, which give respectively $L_n = (167, 250, 500)$ μm. Figure 5-2(b) plots the time-averaged reflectivities R for both directions of pump propagation. The curves are the calculated R for the SDL and for the undamped Rosenbluth analysis. As L_n increases so does R. Moreover, for fixed x endpoints the normalized distance $u = x/L_d$ covered by the profile decreases; L_d increases with L_n for both the SDL ($L_d \sim L_n$) and undamped ($L_d \sim L_n^{1/2}$) analyses. Since L_d is much shorter in the undamped analysis than in the SDL, the SDL does not give the full e^{G_0} amplification of the undamped analysis for large L_n. For the smallest L_n simulated, R from the run and both analytic calculations are close. As L_n increases, R increases substantially above even the undamped calculation and approaches the homogeneous reflectivities ($\sim 10\%$) seen in Chap. 3 for $L_n = 500$ μm.

The system reaches a quasi-steady state, with pulsations related to the bounce time, when the scale length is short, but the dynamics become chaotic and bursty, and similar to the homogeneous runs, for large L_n. Figure 5-3 shows the instantaneous reflectivities for all six runs and displays the transition from pulsation to chaos. As in the average R plot, the reflectivity is consistently higher for $k_0||\nabla n$ (pump propagation to the right) than for $k_0|| - \nabla n$ (pump propagation to the left). The amplitude of the longitudinal field E_x, presented in Fig. 5-4 for $L_n = 167$ μm and both directions of pump propagation, is peaked near the resonance point but shifted along the EPW $\vec{k}_2$. Pulsations in E_x are clearly seen, but occur in a regular pattern which continues throughout the full 7 ps run duration (the plot only shows the first half of the run).

Figure 5-5 depicts the rms spatial profiles of the density perturbation n_1 and scattered light (E^- or E^+) for the runs of Fig. 5-4. In panel (a), $k_0||\nabla n$, the scattered light is amplified where the

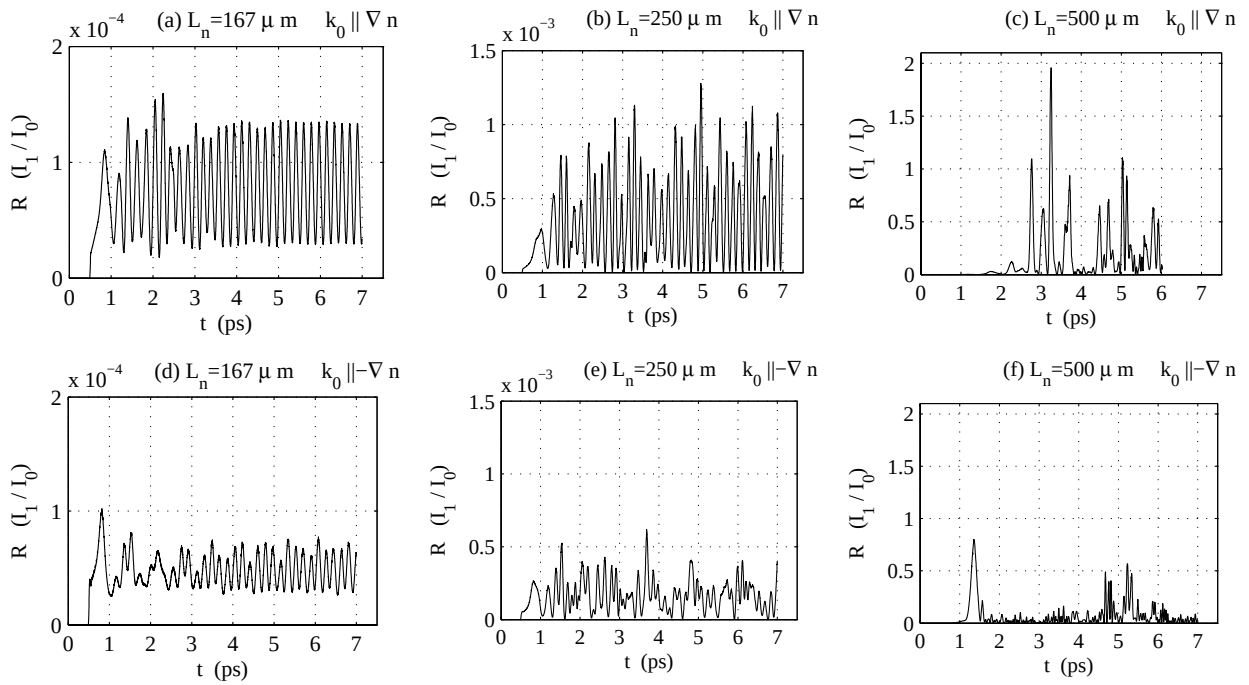

Figure 5-3: Instantaneous R for six inhomogeneous runs. Plots in a column have the same L_n but different direction of k_0.

plasma wave is strong and then propagates to the left. The figure shows two pulses of light, one exiting at the left and another which peaks at 60 μm. The reflectivity for this run is also periodic in time. Figure 5-5(b) shows similar behavior for the case $k_0||-\nabla n$ but with the directions reversed. Figure 5-6 graphs the rms_2 n_1 near the maximum EPW amplitude for the runs of Fig. 5-4. The pulsations for $k_0||\nabla n$ (a) occur with a typical period of 0.19 ps. Taking a typical amplitude of $n_1/n_0 = 9.7 \times 10^{-4}$ gives a bounce period of $\tau_B = 0.12$ ps. Since the wave amplitude is smaller away from this point the bounce period is slightly longer there. For $k_0||-\nabla n$, panel (b), the amplitude is smaller and the pulsation occurs on two time scales, roughly 0.18 ps ("big-to-small peak") and 0.37 ps ("big-to-big peak"). The shorter time scale equals τ_B for $n_1/n_0 = 4.2 \times 10^{-4}$, which is comparable to the actual n_1 in the run.

The threshold scale length L_n for kinetic enhancement can be estimated in the following way. Trapping reduces Landau damping once a resonant particle completes a substantial portion, say half, of a bounce orbit before crossing the plasma. Consider a resonant electron with $v = v_p$ that enters the plasma from one edge. How much of a bounce orbit it experiences is given by the "bounce phase" $\theta_B = \int dx' k_B(x')$ where the bounce wavenumber $k_B = \omega_B/v_p$. The wave amplitude $\hat{n}$ and thus k_B vary with space. If SRS were to reach the convective steady state, one can calculate θ_B for the resulting profiles. If $\theta_B \gtrsim \pi$, then trapping can reduce the Landau damping, at least toward the edge of the box. For simplicity, we use the strong damping limit (SDL) profiles to estimate θ_B; a more detailed calculation including EPW advection could also be carried out. The SDL approach gives $\theta_B = 21.9$ for the runs discussed above with $L_n = 167$ μm (the sharpest gradient considered). This indicates trapping already plays a role at this small L_n. The reflectivity is indeed above the undamped Rosenbluth value by about a factor of 2, and f_e (not shown) shows vortex formation. However, the chaotic stage of kinetic enhancement does not occur until L_n is much larger. At this point the steady state, even with a trapping-reduced damping rate, is never reached.

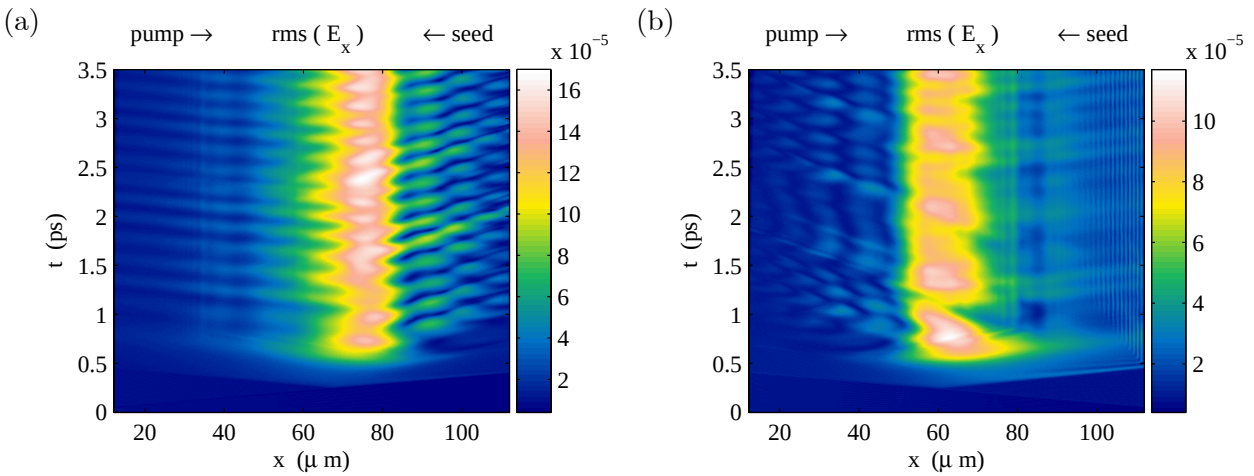

Figure 5-4: rms E_x for inhomogeneous run with L_n=167 μm and (a,b) $k_0||(+,-)\nabla n$. The pulsations continue for the rest of the runs (total time 7 ps).

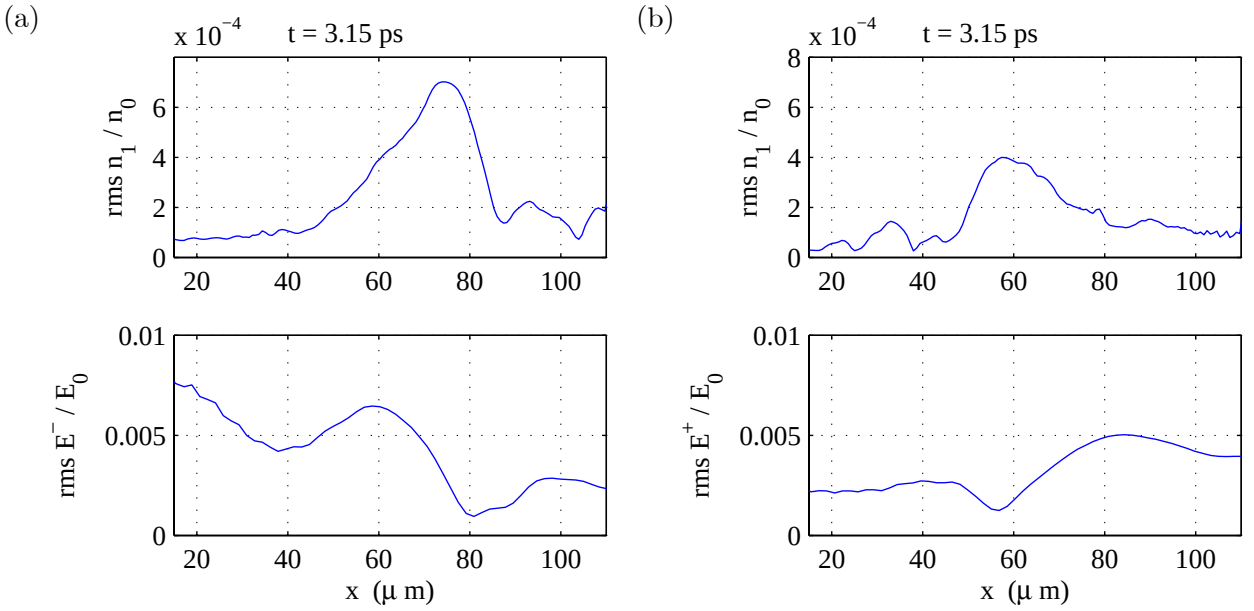

Figure 5-5: rms $n_1 = n_e - n_e(t=0)$ and reflected light for inhomogeneous runs with L_n=167 μm and (a,b) $k_0||(+,-)\nabla n$. The E^- and E^+ signals are filtered to only pass the band from $k\lambda_D = 0.07 - 0.19$, which includes the SRS seed.

A better understanding of the onset of kinetic enhancement in a gradient, as well the stronger SRS when the pump propagates toward higher as opposed to lower density, should be explored in future work.

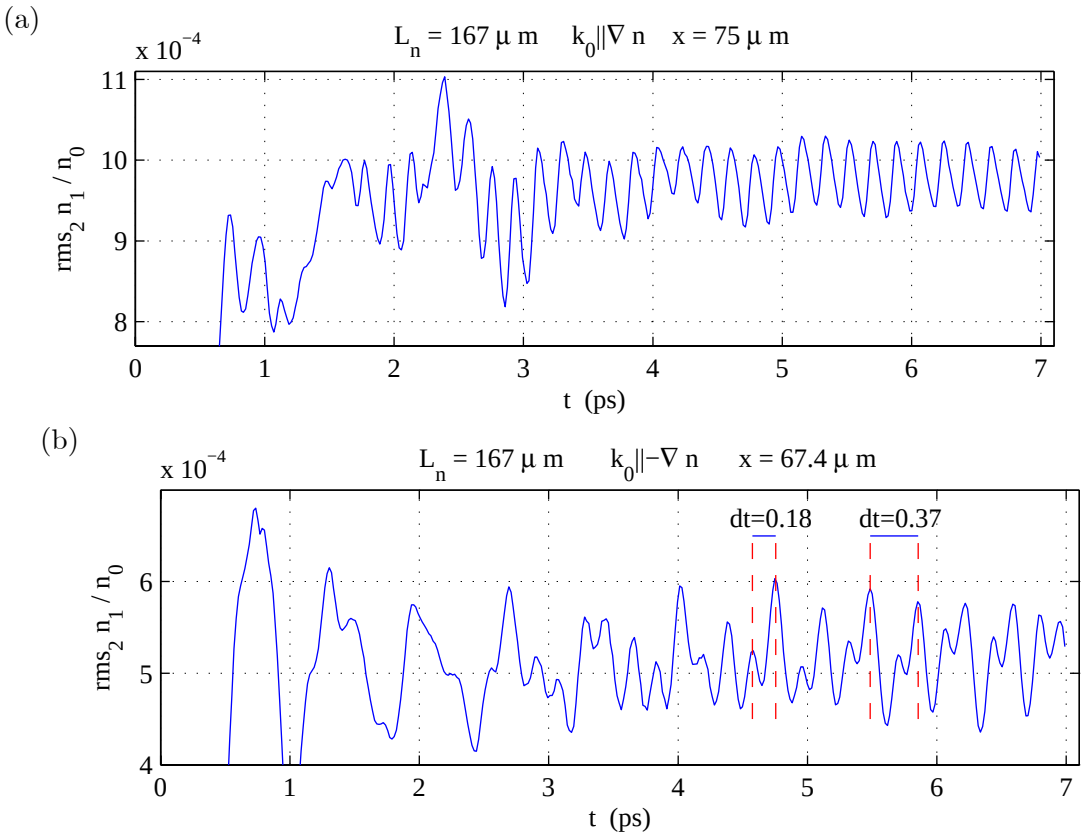

Figure 5-6: $\mathrm{rms}_2\ n_1 = n_e - n_e(t=0)$ for inhomogeneous runs with L_n=167 μm and (a,b) $k_0||(+,-)\nabla n$.

Chapter 6

Conclusions and Future Work

This concluding chapter summarizes the results of this thesis, and suggests future avenues of research which they suggest.

6.1 Conclusions

Our findings, also described in Sec. 1.5, are as follows:

1. **Coupled-mode predictions:** According to the coupled-mode theory of Chap. 2, Raman scattering is a convective rather than absolute instability in ICF hohlraum plasmas, with gain lengths of $\sim 10-100$ μm. Convective SRS is usually in the strong damping limit, where plasma-wave advection is negligible compared to Landau damping. The collisional damping of light and plasma waves is very weak compared to EPW Landau damping. Neglect of collisions, which we do in our simulations, does not change the convective-absolute nature of SRS and has little effect on the gain length. We exactly solve the steady-state coupled-mode equations in the strong damping limit, including pump depletion. The resulting reflectivity rises exponentially with the laser pump intensity until it starts gradually leveling off for reflectivities above 10% (Fig. 2-3(b)).

2. **Kinetic enhancement:** The ELVIS simulation `BC1` of SRS from a homogeneous, 75 μm plasma shows much higher reflectivity than coupled-mode theory predicts. Electron trapping, evident in the distribution function, reduces the Landau damping and thus raises the reflectivity. Also, the EPW frequency downshifts from its linear value, as seen in the $E_x(k,\omega)$ spectra. The system behaves chaotically, with reflected light coming in temporal bursts. Pulses of SRS activity form at the laser entrance and propagate away. Forward SRS and Raman re-scatter of BSRS also develop.

3. **Role of pump strength, temperature, seeding, and sideloss:** The coupled-mode steady state is reached for low pump strength I_0 or high electron temperature (high $k_2\lambda_D$). As we increase I_0 or lower T_e, the reflectivity shows a sharp transition to kinetic enhancement, roughly when a resonant electron undergoes bounce motion before crossing half the plasma. For all T_e considered, with $k_2\lambda_D$ up to 0.45, raising I_o eventually gives kinetic enhancement. The reflectivity is similar in runs like `BC1` but with a smaller BSRS seed, with a broadband

instead of monochromatic seed, and with no plasma-wave damping at the edges. When a Krook operator in the central part of the plasma is included to mimic sideloss, there is again a sharp transition from kinetic enhancement to the coupled-mode steady state with increasing relaxation rate. The sharpness of the transition and independence from seed level suggest SRS becomes an absolute instability due to the trapping-induced Landau damping reduction and evolves to a nonlinearly saturated state. This explains why strong SRS develops in "small" plasmas (several linear convective gain lengths long).

4. **Mobile ions:** The run `iBC`, which matches `BC1` except that it has kinetic helium ions, gives strong, kinetically enhanced SRS until the appearance of a "blob" of activity near the laser entrance, after which there is little scattered light. Once the blob occurs we see many parametric processes going on simultaneously, including Raman and Brillouin re-scatters and LDI activity. However, we see neither pump SBS (perhaps due to lack of seeding) nor LDI of the primary BSRS plasmon (consistent with the high threshold due to strong Landau damping).

5. **Acoustic activity and SEAS:** A generic feature of the runs which show large reflectivity is the presence of two acoustic modes in the $E_x(k,\omega)$ spectrum. Moreover, later in time scattered light is seen which lies between the BSRS and pump frequencies, which may be stimulated electron acoustic scatter (SEAS). A weak SEAS signal was reported in Trident experiments when back SRS was strong [52], [54]. We compare the acoustic features to the "natural" (complex, linear, Landau) and what we term the "$\varepsilon_r = 0$" (small-amplitude, undamped) modes in Chap. 4. The higher and lower phase velocity acoustic modes observed in our runs have the phase velocities predicted for the natural and $\varepsilon_r = 0$ modes, respectively. The potential SEAS reflected light satisfies frequency and wavenumber matching with a point that lies on the $\varepsilon_r = 0$ acoustic mode.

6. **Driven plasma waves in an inhomogeneous plasma:** Plasma waves driven by a fixed external force in a density gradient were examined by expanding the kinetic permittivity operator for slow envelope variation. For linear profile variation and a drive that passes through resonance, an analytic steady-state solution is obtained. This is close to the strong damping limit solution (which neglects plasma-wave advection), except the peak amplitude is shifted in the direction of wave propagation and reaches a smaller maximum as advection becomes more important. Electrostatic ELVIS simulations agree with the envelope theory for weak drive. The numerical peak amplitudes increasingly exceed linear theory and are further shifted in the direction the waves propagate as the drive increases. This could indicate a nonlinear, trapping-induced damping reduction and wavenumber shift. The numerical amplitude is larger when the drive propagates to higher and opposed to lower density; linear theory predicts no such asymmetry.

7. **SRS in a density gradient:** For shallow density gradients there is a kinetic enhancement of SRS, which behaves chaotically as for homogeneous plasmas. This enhancement is well above the inhomogeneous, coupled-mode steady state level calculated in both the strong damping limit and the undamped limit. The reflectivity approaches the coupled-mode value for sharp enough gradients. Pump lasers (and thus BSRS plasmons) that propagate toward higher, instead of lower, density give somewhat higher reflectivities.

6.2 Future work

In light of the research in this thesis, we propose the following future work:

1. **Understanding kinetic enhancement of SRS:** This research shows SRS is kinetically enhanced for a wide range of plasma conditions, but we have not developed a comprehensive theory of it. In particular, which of the many proposed saturation mechanisms [58], [59] is effective was not explored. Even though SRS is chaotic, a simple model that predicts time-averaged reflectivities would be extremely helpful. A criterion for determining when kinetic enhancement takes place should be sought. We have relied on roughly comparing the box size to the bounce length of trapped electrons. This approach is only somewhat accurate, and does not predict the sudden transition with parameter variation from the coupled-mode steady state to kinetic enhancement. The relevance of the bounce length should also be tested with simulations of varying box size.

2. **Acoustic features and SEAS:** Our simulations consistently show $E_x(k,\omega)$ spectra that depart strongly from the linear EPW dispersion curve. The SRS plasmon is both downshifted in frequency and develops a "tail" that merges with an acoustic ($\omega \propto k$) feature extending to $k = 0$. The phase velocity of this feature is $\approx 3.6 v_{Te}$ and agrees with the second most weakly damped Landau root (the "natural acoustic mode" of Chap. 4). There is also a lower phase-velocity ($\approx 1.3 v_{Te}$) acoustic mode matching the "$\varepsilon_r = 0$" mode of Chap. 4, as well as reflected light from stimulated electron acoustic scatter (SEAS) off this feature. A linear instability analysis using the simulation distributions, as opposed to a Maxwellian, would illuminate the nature of these modes, as well as the potential for scattering off them. This can reveal conditions that favor SEAS, which can be tested with appropriate ELVIS simulations. Runs could also explore whether SEAS occurs in conditions similar to the Trident experiments where SEAS was reported [52], [54].

3. **Model for inhomogeneous plasma-wave response:** The ELVIS simulations of plasma waves driven by an external force in Chap. 4 display significant departure from the linear steady-state envelope solution. The larger simulation wave amplitude may stem from a damping reduction caused by trapping. Moreover, the larger response for waves propagating to higher instead of lower density could reflect a nonlinear wavenumber shift. A quantitative model that reproduces the numerical behavior is needed. These simulations can also be used to extract the nonlinear damping and wavenumber shift, akin to the technique of Ref. [25], and compared with theories such as that of Morales and O'Neil [26]. Pathological behavior of the envelope solutions, such as blow-up of the response, were noticed when the full, complex $\partial\varepsilon/\partial k$ was used rather than just its real part. It will be interesting to address whether this contains any physics, and how it relates to the driven response. Since the inhomogeneous SRS runs of Chap. 5 also show an enhanced wave amplitude for EPWs propagating up as opposed to down the density gradient, a nonlinear model for the plasma response may elucidate these results and reveal when kinetic enhancement occurs. The possibility of auto-resonance due to trapping [37], [14] in SRS from inhomogeneous plasmas should be investigated.

4. **Ions:** The ion work in this thesis was preliminary, and mainly intended to see whether LDI or other ion dynamics prevent kinetic enhancement of SRS. There is strong evidence, both theoretical and experimental, that for low $k_2\lambda_D$ (say below 0.3), LDI and subsequent cascades take place and can saturate SRS. It would be helpful to see LDI in an Eulerian Vlasov

simulation and to delineate the transition between LDI- and trapping-dominated behavior by scanning plasma density and temperature, and thus $k\lambda_D$. This would provide an important contact with experiment. Our ion simulation in Chap. 3 revealed many parametric interactions occurs simultaneously, and led to the "blob" of activity after which the reflectivity stayed low. The interplay of these processes, with a proper, broadband noise source for all the relevant modes, needs further investigation. Several papers have shown chaotic SRS dynamics from the coupled-mode equations when re-scatter, cascades, and LDI are allowed (e. g. [40]). Kinetic simulations can reveal more about this phenomenon, and take into account much that is absent from coupled-mode models (such as mode bandwidth and overlap of nearby modes). It is also important to discern if ion motion is necessary for features like the blob to develop, or if SRS re-scatter alone can produce it.

5. **Wave-breaking:** Wave-breaking refers to the upper limit on the amplitude of a wave. Discussions of wave-breaking are generally based on fluid models, either warm or cold, relativistic or nonrelativistic [88–90, 108, 109]. The intuition is the wave breaks once fast fluid elements capable of overtaking slower ones develop: density, velocity, and all fluid variables must remain single-valued. However, overtaking poses no problem to a kinetic description: even in a stable Maxwellian fast particles constantly overtake slower ones. We are not aware of a kinetic discussion of wave-breaking. Our simulations show regular vortices in phase space which become irregular as the plasma wave grows (see Fig. 3-7). The corresponding electric field k spectrum (not presented) shows a single large, well-defined k with several harmonics when the vortices are regular, but becomes very broad for irregular vortices. The correct way to understand wave-breaking kinetically may be to examine under what conditions periodic solutions for the electric field (which is always single-valued, in any description) exist. Above this level the electric field and particle orbits may become chaotic and lead to electron heating. Given the existence of Bernstein-Greene-Kruskal modes of arbitrary amplitude [94], with the trapped-particle distribution tailored for self-consistency, it is not clear what intrinsic limits kinetic theory places on wave amplitude.

6. **2D2V Fokker-Planck simulation:** This thesis demonstrates the importance of kinetic effects and trapping in a 1-D model of SRS. However, 2D and 3D effects also play a role, such as laser focusing (pump spatial variation), speckle sideloss, filamentation, Raman sidescatter (shown in Chap. 2 to have an appreciable growth rate compared to backscatter), and two-plasmon decay. Besides these higher-dimension phenomena, the transverse electron distributions can be non-Maxwellian; this requires one more velocity dimension. As discussed in Sec. 2.5, super-Gaussian (Dum-Langdon-Matte) distributions [72] and ponderomotive modifications to the distribution [74] occur in the transverse direction. Collisions transmit these features to the longitudinal distribution and alter the dispersion and damping of plasma waves from their Maxwellian characteristics [73] . Collisions also de-trap resonant electrons, both by 1-D collisions and pitch-angle scattering (see Sec. 3.7). Relativity has been neglected in this thesis, which nonlinearly downshifts the EPW frequency via the relativistic mass increase. This was modeled by a cubic nonlinearity in the EPW equation of a coupled-mode model for SRS, and shown to produce temporal bursts and chaos, in Ref. [110]. 1-D relativistic PIC simulations display similar behavior [111].

   To our knowledge, no first-principles simulation with enough physics to allow for all these phenomena simultaneously has been carried out. To do so requires a "2D2V" (two space and velocity dimensions) Fokker-Planck time-evolution code. Such simulations would enhance our understanding of these myriad effects and indicate which ones dominate in various situations.

Simplified models that take into account the important physics could then be benchmarked against a few simulations, and then used with confidence. We imagine developing such a code, testing it, implementing the correct diagnostics, exploring the relevant physics effects over interesting parameter regimes, and comparing with reduced descriptions could constitute one or more good Ph. D theses!

7. **Enhancements to ELVIS:** There are several ways ELVIS can be extended, both to improve the physics and its numerical performance. ELVIS, like all Eulerian codes, has very low numerical noise. This allows low-amplitude problems and low-density regions of phase space to be studied. However, the code does not produce fluctuations from which parametric instabilities can grow. We seed BSRS in this thesis with an externally-imposed, small-amplitude light wave. Physically the noise has a continuous spectrum and includes electrostatic noise. A better source of noise, which is broadband, present in both the transverse and longitudinal channels, and distributed throughout the plasma should be added. This is especially important for investigating the coupling of SRS to other parametric processes, such as re-scatter, SBS, and LDI. The ion run in Chap. 3 displays many parametric interactions even with only seeding BSRS, and we must explore the dynamics in the presence of more realistic noise. The low noise in ELVIS allows us to choose seed and noise levels that are well below the numerical fluctuations found in my PIC codes run with typical numbers of particles per cell.

   Several improvements to the run time of ELVIS can be made. ELVIS is currently a serial code and may benefit substantially from parallelization. Brief attempts to use OpenMP on a shared-memory machine produced no speed-up, perhaps because of thread synchronization and other overhead. A non-uniform momentum grid would allow high resolution where trapping and other detailed structure forms, while using few points in smooth regions like the bulk. Care should be taken to see how a non-uniform grid affects the accuracy of interpolation for the momentum shifts, and how the recurrence phenomenon (Appendix A, p. 130) plays out. Although we do not see recurrence in SRS runs, the role of recurrence in non-periodic and driven problem should be explored. A more ambitious step would be to adaptively refine the momentum grid where resolution is needed.

   The time and space step sizes used in SRS runs provide excessive resolution and thus longer run times. Our method for time advancing transverse electromagnetic field requires $c\,dt = dx$. The fastest time scale in the problem is the laser frequency ω_0, while resolving several harmonics of the BSRS plasmon sets the shortest space scale. Typically the dx needed to resolve the plasma activity is several times less than the $c\,dt$ needed to resolve ω_0. Therefore, very high frequencies with no activity are resolved. Since almost all the run time is consumed by advancing the particles (f_e, f_i) as opposed to the e/m fields, it would save time to advance the e/m fields for several smaller time steps during a single particle time step ([112] p. 364). Similarly, the cost of kinetic ions can be made negligible by "sub-cycling" the electrons, or taking several electron steps during one ion step [113].

Appendix A

ELVIS: an Eulerian Vlasov-Maxwell Solver

A.1 Overview: continuum methods for kinetic equations

The velocity distribution of plasma particles is frequently far from collisional equilibrium (e.g., a Maxwellian). This departure from equilibrium distinguishes plasma physics from fluid or solid mechanics, and causes some of the most important aspects of plasma behavior. There is great interest in kinetic models that follow plasma evolution in phase space (position and momentum). The numerical solution of kinetic equations can be substantially more demanding than fluid equations, both conceptually and computationally. Two broad approaches have been used to simulate kinetic equations: continuum or Eulerian (sometimes called Vlasov), and particle-in-cell (PIC) or Lagrangian methods. A continuum method treats the plasma as a "phase-space fluid" instead of as a set of discrete particles, and solves the kinetic equation for the distribution function $f(x,p)$ on a fixed grid in phase space. PIC methods, on the other hand, represents f by a discrete set of finite-sized particles (macro-particles), which move freely in phase space. The forces felt by the particles are found by first calculating the charge and current densities, and the resulting electromagnetic fields, on a fixed spatial grid, and interpolating the force to the particle positions. Continuum methods can be viewed as solving for f on a fixed, Eulerian grid, while PIC methods use a moving, Lagrangian grid.

Both methods have their good and bad points. PIC has the advantage that the number of macro-particles needed does not grow too rapidly as one goes to higher dimensions. However, PIC suffers from high noise levels generated by the numerical single-particle dynamics, analogous to the physical fluctuations in a real plasma (which are of much lower amplitude, since the number of particles in a physical Debye sphere is much larger than in a PIC simulation). The high noise makes it difficult to study linear and weakly nonlinear problems with PIC. Since continuum methods treat f as a phase-space fluid, they lack the fluctuations and noise arising from single-particle motion in PIC. The price one pays is needing more phase-space gridpoints, and thus computer memory and run time, especially in higher dimensions.

Another challenge in kinetic simulations is the so-called recurrence or filamentation problem [114], [115]. Consider a distribution with an initial sinusoidal density perturbation: $f(x,v,t=0) = f_0(v)\,(1+\varepsilon \sin kx)$. If we neglect collisions and forces, f satisfies the free-streaming equation

$\partial_t f + v\partial_x f = 0$. The solution $f(x,v,t) = f_0(v)\,(1+\varepsilon\sin k(x-vt))$ has a velocity-space wavenumber $k_v = kt$ that grows secularly in time, leading to "filaments." This is a real physical effect, which can lead to numerical inaccuracy in an Eulerian code when $1/k_v$ approaches the velocity grid spacing dv. Moreover, density perturbations which physically phase-mix away can be reconstructed, or recur, in a simulation. For the free-streaming example given above, the density $n = \int dv\ f$ is given by

$$n - n_0 = -i\frac{\varepsilon}{2}e^{ikx}\int dv\ f_0\ e^{-iktv} + cc. \tag{A.1}$$

As t increases, the integral over f_0 contains a phase factor that oscillates more rapidly in v. For the Maxwellian case $f_0 = n_0/(v_T\sqrt{2\pi})\exp\left(-(1/2)v^2/v_T^2\right)$ we have

$$n - n_0 = \varepsilon n_0 \sin(kx)\exp\left[-\frac{1}{2}\left(kv_T t\right)^2\right]. \tag{A.2}$$

The resulting density perturbation decays away exponentially. However, this may not happen on a discrete velocity grid. Consider a uniform grid: $v_j = v_{\min} + j\,dv$. There are special times, called the recurrence times, when e^{-iktv_j} is equal for every j. This happens when $kt\,dv = 2\pi$, or t a multiple of $t_{\rm rec} = \lambda/dv$ where $\lambda = 2\pi/k$. At these times $\int dv\ f_0\ e^{-iktv} = n_0$, and $n(x, t = t_{\rm rec}) = n(x, t = 0)$. This recurrence phenomenon is shown below to occur for periodic, electrostatic simulations even when electric forces are included.

Of course, collisions in nature smooth out high-k_v structure. We do not modify the kinetic equation in ELVIS in order to mitigate against filamentation. Dissipation, for instance via a Krook relaxation term, can reduce recurrence, although it may also damp the waves of interest. A numerical hyper-resistivity operator $\nu_4\partial^4 f/\partial v^4$ can damp the high-k_v structures produced by phase-mixing without substantially affecting the linear modes of the system [114], [115]. In driven, nonperiodic problems, such as Raman scattering, we have not observed recurrence phenomena. It has been suggested that recurrence does not happen if the recurrence time $t_{\rm rec}$ is longer than a decorrelation time (for instance, the growth time of an instability being studied, like SRS) [116]. We choose our velocity resolution so that $t_{\rm rec}$ is longer than the linear SRS growth time (calculated using linear Landau damping).

We adopt a continuum method in this work, and call the resulting code ELVIS (for Eulerian Vlasov Integrator with Splines). It is described in Ref. [65] and is based on the algorithm found in Ref. [117]. The low noise level allows us to study Raman scattering when it is weak, and make contact with analytic theory. In addition, we can resolve very fine structures in phase-space. Since we restrict ourselves to one spatial dimension, the computational demands are not too great. The author is very interested in helping others use ELVIS for their own research problems, and is happy to share with them both the code and the associated diagnostic routines. He can be contacted electronically at dstrozzi@alum.mit.edu or david.strozzi@gmail.com.

A.2 ELVIS model, geometry, and governing equations

ELVIS is geared toward studying kinetic effects in Raman scattering. The simplest geometry that allows this has all wavevectors and spatial variation in the longitudinal x direction ($\partial_y = \partial_z = 0$), and all light waves linearly polarized in the transverse y direction. We resolve the plasma kinetically in x. The charge density varies in x, giving rise to an electrostatic field E_x via Gauss'

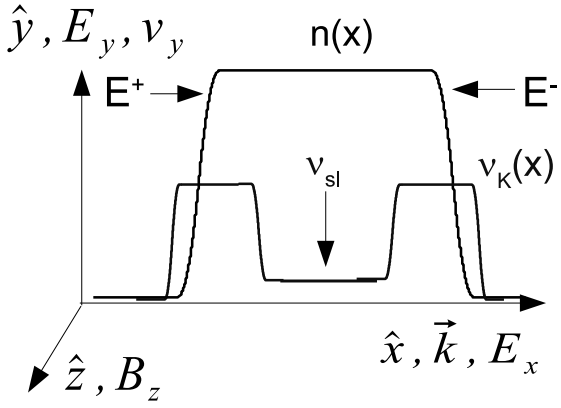

Figure A-1: Geometry for the ELVIS code.

law. The light waves are represented by a transverse electric field E_y and transverse magnetic field B_z. We work with the combinations $E^{\pm} = E_y \pm cB_z$, each of which satisfies a one-dimensional advection equation in our geometry. The particles oscillate transversely due to E_y, giving rise to the "oscillation" or "quiver" motion in the y direction. A cold-fluid description of the transverse dynamics is adequate, with the momentum equation consisting of conservation of canonical y momentum $P_{ys} = m_s v_{ys} + q_s A_y$. ELVIS has the option for a collisional friction term in the transverse momentum equation, although it is not used anywhere in this thesis. The x component of the Lorentz force $\sim v_y B_z$ provides a ponderomotive drive for the plasma wave. The code has both an electrostatic (no transverse fields) and electromagnetic (transverse fields included) mode.

The code internally uses "plasma electromagnetic units," where the scale for length, time, mass, and charge are d_e, ω_p, m_e, and e. Recall that $d_e = c/\omega_p$ is the electron skin depth, $\omega_p = \sqrt{n_0 e^2/\varepsilon_0 m_e}$ is the electron plasma frequency, and $e > 0$ is the positron charge. The velocity, momentum, and electric field scales are c, $m_e c$, and $E_0 \equiv m_e c\omega_p/e$ respectively. We write a species mass m_s and charge q_s as $m_s = \mu_s m_e$ and $q_s = Z_s e$ and $Z_e = -1$. Although each species has its own momentum grid, all are normalized to $m_e c$. From now on we work with normalized quantities. The code accommodates multiple species, and we label species-dependent quantities with a subscript s.

A.2.1 Kinetic equation

The dimensionless kinetic equation for species s is

$$\partial_t f_s + v_s \partial_x f_s + F_s \partial_{p_x} f_s = K_s[f_s],$$

where

$$F_s = Z_s(E_x + v_{ys} B_z), \tag{A.3}$$

$$K_s[f_s] = -\nu_{Ks}(x)\left(f_s - n_s \tilde{f}_{0Ks}\right). \tag{A.4}$$

The velocity $v_{xs} = p_x/(\gamma_s \mu_s)$ with the relativistic factor $\gamma_s = 1$ (nonrelativistic) or $(1 + p_x^2/\mu_s^2)^{1/2}$ (relativistic). In this thesis we always work with the nonrelativistic choice $\gamma_s = 1$. We do not include the contribution of v_y to the relativistic factor γ_s. This is valid since $v_y/ \sim v_{os}/c \ll 1$. γ_s only departs from unity in the high-p_x region of phase space, and $v_x \gg v_y$ there. A Krook

operator on the RHS provides relaxation to a background distribution $\tilde{f}_{0Ks}$, which is normalized so $\int \tilde{f}_{0Ks} dv = 1$. This operator conserves particle number, so that quasi-neutrality is maintained:

$$\left.\frac{dn_s}{dt}\right|_K = \int dv \left.\frac{df_s}{dt}\right|_K = \int dv K_s[f_s] \tag{A.5}$$

$$= -\nu_{Ks} \underbrace{\int dv f_s}_{=n_s} + \nu_{Ks} n_s \underbrace{\int dv \tilde{f}_{0Ks}}_{=1} \tag{A.6}$$

$$= 0. \tag{A.7}$$

However, K_s conserves neither momentum nor energy. $\tilde{f}_{0Ks}$ is a Maxwellian with the initial electron temperature.

We use K_s to model sideloss of particles out of the pump laser beam, as well as to damp plasma waves at the edges of the density profile. In sideloss, particles leave the pump transversely and are replaced by thermal particles. Although this is a multi-dimensional effect, we want to include it approximately in 1-D. As discussed in Sec. 3.7, sideloss is relevant to SRS since it detraps resonant electrons, and thus limits trapping-induced phenomena. In addition, sideloss provides a residual damping of plasma waves after several bounce periods. We imagine sideloss conserves particle number, since particles that escape the beam get replaced by a roughly equal number from the surrounding thermal plasma. The dynamics inside the laser beam may generate high-speed electrons, but the surrounding particle bath consists of lower-speed thermal particles. Therefore, sideloss does not conserve momentum or energy. The fact that K_s lacks these conservation properties does not degrade its use in modeling sideloss. This is, however, a drawback for K_s as a Coulomb collision operator.

We sometimes use K_s with a large ν_{Ks} at the edges of the simulation domain. This damps plasma waves outside the region of interest, and prevents reflection at the ends of the density profile. We let ν_{Ks} vary with x so that we can have an unphysically large one in the edge regions, and smoothly lower it to a nonzero (sideloss) or zero (no sideloss) value in the interior. A linear analysis of the kinetic equation with a Krook operator, and the background distribution $f_0 = n_0 \tilde{f}_{0Ks}$, yields the dispersion relation

$$D(\zeta) \equiv 1 - \frac{1}{2\bar{k}^2} Z'(\zeta) + i \frac{\bar{\nu}}{\bar{k}\sqrt{2}} Z(\zeta) = 0. \tag{A.8}$$

$\zeta = (\bar{\omega} + i\bar{\nu}) / \left(\bar{k}\sqrt{2}\right)$, $\bar{k} = k\lambda_D$, $\bar{\omega} = \omega/\omega_p$, $\bar{\nu} = \nu/\omega_p$, and Z is the plasma dispersion function. For weak damping and in the fluid limit $\zeta \gg 1$,

$$\bar{\omega} \approx \sqrt{1 + 3\bar{k}^2} + i\left(\bar{\nu}_L + \bar{\nu}/2\right). \tag{A.9}$$

$\bar{\nu}_L$ is the Landau damping rate, normalized to ω_p, for $\nu_K = 0$.

A.2.2 Electromagnetic and transverse fields

The transverse momentum equation is

$$\mu_s \partial_t v_{ys} = Z_s E_y. \tag{A.10}$$

The charge density $\rho \equiv \Sigma_s Z_s n_s$ and transverse current density $J_y \equiv \Sigma_s Z_s n_s v_{ys}$. The electric and magnetic fields satisfy

$$\begin{aligned} \partial_x E_x &= \rho, & \text{(A.11)} \\ (\partial_t \pm \partial_x) E^{\pm} &= -J_y, & \text{(A.12)} \\ E^{\pm} &\equiv E_y \pm B_z. & \text{(A.13)} \end{aligned}$$

In the absence of currents, $E^+(E^-)$ is advected to the right (left): $E^{\pm}(x,t) = E^{\pm}(x \mp t, t = 0)$ for $J_y = 0$.

A.3 Grids

The spatial simulation domain extends from $x = 0$ to $x = L$. However, the spatial grid (that is, the region over which quantities are distinct and may evolve) runs from $x = 0$ to $x = x_{\max}$ in uniform steps dx. The difference is important for handling both periodic and non-periodic systems. For periodic systems, L is the periodicity length, and $x_{\max} = L - dx$ since the point at $x = L$ is identified with $x = 0$. However, for non-periodic systems $x_{\max} = L$. In all cases, the spatial grid is uniform and contains N_x points:

$$x_i = (i-1)dx, \qquad i = 1 : N_x, \qquad dx = \frac{x_{\max}}{N_x - 1}. \tag{A.14}$$

dx should be chosen small enough to resolve the highest wavenumber of interest well. This is generally the plasma wavenumber k_2. However, we also want to resolve some harmonics, if they develop. The code allows for an optional "moat" region on both the right and left extremes of the domain, where f is identically zero for all time, but where electromagnetic fields are calculated. This allows for light waves, which propagate in vacuum, to cleanly reach the boundaries. The length of the left and right moats are stored in the variables `xmoatL` and `xmoatR`. The domain looks like: `0------xpL------------xpR--------xmax`. `xpL`=`xmoatL` and `xpR`=`xmax-xmoatR`. `xpL` and `xpR` limit the region over which the plasma evolves.

Since ELVIS is a continuum method, momentum in the kinetic x direction is a grid. The p_x grid is uniform with spacing dp and a total of N_p gridpoints, and is separate for every species (we suppress the species index s in this paragraph):

$$p_j = p_{\min} + (j-1)dp, \qquad j = 1 : N_p, \qquad dp = \frac{p_{\max} - p_{\min}}{N_p - 1}. \tag{A.15}$$

Clustering points around the plasma-wave phase velocity would allow for fewer overall gridpoints, and may be a helpful extension to ELVIS. dp needs to be small enough that v_{Te} is well-resolved, or else the momentum integrals that lead to density and other moments will not be accurate. In addition, the resonant region around the plasma-wave phase velocity v_{p2} needs adequate resolution. The trapping width depends on the wave amplitude, so care must be taken to understand the smallest amplitude plasma waves for which resonant or trapping effects must be correctly handled. For a given wave amplitude, simulations with dp sufficiently larger than the trapping width will not capture Landau damping. In SRS simulations we usually choose dp for electrons such that the trapping width v_{tr} in the unamplified plasma waves (driven by pump and seed) is at least twice dp.

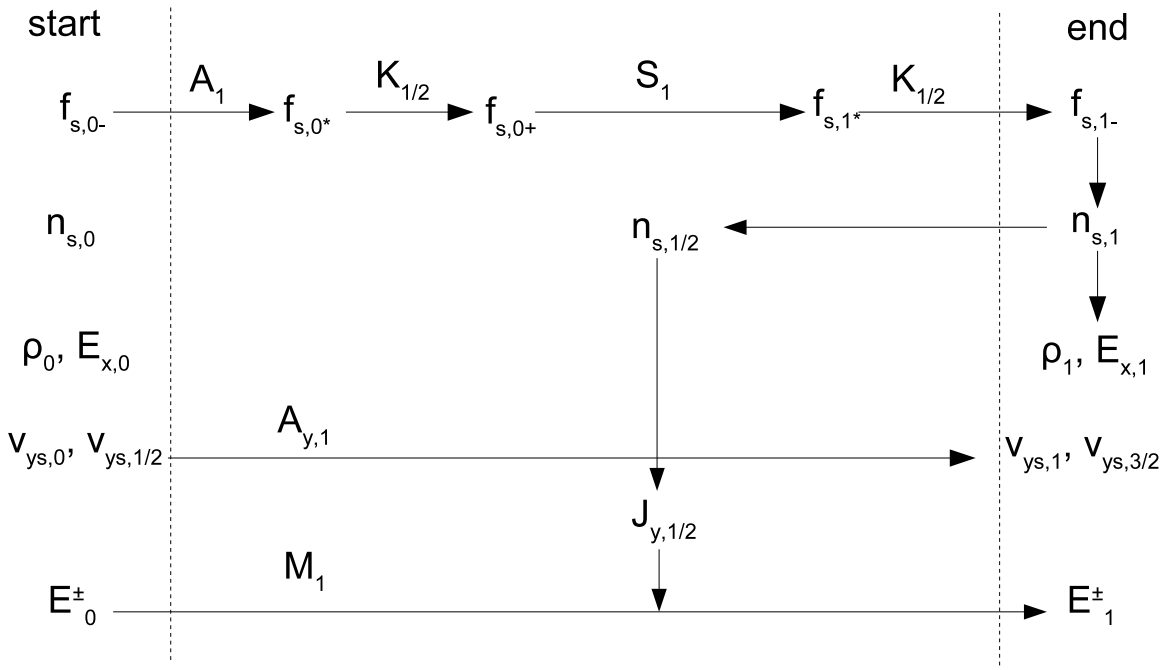

Figure A-2: An "interior" ELVIS timestep.

A.4 Time evolution

This section describes the numerical method ELVIS use to evolve the Vlasov-Maxwell system in time. Operator splitting is used. The algorithm is similar to that given in Ref. [117], to which we refer the reader for a more detailed discussion of the time step's accuracy. Other methods for the time step include symplectic integration extensions of operator splitting [118] and the semi-Lagrangian or Eulerian-Lagrangian method [119].

A.4.1 The overall time step

As in Ref. [117], we "leapfrog" the time advance for the distribution f_s and the transverse e/m fields $E^{\pm}$. To properly combine the two free-streaming shifts of f_s discussed in the next section, the first timestep is different from the following, "interior" ones. Here we detail an interior timestep. The variables have some initial values at the start of the step, and must be advanced to the initial values needed for the next step. We imagine the time step starts at time 0 and ends at time 1 (in units of dt), and use subscripts to denote a variable at a given time. Variables with subscript 1/2 or 3/2 represent fields at half timesteps. The acceleration and Krook operators are thought of as acting on f_s as instantaneous "kicks" at times 0 and 1, leading to the notion of times 0^- and 0^+ immediately before and after time 0 (and similarly for time 1). A full timestep, including a Krook operator and transverse fields, is diagrammed in Fig. A-2. A listing of the operations involved in a timestep, in the order ELVIS performs them, is as follows (the initial parenthesized symbol is the shorthand used in Fig. A-2 for the operation):

1. Given: $f_{s,0^-}$, $n_{s,0}$, $E_{x,0}$, $E_0^{\pm}$, $v_{ys,0}$, $v_{ys,1/2}$.

2. (A_1) Accelerate $f_{s,0^-}$ to $f_{s,0^*}$, which requires $E_{x,0}$, $E_0^{\pm}$, and $v_{ys,0}$.
3. ($K_{1/2}$) Apply Krook operator for half timestep, taking $f_{s,0^*}$ to $f_{s,0^+}$.
4. (S_1) Free-stream $f_{s,0^+}$ by full timestep to $f_{s,1^*}$.
5. ($K_{1/2}$) Apply Krook operator for half timestep, taking $f_{s,1^*}$ to $f_{s,1^-}$.
6. Calculate $n_{s,1}$, ρ_1, and $E_{x,1}$ based on $f_{s,1^-}$.
7. Calculate $n_{s,1/2} = (1/2)(n_{s,0} + n_{s,1})$, density at half-step.
8. Calculate $J_{y,1/2} = \sum_s Z_s v_{ys,1/2} n_{s,1/2}$ at half timestep.
9. (M_1) Advance $E_0^{\pm}$ for full timestep to $E_1^{\pm}$, which includes applying the source $J_{y,1/2}$ at $t = 1/2$.
10. (A_{y1}) Accelerate $v_{ys,1/2}$ for full timestep to $v_{ys,3/2}$ and compute $v_{ys,1} = (1/2)(v_{ys,1/2} + v_{ys,3/2})$.
11. We have found: $f_{s,1^-}$, $n_{s,1}$, $E_{x,1}$, $E_0^{\pm}$, $v_{ys,1}$, $v_{ys,3/2}$.

A.4.2 Evolving f: splitting the time step

The Vlasov equation expresses the constancy of the number of particles along orbits, which are its characteristic curves. Taking a timestep in a continuum method like ELVIS consists of finding the new value of f at fixed phase-space gridpoints, given the old value at these same points (and the electromagnetic fields). This boils down to finding the value of f at the "foot" of the orbit that flows into the gridpoint in question at the new time. Since the foot is in general not a gridpoint, we can take a timestep by interpolating the old value of f at the foot. This interpolation, along with applying the Krook relaxation operator and advancing the electromagnetic fields, is the basis for ELVIS. A recent review and comparison of several time-evolution methods for electrostatic Vlasov problems is given in [120].

In ELVIS we organize the evolution of f with the time operator splitting method, first introduced by Cheng and Knorr for Eulerian Vlasov codes [121]. Operator splitting is a general technique for solving first-order time evolution PDEs; it was introduced in the West by G. Strang [122] and in the Soviet literature by N. Yanencko [123]. The goal is to form a second-order accurate time step for a composite time-evolution operator from second-order accurate steps for its "parts." Consider the equation

$$\frac{df}{dt} = Hf \tag{A.16}$$

where H is an operator and f is a vector (for continuum methods, it contains f at all the grid points of the discretized phase space). The exact solution for f with initial condition $f(t=0) = f_0$ is

$$f(t) = U(t) f_0, \qquad U(t) = \exp tH. \tag{A.17}$$

Suppose we have a numerical evolution operator for taking a single step $\tilde{U}(t)$ and $\tilde{f}(t) = \tilde{U}(t) f_0$ is the numerical solution. We say the method is n^{th} order accurate, or just n^{th}order, if $\tilde{f}(dt) - f(dt) = O(dt^{n+1})$. That is, the numerical and exact solution after a single step agree up to and including order n in dt. We can write $\tilde{U}(dt) = \exp(dt\ H) + O(dt^{n+1})$. Now consider a composite evolution operator,

$$\frac{df}{dt} = (H_1 + H_2)\, f, \tag{A.18}$$

where H_1 and H_2 may not commute. Suppose we have second-order numerical operators $\tilde{U}_1$ and $\tilde{U}_2$ for solving $d_t f = H_1 f$ and $d_t f = H_2 f$, respectively. The splitting theorem states that the operator

$$\tilde{U}(dt) = \tilde{U}_1(dt/2)\tilde{U}_2(dt)\tilde{U}_1(dt/2) \tag{A.19}$$

is a second-order accurate operator for the composite system A.18. This can be seen by computing $\tilde{U}(dt) - \exp dt(H_1 + H_2)$ and Taylor expanding. The expansion of the exponential of a sum of operators which do not commute is related to the Baker-Campbell-Hausdorff formula from Lie groups [124].

Upon discretizing phase space, our kinetic equation becomes

$$\frac{df}{dt} = (H_S + H_A + H_K)\, f \tag{A.20}$$

where $H_{S,A,K}$ are discretized analogs (in x and p, but not in time) of the free-streaming, acceleration, and Krook operators $-v\partial_x$, $-F\partial_{p_x}$ and $K[f]$, respectively. Let U_i be a second-order accurate operator for solving $d_t f = H_i f$ with $i = S,\ A,\ K$. We can apply the splitting theorem twice to arrive at a second-order accurate operator for the full equation:

$$\tilde{U}(dt) = \tilde{U}_S(dt/2)\ \tilde{U}_K(dt/2)\ \tilde{U}_A(dt)\ \tilde{U}_K(dt/2)\ \tilde{U}_S(dt/2) \tag{A.21}$$

For the time being we neglect the computation of the electromagnetic fields. When taking successive timesteps, the last $\tilde{U}_S(dt/2)$ of the first step is immediately followed by the first $\tilde{U}_S(dt/2)$ of the next step (evolving the e/m fields does not affect this). We combine these two steps into a single step $\tilde{U}_S(dt)$. The initial timestep is $\tilde{U}_S(dt/2)\ \tilde{U}_K(dt/2)$ while successive, interior stpes consist of $\tilde{U}_A(dt)\ \tilde{U}_K(dt/2)\ \tilde{U}_S(dt)\ \tilde{U}_K(dt/2)$. The state of f after an interior step is not quite what f is after a whole number of steps from $t = 0$, although this is when output is saved. This does *not* introduce any error into the numerical algorithm. We adopt this approach since it saves a substantial amount of runtime (roughly 1/3 of the runtime, since U_S and U_A take roughly the same time, and U_K takes much less).

A.4.3 Evolving f: shifting by interpolation

The operators H_S and H_A are both advection operators, and the corresponding numerical operators $\tilde{U}_S$ and $\tilde{U}_A$ in ELVIS use cubic spline interpolation to implement them. This subsection details the algorithm for H_S; the one for H_A is analogous.

The evolution equation for H_S is

$$\frac{\partial f}{\partial t} = -v\frac{\partial f}{\partial x}. \tag{A.22}$$

v is a spectator variable for the H_S evolution; we have an independent advection equation like this for every v. An obvious way to try parallelizing the code is to have the advection for different v performed on different processors. Given $f(x,t)$, after a time step dt the new $f\ (x, t + dt)$ is

$$f(x, t + dt) = f(x - v\, dt, t) \tag{A.23}$$

The evolution is nothing more than a shift in x. Let us discretize space, with x_i denoting a gridpoint and $f_i = f(x_i)$. The exact solution is $f_{i+1}(t + dt) = f(x_i - v\, dt, t)$. Since the right-hand side is generally not f evaluated at a gridpoint, we must approximate $f(x_i - v\, dt, t)$ given $\{f_i(t)\}$ for all

i. ELVIS achieves this by interpolation with cubic splines that involve the four gridpoints nearest x_i, taken in the direction appropriate to whether v is positive or negative.

For definiteness we consider in detail the case $v < 0$. We need an approximation to $f(x_i + \delta)$ with $\delta = |v\,|dt > 0$ (this definition with $|v|$ allows shifts for $v > 0$ to be written in a similar form). For spline interpolation, f is represented *at every gridpoint* by a cubic polynomial $F_i(x)$:

$$F_i(x) = f_i + p_i dx^{-1}\,(x - x_i) + s_i dx^{-2}\,(x - x_i)^2 + g_i dx^{-3}(x - x_i)^3. \tag{A.24}$$

$f_i = f\,(x_i)$ so by construction $F_i(x_i) = f(x_i)$. There are still $3N_x$ coefficients p_i, s_i, and g_i to determine, where N_x is the total number of x gridpoints. Equations for these coefficients are obtained by requiring the continuity of neighboring F_i's and several derivatives at the appropriate gridpoints. In particular, the matching conditions for F_{i-1} and F_i are $F_{i-1}(x_i) = F_i(x_i)$, $F'_{i-1}(x_i) = F'_i(x_i)$, and $F''_{i-1}(x_i) = F''_i(x_i)$. These equations hold for all "interior" gridpoints, and must be supplemented by boundary conditions at the edges of the grid. Evaluating the matching conditions gives the following system:

$$\begin{aligned} f_{i-1} + p_{i-1} + s_{i-1} + g_{i-1} &= f_i; & \text{(A.25)}\\ p_{i-1} + 2s_{i-1} + 3g_{i-1} &= p_i; & \text{(A.26)}\\ s_{i-1} + 3g_{i-1} &= s_i. & \text{(A.27)} \end{aligned}$$

Taking linear combinations of these equations at nearby gridpoints gives a tridiagonal system for the unknowns in terms of the known f_i's:

$$\begin{aligned} p_{i+1} + 4p_i + p_{i-1} &= -3f_{i-1} + 3f_{i+1}; & \text{(A.28)}\\ s_{i+1} + 4s_i + s_{i-1} &= 3f_{i-1} - 6f_i + 3f_{i+1}; & \text{(A.29)}\\ g_{i+1} + 4g_i + g_{i-1} &= -f_{i-1} + 3f_i - 3f_{i+1} + f_{i+2}. & \text{(A.30)} \end{aligned}$$

For interpolation to the right, we approximate $\bar{f}_i \equiv f(x_i + \delta)$ by

$$\bar{f}_i \approx F_i(x_i + \delta) = f_i + p_i\Delta + s_i\Delta^2 + g_i\Delta^3 \tag{A.31}$$

with $\Delta \equiv \delta/dx$. We can form a tridiagonal system for the $\bar{f}_i$, all shifted by the same δ from x_i, in terms of known quantities f_i, by taking $\bar{f}_{i-1} + 4\bar{f}_i + \bar{f}_{i+1}$. The result is

$$\bar{f}_{i-1} + 4\bar{f}_i + \bar{f}_{i+1} = a_{-2}f_{i+2} + a_{-1}f_{i+1} + a_0 f_i + a_1 f_{i-1}, \tag{A.32}$$

where

$$\begin{aligned} a_1 &= 1 - 3\Delta + 3\Delta^2 - \Delta^3, & \text{(A.33)}\\ a_0 &= 4 - 6\Delta^2 + 3\Delta^3, & \text{(A.34)}\\ a_{-1} &= 1 + 3\Delta + 3\Delta^2 - 3\Delta^3, & \text{(A.35)}\\ a_{-2} &= \Delta^3. & \text{(A.36)} \end{aligned}$$

For $v > 0$ the logic is similar and leads to the system

$$\bar{f}_{i-1} + 4\bar{f}_i + \bar{f}_{i+1} = a_{-2}f_{i-2} + a_{-1}f_{i-1} + a_0 f_i + a_i f_{i+1}. \tag{A.37}$$

The a's are defined *exactly as for* $v < 0$, with $\delta = |v\,|dt$ in both cases. The system for $\bar{f}_i$ can be

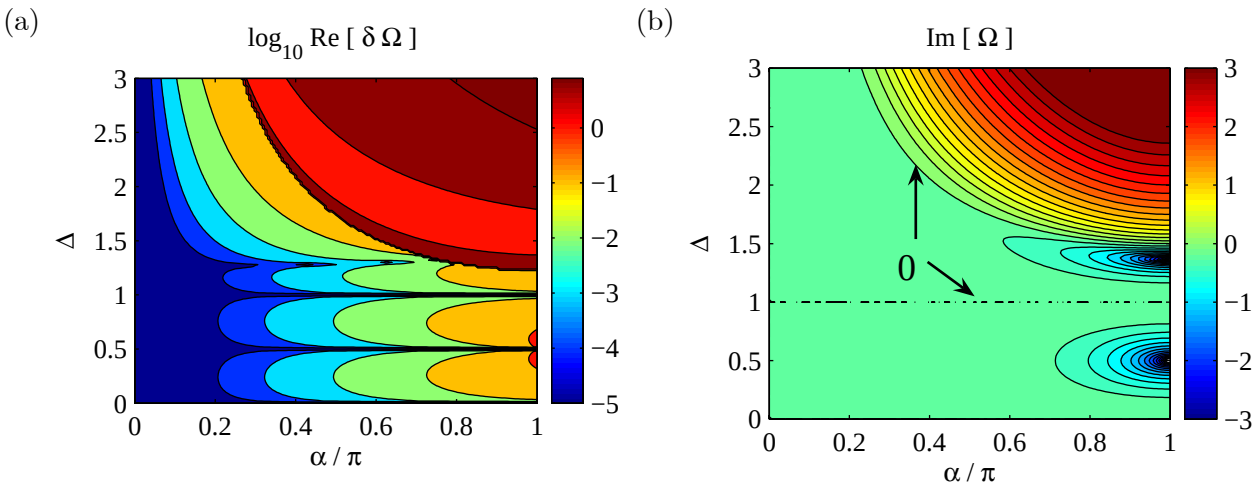

Figure A-3: (a) Dispersion error and (b) numerical damping/growth for cubic spline advection. In (b), $\mathrm{Im}\,\Omega < 0$ below the zero contour in the upper-right corner, and $\mathrm{Im}\,\Omega = 0$ for $\Delta = 1$.

written in matrix form, for both cases, as

$$T\bar{f} = A_{\pm} f. \tag{A.38}$$

T represents the tridiagonal 1-4-1 system on the LHS: $(T\bar{f})_i = \bar{f}_{i-1} + 4\bar{f}_i + \bar{f}_{i+1}$. $A_{\pm}$ represents the RHS and is

$$(A_{\pm} f)_i = a_{-2} f_{i\mp 2} + a_{-1} f_{i\mp 1} + a_0 f_i + a_1 f_{i\pm 1}. \tag{A.39}$$

$A_+ (A_-)$ applies for $v > 0$ ($v < 0$).

To understand the accuracy of spline advection, we perform the standard Fourier analysis of the method. The original PDE $\partial_t f = -v\partial_x f$, Eq. (A.22), is a linear, autonomous equation with exact pure Fourier solutions $f = \exp i(kx - \omega t)$ with $\omega = kv$ and $k > 0$, $v > 0$. The matrices T and $A_{\pm}$ acting on this solution become

$$T\bar{f} \quad \rightarrow \quad \hat{T}\bar{f} = (4 + 2\cos\alpha)\bar{f} \tag{A.40}$$

and

$$A_{\pm} f \quad \rightarrow \quad \hat{A}_{\pm} f = \left(a_{-2} e^{\mp 2i\alpha} + a_{-1} e^{\mp i\alpha} + a_0 + a_1 e^{\pm i\alpha}\right) f \tag{A.41}$$

where $\alpha \equiv k\,dx$. $\hat{T}$ and $\hat{A}_{\pm}$ are scalars, not matrices. They depend only on α and $\Delta = |v|dt/dx$. Our time advance states $f(t + dt) = \bar{f}(t)$. For the pure Fourier solution, this reads $f(t)\exp(-i\omega\,dt) = \bar{f}(t)$, or

$$e^{-i\Omega} = \frac{\hat{A}_{\pm}}{\hat{T}} \tag{A.42}$$

with $\Omega \equiv \omega\,dt$. Eq. (A.42) furnishes $\Omega(\alpha, \Delta)$. The Fourier solution is recovered if $\Omega = kv\,dt = \alpha\Delta$, or $\delta\Omega \equiv \Omega - \alpha\Delta = 0$. $\mathrm{Re}[\delta\Omega]$ indicates a phase or dispersive error, while $\mathrm{Im}[\Omega]$ constitutes numerical damping or growth.

Figure A-3 shows (a) $\mathrm{Re}[\delta\Omega]$ and (b) $\mathrm{Im}[\Omega]$ for a range of α and Δ. Since $k = \pi/dx$ is the highest k we can resolve on the grid (the Nyquist k) we only need to go up to $\alpha = \pi$. For electromagnetic runs $dx = c\,dt$ so that $\Delta = v/c < 1$; for electrostatic runs dt and dx are chosen independently,

and Δ can exceed unity. The phase dispersion is very small except for the upper-right corner of panel (a). Similarly, Im[Ω] is always negative outside this region, which indicates cubic spline advection introduces numerical damping rather than growth. Growth, and thus possibly numerical instability, do occur for $\Delta \gtrsim 1.5$ for high α. We have not observed any loss of accuracy or instability in electrostatic runs when $\Delta > 1.5$. Note that for $\Delta = 1$, corresponding to a shift by exactly one grid point, there is no frequency error: $\Omega = \alpha$.

A.4.4 Evolving f: the Krook operator

For the Krook operator K_s, the numerical evolution operator $\tilde{U}_K$ must be a second-order accurate solution to $\partial f/\partial t = -\nu(x)\left(f - n\tilde{f}_{0K}\right)$. Since the Krook operator does not change the density, we treat n as a constant. The exact solution to this equation is

$$f(t) = f(0)e^{-\nu t} + n\tilde{f}_{0K}(1 - e^{-\nu t}). \tag{A.43}$$

We use this for the Krook time evolution operator; since it is the exact solution, it is certainly second-order accurate. For more analysis of operator splitting that involves damping terms like the Krook operator, see Ref. [125]. Note that $\tilde{f}_{0K}$ needs to be normalized to unity, and this is done numerically at the start of the run. That is, we calculate an unnormalized form of $\tilde{f}_{0K}$ and then divide by the density computed from this distribution. For instance, to use a Maxwellian $\tilde{f}_{0K}$ first set $\tilde{f}_{0K} = \exp(-v^2/(2v_T^2))$, numerically calculate the density with the same algorithm that is used during a time step, and then normalize $\tilde{f}_{0K}$. When an unnormalized $\tilde{f}_{0K}$ is used, such as a Maxwellian that is analytically normalized over an infinite velocity domain (that is, $\int_{-\infty}^{\infty} dv \tilde{f}_{0K} = 1$), it will not be exactly normalized according to the density calculation routine. A steady loss of particles results in this case, but it does not for a numerically normalized $\tilde{f}_{0K}$.

A.4.5 Solving for E_x

We need to find E_x over the whole spatial grid. ELVIS contains two methods for finding E_x: one based on Fourier series and another based on finite differences. The Fourier method can only be used for periodic systems, while the finite-difference method can be used for periodic or non-periodic ones. The runs in this thesis were computed with the finite-difference method.

Finite-difference method

This method was suggested by A. B. Langdon and is based on finding E_x at fictitious half-gridpoints. We first find E_x at the half-points through a centered finite-difference discretization of Gauss' law:

$$E_{x,i+1/2} - E_{x,i-1/2} = dx\ \rho_i. \tag{A.44}$$

$E_{x,i}$ at the gridpoints is found by averaging:

$$E_{x,i} = \frac{1}{2}(E_{x,i+1/2} + E_{x,i-1/2}) \tag{A.45}$$

An additional boundary condition is needed to solve for E_x at the half-gridpoints. For periodic systems, $E_x(x+L) = E_x(x)$. With $x = dx/2$, and recalling there are N_x distinct points on the grid,

we find $E_{x,N_x+1/2} = E_{x,1/2}$. The system of equations at the half-gridpoints can be put in matrix form:

$$ME = \rho \tag{A.46}$$

where

$$M = \begin{bmatrix} -1 & 1 & 0 & & & \\ 0 & -1 & 1 & 0 & & \\ & & ... & & & \\ & & & 0 & -1 & 1 \\ 1 & 0 & 0 & 0 & 0 & -1 \end{bmatrix}, \tag{A.47}$$

$$E = [E_{1/2}, E_{3/2}, ..., E_{N_x-1/2}], \tag{A.48}$$

$$\rho = [\rho_1 ... \rho_{N_x}]. \tag{A.49}$$

The blank entries in M are zero. As it stands this system has the same number of equations as unknowns, but M is non-invertible. This reflects the fact that we have not yet completely imposed boundary conditions for Gauss' law. We apply so-called "short-circuit" boundary conditions [112], which stipulates that the electrostatic potential ϕ is periodic. Integrating $E_x = -\partial_x \phi$ over the periodic domain gives the average value of E_x must be zero. We arbitrarily set $E_{x,1/2}$ to zero, which allows us to solve the system Eq. (A.46) from the first column down, and then offset the resulting E_x to ensure it has zero average.

To find the accuracy of this method, consider interior points and let $e_i = E_{x,i} - E_x(x_i)$ be the error. $E_{x,i}$ is the numerical result, and $E_x(x_i)$ the exact one. Then

$$e_i = E_{x,i-1/2} + \frac{dx}{2}\rho_i - E_x(x_i). \tag{A.50}$$

Assume $E_{x,i-1/2}$ is the exact result $E_x(x_i - dx/2)$. What error results in $E_{x,i}$? By Taylor expanding $E_{x,i-1/2}$, we find $e_i = (dx^2/8)E_i''(x_i)$. The error is thus second-order in dx.

Fourier method

For a periodic system, we can solve Gauss' law directly in wavenumber space. Integrating Gauss' law over the periodicity length L gives $E_x(L) - E_x(0) = \varepsilon_0^{-1} Q$ where $Q = \int_0^L \rho \, dx$ is the total system charge. If E_x is periodic, $E_x(L) = E_x(0)$, and $Q = 0$. We set the $k = 0$ mode of $\rho(k)$ to zero. The Fourier algorithm is thus:

- Given $\rho(x)$.
- Find $\tilde{\rho}(k) = \text{fft}(\rho(x))$ and set $\tilde{\rho}(0) = 0$.
- Find $\tilde{E}(k \neq 0) = -(i/k)\tilde{\rho}(k)$ and $\tilde{E}(0) = 0$.
- Find $E(x) = \text{ifft}(\tilde{E}(k))$.

fft denotes the fast Fourier transform and is computed with the FFTW library [126].

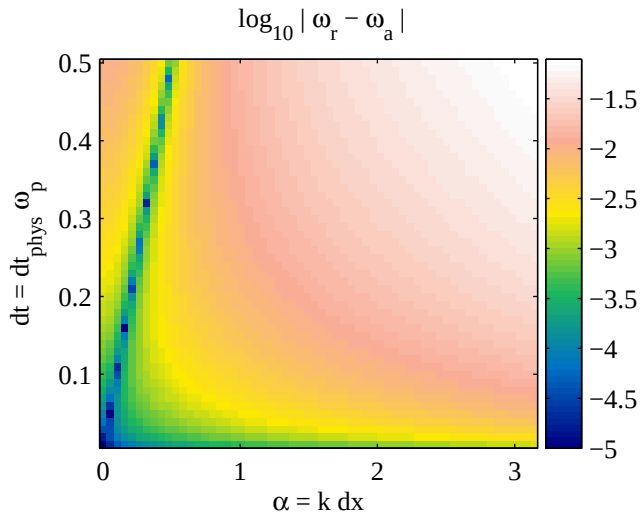

Figure A-4: Phase error for the Langdon-Dawson method used to advance the transverse fields v_{ye} and $E^{\pm}$. The error becomes large exactly at $\alpha = \pi$ (not shown; the absissa ends at $\alpha = 3.14$).

A.4.6 Evolving the transverse fields

As discussed in the overall time step, the transverse fields v_{ys} and $E^{\pm}$ are used in the force that accelerates f from time 0^- to 0^*, while the current density J_y acts as a source for $E^{\pm}$ at time $dt/2$. We need v_{ys} at both the full and half timesteps. To do this, we evolve v_{ys} from one half timestep to another, and average these values to find v_{ys} at the full timesteps. Advancing v_{ys} is done with a forward Euler step:

$$v_{ys}(3dt/2) = v_{ys}(dt/2) + dt\frac{Z_s}{\mu_s}E_y(dt). \tag{A.51}$$

The fields $E^{\pm}$ are advanced following the Langdon-Dawson method, described on p. 133 of [112]:

$$E^{\pm}(x, t + dt) = E^{\pm}(x \mp dx, t) - dt\, J_y(x \mp dx/2, t + dt/2). \tag{A.52}$$

This approach requires $dt = dx$, and corresponds to a shift of one gridpoint in the absence of J_y. Discretizing Eq. (A.52) yields

$$E_i^{\pm}(dt) = E_{i\mp1}^{\pm}(0) - dt\, J_{y,i\mp1/2}(dt/2). \tag{A.53}$$

$J_{y,i\mp1/2}(dt/2)$ is found by averaging: $J_{y,i\mp1/2}(dt/2) = (1/2)(J_{y,i}(dt/2) + J_{y,i\mp1}(dt/2))$. To compute $J_y(dt/2)$ we need both $v_y(dt/2)$ and $n_s(dt/2)$. We store v_y at half timesteps so we have the former, but we only know f_s at the full timesteps. We average to find $n_s(dt/2) = (1/2)(n_s(dt) + n_s(0))$.

The advantage of this method for the transverse dynamics is that it has no numerical dissipation and very little dispersion error. This is related to the similar behavior of cubic spline interpolation for a shift of one gridpoint. To see this, consider just the transverse evolution, for only electrons, and set $n_e = 1$ (constant). This is sufficient to produce EMW's in a plasma, which do not involve

any density perturbation. The governing PDEs, with $J_y = -v_{ye}$, are

$$(\partial_t \pm \partial_x) E^{\pm} = v_{ye}, \tag{A.54}$$

$$\partial_t v_{ye} = -\frac{1}{2}\left(E^+ + E^-\right). \tag{A.55}$$

Fourier analyzing the system gives the familiar EMW dispersion relation $\omega^2 = 1 + k^2$. How good is our numerical method at reproducing this? The evolution of Fourier modes $E^{\pm} = \mathcal{E}^{\pm} \exp i(kx - \omega t)$ and $v_{ye} = V e^{-i\omega dt/2} \exp i(kx - \omega t)$ under the discretized algorithm can be written after some algebra as

$$\begin{bmatrix} \frac{dt}{2} g_\omega & \frac{dt}{2} g_\omega & g_\omega - 1 \\ g_k g_\omega - 1 & 0 & -\frac{dt}{2}(1 + g_k) \\ 0 & g_\omega - g_k & -\frac{dt}{2}(1 + g_k) \end{bmatrix} \begin{bmatrix} \mathcal{E}^+ \\ \mathcal{E}^- \\ V \end{bmatrix} = 0. \tag{A.56}$$

$g_k \equiv e^{ikdx}$ and $g_\omega \equiv e^{-i\omega dt}$.

The dispersion relation obtains by setting the determinant of the matrix to zero. This gives

$$g_\omega + 2\Lambda g_\omega + 1 = 0, \tag{A.57}$$

$$\Lambda \equiv \frac{dt^2}{4}(1 + \cos\alpha) - \cos\alpha. \tag{A.58}$$

Eq. (A.57) gives ω in terms of α and dt (recall we work in normalized units where $c = \omega_p = 1$). There is no dissipation if ω is real, or equivalently if $|g_\omega| = 1$. By examining the discriminant $(\Lambda^2 - 1)$ it is easy to show that $|g_\omega| = 1$ for all α provided $dt < 2$. In physical units this restricts us to timesteps $dt_{\rm phys}\omega_p < 2$, which is irrelevant: we always choose $dt_{\rm phys} \ll 1/\omega_p$ or plasma oscillations would not be resolved! There is, however, some numerical dispersion, although it is small. Figure A-4 plots the phase error $|\,\mathrm{Re}[\omega] - \omega_a|$ where $\omega_a = (1 + k^2)^{1/2}$ is the analytic EMW frequency for the original PDEs.

A.5 Code logistics

ELVIS is written in Fortran 95 and uses C-style pre-processing. General aspects of a run (such as whether it is electrostatic or electromagnetic, how to solve for E_x, whether to include a Krook operator) are specified in the header file run.h. Input is done via the file run.F90. This itself is a Fortran source file, with variable declarations, so mistakes made in modifying it can prevent the code from compiling. The code is recompiled every time it is run with different input.

ELVIS saves its output to binary files ending in .dat. There is also one text file readme.dat which contains header info about the run and a user-specified trace of information printed out every several timesteps. There is an extensive set of Matlab scripts for doing post-processing. Runs do not have to finish for the output data files to be loaded and processed in Matlab.

A.6 Diagnostics

This section describes some of the diagnostics used to check and process ELVIS output. All ELVIS post-processing is done with Matlab scripts.

A.6.1 Conserved quantities

Conservation laws are important for understanding physics as well as checking the accuracy of a numerical code. We discuss here some conserved quantities for nonrelativistic, electrostatic ELVIS simulations (no transverse fields), with no Krook operator or external drive, and only electrons mobile. We assume the boundary conditions are such that boundary effects do not change these relations (for instance, particles are not lost by leaving the simulation domain). Periodic boundaries are one way to ensure this.

The electrostatic Vlasov-Poisson system conserves many integrated functionals I_g of the distribution, where

$$I_g = \int dx\, dv\, g(f) \tag{A.59}$$

and g is an ordinary function. $d_t I_g$ is given by

$$\begin{aligned}
\frac{dI_g}{dt} &= \int dx\, dv\, g'(f)\partial_t f && \text{(A.60)}\\
&= \int dx\, dv g'(f)(-v\partial_x f - a\partial_v f) && \text{(A.61)}\\
&= \int dx\, dv\, (-v\partial_x g - a\partial_v g) && \text{(A.62)}\\
&= -\int dv\, v\ \ g|_{x_1}^{x_2} - \int dx\, a\ \ g|_{v_1}^{v_2}\,. && \text{(A.63)}
\end{aligned}$$

As long as the differences of g at the endpoints vanish, $d_t I_g = 0$. Commonly used functionals that result from $g(f) = f$, f^2, and $-f\log f$ are, respectively, the number $N = \int dx\, dv\, f$, the square integral or L_2 norm $F_2 = \int dx\, dv\, f^2$, and the entropy $S = -\int dx\, dv\, f \log f$. When computing S numerically we neglect points with $f < 0$, which can develop due to cubic spline interpolation.

Momentum and energy conservation are also important, and are found by taking moments of f against v and v^2. For electrostatic systems the electric field E_x carries no momentum, so the momentum $P \equiv \int dx\, dv\, f\, mv$ and $d_t P = \int dx\, nma$. This simply states that the rate of change of electron momentum is given by the integral of the force density. It is important to realize that in simulations with fixed ions momentum is *not* conserved. Physically, for any force experienced by the electrons an equal and opposite reaction force is felt by the ions. When ions are allowed to move the total electron and ion momentum is conserved. E_x carries energy, and the conserved energy is $W = W_K + W_E$ where $W_K \equiv \int dx\, dv\, (mv^2/2)f$ is the kinetic energy and $W_E \equiv \int dx\, (\varepsilon_0/2)E^2$ is the electrostatic energy. Energy is exchanged between the two components via Joule heating: $d_t W_K = -d_t W_E = \int dx\, JE$ with $J = -e\int dv\, fv$ the electric current. These conservation laws can easily be extended to include the transverse electromagnetic fields. Care must be taken in accounting for boundary contributions, both due to light waves leaving the domain and external injection of light waves (such as the pump and seed in SRS runs). In addition, our Krook operator conserves number but neither momentum nor energy.

A.6.2 Instantaneous frequency

Given a time signal $f(t)$, we sometimes wish to imagine it as having a single, time-varying frequency. For instance, in the SRS run `BC1` the streaked E^- spectrum in Fig. 3-4(b) shows an upshift of ω_1

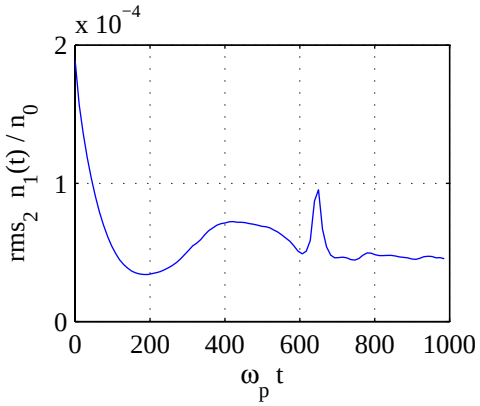

Figure A-5: Density perturbation $n_1 = n_e - n_0$ near box center for run `ES`.

with time. Of course, we can Fourier analyze the signal over the whole time interval, and find the signal is not monochromatic. But it is illuminating to see what the main frequency is at a given time, or the "instantaneous frequency." The windowed Fourier transform used to make streaked spectra like 3-4(b) gives a rough sense of this, but has limited frequency resolution and does not clearly indicate the main frequency.

The idea is to relate the instantaneous frequency $\omega(t)$ to the instantaneous period $\tau(t)$, or time between successive maxima of f. We know f only at a set of discrete points; we assume the sampling rate is sufficient to adequately resolve the maxima in f. We determine if a time point is a "near-maximum" by examining it and its nearby neighbors. We then approximate the time for which f is a maximum by fitting a polynomial (usually 4^{th} order) to a set of points (usually 9) around the near-maximum point. Doing this for all numerical near-maxima gives a list of times f is a maximum. From this we deduce τ as the difference between successive times, and thus ω. When ω varies slowly with respect to τ we sometimes average ω over several successive times to smooth the resulting figures.

A.7 Benchmarks

This section contains periodic, electrostatic simulations to demonstrate ELVIS's performance for electron plasma waves (EPWs) and ion acoustic waves (IAWs).

A.7.1 Electron dynamics: plasma waves and recurrence

The electron dynamics are illustrated in the electrostatic run labeled `ES`, which simulates a periodic, fixed-ion plasma with $n_0 = 5 \times 10^{26}$ m^{-3} and $T_e = 2$ keV. The plasma extends for one wavelength λ corresponding to $k\lambda_D = 0.3$. The grid spacings are $dx = \lambda/50$, $dt = 0.2/\omega_p$, and $dp_e = 2 \times 10^{-3} m_e c$. The plasma initially has a Maxwellian distribution but a perturbed density $n_e(t = 0) = n_0(1 + \varepsilon \sin kx)$ with $\varepsilon = 2 \times \times 10^{-3}$. This initial condition generates a standing wave, or two oppositely-travelling waves each with half the amplitude. Figure A-5 graphs the density perturbation $n_1 = n_e - n_0$ near the box center. Three separate phenomena are visible. Initially

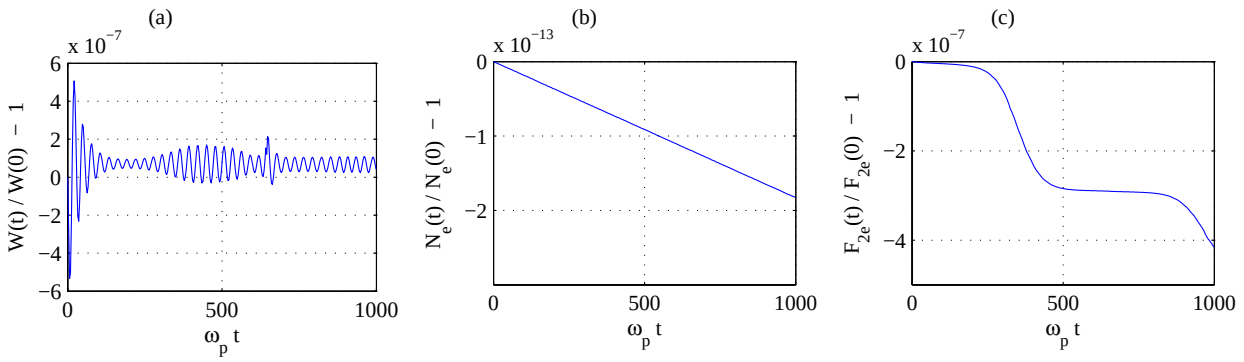

Figure A-6: Relative changes in (a) total energy W, (b) electron number N_e, and (c) electron L_2 norm F_{2e} for run `ES`.

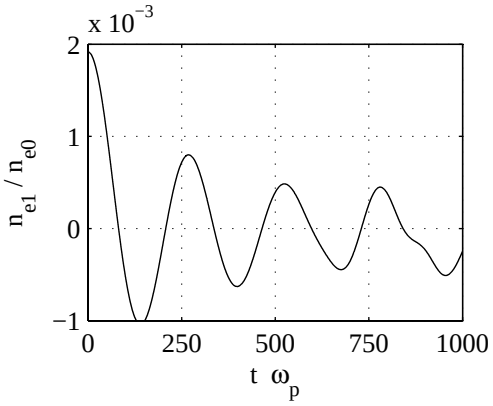

Figure A-7: Density perturbation at $x = 0.296\lambda$ for mobile-ion run IAW.

the wave is Landau damped, with an amplitude e-folding time of $79.2\omega_p^{-1}$. The bounce period of trapped electrons in the initial traveling-wave amplitude is $\tau_B = 199\omega_p^{-1}$, which leads to the rebound in wave amplitude (see Chap. 4 for a full discussion). Finally, at the recurrence time $t_{\rm rec} = \lambda/dv = 654\omega_p^{-1}$ the amplitude suddenly spikes up. The conservation properties of ELVIS are demonstrated in Fig. A-6, which presents the relative changes in total energy W, electron number N_e, and L_2 norm F_{2e}.

A.7.2 Ion dynamics: ion acoustic waves

ELVIS can in principle handle an arbitrary number of kinetic species, although all work in this thesis includes at most one mobile ion species. All kinetic species are updated with the same numerical algorithm. As a benchmark of the ion dynamics, consider IAWs generated by an initial density perturbation similar to the EPW excitation in the prior subsection. We excite IAWs with an initial sinusoidal perturbation to both the electron and ion densities at $t = 0$. The distributions are initially Maxwellian. The linear theory of IAWs states the ion density fluctuation n_{i1} slightly overshoots the electrons due to larger ion inertia. In particular, $|n_{i1}| = (|n_{ei}|/Z_i)(1 + (k\lambda_D)^2)$. We use this ratio for the applied density fluctuations, so that the excited EPW is minimal.

The periodic, electrostatic run `IAW` demonstrates ELVIS gives the correct IAW dispersion be-

havior. The parameters are $n_0 = 5 \times 10^{26}$ m^{-3}, $T_e = 2$ keV, $Z_i = 2$, $m_i = 200m_e$, and $T_i = 500$ eV. We use a small mass ratio so we do not have to run for long times to resolve IAW periods and to avoid recurrence effects in the electron motion. For the wave, we choose $k\lambda_D = 0.2$ and a traveling-wave amplitude $n_{e1} = 10^{-3}n_0$. The kinetic IAW dispersion relation gives the complex root $\omega/\omega_p = 0.0243 - 1.90 \times 10^{-3}i$. The electron perturbation n_{e1} at one location is plotted in Fig. A-7 and displays IAW oscillation and damping. The time and relative heights of the 2$^{\text{nd}}$ and 3$^{\text{rd}}$ maxima (slightly after $t\omega_p = 250$, 500) give a numerical frequency of $\omega_{\text{num}}/\omega_p = 0.0244 - 1.94 \times 10^{-3}i$, very close to the linear value. The departure from a damped sinusoid for late times is due to harmonic generation and numerical recurrence.

Appendix B

Plasma Waves Driven by Two Light Waves

This appendix derives the linear electron plasma waves driven by the beating of two light waves from a kinetic description. The two light waves, labeled 0 and 1, propagate in the x direction and are linearly polarized in y. The resulting electric and magnetic fields are

$$E_y = \frac{1}{2}\tilde{E}_{y0}e^{\iota\psi_0} + cc + \frac{1}{2}\tilde{E}_{y1}e^{\iota\psi_1} + cc; \tag{B.1}$$

$$B_z = \frac{1}{2}\tilde{B}_{z0}e^{\iota\psi_0} + cc + \frac{1}{2}\tilde{B}_{z1}e^{\iota\psi_1} + cc. \tag{B.2}$$

$\psi_j \equiv (k_j x - \omega_j t)$ is the wave phase. We represent any physical field g in the Fourier domain by $g = (1/2)\tilde{g}e^{i\theta} + cc$ where θ is a real phase. The light waves induce a transverse electron oscillation velocity. The cold fluid y momentum equation, equivalent to conservation of canonical y momentum, is

$$\partial_t v_y = -\frac{e}{m_e}E_y. \tag{B.3}$$

In the Fourier domain this gives, for a single light wave $j = 0, 1$, $\tilde{v}_{yj} = -ie/(m_e\omega_j)\tilde{E}_{yj}$. The z component of Faraday's law $\partial_t B_z = -\nabla \times \vec{E}$ gives $\tilde{B}_{zj} = (k_j/\omega_j)\tilde{E}_{yj}$, or $\tilde{B}_{zj} = i(m_e/e)k_j\tilde{v}_{yj}$.

The light waves exert a ponderomotive force in the x direction via the $\vec{v}\times\vec{B}$ force. This produces several drive terms with all phases $\pm\psi_i \pm \psi_j$ (all four sign choices are driven). Only the drives with frequencies near ω_p excite an appreciable plasma response. We take $\omega_0 - \omega_1 \approx \omega_p$ and focus on the phase $\psi \equiv (kx - \omega t) = \psi_0 - \psi_1$. This choice resembles the EPW (mode 2) in SRS, which satisfies $\psi_2 = \psi_0 - \psi_1$.

The 1-dimensional non-relativistic Vlasov equation for electrons is

$$\left[\partial_t + v\partial_x + a\partial_v\right] f_e = 0. \tag{B.4}$$

The x acceleration a is

$$a = -\frac{e}{m_e}(E_x + v_y B_z). \tag{B.5}$$

E_x is the self-consistent longitudinal electric field given by Gauss' law:

$$\partial_x E_x = -\frac{e}{\varepsilon_0} n_1. \tag{B.6}$$

The total electron density $n_e = n_0 + n_1$ where n_0 is cancelled by a stationary ion background and $n_1 = (1/2)\tilde{n}_1 e^{i\psi_0} + cc$. We write $f_e = f_0 + (1/2)\tilde{f} e^{i\psi} + cc$ where $f_0(v)$ is the homogeneous equilibrium. f_e has units of 1/(speed * volume). The density perturbation is related to the perturbed distribution by

$$\tilde{n}_1 = \int_{-\infty}^{\infty} dv\ \tilde{f}. \tag{B.7}$$

In the Fourier domain, $E_x = (1/2)\tilde{E}_x e^{i\psi} + cc$ and $\tilde{E}_x = (ie/\varepsilon_0 k)\tilde{n}_1$.

The resonant part of $v_y B_z$ which drives an EPW with phase ψ is

$$[v_y B_z]_{\text{res}} \equiv \frac{1}{2}\alpha_{\text{res}} e^{i\psi}, \qquad \alpha_{\text{res}} = \frac{1}{2}\left(\tilde{v}_{y0}\tilde{B}^*_{z1} + \tilde{v}^*_{y1}\tilde{B}_{z0}\right). \tag{B.8}$$

We drop the nonresonant terms in $v_y B_z$ from the acceleration a. We now linearize the Fourier-domain Vlasov equation, treating all the remaining terms in a as the same order as $\tilde{f}$. We keep only terms with phase $e^{i\psi}$:

$$-i(\omega - kv)\tilde{f} - \left(i\frac{\omega_p^2}{n_0 k}\tilde{n}_1 + \frac{e\alpha_{\text{res}}}{m_e}\right) f_0' = 0, \tag{B.9}$$

with $f_0' = df_0/dv$ and $\omega_p^2 = n_0 e^2/(\varepsilon_0 m_e)$. We divide through by $(\omega - kv)$ and integrate over v:

$$-i\tilde{n}_1 - \left(i\frac{\omega_p^2}{n_0 k}\tilde{n}_1 + \frac{e\alpha_{\text{res}}}{m_e}\right)\int_{-\infty}^{\infty} dv \frac{f_0'}{\omega - kv} = 0. \tag{B.10}$$

The integral can be expressed in terms of the susceptibility χ, given in the thesis preamble:

$$\chi = \frac{\omega_p^2}{k^2 n_0}\int_{-\infty}^{\infty} dv \frac{f_0'}{v_p - v}. \tag{B.11}$$

$v_p \equiv \omega/k$ is the EPW phase velocity. Eq. (B.10) becomes

$$-i\tilde{n}_1 - \left(i\tilde{n}_1 + \frac{n_0 k e}{\omega_p^2 m_e}\alpha_{\text{res}}\right)\chi = 0. \tag{B.12}$$

Rearranging, this yields

$$\hat{\varepsilon}\tilde{n}_1 = i\frac{n_0 k e}{\omega_p^2 m_e}\chi\alpha_{\text{res}}, \tag{B.13}$$

where $\hat{\varepsilon} \equiv 1 + \chi$ is the unitless permittivity.

It is helpful to write α_{res} in terms of $\tilde{v}_{yj}$:

$$\alpha_{\text{res}} = \frac{i}{2}\frac{m_e}{e} k \tilde{v}_{y0}\tilde{v}^*_{y1}. \tag{B.14}$$

We used the fact that $k = k_0 - k_1$. Inserting this into Eq. (B.13) yields

$$\hat{\varepsilon}\frac{\tilde{n}_1}{n_0} = -\frac{1}{2}\left(k\lambda_D\right)^2 \chi \frac{\tilde{v}_{y0}\tilde{v}_{y1}^*}{v_{Te}^2}. \tag{B.15}$$

The driven-wave amplitude $\hat{n} \equiv |\tilde{n}_1|/n_0$ satisfies

$$\hat{n} = \frac{1}{2}\left(k\lambda_D\right)^2 \left|\frac{\chi}{\hat{\varepsilon}}\right| \frac{v_{os0}v_{os1}}{v_{Te}^2}. \tag{B.16}$$

$v_{osi} = |\tilde{v}_{yi}|$. In terms of a light wave's intensity I, vacuum wavelength λ_v, and index of refraction η,

$$\left(\frac{v_{osi}}{c}\right)^2 = 7.3 \times 10^{-4} \frac{I_{15}\lambda_{v,\mu}^2}{\eta}. \tag{B.17}$$

I_{15} is in units of 10^{15} W/cm^2 and $\lambda_{v,\mu}$ is in microns. We can approximate χ and $\hat{\varepsilon}$ for the case that the beat mode (k, ω) is a weakly-damped natural mode. In particular, $\hat{\varepsilon}_r(k, \omega) = 0$. In this limit, $\chi \to -1$, $\hat{\varepsilon} \to i\hat{\varepsilon}_i$, and $\hat{\varepsilon}_i = 2\nu/\omega_p$ where ν is the EPW's temporal damping rate. Eq. (B.16) becomes

$$\hat{n} \approx \frac{1}{4}\left(k\lambda_D\right)^2 \frac{\omega_p}{\nu} \frac{v_{os0}v_{os1}}{v_{Te}^2}. \tag{B.18}$$

Bibliography

[1] D. J. Strozzi, A. K. Ram, and A. Bers, Phys. Plasmas **10**, 2722 (2003).

[2] M. Abramowitz and I. A. Stegun, *Handbook of Mathematical Functions*, Dover Publications, Inc., New York, NY, 1970.

[3] B. D. Fried and S. D. Conte, *The Plasma Dispersion Function: The Hilbert Transform of the Gaussian*, Academic Press, New York, 1961.

[4] V. N. Faddeeva and N. N. Terent'ev, *Tables of Values of the function* $w(z) = e^{-z^2}(1 + (2i/\sqrt{\pi}) \int_0^z e^{t^2}\, dt$ *for complex argument*, Gosud. Izdat. Teh-Teor. Lit., Moscow, 1954, English translation, Pergamon Press, New York, 1961.

[5] J. A. C. Weideman, SIAM J. Numer. Anal. **31**, 1497 (1994).

[6] G. R. Smith, Phys. Fluids **27**, 1499 (1984).

[7] H. Schamel, Phys. Plasmas **7**, 4831 (2000).

[8] D. W. Forslund and P. D. Goldstone, Los Alamos Science, p. 4 (Spring/Summer 1985), available at `http://library.lanl.gov/cgi-bin/getfile?00326952.pdf`.

[9] J. Lindl, Phys. Plasmas **2**, 3933 (1995).

[10] J. Lindl et al., Phys. Plasmas **11**, 339 (2004).

[11] J. C. Fernández, J. A. Cobble, D. S. Montgomery, M. D. Wilke, and B. B. Afeyan, Phys. Plasmas **7**, 3743 (2000).

[12] B. I. Cohen, B. F. Lasinski, A. B. Langdon, and E. A. Williams, Phys. Plasmas **4**, 956 (1997).

[13] A. V. Maximov, R. M. Oppitz, W. Rozmus, and V. T. Tikhonchuk, Phys. Plasmas **7**, 4227 (2000).

[14] E. A. Williams et al., Phys. Plasmas **11**, 231 (2004).

[15] C. M. Aldrich, B. Bezzerides, D. F. DuBois, and H. A. Rose, Comments Plas. Phys. Controlled Fusion **10** (1986).

[16] E. S. Dodd, B. Bezzerides, D. DuBois, and H. X. Vu, presented at the 35^{th} Annual Anomalous Absorption Conference, Fajardo, Puerto Rico, USA, 2005.

[17] M. V. Goldman and D. F. DuBois, Phys. Fluids **8**, 1404 (1965).

[18] T. O'Neil, Phys. Fluids **8**, 2255 (1965).

[19] L. M. Al'tshul' and V. I. Karpman, Sov. Phys. JETP **22** (1966).

[20] V. E. Zakharov and V. I. Karpman, JETP **16**, 351 (1963).

[21] P. M. Platzman and S. J. Buchsbaum, Phys. Fluids **4**, 1288 (1961).

[22] D. W. Forslund, J. M. Kindel, and E. L. Lindman, Phys. Fluids **18**, 1002 (1975).

[23] D. W. Forslund, J. M. Kindel, and E. L. Lindman, Phys. Fluids **18**, 1017 (1975).

[24] J. F. Drake et al., Phys. Fluids **17**, 778 (1974).

[25] B. I. Cohen and A. N. Kaufman, Phys. Fluids **20**, 1113 (1977).

[26] G. J. Morales and T. M. O'Neil, Phys. Rev. Lett. **28**, 417 (1972).

[27] B. I. Cohen and A. N. Kaufman, Phys. Fluids **21**, 404 (1978).

[28] K. Estabrook, W. L. Kruer, and B. F. Lasinski, Phys. Rev. Lett. **45**, 1399 (1980).

[29] K. Estabrook and W. L. Kruer, Phys. Rev. Lett. **53**, 465 (1984).

[30] D. J. Kaup, A. Reiman, and A. Bers, Rev. Mod. Phys. **51**, 275 (1979), erratum **51**, 915 (1979). Note: The reprint from Rev. Mod. Phys. incorporates all the corrections indicated in the published erratum.

[31] M. N. Rosenbluth, Phys. Rev. Lett. **29**, 565 (1972).

[32] D. F. DuBois, D. W. Forslund, and E. A. Williams, Phys. Rev. Lett. **33**, 1013 (1974).

[33] F. W. Chambers and A. Bers, Phys. Fluids **20**, 466 (1977).

[34] D. R. Nicholson and A. N. Kaufman, Phys. Rev. Lett. **33**, 1207 (1974).

[35] D. R. Nicholson, Phys. Fluids **19**, 889 (1976).

[36] A. Reiman, Rev. Mod. Phys. **51**, 311 (1979).

[37] L. Friedland, Phys. Rev. Lett. **69**, 1749 (1992).

[38] C. C. Chow, A. Bers, and A. K. Ram, Phys. Rev. Lett. **68**, 3379 (1992).

[39] A. Salcedo, *Coupled Modes Analysis of SRS Backscattering, with Langmuir Decay and Possible Cascadings*, PhD thesis, Electrical Engineering and Computer Science Department, Massachusetts Institute of Technology, 2001.

[40] A. Salcedo, R. J. Focia, A. K. Ram, and A. Bers, Nucl. Fusion **43**, 1759 (2003).

[41] S. J. Karttunen, Phys. Rev. A **23** (1981).

[42] J. A. Heikkinen and S. J. Karttunen, Phys. Fluids **29**, 1291 (1986).

[43] G. Bonnaud and D. Pesme, Stimulated raman scattering and ion dynamics: the role of langmuir wave non-linearities, in *Proc. 8th Int. Workshop on Laser Interaction and Related Plasma Phenomena (Monterey, California, 1987)*, volume 8, page 375, New York, 1988, Plenum.

[44] G. Bonnaud, D. Pesme, and R. Pellat, Phys. Fluids B **2**, 1618 (1990).

[45] T. Kolber, W. Rozmus, and V. T. Tikhonchuk, Phys. Plasmas **2**, 256 (1995).

[46] T. Kolber, W. Rozmus, and V. T. Tikhonchuk, Phys. Fluids B **5**, 138 (1993).

[47] R. P. Drake and S. H. Batha, Phys. Fluids **3**, 2936 (1991).

[48] J. C. Fernández et al., Phys. Rev. Lett. **77**, 2702 (1996).

[49] R. K. Kirkwood et al., Phys. Rev. Lett. **77**, 2706 (1996).

[50] K. L. Baker, *Saturation of Langmuir Waves in Laser-Produced Plasmas*, PhD thesis, University of California, Davis, 1996.

[51] K. L. Baker et al., Phys. Rev. Lett. **77**, 67 (1996).

[52] R. J. Focia, *Investigation and Characterization of Single Hot Spot Laser-Plasma Interactions*, PhD thesis, Electrical Engineering and Computer Science Department, Massachusetts Institute of Technology, 2001.

[53] D. S. Montgomery et al., Phys. Plasmas **9**, 2320 (2002).

[54] D. S. Montgomery et al., Phys. Rev. Lett. **87**, 155001 (2001).

[55] J. L. Kline et al., Phys. Rev. Lett. **94**, 175003 (2005).

[56] H. X. Vu, B. Bezzerides, and D. F. DuBois, J. Comput. Phys. **156**, 12 (1999).

[57] H. X. Vu, D. F. DuBois, and B. Bezzerides, Phys. Rev. Lett. **86**, 4306 (2001).

[58] H. X. Vu, D. F. DuBois, and B. Bezzerides, Phys. Plasmas **9**, 1745 (2002).

[59] S. Brunner and E. J. Valeo, Phys. Rev. Lett. **93**, 145003 (2004).

[60] H. A. Rose and D. A. Russell, Phys. Plasmas **8**, 4784 (2001).

[61] H. A. Rose, Phys. Plasmas **10**, 1468 (2003).

[62] L. Nikolić, M. M. Škorić, S. Ishiguro, and T. Sato, Phys. Rev. E **66**, 036404 (2002).

[63] W. L. Kruer, K. Estabrook, B. F. Lasinski, and A. B. Langdon, Phys. Fluids **23**, 1273 (1980).

[64] F. W. Chambers, *Space-time evolution of instabilities in laser-plasma interactions*, PhD thesis, Physics Department, Massachusetts Institute of Technology, 1975.

[65] D. J. Strozzi, M. M. Shoucri, and A. Bers, Comput. Phys. Comm. **164**, 156 (2004).

[66] D. J. Strozzi, M. M. Shoucri, A. Bers, E. A. Williams, and A. B. Langdon, J. Plasma Phys. (2005), submitted.

[67] A. Bers, Linear waves and instabilities, in *Physique des Plasmas - Les Houches 1972*, edited by C. DeWitt and J. Peyraud, Gordon and Breach, New York, 1975.

[68] B. Coppi, M. N. Rosenbluth, and R. N. Sudan, Ann. Phys. **55**, 207 (1969).

[69] C. C. Chow and A. Bers, Phys. Rev. A **47**, 5144 (1993).

[70] A. Bers, Space-time evolution of plasma instabilities - absolute and convective, in *Handbook of Plasma Physics, Vol. 1*, edited by M. N. Rosenbluth and R. Z. Sagdeev, chapter 3.2, North-Holland, Amsterdam, 1983.

[71] R. J. Briggs, *Electron-Stream Interaction with Plasmas*, MIT Press, Cambridge, MA, 1964.

[72] A. B. Langdon, Phys. Rev. Lett. **44**, 575 (1980).

[73] B. B. Afeyan, A. E. Chou, J. P. Matte, R. P. J. Town, and W. J. Kruer, Phys. Rev. Lett. **80**, 2322 (1998).

[74] V. B. Krapchev, Phys. Rev. Lett. **42**, 497 (1979).

[75] C. L. Tang, J. Appl. Phys. **37**, 2945 (1966).

[76] J. D. Huba, *NRL Plasma Formulary*, Naval Research Lab, Washington, DC, 2000.

[77] W. L. Kruer, *The Physics of Laser Plasma Interactions*, Addison-Wesley, Redwood City, CA, 1988.

[78] G. Bekefi, *Radiation Processes in Plasmas*, John Wiley and Sons, New York, 1966.

[79] C. Oberman and G. Auer, Phys. Fluids **17**, 1980 (1974).

[80] R. L. Berger, E. A. Williams, and A. Simon, Phys. Fluids B **1**, 414 (1989).

[81] A. Einstein, Phys. Zeit. **18**, 121 (1917).

[82] K. Y. Sanbonmatsu, H. X. Vu, D. F. DuBois, and B. Bezzerides, Phys. Rev. Lett. **82**, 932 (1999).

[83] P. Y. Cheung et al., Phys. Rev. Lett. **62**, 2676 (1989).

[84] D. F. DuBois, D. Russel, and H. A. Rose, Phys. Plasmas **2**, 76 (1995).

[85] C. J. Walsh, D. M. Villeneuve, and H. A. Baldis, Phys. Rev. Lett. **53**, 1445 (1984).

[86] D. M. Villeneuve, H. A. Baldis, and J. E. Bernard, Phys. Rev. Lett. **59**, 1585 (1987).

[87] H. A. Baldis et al., Phys. Rev. Lett. **62**, 2829 (1989).

[88] T. Katsouleas and W. B. Mori, Phys. Rev. Lett. **61**, 90 (1988).

[89] T. P. Coffey, Phys. Fluids **14**, 1402 (1971).

[90] J. M. Dawson, Phys. Rev. **113**, 383 (1959).

[91] H. A. Rose, D. F. DuBois, and B. Bezzerides, Phys. Rev. Lett. **58**, 2547 (1987).

[92] A. B. Langdon and D. E. Hinkel, Phys. Rev. Lett. **89**, 015003 (2002).

[93] A. Bers, *Plasma Physics and Plasma Electrodynamics*, Oxford University Press, Oxford, UK, in preparation.

[94] I. B. Bernstein, J. M. Greene, and M. D. Kruskal, Phys. Rev. **108**, 546 (1957).

[95] A. J. Lichtenberg and M. A. Lieberman, *Regular and Chaotic Dynamics*, Springer-Verlag, New York, NY, second edition, 1992.

[96] H. Goldstein, *Classical Mechanics*, Addison-Wesley, Reading, Mass., second edition, 1980.

[97] R. Sugihara and T. Kamimura, J. Phys. Soc. Japan **33**, 206 (1972).

[98] M. Porkolab and R. P. H. Chang, Rev. Mod. Phys. **50**, 745 (1978).

[99] J. H. Malmberg and C. B. Wharton, Phys. Rev. Lett. **19**, 775 (1967).

[100] C. B. Wharton, J. H. Malmberg, and T. M. O'Neil, Phys. Fluids **11**, 1761 (1968).

[101] W. M. Manheimer and R. W. Flynn, Phys. Fluids **14**, 2393 (1971).

[102] A. Lee and G. Pocobelli, Phys. Fluids **15**, 2351 (1972).

[103] R. L. Dewar, Phys. Fluids **15**, 712 (1972).

[104] D. C. Barnes, Phys. Plasmas **11**, 903 (2004).

[105] L. D. Landau, J. Phys. U.S.S.R. **10** (1946).

[106] M. N. Rosenbluth, R. B. White, and C. S. Liu, Phys. Rev. Lett. **31**, 1190 (1973).

[107] D. Pesme, G. Laval, and R. Pellat, Phys. Rev. Lett. **31**, 203 (1973).

[108] A. I. Akhiezer and R. V. Polovin, Zh. Eksp. Teor. Fiz. **30**, 915 (1956), [Sov. Phys. JETP **3**, 696 (1956)].

[109] W. B. Mori and T. Katsouleas, Phys. Scripta **T30**, 127 (1990).

[110] M. S. Jovanović and M. M. Škorić, Phys. Scripta **54**, 200 (1996).

[111] S. Miyamoto, K. Mima, M. M. Škorić, and M. S. Jovanović, J. Phys. Soc. Japan **67**, 1281 (1998).

[112] C. K. Birdsall and A. B. Langdon, *Plasma Physics via Computer Simulation*, Springer-Verlag, New York, NY, 1989.

[113] J. C. Adam, A. G. Serveniere, and A. B. Langdon, J. Comput. Phys. **47**, 229 (1982).

[114] G. Hammett, presented at the 18$^{\text{th}}$ International Conference on the Numerical Simulation of Plasma, Falmouth, Massachusetts, USA, 2003.

[115] T. Dannert and F. Jenko, Comput. Phys. Commun. **163**, 67 (2004).

[116] S. Brunner, private communication.

[117] A. Ghizzo et al., J. Comput. Phys. **90**, 431 (1990).

[118] T.-H. Watanabe, H. Sugama, and T. Sato, J. Phys. Soc. Japan **70**, 3565 (3002).

[119] E. Sonnendrucker, J. Roche, P. Bertrand, and A. Ghizzo, J. Comput. Phys. **149**, 201 (1999).

[120] E. Pohn, M. Shoucri, and G. Kamelander, Comput. Phys. Commun. **166**, 81 (2005).

[121] C. Z. Cheng and G. Knorr, J. Comput. Phys. **22**, 330 (1976).

[122] G. Strang, SIAM J. Numer. Anal. **5**, 506 (1968).

[123] N. N. Yanencko, *The Method of Fractional Steps*, Springer-Verlag, New York, 1970.

[124] Eric W. Weisstein. "Baker-Campbell-Hausdorff Series." From MathWorld–A Wolfram Web Resource. http://mathworld.wolfram.com/Baker-Campbell-HausdorffSeries.html.

[125] C. H. Cooke, J. Comput. Phys. **67**, 472 (1986).

[126] Matteo Frigo and Steven G. Johnson, FFTW homepage `http://www.fftw.org/`.